INTERPRETING GPS OBSERVATIONS

OF THE MEGATHRUST EARTHQUAKE CYCLE:

INSIGHTS FROM NUMERICAL MODELS

MARIO D'ACQUISTO

Members of the reading committee:

Prof. dr. W. Spakman
Department of Earth Sciences
Utrecht University

Prof dr. A.F. Deuss
Department of Earth Sciences
Utrecht University

Prof. dr. O. Oncken
Department 4: Geosystems
GFZ German Research Centre for Geosciences

Prof. dr. A. Hooper
School of Earth and Environment
University of Leeds

Prof. dr. R. Malservisi
School of Geosciences
University of South Florida

Cover illustration: bathymetry and topography from the SYNBATH model (Sandwell *et al.*, 2022) in the surroundings of the Japan trench, visualized using the Generic Mapping Tools (GMT) (Wessel *et al.*, 2019).

INTERPRETING GPS OBSERVATIONS

OF THE MEGATHRUST EARTHQUAKE CYCLE:

INSIGHTS FROM NUMERICAL MODELS

INTERPRETATIE VAN GPS-WAARNEMINGEN

VAN DE AARDBEVINGSCYCLUS BIJ SUBDUCTIE ZONES:

INZICHTEN UIT NUMERIEKE MODELLEN
(met een samenvatting in het Nederlands)

Proefschrift

ter verkrijging van de graad van doctor aan de Universiteit Utrecht op gezag
van de rector magnificus, Prof. Dr. H.R.B.M. Kummeling, ingevolge het
besluit van het college voor promoties in het openbaar te verdedigen op
vrijdag 14 april 2023 des middags te 2.15 uur

door

Mario D'Acquisto

geboren op 15 september 1994 te Rome, Italië

Promotor: Prof. dr. J.A. Trampert

Copromotor: Dr. R.M.A. Govers

Contents

1
Introduction

1.1 Background: Geodesy and Understanding the Megathrust Earthquake Cycle

1.1.1 Introduction

The work in this thesis concerns the megathrust earthquake cycle at subduction zones. Subduction zones are where one tectonic plate sinks beneath another ("subducts"). The megathrust dips down from an oceanic trench and is the interface zone between the subducting and overriding plate. The megathrust accommodates the continuous relative motion between the two plates on geological time scales. At any one time, most megathrusts are locked, in scattered patches, by high friction that prevents fault slip. Megathrust earthquakes result from sudden, rapid slip along the megathrust when shear stresses accumulate up to the point that they overcome the frictional strength of these locked patches ("asperities"). The concept of the earthquake cycle is tightly connected to the theory of interseismic elastic stress accumulation and coseismic rebound that Reid (1908) developed following the 1906 San Francisco earthquake on the strike-slip San Andreas fault. The cycle of stress accumulation and release at subduction zones begins and ends with a great megathrust earthquake, with a recurrence interval decades to centuries long (Allen *et al.*, 1965; Allen *et al.*, 1970; Tobin and Sykes, 1968; Shimazaki and Nakata, 1980; Sieh, 1981). The earthquake cycle involves three main stages: the earthquake is the coseismic stage that lasts less than a second for small earthquakes, and up to 10 minutes during the largest earthquakes; the postseismic stage is a period of days to decades of relatively rapid changes in surface deformation and sea level following the earthquake; the interseismic stage is the period,

1

up to millennia in length, leading to the next earthquake. Despite the name, the earthquake cycle it is not cyclic in the physics sense of being strictly regular, and particularly the largest earthquakes occur irregularly (Sieh, 1981) and sometimes in clusters (Meltzner *et al.*, 2010; Meltzner *et al.*, 2015; Philibosian *et al.*, 2014; Philibosian *et al.*, 2017; Melnick *et al.*, 2017).

Great megathrust earthquakes, defined as having a moment magnitude M_W above 8, are the most powerful earthquakes that occur on Earth. They pose significant risks to the human populations and activities located in coastal areas above subduction zones. Great megathrust earthquakes also represent one of the most dramatic manifestations of plate tectonics. Considerable scientific effort is therefore directed towards the study of these earthquakes. Earthquake seismology focuses on recording and analyzing ground and subsurface motion (waves and shaking) during earthquakes. Kinematic geodesy measures surface deformation that occurs during all stages of the earthquake cycle, including deformation associated with earthquakes. The fields of earthquake geology and paleogeodesy study and interpret geological records of the earthquake cycle. In this thesis, I focus on the interpretation of geodetic observations related to the megathrust earthquake cycle.

Scientific understanding of the megathrust earthquake cycle evolved over time. A mechanical understanding of deformation at subduction zones was enabled by the first explorations of their structure. Vening Meinesz (1931) and Vening Meinesz (1932) observed negative gravity anomalies offshore, parallel to island arcs, and proposed that they were caused by lithospheric flexure. Wadati (1935), Benioff (1954), and Hirokichi *et al.* (1957) mapped seismologically determined locations of earthquake hypocenters, which defined planes (the Wadati-Benioff zones) dipping down from oceanic trenches under volcanic arcs and orogens. Isacks *et al.* (1968) and Isacks *et al.* (1969) used focal mechanisms determined from seismological observations to infer that the shallow earthquakes in the Wadati-Benioff zones are caused by underthrusting along a fault plane parallel to the dip of the zone itself. This suggested that an oceanic lithospheric plate was being underthrust beneath another in these regions. These were termed subduction zones and were rapidly acknowledged (Sales, 1968; Dickinson, 1970; Dietz and Holden, 1970; Hamilton, 1970) to play a crucial role in the process of continental drift (Wegener, 1912; Wegener, 1924; Wilson, 1963; Wilson, 1965; Wilson, 1966) and in the mantle convection that accommodates continental drift (Holmes, 1928; Holmes, 1931).

Early observations of surface deformation during great earthquakes were made in the first half of the 20th century, using classical geodetic methods, specifically triangulation, leveling, and relative sea level change. Some observations recorded the static surface offsets caused by large megathrust earthquakes

in Japan, most notably the 1923 South Kanto (Miyabe, 1931; Muto, 1932), 1944 Tonankai and 1946 Nankaido earthquakes (Okuda, 1950; Miyabe, 1955). Later, the 1960 M_W 9.4–9.6 Valdivia (Chile) and 1964 M_W 9.2 Alaska (USA) megathrust earthquakes prompted major scientific investigations of their co-seismic deformation (Weischet and Huene, 1963; Plafker, 1965; Plafker, 1969; Plafker, 1972; Plafker and Savage, 1970). These investigations described significant horizontal and vertical surface motion, with maxima greater than 20 m, resulting from underthrusting. Meade (1965) and Meade (1971) and Hofmann *et al.* (1968) used classical geodesy and optical ranging methods to observe surface motion during the interseismic period on the San Andreas strike-slip fault. These observations were later used to infer the mechanical behavior of major plate boundary faults and regions, in the context of increasing acceptance and refinement of the theory of plate tectonics.

1.1.2 Evolving Understanding and Physics-Based Models

The mechanical behavior of the subduction zone consists of processes occurring largely in the subsurface, on and around the megathrust. However, scientific observations of the deformation can only be made at the Earth's surface, or above it or at relatively shallow depths beneath it. In particular, geodetic observations, which can describe motion throughout the megathrust earthquake cycle, commonly observe the motion of the solid surface. Using these observations to study the deformation associated with the megathrust earthquake cycle thus requires tools that link surface observations to relevant subsurface processes and properties. The necessary tools are physics-based models, i.e., structures, systems or procedures that simulate the features and behavior of (some parts or aspects of) the world in accordance with physical laws. Models focusing on the megathrust earthquake cycle generally need to cover vastly different timescales and/or spatial scales and to have arbitrarily variable parameters within a large space of possible values. Therefore, the models generally used are quantitative, i.e., based on mathematics, as opposed to analog, i.e., scaled physical representations of the subject of the study. More specifically, the quantitative models used are based on mathematical descriptions of continuum mechanics, i.e., the relationships between forces, mass and motion in a continuous medium.

Simulating the deformation that results from given model parameters, representing physical properties and structure, is called forward modeling. Quantitative models can also be used to solve inverse problems, i.e., determining the model parameters producing deformation that best approximates given obser-

vations of the real world. Inverse models use a forward modeling component that links model parameters and observable quantities, together with deterministic or probabilistic inversion methods that infer the parameters that best explain the observed data. Quantitative forward models can be either numerical or analytical. Analytical models consist of mathematical functions (closed-form solutions) that solve mathematical equations describing the relevant physical laws. An example of an analytical model is a Green's function describing deformation in semi-infinite elastic half-space due to discontinuous displacement (e.g., Steketee, 1958). Numerical models compute solutions to the physics equations via a variety of numerical algorithms. An example of a type of numerical models is finite element models. Finite element methods discretize a relevant spatial domain into a set of elements defined by a polygon mesh. They then use the discretization to transform relevant differential equations into a system of linear equations whose solution approximates the differential equation solution at all mesh nodes (e.g., Zienkiewicz, 1971; Bathe and Wilson, 1976). Both analytical and numerical models have proved very valuable means to understand the megathrust earthquake cycle.

The increasing availability and quality of seismological and geodetic observations since the 1970s led to the introduction of the first physics-based quantitative models of deformation resulting from fault slip. In particular, Savage and Burford (1973) quantitatively linked geodetic observations to fault creep by modeling the surface motion resulting from slip in a uniform, linearly elastic, continuous medium (Steketee, 1958; Weertman and Weertman, 1964). They found that portions of the San Andreas fault appeared to be undergoing creep, i.e., slow, steady slip, while nearby portions were instead locked, with strain probably accumulating in the surrounding region. Other studies instead focused on the observed deformation during great earthquakes (Chinnery, 1961; Hastie and Savage, 1970; Plafker, 1972; Shimazaki, 1972; Kanamori and Cipar, 1974). They also employed models describing the deformation of a homogenous elastic half-space in response to slip, in this case the coseismic fault slip. Meanwhile, Mescherikov (1968) and Scholz (1972) focused on the cyclical nature of deformation in zones hosting great earthquakes. They observed how slow movement at a roughly constant rate alternated with period of movement at different rates, consisting of a sometimes present slight increase in rate of motion for some time before the earthquake, followed by sudden rapid coseismic motion and rapidly decaying postseismic motion. They also recognized that the rapid surface motion caused by the earthquake was opposite in direction to interseismic motion. Scholz (1972), studying strike-slip faults, explicitly suggested that motion throughout the earthquake cycle could be modeled as resulting from elastic deformation in response to slip.

In such a model, interseismic slip occurs in the opposite sense as coseismic slip and correspond to the lack of slip, i.e. the build-up of slip deficit, which accumulates elastic strain, as already suggested by Scholz and Fitch (1969), and accordingly increases frictional shear tractions on the fault (Walsh, 1968). Modeling slip in an elastic half-space was thus established as a useful means to link surface deformation to motion on major faults, during both coseismic and interseismic periods. The introduction of the moment magnitude scale by Hanks and Kanamori (1979) yielded independent constraints on coseismic slip magnitude and dimensions of the rupture surface.

1.1.3 Postseismic Relaxation and Different Modeling Approaches

Savage and Prescott (1978), Spence and Turcotte (1979), and Thatcher and Rundle (1979) summarized and improved the understanding of the earthquake cycle. In their understanding, mantle flow and aseismic creep on non-locked portions of the fault allowed elastic strain to build up next to the locked portions. When a locked portion ruptured, it hosted seismogenic slip, after which build-up of strain resumed. These studies also began to develop and apply more sophisticated models of subsurface deformation. Following early work that postulated and modeled viscous flow in the asthenosphere (Elsasser and Runcorn, 1969; Bott and Dean, 1973), they introduced the use of analytical models of response to a slip in an elastic plate overriding a viscoelastic half-space (Nur and Mavko, 1974; Rundle, 1978). Savage and Prescott (1978) and Spence and Turcotte (1979) focused on major strike-slip faults, while Thatcher and Rundle (1979) on a subduction megathrust. These studies marked the start of the use of variously sophisticated physics-based models to explain geodetic observations, and simultaneously of the debate about which models were sufficient, necessary, and ultimately more accurate in describing the deformation within the Earth.

A key motivation for Thatcher and Rundle (1979) was the desire to explain the postseismic surface motion observed geodetically after the Nankaido and South Kanto megathrust earthquakes (Okada and Nagata, 1953; Matuzawa, 1964; Ando, 1975). Because of the limitations of geodetic methods available at the time (i.e., leveling and tide gauges, mainly), the observations consisted primarily of vertical displacement time series at a few locations. These showed subsidence in the early postseismic period over several tens of km from the coast, in contrast with coseismic uplift and with a pattern of near-coastal subsidence and uplift farther afield in the late interseismic period. Building on previous efforts (Fitch and Scholz, 1971; Bischke, 1974; Nur and Mavko, 1974;

Smith, 1975), Thatcher and Rundle (1979) developed a model of the megathrust earthquake cycle in which postseismic deformation was due to a combination of afterslip and viscous relaxation. Afterslip, i.e., postseismic slip caused by coseismic stress changes, occurred on the deeper portion of the megathrust, downdip of the section that ruptured coseismically. Viscous relaxation, i.e., the postseismic bulk viscous flow relaxing (reducing) the stress changes caused by the earthquake, occurred in a viscoelastic half-space with Maxwell rheology (Jaeger, 1956). This half-space represented the asthenosphere and underlay elastic plates. Thatcher and Rundle (1979) concluded that viscoelastic relaxation alone was not sufficient to explain postseismic surface motion, as had been proposed by Nur and Mavko (1974) using different analytical solutions for the response of an elastic plate and Maxwell viscoelastic half-space to slip.

The necessity of considering viscous deformation was not immediately accepted by all researchers. Savage (1983) argued that deep afterslip alone, rather than a combination of afterslip and viscoelastic relaxation, explained the vertical postseismic displacement observed following the Nankaido earthquake. This study also applied the conceptual framework of Scholz and Fitch (1969) and Scholz (1972) to a subduction zone context, inaugurating the use of a backslip approach for the interseismic phase of the megathrust earthquake cycle. In this approach, the superposition of two elastic deformation processes simulated strain accumulation due to interseismic subduction, with the slab moving downdip at depth but held in place at shallower depths by the locked megathrust. One of the two processes was the slab sinking at a uniform rate, with respect to the overriding plate and underlying asthenospheric wedge. The other process was slip in the direction opposite to that of subduction (i.e., backslip) in the coupled portion of the megathrust only, adding up to no net slip (i.e., locking) on the megathrust and no locking on the slab-wedge interface.

Thatcher and Rundle (1984), in contrast with Savage (1983), argued again that their model including viscous flow was more accurate and better explained observations made in Japan during different stages of the earthquake cycle, particularly interseismic vertical velocities in the southwest. They also remarked that the interseismic velocity pattern in northeast Japan, in contrast, could be explained neither by their model nor by an elastic half-space one, and that postseismic evolution was more observed complex than their model results. Their viscoelastic earthquake cycle model built on previous mathematical model development by Rundle (1976), Rundle (1978), Rundle (1980), Rundle (1982), and Rundle and Jackson (1977) and improved on previous studies of the megathrust earthquake cycle in two ways: it included the effects of interseismic viscous flow induced by subduction of the slab, mechanically coupled to the overlying asthenospheric wedge, and gravity-induced buoyancy

(isostatic) effects. At the same time, another series of studies had developed a numerical modeling methodology that could simulate viscous and viscoelastic material with non-linear as well as linear viscosities (i.e., relationships between stress σ and strain rate $\dot{\varepsilon}$), with arbitrary geometry and slip distribution (Melosh, 1976; Melosh, 1978; Melosh and Raefsky, 1983; Melosh and Raefsky, 1980; Melosh and Raefsky, 1983; Melosh and Fleitout, 1982).

1.1.4 Development of Satellite Geodesy and Related Models

The advent of space-based geodesy revolutionized the study of deformation associated with the megathrust earthquake cycle. Radar observations from spacecraft, especially synthetic aperture radar interferometry (InSAR), were valuable (e.g., Massonnet *et al.*, 1993; Peltzer *et al.*, 1996; Massonnet and Feigl, 1998), as were gravity field measurements from satellites (e.g., Han *et al.*, 2006; Ogawa and Heki, 2007; Panet *et al.*, 2007; Götze and Mahatsente, 2010) and observations of the geoid via satellite altimetry (e.g., McAdoo, 1981; Horai, 1982). Particularly useful were observations from global navigation satellite systems (GNSSs), beginning with those from Global Positioning System (GPS) in the late 1980s (see Segall and Davis, 1997, for an early review). In fact, GNSS observations of displacement provided a much clearer picture of surface motion than before, at least in horizontal directions. Vertical displacement determined by GPS initially had uncertainties too high to be useful. Interseismic GPS observations showed slow landward motion of the coast and thus compression of broad regions adjacent to overriding plate margins known to host earthquakes (Snay and Matsikari, 1991; Dixon, 1993; Freymueller and Kellogg, 1993). This deformation was shown to be consistent with elastic strain accumulation due to interplate convergence with a locked megathrust in a fully elastic medium in two-dimensional (2D) (Hyndman and Wang, 1993; Hyndman and Wang, 1995; Dragert *et al.*, 1994; Dragert and Hyndman, 1995) and three-dimensional (3D) models (Verdonck, 1995; Flück *et al.*, 1997). GPS observations also showed a lack of significant strain accumulation in portions of subduction zones not known to host great earthquakes, such as the Shumagin Islands area in Alaska (Larson and Lisowski, 1994). One exciting finding regarding interseismic deformation was the recognition of slow slip events on the megathrust (Heki *et al.*, 1997; Hirose *et al.*, 1999). Overall, GPS observation provided insight into the interseismic behavior of the subduction system, showing where elastic strain was being accumulated, not accumulated, or slowly released.

Wang *et al.* (1994) constructed a 2D megathrust earthquake cycle model

and investigated what features, if any, could explain precise interseismic observations on Vancouver Island in Cascadia, including at GPS sites. The model incorporated a viscoelastic asthenospheric mantle, with lower viscosity in the asthenospheric wedge than in the sub-slab mantle, and a viscoelastic shear zone as the downdip continuation of the megathrust. Wang *et al.* (2001) successfully used a 3D viscoelastic earthquake cycle model to explain interseismic velocities at a greater number of stations in the Cascadia subduction zone. Hetland and Hager (2006) further investigated the effect of including a viscoelastic asthenosphere in modeling interseismic deformation within an earthquake cycle. They found that including repeated earthquake cycles in the model allows for stresses to build up, in a spin-up process, after which the interseismic surface deformation is invariant from cycle to cycle and resembles a fully elastic model. Other studies, however, constructed fully elastic models that successfully explained interseismic deformation, accounting for a downdip transition from the fully locked brittle megathrust to a fully, stably creeping shear zone (Wang *et al.*, 2003; McCaffrey *et al.*, 2007). All these studies showed that the interseismic loading of a megathrust system with a viscoelastic mantle was different than that of an elastic system, but did not agree on the need to include a viscoelastic rheology to explain interseismic GNSS observations.

While interseismic deformation was being observed and modeled in greater detail, geodetic evidence of postseismic viscous relaxation had been accumulating. The velocities of GPS sites in Chile, in the area where the 1960 earthquakes occurred, were directed landward close to the coast, consistently with interseismic convergence and strain accumulation due to a locked megathrust, but were directed oceanward farther inland (Kendrick, 1997; Klotz *et al.*, 2001). This was interpreted as evidence of long-lived postseismic viscous relaxation, on the basis of numerical models with Maxwell viscoelastic mantles (Khazaradze *et al.*, 2002; Hu *et al.*, 2004; Wang, 2007). Similarly to Chile, oceanward GPS velocities were observed in the plate interior (western Kenai peninsula and Anchorage area) of the region affected by the 1964 Alaska earthquake, directed opposite to velocities closer to the trench (Cohen and Freymueller, 1997; Savage *et al.*, 1998; Savage *et al.*, 1999; Freymueller *et al.*, 2000; Freymueller *et al.*, 2008; Sauber *et al.*, 2006). This was also explained invoking enduring postseismic relaxation, at first only modeling deep afterslip in an elastic medium (Freymueller *et al.*, 2000; Zweck *et al.*, 2002). Later, combined models of afterslip and viscous relaxation were introduced (Sauber *et al.*, 2006; Suito and Freymueller, 2009), which showed that considering both postseismic relaxation mechanisms was important to explain postseismic surface motion.

1.1.5   Modern Understanding of Postseismic Motion

The 21st century has so far seen several great megathrust earthquakes, the most powerful of which were the 2004 M_W 9.1–9.3 Sumatra-Andaman and 2011 M_W 9.1 Tohoku. The coseismic and postseismic displacements associated with these and other great megathrust earthquakes was extensively observed by networks of GPS stations and allowed leaps in the scientific understanding of the megathrust earthquake cycle.

The Sumatra-Andaman earthquake was the largest in magnitude since the 1964 Alaska event. Deformation associated with it was recorded, apart from seismological and gravity observations, by GPS observations, including high-frequency as well as daily GPS displacement time series. GPS observations captured coseismic motion and helped ascertain the extremely large extent of the megathrust rupture (Banerjee *et al.*, 2005; Banerjee *et al.*, 2007; Vigny *et al.*, 2005; Kreemer *et al.*, 2006). GPS observations also shows substantial postseismic motion, with velocities directed oceanward in their horizontal component all over the overriding Sunda plate (Hashimoto *et al.*, 2006; Pollitz *et al.*, 2006; Banerjee *et al.*, 2007; Paul *et al.*, 2007; Gahalaut *et al.*, 2008a). Some studies incorporated afterslip alone in their models attempting to reproduce viscous relaxation (Hashimoto *et al.*, 2006; Hsu *et al.*, 2006; Banerjee *et al.*, 2007; Paul *et al.*, 2007). Hashimoto *et al.* (2006) justified the decision to not include viscoelastic relaxation as due to the characteristic timescale of decay of postseismic signals, shorter than would be expected from viscous relaxation. However, Pollitz *et al.* (2006) and Pollitz *et al.* (2008) explained postseismic observations by modeling afterslip and asthenospheric viscous relaxation with a Burgers viscoelastic rheology (Ivins, 1996; Pollitz, 2003). Such a rheology includes two distinct viscosities and thus characteristic relaxation times and could thus explain both the rapidly decaying postseismic signals and the longer-lived postseismic relaxations, lasting for decades. Pollitz *et al.* (2008) also considered the effect of a spatially heterogeneous viscosity structure, building on previous finite element modeling advancements (Masterlark, 2003; Hu *et al.*, 2004), finding that it better explained vertical displacements. These studies showed that a combination of afterslip and viscous relaxation best explained observed postseismic deformation and that spatio-temporal rheological complexity was needed to reproduce the data.

The 2011 Tohoku earthquake was, and arguably still is, the great megathrust earthquake whose deformation was best recorded, in terms of the variety, spatial coverage and accuracy of observations (e.g., Wang *et al.*, 2018b, for an overview). Geodetic observations consisted most notably of displacement time series from onshore GNSS stations and from offshore GPS-acoustic (GPS-A)

observations, which use GNSS positioning of a vessel or buoy on the ocean surface and acoustic ranging between the ship and a cluster of fixed transponders to precisely locate a station on the ocean floor (Purcell *et al.*, 1993; Kido *et al.*, 2017, e.g.,). These observations were inverted into detailed distributions of coseismic slip (e.g., for compilations of coseismic slip models; cf. Tajima *et al.*, 2013; Brown *et al.*, 2015; Sun *et al.*, 2017). Coseismic slip was unusually large in the shallow, near-trench portion of the megathrust (e.g. Meng *et al.*, 2011; Sun *et al.*, 2017), although different inversions disagreed on exactly how large it was and whether it peaked at the trench or at greater depths (Wang *et al.*, 2018a). Postseismically, onshore GNSS observations showed substantial oceanward velocities, consistently with the expected motion of the overriding plate due to both viscous relaxation and afterslip (e.g. Wang *et al.*, 2012). Remarkably, however, some offshore GPS-A observations, on the overriding plate near the trench, showed landward motion beginning shortly (less than two months) after the earthquake (Guard, 2013; Sun *et al.*, 2014; Watanabe *et al.*, 2014) and occurring at a faster rate than interplate convergence. This contradicted the expectation that landward motion would progressively spread over the overriding plate over years, at rates no higher than interseismic convergence, as relocking is restored and its effect prevails over postseismic relaxation (Wang *et al.*, 2012). Please refer to Chapter 4, Figure 4.1 for a schematic cross-sectional overview of postseismic deformation following a large megathrust earthquake, showing onshore and offshore motion after the 2011 Tohoku earthquake. Sun *et al.* (2014) reproduced GNSS and GPS-A observations of postseismic displacement following the Tohoku earthquake by incorporating afterslip and viscous relaxation, with a relatively low viscosity, in a 3D model. In particular, viscous flow was needed to explain the fast near-trench landward motion of the overriding plate, while shallow afterslip could explain the offshore GPS-A sites moving oceanward. The results of Sun *et al.* (2014) were substantially confirmed by later studies, which essentially established the importance of viscous relaxation. These later studies also added nuance and complexity to the subsurface features that they used to explain postseismic observations (Watanabe *et al.*, 2014; Yamagiwa *et al.*, 2015; Freed *et al.*, 2017; Suito, 2017; Noda *et al.*, 2018; Agata *et al.*, 2019; Muto *et al.*, 2019; Fukuda and Johnson, 2021; Dhar *et al.*, 2022). For instance, Freed *et al.* (2017) pointed out the importance of a layered viscosity structure and a cold nose in the asthenospheric wedge in explaining vertical surface displacement. Suito (2017) argued for a low-viscosity layer at the top of the oceanic mantle, underlying the subducting plate, to explain both far- and near-field horizontal postseismic motion simultaneously. Agata *et al.* (2019) and Dhar *et al.* (2022) went beyond a biviscous Burgers rheology while reproducing GNSS observations of postseismic motion due to

the Tohoku earthquake. They used asthenospheric rheologies more consistent with laboratory experiments (Hirth and Kohlstedt, 2003; Karato and Jung, 2003), with non-linear, power-law stress-strain rate relationships, as first applied in forward megathrust cycle modeling by Melosh (1976), Melosh (1978), Melosh and Raefsky (1983), Melosh and Raefsky (1980), Melosh and Raefsky (1983), and Melosh and Fleitout (1982).

1.1.6 Further Complexities and Open Questions

Analysis of the postseismic displacement time series observed via satellite geodesy following 21st-century megathrust earthquakes was not geographically restricted to Sunda and Japan. For instance, Chile was also an important source of data, as it hosted three great megathrust earthquakes in the 2010s: M_W 8.8 2010 Maule, M_W 8.1 2014 Iquique, and M_W 8.3 2015 Illapel. Boulze et $al.$ (2022) analyzed the spatial pattern of cumulative postseismic GNSS displacement after the three Chilean earthquakes and concluded that they were similar, despite the different magnitudes. This strongly suggested that the mantle behaved according to a linear (Maxwell or Burgers) viscoelastic rheology, as opposed to a rheology with power-law viscosity. In contrast, however, Peña et $al.$ (2019), Peña et $al.$ (2020), and Peña et $al.$ (2021) found that a combined viscous relaxation and afterslip model with power-law rheology in the viscoelastic lower crust and upper mantle better explained GPS observations following the Maule earthquake, compared to linear rheologies.

Other studies of postseismic deformation caused by great megathrust earthquakes considered processes different from viscous flow and afterslip. As recognized by Wang et $al.$ (2012), relocking of the megathrust plays an important role in determining the evolution of surface motion in the postseismic period. In fact, the progressive ramping-down of afterslip allows for renewed locking of the megathrust, and as the signature of viscous relaxation also decreases, the effect of interplate convergence with a newly locked megathrust leads to landward motion and shortening progressively extending over the overriding plate. Bedford et $al.$ (2016) thus attempted to isolate the effect of relocking from that of afterslip and viscous relaxation by analyzing the direction of motion described by GNSS displacement time series after the Maule earthquake, possible because of the obliqueness of interplate convergence. They concluded that relocking happens rapidly, between instantly and 1 year after the rupture. Remy et $al.$ (2016) instead analyzed postseismic GNSS observations following the smaller (M_W 8.0) 2007 Pisco (Peru) earthquake to determine the decay of afterslip, ignoring viscous relaxation, and concluded that the rapid decay (with a characteristic timescale of less than 3 years) implied rapid relocking,

as a lack of postseismic slip implies, mechanically, that the megathrust is newly coupled. However, there have been no efforts to incorporate megathrust relocking into a forward modeling approach that can capture the other key postseismic processes.

As several approaches and models were used to explain increasingly extensive and complex postseismic observations starting after the 2004 Sumatra-Andaman earthquake, different approaches were applied to interpreting interseismic observations and highlighted different kinds of complexities in subsurface behavior. Various sophisticated inversion schemes, both deterministic and probabilistic, were set up to determine where on megathrusts elastic strain are being accumulated, as slip deficit is building up, and where and when they are not accumulated or released, by stable creep or episodic slow slip (e.g., Yoshioka *et al.*, 2005; Suwa *et al.*, 2006; Chlieh *et al.*, 2008; Moreno *et al.*, 2008; Loveless and Meade, 2011; Loveless and Meade, 2016; Métois *et al.*, 2012; Métois *et al.*, 2013; Métois *et al.*, 2014; Métois *et al.*, 2016; Nocquet *et al.*, 2014; Gombert *et al.*, 2018). For the forward modeling of surface motion resulting from fault locking, these studies used analytical solutions for dislocation in an elastic half-space, usually taken from Okada (1985), and applied the backslip approach introduced by Savage (1983). Such a methodology is computationally inexpensive and enables the use of those sophisticated, computationally demanding inversion schemes. The results of these inversions detailed the heterogenous spatial distribution of interplate coupling, expressed as a fraction of the stable long-term interplate convergence rate. Furthermore, areas of strong coupling generally agreed with the location of ruptures producing great megathrust earthquakes (e.g., Suwa *et al.*, 2006; Chlieh *et al.*, 2008; Hashimoto *et al.*, 2009; Liu *et al.*, 2010; Moreno *et al.*, 2010; Loveless and Meade, 2011; Protti *et al.*, 2014; Métois *et al.*, 2016; Gombert *et al.*, 2018), even confirming expectations of studies that preceded recent earthquakes (e.g., Métois *et al.*, 2012; Métois *et al.*, 2013; Métois *et al.*, 2014). This corroborated the criteria elaborated in the 1960s and 1970s for where to expect great earthquakes in the near future (cf. Section 1.1.1; Fedotov, 1965; Tobin and Sykes, 1968; Kelleher *et al.*, 1973; Ando, 1975).

Li *et al.* (2018b) went beyond the use of elastic models in inverting GNSS observations into interseismic coupling distributions. They recognized that viscous flow in the asthenosphere implied a different response of the mechanical system to loading compared to a fully elastic Earth, including during stable interseismic convergence with a locked megathrust. They thus employed a 3D finite element model with Maxwell viscoelastic asthenospheres underlying the two elastic plates in the deterministic inversion of the GNSS velocities into a megathrust coupling distribution for the Cascadia subduction zone. They

showed that strong coupling needed to extend to shallower depths to explain the observed surface velocities, compared to inversions that assumed an entirely elastic subsurface. Itoh *et al.* (2019) not only used Maxwell viscoelastic asthenospheric mantles in a finite element model, but also found that interseismic observations in the southern Kurile subduction zone were best explained by a heterogeneous asthenospheric wedge and overriding plate, with greater compliance in the arc and (to a lesser extent) back-arc regions, compared to the forearc. Itoh *et al.* (2021) then used such a heterogenous overriding plate and asthenospheric wedge to invert observed interseismic velocities at GNSS stations in that subduction zone into a coupling distribution, finding that a shallower depth of full coupling was needed to explain observations compared to previous inversions with simpler models. Herman *et al.* (2018) instead called attention to the physical meaning of interseismic coupling inversions. They used a geometrically simple finite element model with a Maxwell viscoelastic mantle wedge to show how slip deficit accumulated in regions of the megathrust adjacent to fully coupled asperities, because of the mechanical continuity of the plate on either side, in a phenomenon they called pseudo-coupling. Herman and Govers (2020) applied the pseudo-coupling concepts, although using analytical solutions for slip in an elastic half-space, to perform a probabilistic inversion of GNSS observations along the Andean subduction zone into the location and geometry of truly locked asperities. They found that relatively small asperities (less than 50 km in linear size) could explain observations and defined a locking distribution in agreement with known ruptures and previous coupling inversions. However, despite these various advances in the understanding of megathrust behavior and of the role of viscoelastic rheologies in the interseismic period, elastic half-space forward models continue to be routinely used to invert GNSS velocities into distributions of interplate coupling expressed as fractions of the interplate convergence rate.

Inversions of geodetic observations into megathrust coupling not only captured snapshots of locking averaged over certain time periods, but also revealed temporal variations in such coupling (e.g., McCaffrey *et al.*, 2000; Nishimura *et al.*, 2004; Loveless and Meade, 2016). According to Loveless and Meade (2016), these variations included preseismic increases in the size of the locked areas of the megathrust along the Japan trench before the 2011 Tohoku earthquake and postseismic increase in the locked areas hundreds of km away from the rupture zone. However, other studies cast doubt on whether these apparent postseismic changes in coupling reflected effective changes of locking on the megathrust. Heki and Mitsui (2013) interpreted the surface velocity increase in the landward direction, associated with the Tohoku earthquake and later mapped by Loveless and Meade (2016) into increased megathrust coupling,

as caused by interplate convergence acceleration due to an altered force balance. Melnick *et al.* (2017) observed similar velocity changes associated with the 2010 Maule earthquake and proposed they could be explained by bending associated with postseismic relaxation. Melnick *et al.* (2017) further argued that the deformation they proposed as explanation of the landward velocity increases associated with the 2010 Maule earthquake also triggered the 2015 Illapel megathrust earthquake and possibly explained geological evidence of clustering in paleoseismic megathrust activity (Meltzner *et al.*, 2010; Meltzner *et al.*, 2015; Philibosian *et al.*, 2014; Philibosian *et al.*, 2017). Meanwhile, Nocquet *et al.* (2014) had analyzed classical geodetic, GNSS, and paleoseismic geological observations. They had concluded that the 1906 M_W 8.8 earthquake in the Ecuador-southern Colombia subduction zone followed a period of seismic quiescence and inaugurated a new supercycle of increased seismogenic strain release, during which two co-located megathrust earthquakes released more strain than accumulated since the 1906 event. These studies prompted a more general questioning (Loveless, 2017) of the validity of the common assumption that the megathrust earthquake cycle involves regularly periodic ruptures of fixed asperities, each associated with interseismic strain accumulation in a given pattern at a constant rate. However, little agreement exists regarding the nature of the spatio-temporal interaction of different asperities, or indeed even what the spatiotemporal evolution in the coupling distribution is. For instance, Mavrommatis *et al.* (2014), Mavrommatis *et al.* (2017), and Abe and Yoshioka (2022) concluded that the size of locked asperities along the Japan Trench gradually decreased over the years before the 2011 Tohoku earthquake, in contrast with the inversion results of Loveless and Meade (2016), and proposed a physics-based model of reduction in asperity size through time, invoking thermal pressurization. Saillard *et al.* (2017) instead analyzed GNSS velocities, historical earthquake records, and coastal geomorphology of the Andean subduction zone and found that locked areas evidenced by geodesy coincided with historical ruptures and recesses in the coastline. They thus concluded that long-lived asperities probably exist on the megathrust as frictional, physical features. Yuzariyadi and Heki (2021) analyzed interseismic GNSS displacement time series and highlighted landward increases in velocities in areas located laterally to the rupture following four other megathrust earthquakes worldwide, apart from those associated with the Tohoku and Maule earthquakes and first noticed respectively by Heki and Mitsui (2013) and Melnick *et al.* (2017). The mechanism responsible for these fairly commonly observed postseismic motions remains unclear.

1.2 Purpose and Approach

1.2.1 General Goals and Methods

The purpose of this thesis is to investigate some open scientific questions related to the study of megathrust earthquake cycles. It makes use of the advancements in understanding of the paste few decades while taking the opportunity to clarify some aspects of deformation during the cycle that remain poorly understood, explored, or agreed upon.

Great effort has been devoted to explain specific observations using models. Many recent (and not-so-recent) studies focus on specific geodetic observations in specific subduction zones and choose specific methods that best allow interpreting those observations. These methods involve models, often numerical, that incorporate some physics in an attempt to link subsurface deformation and dynamics, which cannot be observed directly, to observations recorded on Earth's surface (or from orbit). The results of these models generally explain observations very successfully and can be greatly insightful. However, it is important to recognize that a successful inverse model does not imply that the deformation in the model closely approximates the reality of subsurface deformation. This is the case because of the great degree of non-uniqueness of the possible models that fit observations, as well as because of the complexity of the subsurface structure and rheology and of the processes that occur there. Additionally, as seen in Section 1.1, the models that are effective and convenient to use for one phase of the cycle are not necessarily convenient for all phases, and there is much disagreement regarding which processes should be incorporated in models that attempt to explain observations made in different phases.

In this thesis, I investigate processes what may be expected to occur near multiple, if not all, subduction zones globally. This approach involves building forward models of the cycle that incorporate their main physical features like approximate geometry, an elastic slab and overriding plate, and viscoelastic asthenosphere. It then uses the results of these models to gain insight into general processes that can explain widespread geodetic observations. Given the greater accuracy of the horizontal component of GNSS displacement time series and velocities and the greater complexity apparently needed to explain the vertical displacements and velocities, in this thesis I focus on horizontal motion. The models in this thesis are similar to each other. They use forward numerical modeling methods that allow largely arbitrary physical parameters and treatment of internal and external boundaries. More specifically, the models use the finite element technique, which allows arbitrary model mesh

resolution and arbitrary geometry of the volumes within the models. Additionally, the volumes can have discrete boundaries between them, which can host relative motion, freely, with a resisting traction, or by an imposed slip or slip rate (Melosh and Raefsky, 1981; Melosh and Williams, 1989). The numerical modeling software used to solve the mechanical equilibrium equation over time is GTECTON (Govers and Wortel, 2005; Govers *et al.*, 2018).

In this thesis, I construct 3D earthquake cycle models with viscoelastic mantle underlying elastic plates. This choice is made in accordance with the wide consensus that 3D viscoelastic flow is needed to explain postseismic observations (e.g., Wang *et al.*, 2012; Sun *et al.*, 2014; Watanabe *et al.*, 2014; Yamagiwa *et al.*, 2015) and with the recognition that it is relevant also for interseismic loading of the material on either side of the megathrust (Hetland and Hager, 2006; Li *et al.*, 2018b). Each model is spun up via multiple earthquake cycles, as the response of viscoelastic material to a repeated cycle differs from the response to the first earthquake cycle with non-zero initial stresses (Hetland and Hager, 2006). The two main postseismic relaxation mechanisms, viscous relaxation and afterslip, are included. Relocking is also included, and its timing is the subject of Chapter 3. To avoid having to arbitrarily impose a realistic coseismic slip distribution driving deformation, and to capture the loading and unloading of the plates and asthenosphere during convergence and earthquake-associated deformation, the models are driven by imposed convergence of the plates, by the coupling and pseudo-coupling due to fully locked asperities (after Herman *et al.*, 2018), and by imposed periodic unlocking and relocking of each asperity. Along-trench variation in subduction zone geometry and rheological heterogeneity in either the plates or mantle are excluded from the models, unless when deliberately introduced to investigate specific mechanisms. This follows from the choice of not aiming to reproduce specific observations, which requires complexity, but of investigating mechanisms, which is only made more difficult by additional complexity. For the sake of simplicity and ease of analysis of model sensitivities to other parameters, and since no single study in the thesis focuses on capturing the entirety of postseismic deformation over timescales varying from months to decades after the earthquake, a linear Maxwell viscosity is used. This viscosity is varied by orders of magnitude depending on the specific goal of the study and also to test the sensitivity of the model results to values that are more in line with the long-term or short-term decay of postseismic deformation in subduction zones worldwide.

1.2.2 Content of This Thesis

The rest of this thesis consists of three chapters, focusing on different observations. In the next, Chapter 2, I analyze the spatial distribution of interseismic velocities in connection with the loading of the overriding plate. The motivation for this work is that interseismic velocities decrease rapidly with distance from the trench and reach near-zero values within several hundreds of km, while coseismic displacements extend to thousands of km from the trench during large megathrust earthquakes. Additionally, analyses of interseismic deformation at subduction zones generally focus on specific geographical regions and on inverting observations into coupling distributions. They often do so via elastic half-space models or via finite element models with boundaries relatively close to the trench, generally ignoring some rheological and mechanical structure, especially in the plates. This chapter instead considers the far-field velocity field over the entirety of the overriding plate, where interseismic GNSS velocities are available, at three well-instrumented subduction zones. The goal is to better understand what features are needed to explain the far-field distribution of interseismic velocities. The study separates the observed velocities into locally trench-perpendicular and trench-parallel components, interpolates them into continuous fields, and observes a discontinuity ("hurdle") in the trench-perpendicular gradient of both components, generally following major geological or tectonic boundaries. It then successfully tests the hypothesis that a discontinuity in plate compliance can explain the hurdle. It also explores the sensitivity of the results to bulk mechanical parameters, including the specific compliance contrast, to different megathrust locking distributions, and to the characteristic timescale of relaxation in relation to the earthquake recurrence interval. The key implication is that the contrast between the deformed, tectonically young plate margin region and the more stable plate interior is important to explain the observed macroscopic distribution of interseismic velocities.

The last two chapters focus on postseismic deformation and discuss poorly understood, apparent or real, locking behavior of the megathrust. In particular, Chapter 3 investigates the apparent increases in coupling inferred to have occurred after six different megathrust earthquakes, for which different alternative mechanisms were proposed (Heki and Mitsui, 2013; Melnick *et al.*, 2017; Yuzariyadi and Heki, 2021). The goal is to investigate the deformation that can be explained by a regular earthquake cycle, with no variations in coupling nor slab acceleration. The hypothesis is that plate bending during postseismic relaxation can explain the observed landward increases in surface velocities, as proposed by Melnick *et al.* (2017). The study finds that viscous

relaxation following the earthquake can produce landward velocity increases in portions of the overriding plate located laterally along the trench. It investigates this mechanism, finding it can indeed be described as in-plane bending of the overriding plate, driven by the oceanward viscous flow in the asthenospheric wedge. However, the intensity and temporal persistence of observed velocity changes cannot be explained by this mechanisms, regardless of the several different model parameters tested. The hypothesis is thus falsified, with the exciting implication that further work is needed to ascertain the cause of observations. Another important implication is that the observed landward velocity increases probably results from increased slip deficit accumulation in the regions of the subduction zones where they are observed, with implications for seismic hazard.

Finally, Chapter 4. This was observed shortly after the Tohoku earthquake and prompted many models of postseismic viscous relaxation, indeed definitively establishing the importance of viscoelastic rheologies in the study of the megathrust earthquake cycle (Sun *et al.*, 2014; Watanabe *et al.*, 2014; Yamagiwa *et al.*, 2015; Freed *et al.*, 2017; Suito, 2017; Noda *et al.*, 2018; Agata *et al.*, 2019; Muto *et al.*, 2019; Fukuda and Johnson, 2021; Dhar *et al.*, 2022). The chapter also focuses more broadly on postseismic deformation, and specifically on another mechanism, megathrust relocking, whose timing remains poorly understood. In fact, the chapter hypothesizes a connection between megathrust relocking and postseismic observations of rapid near-trench overriding plate motion, postulating that relocking is needed for such observations. Model results show that this is indeed the case, which is interpreted to indicate that the offshore landward motion reflects the landward motion of the slab as a result of deep afterslip and of viscous relaxation in the sub-slab mantle. They also indicate that such landward motion needs a locked shallow megathrust relocking to transmit to the tip of the overriding plate. The chapter also discusses the implications for the frictional nature of the shallow megathrust of the need for it to be locked shortly after the earthquake.

Chapter 2 was submitted as a manuscript for publication in Geophysical Journal International; a moderate revision of the manuscript is currently under review. Chapter 3 was published in Journal of Geophysical Research: Solid Earth as D'Acquisto *et al.* (2023). Chapter 4 was published in Geophysical Research Letters as D'Acquisto and Govers (2023).

2

Reconciling the conflicting extent of overriding plate deformation before and during megathrust earthquakes in South America, Sunda, and northeast Japan

2.1 Introduction

The great megathrust earthquakes of the previous decades happened after or during the deployment of continuous geodetic networks. Many studies focused on constraining the coseismic fault slip during these earthquakes by combining geodetic with seismological observations (e.g., Simons *et al.*, 2011; Vigny *et al.*, 2011). Postseismic processes like relocking, afterslip and viscoelastic flow started to become apparent in the geodetic measurements shortly after these events and continue today, spawning a rich variety of studies that cast new light on processes and rheological properties. The first earthquake that revealed the widespread extent of coseismic deformation via satellite geodesy
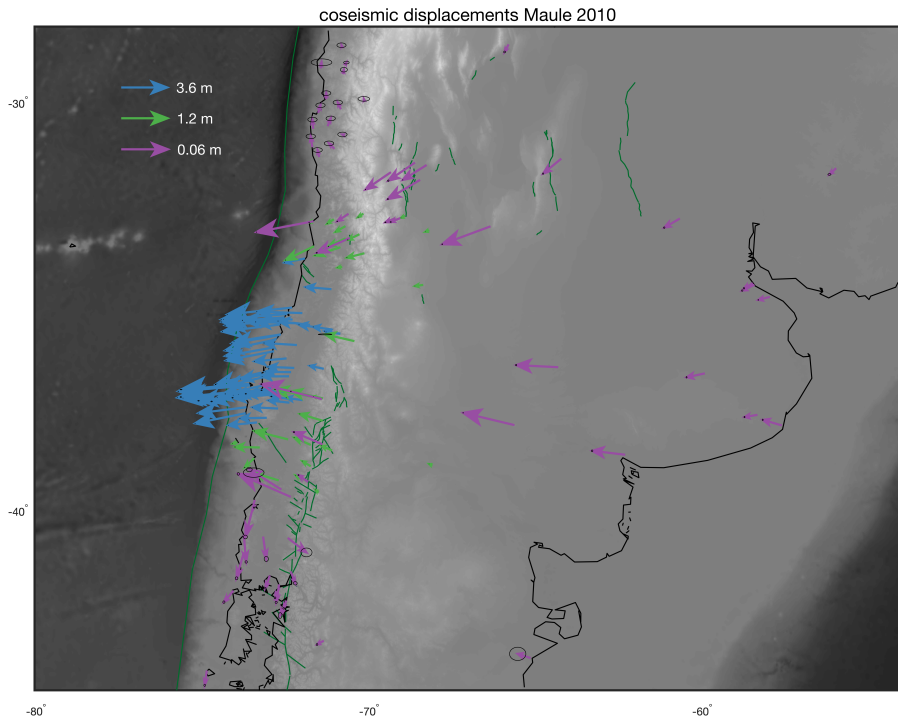
Figure 2.1 Horizontal coseismic displacements observed at GNSS sites during the 2010 Maule earthquake. Observations are sourced from Delouis *et al.* (2010), Lin *et al.* (2013), Moreno *et al.* (2012), Tong *et al.* (2010), and Vigny *et al.* (2011).

was the Mw 9.2 2004 Sumatra-Andaman earthquake. Remarkably, coseismic displacements were recorded at GNSS stations more than 3,000 km away from the megathrust (Vigny *et al.*, 2005). Similarly, GNSS stations far into the South American continent recorded displacement due to the Mw 8.8 2010 Maule (Chile) earthquake as far as 1,700 km from the trench (Figure 2.1; Pollitz and Thatcher, 2010). Likewise, Wang *et al.* (2011) observed significant coseismic static offsets up to 2,500 km away from the epicenter following the Mw 9.0 2011 Tohoku earthquake.

Strain that has accumulated during interseismic periods (mostly) recovers during large megathrust earthquakes and resulting postseismic relaxation (e.g., Wang *et al.*, 2012) and, in at least some cases, also in slow-slip events (SSEs) (e.g., Dixon *et al.*, 2014; Protti *et al.*, 2014; Voss *et al.*, 2017). Several studies

have focused on determining the interseismic megathrust locking pattern and correlating it to the coseismic slip pattern (e.g., Moreno *et al.*, 2010; Loveless and Meade, 2011; Protti *et al.*, 2014; Malservisi *et al.*, 2015; Nocquet *et al.*, 2017). Observed interseismic velocities (relative to a stable overriding plate reference) are directed landward and decrease with distance from the trench. Interseismic strain buildup seems to focus closer to the margin of the overriding plate, within several hundreds of kilometers from the trench (e.g. Drewes and Heidbach, 2012; Kreemer *et al.*, 2014; McKenzie and Furlong, 2021; Simons *et al.*, 2007), compared to deformation due to the largest megathrust earthquakes. In many locations, a distinct break in the slope of the interseismic velocity gradient is observed; from a high velocity gradient near the trench to a small velocity gradient farther away (Brooks *et al.*, 2003; Khazaradze and Klotz, 2003; Nocquet *et al.*, 2014; McFarland *et al.*, 2017).

Explanations of the observations vary. The decrease in interseismic velocities with increasing distance from the trench can often be reproduced using a model with a (partly) locked megathrust fault in an elastic halfspace (Chlieh *et al.*, 2008; Ruegg *et al.*, 2009; Liu *et al.*, 2010; Métois *et al.*, 2012). For parts of the South American plate, Norabuena et al. (1998) pointed out that interseismic strain accumulation is higher farther inland than could be explained by megathrust locking in a fully elastic Earth. Studies focusing on the Central Andes (Norabuena *et al.*, 1998; Bevis *et al.*, 2001; Brooks *et al.*, 2003; McFarland *et al.*, 2017; Shi *et al.*, 2020) therefore adopted a seismically active backthrust to explain the observed presence of interseismic strain accumulation and of a stable interior beyond the backthrust. Other studies identify slivers or microplates that are bounded by major faults and that are interpreted as decoupled from the rest of the overriding plate, thus deforming and rotating with respect to the plate interior (Métois *et al.*, 2014; Nocquet *et al.*, 2014). Both explanations rely on active faults or shear zones, such as backthrusts with a trench-perpendicular length of 200 km (Weiss *et al.*, 2016; McFarland *et al.*, 2017), that reach deep into the lithosphere and allow near-independent motion of adjacent tectonic domains.

As stated above, interpretations of interseismic strain accumulation are commonly based on fully elastic models, in which overriding plate velocities decrease rapidly with distance from the trench. Postseismic stress relaxation demonstrates however that the asthenosphere behaves viscoelastically. Models with a viscoelastic asthenosphere rheology predict interseismic velocities that decrease more gradually with distance from the trench compared to elastic models (Wang *et al.*, 2012). For increasingly higher asthenospheric viscosities, model results converge to elastic-like behavior with strain accumulation that is more concentrated in the near-trench region (Trubienko *et al.*, 2013; Li *et*

al., 2015; Li *et al.*, 2020; Shi *et al.*, 2020). Lower model viscosities result in interseismic velocities that remain significant up to thousands of kilometers into the overriding plate. To match the observed interseismic velocities with their viscoelastic models, Trubienko *et al.* (2013) and Li *et al.* (2015) use long-term (Maxwell) viscosities effectively in the range of 4.0–5.1 $cdot 10^{19}$ Pa·s when accounting for the use of plane-strain two-dimensional (2D) models on the relaxation timescale (Melosh and Raefsky, 1983). These values are well beyond the high end of the range of estimates of asthenospheric wedge viscosities (4.0–$10 \cdot 10^{18}$ Pa · s) from recent studies of postseismic viscous relaxation (Hu and Wang, 2012; Broerse *et al.*, 2015; Klein *et al.*, 2016; Li *et al.*, 2018a; Qiu *et al.*, 2018; Agata *et al.*, 2019; Muto *et al.*, 2019; Fukuda and Johnson, 2021, see Section 5.2).

The South American margin has played a significant role in the development of ideas about interseismic strain accumulation because of the presence of an extensive continental plate interior. In other subduction zones, the gradient of interseismic velocities is also observable over a wide distance, although the view is fragmented because of offshore regions with no GNSS observations Figures 2.2 and 2.3. Interseismic velocities in Sumatra before the 2004 earthquake show a distinct decrease with distance from the trench (Prawirodirdjo *et al.*, 2010; Simons *et al.*, 2007), even though the trench-parallel motions are strongly affected by the Sumatran Fault (Genrich *et al.*, 2000). Similarly, landward velocities in northern Honshu (Japan) and Hokkaido, recorded before the 2003 Tokachi and 2011 Tohoku earthquakes (Sagiya *et al.*, 2000), show a steep decrease with distance from the trench. More significant difficulties in observing the interseismic velocity gradient arise in other subduction margins like Cascadia, where other tectonic processes overprint the interseismic locking signal, like the Mendocino Crustal Conveyor (Furlong and Govers, 1999) and the northward migration of the Sierra Nevada-Great Valley block (Williams *et al.*, 2006). In southern Honshu and Shikoku, strain rates due to convergence on the Japan trench and Nankai trench are superimposed, which makes it difficult to isolate the far-field interseismic velocity pattern. As discussed in (Govers *et al.*, 2018), continental Alaska shows continuing postseismic relaxation following the 1964 Prince William Sound earthquake. For these reasons, we focus on regions which, although exhibiting tectonic complexities, show identifiable signatures of interplate convergence and megathrust locking and for which data unaffected by postseismic relaxation are available: South America, Sunda, and northern Japan.

In the present study we address the apparently contrasting geodetic observation that interseismic deformation of the overriding plate focusses within several hundreds of kilometers from the trench, whereas coseismic strain re-

lease extends over much greater distances. We observe a break in the slope of trench-parallel and trench-perpendicular velocity components as a function of trench distance, which we refer to as a hurdle. Long-lived subduction tectonically accretes blocks and deforms the overriding plate, by an amount that depends on existing lithospheric compliance contrasts (Mouthereau *et al.*, 2013; Pearson *et al.*, 2013). These compliance contrasts, inherited and resulting from tectonic rejuvenation, remain visible today as significant contrasts in the effective elastic thickness of the lithosphere (Watts, 2015) that correlate with tectonic boundaries between different blocks (Watts *et al.*, 1995; Stewart and Watts, 1997). Convergent deformation, including backthrusts, likely localizes at these naturally occurring contrasts. Here we consider the possibility that these lateral contrasts cause the hurdle-like behavior of the overriding plate. Because of our context of the earthquake cycle we consider contrasts in elastic properties.

Our study consists of two main elements: mapping the patterns of interseismic velocities, and interpreting interseismic velocity gradients in terms of mechanical contrasts. We characterize the spatial pattern of horizontal interseismic surface motion along the South America Trench, the Sunda Trench and Japan Trench based on available observations Section 2.2. Near-trench regions are typically (much) more densely instrumented than intermediate and far-field regions, and interseismic velocities of benchmarks have variable uncertainties. We account for how these factors propagate into uncertainties in the interpolated velocity fields. We estimate the approximate location of the hurdle, the dominant break in the slope of interseismic velocities, and discuss its significance.

To test our hypothesis that hurdle-like behavior is related to elastic contrasts in the overriding plate, we construct a three-dimensional viscoelastic numerical model (Section 2.3), analyze our model results and their robustness (Section 2.4). Next, we discuss their significance and possible interpretations in the context of other proposed causes (Section 2.5). We conclude (Section 2.6) that a mechanical contrast in the overriding plate, with a more compliant near-trench region and a less compliant far-field region, is a likely candidate for explaining both the interseismic and coseismic observations in the three analyzed subduction zones.

2.2 Analysis of Interseismic Velocity Observations

2.2.1 Data Selection

We compile previously published horizontal velocities along three convergent margins with abundant interseismic GNSS observations: the Peru-Chile Trench (South America) (Kendrick *et al.*, 2001; Klotz *et al.*, 2001; Brooks *et al.*, 2003; Brooks *et al.*, 2003; Brooks *et al.*, 2011; Chlieh *et al.*, 2004; Gagnon *et al.*, 2005; Ruegg *et al.*, 2009; Seemüller *et al.*, 2010; Drewes and Heidbach, 2012; Métois *et al.*, 2012; Métois *et al.*, 2013; Métois *et al.*, 2014; Alvarado *et al.*, 2014; Nocquet *et al.*, 2014; Blewitt *et al.*, 2016; Weiss *et al.*, 2016; McFarland *et al.*, 2017; Klein *et al.*, 2018b), the Sunda Trench (Sumatra and Java, Indonesia) (Genrich *et al.*, 2000; Bock *et al.*, 2003; Simons *et al.*, 2007; Chlieh *et al.*, 2008; Prawirodirdjo *et al.*, 2010; Kreemer *et al.*, 2014; Koulali *et al.*, 2017), and the Japan Trench (Sagiya *et al.*, 2000; Apel *et al.*, 2006; Jin and Park, 2006; Liu *et al.*, 2010; Nishimura, 2011; Ohzono *et al.*, 2011; Shestakov *et al.*, 2011; Yoshioka and Matsuoka, 2013; Kreemer *et al.*, 2014; Freed *et al.*, 2017). To prevent contamination by postseismic velocities that are oceanward and opposite to landward interseismic velocities, we exclude velocities following significant ($M_w \geq 7.5$) earthquakes in the trench-perpendicular sector of the subduction zone where the megathrust event occurred (see Figure 2.2), unless the published velocities were explicitly corrected for postseismic transients. Please refer to the Tables 2.1 to 2.3 for more details on the observation period of data sources and possible postseismic corrections. We use velocities expressed in the global reference frame ITRF (Altamimi *et al.*, 2011). For the majority of our data sources we make use of the velocity tables from (Kreemer *et al.*, 2014), who have estimated a translation rate and rotation rate for each published set of velocities to express velocities in the same IGS08 reference frame (the IGS realization of ITRF2008; Rebischung *et al.*, 2012). We feature velocities expressed in ITRF2005, ITRF2008, and ITRF2014; differences resulting from these different realizations are well below the 1 mm $\cdot$ yr^{-1} level (Métivier *et al.*, 2020). We also include velocities from Weiss *et al.* (2016), which are only provided in a self-determined, non-explicit South America reference frame. However, biases because of different reference frames are small: the mean difference in velocities between those of Weiss and the South America far-field velocities of Blewitt *et al.* (2016) is below 0.2 mm $\cdot$ yr^{-1}.

Subsequently, we transform ITRF-expressed velocities to the overriding plate reference. For the sites in South America and Japan we apply the South

America and Okhotsk Euler poles, respectively, of Kreemer *et al.* (2014). For Sumatra we make use of the Sunda Euler pole of Simons *et al.* (2007), who identify Sundaland as a coherent block moving independently of the South China block farther north. More information about data sources is available in Section 2.9.2 and Tables 2.1 to 2.3. The resultant interseismic velocities, described in a consistent reference frame throughout each studied region, show a clear contrast between high near-trench velocities and a stable interior (fig. 2.2).

2.2.2 Velocity Decomposition Into Trench-Perpendicular and -Parallel Components

We define a conformal projection using a Schwarz-Christoffel map (Driscoll, 2002) to identify trench-perpendicular and -parallel directions in our study areas. This produces a coordinate system that smoothly grades, from precisely aligned (parallel and perpendicular) to the trench at the trench, to aligned with the broad regional trend of the trench in the plate interior. From the mathematical mapping of geographical coordinates into local trench-perpendicular and -parallel coordinates we derive the angles between the two orthogonal coordinate systems at an arbitrary location, allowing us to compute the trench-perpendicular and trench-parallel components of each velocity vector. Figures S1-S3 in the Supporting Information show the mapping of the local coordinate grid into geographical coordinates (also shown in Figure 2.2) and the decomposition of the velocities in locally trench-parallel and trench-perpendicular components.

2.2.3 Interpolation of the Decomposed Velocity Fields

Most geodetic studies of GNSS interseismic deformation have focused on the deforming zones close to the margin for the purpose of estimating megathrust locking. In most regions, GNSS stations are unevenly distributed, much more densely in near-trench areas than farther away from the trench, in the far-field plate interior that is used as the stable reference. To obtain homogeneously-distributed velocity amplitudes and estimate the location of velocity gradient discontinuities, we separately interpolate the observed trench-perpendicular and -parallel velocity components. We account for the propagation of observational uncertainty and for the potential velocity variability in between observation sites in the following way. We interpolate the velocities and estimate uncertainties using ordinary kriging (Wackernagel, 2003), a weighted mean method that relies on the statistics of the observed data. The mean, variance and correlation of the velocity field are spatially heterogeneous, so

velocities with respect to stable South America

velocities with respect to stable Sunda
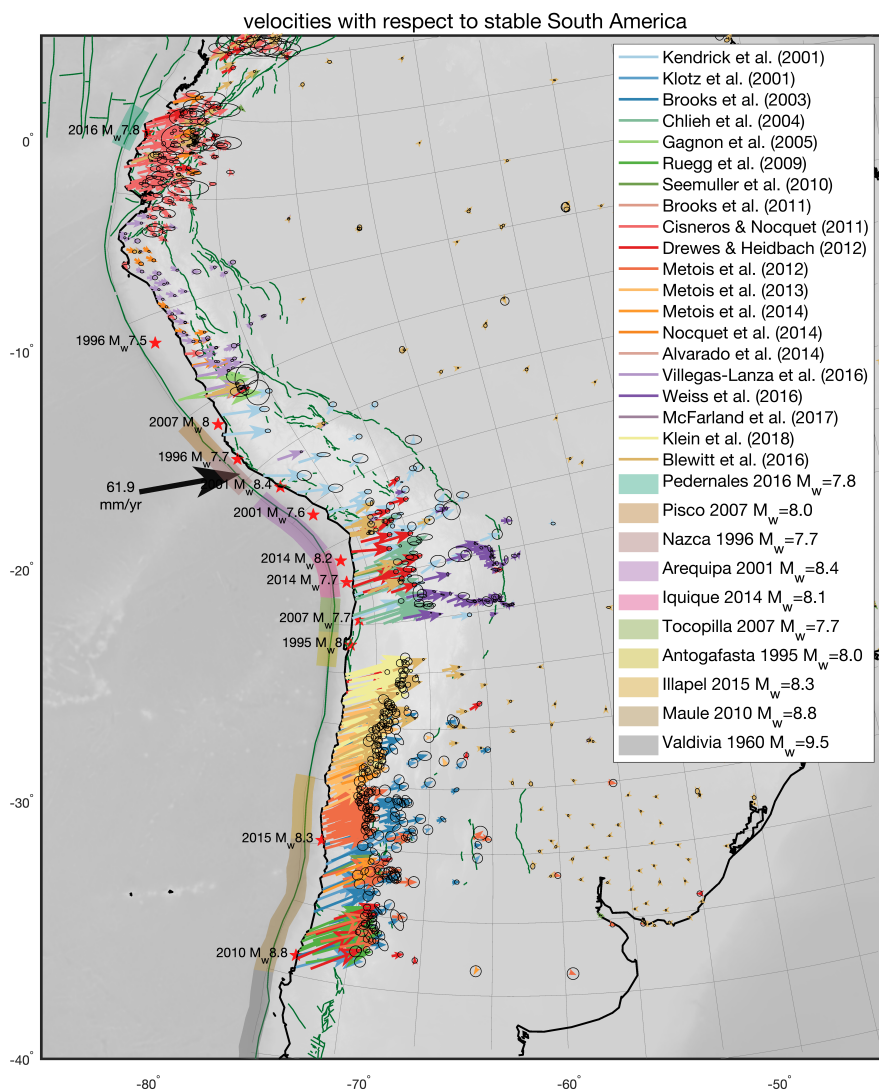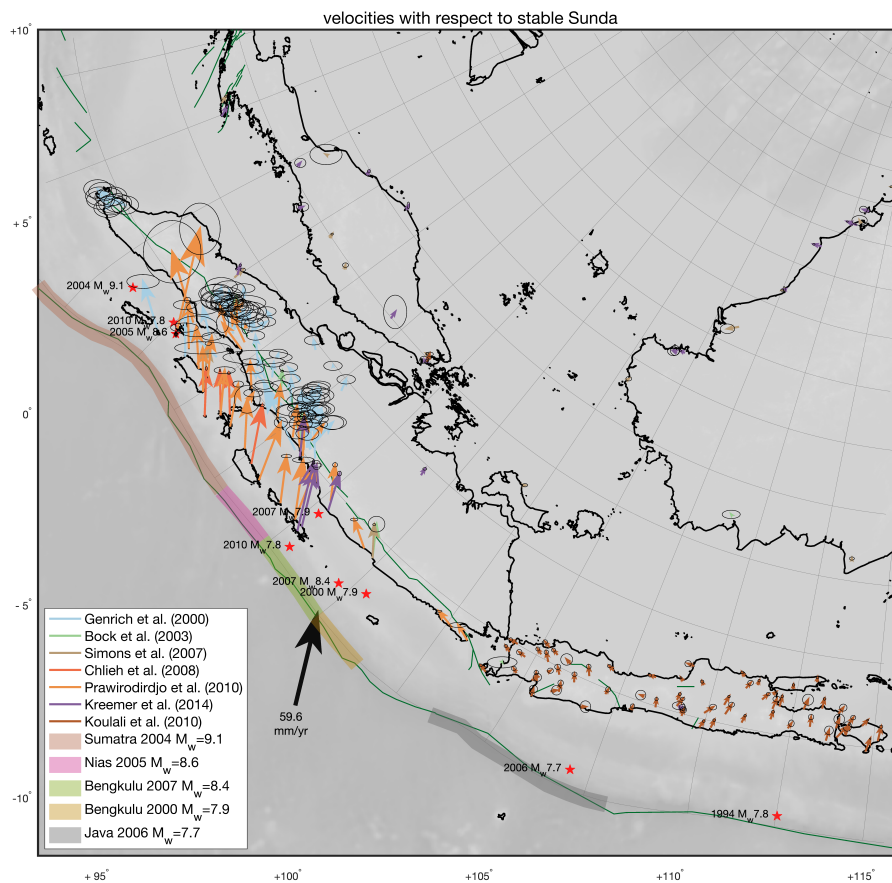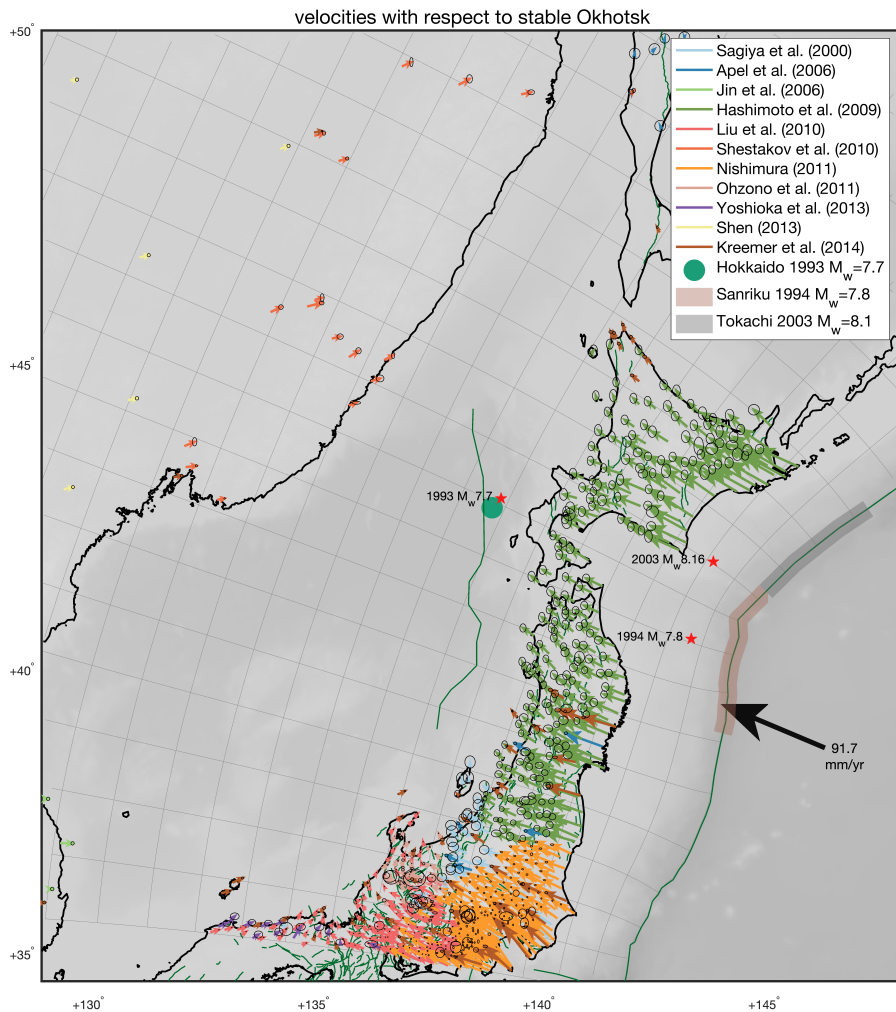
Figure 2.2 Interseismic GNSS data that we use in our study regions. Panels show published geodetic velocities, coastlines and topography, and active faults in green. Thick black arrows show interplate convergence velocities from Kreemer *et al.* (2014) (South America), Simons *et al.* (2007) (Indonesia), and Kreemer *et al.* (2014). Red stars show epicenters of earthquakes ($M_w \geq 7.5$) that affect our data selection as follows. In each segment of the subduction zone that hosted such earthquake, we discard all velocities from our estimate of the interseismic velocity field. Specifically, we exclude data in the region affected by coseismic displacements and postseismic transients indicated by colored sections of the trench. In South America, we thus exclude all data after the 1995 Antofagasta earthquake. Similarly, we exclude all post-2011 Tohoku data in Japan. Velocities increase towards the west in southwest Hokkaido likely due to postseismic relaxation after the 1993 Hokkaido Nansei earthquake (Ueda *et al.*, 2003), which is why we exclude these data also. We set data exclusion zones stretching from the indicated parts of the trench to a given distance from the trench (1000 km and 1500 km for events larger than $M_w \geq 8.7$), which we apply to data collected after the events. Gray lines show the conformal grid that we use to identify trench-perpendicular/parallel directions.

we define natural neighborhoods to construct correlograms that describe the local variability of the velocity field (Broerse et al., in prep.; Fouedjio and Séguret, 2016; Machuca-Mory and Deutsch, 2013). We specifically account for the curvature of the Earth in the computation of distances and the choice of covariance models in the kriging procedure. Further technical details are in Section 2.9.2 and Figures 2.15 to 2.26 in Section 2.9.

The uncertainties we compute for our interpolated velocity field reflect both the uncertainty of velocity observations (i.e., data uncertainty) and the expected variance of the velocity field between observation points. Figures 2.24 to 2.26 show that uncertainties of the interpolated velocity field are small in regions with little variability in observed velocities, but increase substantially with distance from observation points in regions where observed velocities vary significantly in between observation points.

2.2.4 Estimation of the Hurdle Location

The hurdle constitutes the main discontinuity in velocity gradients separating the interseismically deforming margin from the stable interior. We use the gridded interpolated velocity fields together with their uncertainty estimates to estimate the hurdle location as function of distance from the trench. First, we take trench-perpendicular profiles, which are equidistant at the trench, through the 2D interpolated field, 277 in total for South America, 64 for Sunda, and 51 for Japan. Subsequently, we fit a piece-wise continuous function consisting of two linear segments to the velocity as function of distance along the profile. We use weighted non-linear least squares with a Trust Region algorithm, using as weights the inverse of variances from the kriging. The junction between the two segments, located in the fitting process, constitutes the hurdle. We propagate the velocity uncertainties to the uncertainties of the hurdle location, approximated by linearization of the non-linear problem (cf. Section 2.9.2). Figures 2.3 to 2.5 show maps of our estimated hurdle locations for each of the subduction zones and selected trench-perpendicular profiles of interpolated velocities with their uncertainties, nearby GNSS observations, and hurdle locations.

2.2.5 Data Analysis Results

Both velocity components decrease steeply with distance from the trench up to a hurdle, behind which a far-field region starts with low velocity amplitudes and gradients Figures 2.3 to 2.5. The hurdle location can be constrained best when both the velocity uncertainties are small and there exists a strong

discontinuity between the near-field and far-field velocity gradient. Trench-perpendicular velocities in particular show a steep near-trench decrease, except above sections of the megathrust that are not locked over an extensive trench-parallel distance. Such unlocked portions of the subduction interface are characterized by low interseismic velocity magnitudes e.g., Matsu'ura and Sato, 1989, e.g., in northern Peru (4–9°S) (Herman and Govers, 2020; Nocquet *et al.*, 2014) and Java (Koulali *et al.*, 2017). Trench-parallel velocities show a more complex behavior, particularly where the convergence obliquity changes direction (inverting the sign of near-trench trench-parallel velocities) and fore-arc slivers have been suggested to exist (Nocquet *et al.*, 2014; Métois *et al.*, 2016; Herman and Govers, 2020). Nevertheless, trench-parallel velocities also suggest a hurdle, beyond which amplitudes are near-zero and the slope is very shallow.

In South America, we can identify the trench-perpendicular hurdle as the location of the transition between rapid near-trench decay and the other, shallower slope in the far-field. Along the margin, the hurdle location can generally be estimated reliably, as observations constrain the decrease from large near-trench to low plate interior velocities, within uncertainty bounds (Figure 2.3). The hurdle is located at distances from the trench varying between 400 and 1000 km, except for the section of subduction zone with weakly coupled megathrust in Northern Peru (4–9°S). The hurdle location generally largely tracks the eastern margin of the Andean orogen (Figure 2.6a). Only landward of the weakly locked megathrust of Northern Peru, the trench-perpendicular gradient in the velocity component is low and the hurdle location is identified at distances beyond 1000 km from the trench, although the uncertainty on the location is very large and the nearest location within the confidence interval still tracks the eastern boundary of the orogen. The hurdle lies a few tens of km landward of the backthrust in south-central Peru (10–13°S). Further to the south, in Bolivia (14–2°S), it follows the backthrust at the base of the mountain range. In northernmost Argentina there is no clear, active backthrust, but the hurdle traces the border of the Puna plateau. Immediately to the south, around 30°S, the hurdle is located in the middle of the Sierras Pampeanas.

For South America, the hurdle for trench-parallel velocities is located between 220 and 800 km from the trench, excluding the weakly coupled megathrust section. It is always closer to the trench or coincident with the trench-perpendicular hurdle within uncertainties. Velocities beyond the hurdle are near, but not always exactly, zero: the trench-perpendicular component is between -1 and 4 mm $\cdot$ yr^{-1} in amplitude, while the trench-parallel component is between -1 and 2 mm $\cdot$ yr^{-1}.

Observations of interseismic velocities in Sumatra are sparser than in South

America. In the southeast of the island, both velocity components are small and have low gradients, including the near-trench region (Figure 2.4). This reflects low megathrust coupling in that region (Chlieh *et al.*, 2008) and does not allow us to locate any hurdle. In central Sumatra, where near-trench velocities indicate strong interplate coupling and data coverage is much denser, we infer a hurdle in the trench-perpendicular component, bounding the zone of near-uniform low velocities in the interior of Sunda (Simons *et al.*, 2007). The hurdle runs through the middle of the island, roughly coinciding with the southwestern edge of the Sibumasu terrane reported by Hutchison (2014) and Metcalfe (2011) (Figure 2.6b), as well as with the northeastern boundary of the zone of active orogenic deformation as indicated by Hall and Sevastjanova (2012). Trench-parallel velocities do not show a uniform decrease with distance from the trench, but rather are near-uniform on the Indian Ocean coast of central Sumatra and in the smaller offshore islands, and have a steep gradient over the Sumatran Fault (Prawirodirdjo *et al.*, 2010; Genrich *et al.*, 2000), behind which the parallel velocities steeply decrease to zero. We thus do not estimate the hurdle location for trench-parallel velocities in Sumatra. In Java, both velocity components are low throughout, indicating low megathrust coupling (Koulali *et al.*, 2017), and the lack of observations to the northeast of the island, in the Java Sea, prevents us from confidently identifying a hurdle.

Along the Japan trench, trench-perpendicular velocities decrease steeply with distance from the trench, with a constant or gently decreasing slope, in the vast majority of Hokkaido (trench locations north of 42°N) and most of central-northern Honshu (south of 40°N). The resulting hurdle location is 450–600 km away from the trench (Figure 2.5). It broadly follows the eastern margin of the Sea of Japan, a few tens of km offshore except for where it touches the northernmost tip of Hokkaido (Figure 2.6c). On the other side of the Sea of Japan, observations in Manchuria and South Korea constrain the velocity field at intermediate to far distances, helping locate the hurdle. The trench-perpendicular and trench-parallel velocities in those sites are uniformly negative (around 5 mm·yr^{-1}, both trenchward and right-lateral, respectively), indicating limited transpressional motion between Manchuria, inferred to be part of the Amurian plate, and the Okhotsk plate reference (Weaver *et al.*, 2003; Petit and Fournier, 2005). Off the northwestern shore of south-central Honshu (south of 40° latitude), observations in the intermediate- and far-field are not available and the velocity field is interpolated relying on observations far to the northwest and west, in Manchuria and South Korea. Nevertheless, the existence of a hurdle a short distance offshore in the Sea of Japan is supported by the steep, near-linear decrease with distance of trench-perpendicular velocities in Honshu and by the trench-perpendicular velocities on its north-

western coast being similar to those at the northwestern tip of Hokkaido and within less than 10 mm · yr^{-1} of those in Manchuria. The Okhotsk-Amurian plate boundary, inferred here to cross Honshu by Bird (2003), does not affect the slope of trench-perpendicular velocities with distance from the trench. In northernmost Honshu and the southwestern most tip of Hokkaido (for trench locations between 40° and 42°N), both the trench-perpendicular velocities and their trench-perpendicular gradients are lower, possibly reflecting lower inter-plate coupling than in laterally adjacent portions of the megathrust (Suwa *et al.*, 2006; Hashimoto *et al.*, 2009) or incomplete postseismic transient corrections for the 1994 Sanriku earthquake (Loveless and Meade, 2010).

Trench-parallel velocities in northern Honshu are low, while the uncertainties of available interseismic velocities are relatively high. This, combined with the narrow width where observations are possible, makes it difficult to identify a hurdle in the trench-parallel component. Additionally, trench-parallel velocities vary in sign across the study area. This clearly reflects in part small changes in the strike of the trench which, combined with the overall head-on character of the convergence, changes the sign of the trench-parallel component of the velocity of the downgoing (Pacific) plate with respect to the overriding (Okhotsk) one. Interpolated trench-parallel velocities seem to decrease to uniform values (-5–-6 mm · yr^{-1},) within ~ 600 km of the trench in northern Hokkaido and within ~ 300–400 km in northern Honshu. However, precisely locating the hurdle is difficult because GNSS observations are only available onshore, in Japan and Manchuria, not in the Sea of Japan. Therefore, we do not perform our parallel hurdle location estimation in northern Japan.

We also performed the data analysis for Japan expressing all velocities with respect to the Amurian plate, rather than the Okhotsk plate, see Figure 2.27. This results in an increase of all trench-perpendicular velocities by ~ 6 mm · yr^{-1}, making them positive everywhere and reaching very close to 0 in Manchuria. However, the estimated trench-perpendicular hurdle location remains unchanged. Trench-parallel velocities increase uniformly also, by 5 mm · yr^{-1}. They thus become largely positive (dextral), except for a few isolated areas. Therefore, even though Manchuria is arguably on a different plate than Hokkaido and northern Honshu and it moves with respect to a stable Okhotsk reference, it seemingly behaves as the stable plate interior of the Japan Trench subduction zone. The estimated hurdle location is indifferent to whether the Okhotsk or Amurian plate is used as a reference.

2.2.6 Discussion and Conclusions of the Data Analysis

Trench-perpendicular velocities decrease with distance from the trench in a semi-linear fashion to low values, and both the velocities and the velocity gradient are distinctly lower beyond that. We refer to the region where the velocity gradient changes as a hurdle. The existence and location of the hurdle is supported by the fact that 1) the near-trench trend in velocities is derived from abundant observations, and that 2) observed velocities close to the hurdle are small and similar in value to observations much farther from the plate margin. The inferred hurdle differs therefore from the potentially detrimental effect that uneven spatial distribution of GNSS stations can have on interpolated strain rates and gradients in that it may result in spurious high-strain areas (e.g. Hackl *et al.*, 2009). Our interpolation procedure is designed to give robust estimates of velocities including uncertainties that arise from both uneven spatial sampling and data uncertainties, and we propagate these uncertainties into our hurdle estimates.

The hurdle for trench-perpendicular velocities is located within 1000 km or less of the trench along the three studied subduction zones. Trench-parallel velocities sometimes have complex patterns, partly due to curvature of the margin. In South America, parallel velocities also decrease semi-linearly with distance from the trench up to a hurdle that roughly coincides with the trench-perpendicular hurdle, or that is located closer to the trench. Hurdle locations broadly, but not precisely, follow the inland boundary of the orogen wherever such boundary is clearly expressed.

That the trend of trench-perpendicular velocities as function of distance deviates from a smooth decrease was first noted by Norabuena *et al.* (1998) for the northern portion of the Central Andes (the Altiplano of Peru and Bolivia) and Brooks *et al.* (2003) for the Southern Andes. The authors focus on the locally steep velocity gradient at the eastern edge of the Andes and explain the observations by active back-arc convergence or sliver motion, which has remained a popular explanation (Bevis *et al.*, 2001; Brooks *et al.*, 2003; Brooks *et al.*, 2011; Kendrick *et al.*, 2006; Métois *et al.*, 2013; Weiss *et al.*, 2016; McFarland *et al.*, 2017; Herman and Govers, 2020; Shi *et al.*, 2020). This explanation implies that interseismic strain accumulation involves non-recoverable strain on active backthrust faults or shear zones. The fold-and-thrust belt at the eastern margin of the Altiplano-Puna plateau, at roughly 11–22°S latitude, is bounded by a well-defined thrust front and is indeed considered to be actively deforming, despite little recent seismic activity (Brooks *et al.*, 2011; Wimpenny *et al.*, 2018). Farther north in Peru (4–11°S) and farther south in Argentina (around 31°S), earthquakes indicate that permanent strain occurs

by thrusting in the eastern foreland of the Andes (Jordan *et al.*, 1983; Sébrier *et al.*, 1988; Alvarado and Ramos, 2011; Rivas *et al.*, 2019). However, active and continuous backthrusts faults appear to be absent in some locations, specifically at 22–29°S and south of 32°S latitude in South America, throughout Sumatra and Java, and south of 39°N and north of 45°N off the west coast of Japan. Elsewhere, in the Sea of Japan, the inferred active faults marking the Okhotsk-Amur plate boundary do not coincide with the location of the hurdle (Figures 2.3 to 2.6).

Even where active backthrusts have been observed, their role in explaining the spatial distribution of surface velocities may have been overestimated because of unrealistic model assumptions. Most studies that model the effect of back-arc convergence on interseismic velocities assume a fully elastic Earth during the entire earthquake cycle. This is a particularly unrealistic assumption during the late interseismic period, when the mantle wedge is effectively fluid, and it strongly underestimates far-field horizontal velocities and therefore may lead to incorrect interpretations of the observations (Trubienko *et al.*, 2013; Li *et al.*, 2015). Shi *et al.* (2020) do use a more realistic viscoelastic rheology to arrive at the conclusion that the backthrust is the cause of velocity distribution. However, they assume a hard backstop on their model overriding plate at a distance only ∼ 150 km from the back-arc thrust front. The decrease in trench-perpendicular velocities with distance from the trench is less linear than observed in their model, while the backthrust included in their model produces only local velocity offsets at the backthrust. Other modeling studies invoking back-arc convergence require basal detachment faults extending in the trench-normal direction for ∼ 200 km or more (Brooks *et al.*, 2011; Weiss *et al.*, 2016; McFarland *et al.*, 2017). This may be unrealistic, considering that the E-W extent of the currently active central Andean back-arc fold-and-thrust belt is only ∼ 70 km wide (Pearson *et al.*, 2013). Other authors treat the contact between the Andean orogen and the South American interior as a plate boundary, implying that it cuts through the entire lithosphere, slipping freely at depth, and that it is laterally continuous all along the orogen. Because of the extreme spatial extent and continuity of the modeled thrusts or plate boundaries, these studies probably overestimate the geodetic imprint of the localized shortening at the eastern edge of the Andes. Additionally, seen at the continental scale, the sharp, localized velocity decrease that has been used as evidence for backthrust slip (Norabuena *et al.*, 1998; Brooks *et al.*, 2011; Weiss *et al.*, 2016; Shi *et al.*, 2020), constitutes a relatively minor deviation from a general trend of steep but gradual decrease over the whole orogen (Figure 2.3, profiles B and C). Furthermore, the aforementioned studies investigating the spatial distribution of interseismic velocities do not consider

whether significant far-field coseismic displacements can be explained by their models. Within the framework of the earthquake cycle, we think there should be consistency in terms of coseismic slip and slip deficit accumulation, response of fault slip and creep to the stress evolution during the cycle, and boundary conditions.

Active faults are the possible cause of hurdle behavior in some regions. North of $\sim 2°$S in South America, in southern Ecuador and Colombia, convergence is highly oblique and subparallel to a system of strike-slip and thrust faults (Veloza *et al.*, 2012) that roughly coincides with the location of the hurdle in both velocity components. Localization of interseismic velocities might be chiefly caused by the fault system, consistently with the interpretation of this fault system as bounding a distinct, internally deforming North Andean sliver (e.g., Alvarado *et al.*, 2016; Kellogg *et al.*, 1995; Nocquet *et al.*, 2014; White *et al.*, 2003). In Sumatra, trench-parallel velocities seem to be governed by the active strike-slip Sumatra Fault (Prawirodirdjo *et al.*, 2010; Genrich *et al.*, 2000). Trench-parallel velocities also suggest localized strike-slip motion between southern Hokkaido (on the Okhotsk plate per Bird, 2003) and northern Manchuria (on the Amurian plate), but the lack of GNSS observations in the Sea of Japan precludes a specific localization of the boundary from a purely geodetic perspective.

Trench-perpendicular velocities in all three study areas show a consistent steep decrease with distance from the trench. Trench-parallel velocities in South America, away from the North Andean sliver, show a similar trend. This suggests a more universal cause of the observed hurdles than fault zones. We find no correlation between shallow megathrust dip and hurdle location, since the dip changes very little along the studied trenches (Figure 2.6). We therefore focus on a possible explanation involving the overriding plate. Although the thrust faults in the Andean back-arc are unlikely to directly account for the decrease in observed velocities as we move away from the trench, they are likely associated with a mechanical contrast between the deformed and partly accreted Andean region and the interior of the South America plate. We thus hypothesize that such a contrast exists in this and other subduction zones, that it is responsible for the behavior of interseismic velocities, and that a uniform overriding plate cannot account for observations.

The effective elastic thickness T_e derived from flexure observations is much lower at the margin than in the interior of South America (Pérez-Gussinyé *et al.*, 2007; Pérez-Gussinyé *et al.*, 2008; Stewart and Watts, 1997). Variations in effective elastic thickness may derive from variations in thickness, composition, temperature, rheology, and on the age of the load (Burov and Diament, 1995; Watts, 1981). The effective elastic thickness is derived from lithospheric

flexure on geological time scales and is not directly applicable to the predominantly horizontal plate loading over interseismic timescales. It is very likely however that a relevant mechanical contrast exists. The load-bearing capacity of the low-viscosity mantle wedge is negligible on (interseismic) time scales, meaning that the contrast is most likely related to properties of the overriding plate. The bulk of the interseismic shortening of the overriding plate is recovered during megathrust earthquakes, so it can be considered largely elastic. A mechanical contrast that is relevant in the context of earthquake cycles is thus a compliance contrast or thickness contrast. Below we present mechanical models aimed at exploring our hypothesis that (interseismic) hurdles are a consequence of such contrast, whilst also showing significant coseismic displacements beyond the hurdle.

The presence of stiff cratonic lithosphere in the interior of the South American plate in central Argentina was proposed as the explanation for the relatively low horizontal postseismic velocities in the region (compared to model results without such a craton) by Klein *et al.* (2016). Itoh *et al.* (2019) instead showed that a compliant arc and back-arc region can explain the high gradient of onshore horizontal interseismic velocities with distance from the trench in Hokkaido. We hypothesize that a mechanical contrast between more compliant lithosphere at the convergent margin of the overriding plate (in the arc and back-arc region) and less compliant lithosphere of the interior of the plate can explain the observed near-trench localization of high spatial gradients of horizontal surface velocities. We thus propose that such a contrast, while avoiding artificially fixed model edges in the vicinity of the trench, can produce a hurdle in interseismic velocities and surface motion generally consistent with observations throughout the seismic cycle, even though we specifically focus here on interseismic observations.

2.3 Numerical Model

2.3.1 General Concept

To study the interseismic and coseismic surface deformation field we develop a three-dimensional (3D) mechanical model. We seek to explain observation trends at different margins, i.e., the semi-linear decrease of interseismic velocities from the trench to the hurdle, the low interseismic strain accumulation beyond it, but significant far-field coseismic displacements due to a megathrust earthquake. We test whether these trends may be a consequence of a compliancy contrast in the overriding plate. In the context of our model, we

use a contrast in Young's modulus E and shear modulus G, with the same ratio between the two moduli, in an overriding plate with a uniform thickness and Poisson's ratio ν. Rather than representing realistic averages of the elastic properties of the lithosphere, the model Young's modulus values proxy for a more general ability of the plate to resist intraplate stresses resulting from the total thickness, composition, and thermal state of the real lithosphere. The modeled contrast in the elastic properties of the overriding plate consists of a relatively low Young's modulus in the "near-trench" region and a higher modulus in the far-field. The assumed geometry of the slab and overriding plate in the model is not specific for any margin and instead follows a realistic trench-perpendicular slab profile (Figure 2.7). We consequently do not expect to reproduce specific regional observations with the model.

Model deformation is driven by slab motion and periodic unlocking of asperities. The slab itself is kinematically driven, as updip and downdip end of the slab are driven at the interplate convergence rate. Coseismic slip and afterslip are not imposed kinematically and are instead physically determined, together with viscous relaxation, by the asperity size and location and by the mechanical properties of the material in the model. Govers *et al.* (2018) show that coseismic slip increases per earthquake cycle until no variation occurs from one cycle to the next and physically consistent prestresses have developed.

2.3.2   Model Domain and Rheology

We have chosen the model domain size so that boundaries and boundary conditions do not affect the results in our region of interest; the trench-perpendicular (x) model extent is 2200 km, 2000 km in the trench-parallel direction (y) direction, and 338 km in the depth (z) direction. The trench is located at $x = 0$, while the oceanward model boundary is located at $x = -212$ km. The surface downgoing plate has its upper surface at a depth of 8 km, and the overriding plate at z=0. The subducting plate has a thickness of 80 km, consistent with the seismologically detected depth of the lithosphere-asthenosphere boundary of various oceanic plates (Kawakatsu *et al.*, 2009; Kumar and Kawakatsu, 2011). The overriding plate has a uniform 40 km thickness, except at the taper due to the megathrust geometry at the bottom and at the slope down to the trench over 18 km horizontal distance.

The model slab and the overriding plate are elastic, and the mantle wedge and sub-slab asthenosphere are viscoelastic with a Maxwell rheology. We model seismic cycles with quasi-dynamic slip on discrete faults and shear zones (see Section 2.3.4 and Govers *et al.*, 2018, Section 2). After model spin-up, the model has identical megathrust earthquake cycles with a return period of

300 years. Postseismic relaxation in the model involves the two most relevant large-scale processes, afterslip and viscous relaxation (Bürgmann and Dresen, 2008; Diao *et al.*, 2014; Broerse *et al.*, 2015; Klein *et al.*, 2016). Our reference model has a mantle viscosity η of 10^{19} Pa $\cdot$ s. Throughout the model domain, outside of the overriding plate, the elastic moduli are uniform: Poisson's ratio ν is 0.25 and Young's modulus E is 100 GPa, consistently with values from PREM (Dziewonski and Anderson, 1981) in the 0–40 km depth range. In particular, the ν value of 0.25 consists of the common Poisson solid assumption (e.g., Melosh and Raefsky, 1983) and is very consistent with the values determined for lower crustal and mantle lithologies, while being at the lower end of the realistic range for the upper crust. The return period thus is ~ 37.9 characteristic relaxation (Maxwell) times long, so that about 55% of the model cycle period is interseismic, given that the earthquakes on the different asperities within one cycle occur within 40 years of each other (Govers *et al.*, 2018).

2.3.3 Numerical Method

We use a finite element method to solve the time-dependent 3D mechanical equilibrium equations for given material properties and boundary conditions including a free surface, as detailed below. Finite element platform GTEC-TON version 2021.0 uses the Portable, Extensible, Toolkit for Scientific Computation (PETSc version 3.10.4; Balay *et al.*, 1997; Balay *et al.*, 2021b; Balay *et al.*, 2021a) and OpenMPI (version 3.0.0; Gabriel *et al.*, 2004) to solve the time-dependent mechanical problem in parallel (e.g., Govers and Wortel, 2005; Govers *et al.*, 2018).

Each model includes 384,566 nodes arranged in 2,238,109 tetrahedral elements and 1,284,193 total degrees of freedom. These choices are based on pilot models to find a mesh where surface deformation is insensitive to further grid refinement. A posteriori estimates of the model error (Verfürth, 1994) for the selected mesh are small enough to support our conclusion that our results are accurate within a few %.

2.3.4 Modeling the Megathrust

Dynamic differential slip on the megathrust is modeled using the slippery nodes technique (Melosh and Williams, 1989). Five asperities on the otherwise freely-slipping megathrust are fully coupled (locked) during all stages of the earthquake cycle, except during the coseismic phase when unlocked asperities can slip freely. Treating the megathrust away from the asperities as freely

sliding is consistent with observations of megathrust regions immediately up- and downdip of the asperities sliding stably and with low friction (Scholz, 1998; Ikari *et al.*, 2011; Hardebeck, 2015).

The asperities are circular in map view and have a diameter of 50 km, consistent with the inversion results of Herman and Govers (2020). They are centered at a horizontal distance of 120 km from the trench and 100 km from each other, resulting in accumulation of slip deficit (locking and pseudo-locking) on and around the asperities, over an along-trench distance of 500 km (Herman *et al.*, 2018). At the start of each new 300-year cycle, the middle asperity first has its coseismic phase. After a delay of 20 years, the intermediate asperities have their coseismic phase. After 20 more years, the outer asperities have the coseismic phase. Each asperity has its coseismic phase every 300 years. Every coseismic phase is instantaneous and consists of the relevant asperities being unlocked, the megathrust slipping freely, and the asperities being relocked, all with no model time elapsing. All slip deficit accumulated on the megathrust interseismically due to each asperity is released during its coseismic phase. The distribution of coseismic slip is thus determined by the asperities and by the mechanical properties of the plates and asthenospheric mantle. Coseismic slip can occur at depths shallower than 40 km, as that is the maximum depth of the overriding plate and thus of the megathrust.

Coseismic slip, although traditionally thought to not extend to very shallow depth because of unconsolidated material in the hanging-wall (Kanamori, 1972; Moore and Saffer, 2001), can indeed propagate up to the trench (Fujiwara *et al.*, 2011; Sladen and Trevisan, 2018). We minorly restrict coseismic slip on the updip portion of the megathrust, above 15 km depth, by applying (small) shear tractions that are proportional to the coseismic fault slip amplitude, with a spring constant of $200 \, \text{Pa} \cdot \text{m}^{-1}$.

Downdip of the megathrust, the contact between the subducting plate and the mantle wedge (depths > 40 km in our models) is often viewed as a vis-coelastic shear zone (van Keken *et al.*, 2002; Tichelaar and Ruff, 1993). In our model, we represent it as a discrete interface that slips freely interseismi-cally and is fully locked coseismically. Additionally, immediately after each coseismic phase, we include an instantaneous afterslip phase, during which the shear zone, together with the megathrust outside of the asperities, slips freely until mechanical equilibrium is reached. The shear zone thus resolves coseismic stress changes as much as possible via afterslip and creeps interseis-mically, but behaves as part of the mechanical continuum responding elastic to coseismic slip on the megathrust. This implementation has the significant benefit of avoiding the computationally demanding simulation of viscous flow in a narrow channel, while capturing the main features of interseismic and

coseismic behavior and while producing afterslip with no need to impose it kinematically. Govers *et al.* (2018) used a similar approach, and they defined "primary afterslip" as immediate viscous slip on the shear zone in response to coseismic stress changes that is generally thought to occur much more quickly than bulk viscous relaxation in the mantle wedge (Govers *et al.*, 2018; Muto *et al.*, 2019). "Secondary" afterslip also occurs on the deep shear zone, over time, in response to bulk viscous relaxation during the postseismic phase.

Afterslip on the deep shear zone is commonly assumed to occur at depths shallower than about 80–100 km (Diao *et al.*, 2014; Sun *et al.*, 2014; Yamagiwa *et al.*, 2015; Hu *et al.*, 2016b; Freed *et al.*, 2017). Klein *et al.* (2016) showed that allowing relative motion between the mantle wedge and the slab, by introducing a narrow low-viscosity zone between 70 and 135 km depth along the top of the slab, produces little change in postseismic horizontal surface motion. In our model, we therefore allow afterslip, and interseismic slip deficit accumulation, on the shear zone downdip of the megathrust only at depths smaller than 100 km.

We aim to capture deformation and flow of the mantle wedge and asthenosphere in response to stress changes during the earthquake cycle. To exclude modeling steady-state mantle flow on geological time scales that is irrelevant for the seismic cycle, we use the finite element split node technique (Melosh and Raefsky, 1981) to impose the slab velocity beyond a depth of 100 km. Similarly, we avoid driving long term sub-slab asthenosphere by applying the slab velocity along the base of the slab. We remove a small residue of long-term deformation of the model related to stretching and unbending of the slab that we identify from an identical model without asperities or earthquakes. This approach facilitates loading of the mantle wedge and sub-slab asthenosphere by non-steady velocity/stress perturbations during all stages of the earthquake cycle, without neglecting the role of the viscoelastic rheology of either the oceanic or the continental mantle.

2.4 Modeling Results and Analysis

2.4.1 Reference Model

In our reference model, the overriding plate has a Young's modulus of 50 GPa within 700 km horizontal distance from the trench and of 250 GPa beyond. Figure 2.8 shows the resulting surface deformation. Figure 2.8a,c show interseismic velocities 260 years after the last earthquake on any asperity, i.e., after $\sim$ 33 Maxwell times and immediately before the next 40-year earthquake

sequence on the five asperities. Both the trench-perpendicular and trench-parallel velocity components decrease with distance from the locked asperities. The transect through the central asperity in fig. 2.8c (solid line) shows a roughly linear decrease in the trench-perpendicular velocity with distance from the trench, from the peak value (above the asperity) to the location of the contrast, where the gradient decreases sharply. Here, the trench-perpendicular velocity is $\sim 10\%$ of the interplate convergence rate and $\sim 8\%$ of the peak value. Beyond the contrast, the trench-perpendicular velocity in the far-field decreases gradually to zero at the far end of the model, which is a consequence of the model boundary condition there. Trench-parallel velocities along this transect instead decay with a progressively shallower slope away from the peak (Figure 2.8c). They reach a near-zero value at the compliance contrast and reach $\sim 10\%$ of the peak value ~ 200 km closer to the trench. The steeper decrease in the trench-parallel component causes velocity directions in the locked portion of the subduction zone to rotate from convergence-parallel to trench-perpendicular with distance from the trench (Figure 2.8a). The results thus show slow and mostly trench-perpendicular interseismic strain accumulation beyond the contrast. The mechanical contrast thus results in hurdle-type behavior comparable to what we infer from the GNSS data. The hurdle is expressed in both horizontal velocity components, albeit more clearly in the trench-perpendicular velocities.

Interseismic velocities 500 km to the north of the middle of the model (Figure 2.8a,c) are substantially slower than above the central asperity. They are higher than velocities 500 km to the south of the central asperity, showing that oblique convergence results in a distinctly asymmetric pattern of interseismic strain accumulation. Particularly the trench-parallel velocity differs. Trench-parallel velocities along the northern transect in Figure 2.8a,c increase with distance from the trench before decreasing again. Figure 2.8a shows that, in a trench-perpendicular profile 500 km the south of the middle of the model, trench-parallel velocities decrease with distance from the trench. Trench-perpendicular velocities on both lateral sides decrease with distance from the trench. The imprint of the contrast on the (gradient of the) velocities is less pronounced away from locked asperities than in the central region.

Unlocking of the central model asperity results in coseismic slip on the megathrust. The coseismic slip on the megathrust corresponds to a moment magnitude $M_W = 8.7$, computed using the average elastic shear modulus of the overriding and subducting plates. Figure 2.8b shows coseismic horizontal surface displacements in the overriding plate. The displacement magnitude is highest (~ 11 m) and obliquely ocean directed above the ruptured asperity. Figure 2.8d shows a steep decrease of trench-perpendicular displacement

with distance from the trench, and a change in the gradient at the mechanical contrast. Trench-parallel displacements are less affected by the contrast. However, both components are significantly non-zero beyond the compliance contrast.

2.4.2 Lateral Compliance Contrast Versus a Homogeneous Plate

We compare the results of our reference model with results from two other models, both with an overriding plate with a uniform Young's modulus, and all else the same as in the reference model (Figure 2.8c). We find that a uniform value of 10 GPa produces a steep decrease in both interseismic velocity components, i.e., it concentrates interseismic strain closer to the trench. However, it lacks significant trench-perpendicular coseismic displacement in the far-field, with amplitudes below 10 mm at distances from the trench greater than 800 km, unlike our reference model. Furthermore, 10 GPa is a very low value for the Young's modulus of the whole lithosphere in the far-field as well as near-field. Conversely, a uniform, realistic value of 100 GPa for the overriding plate produces large far-field coseismic displacement. However, its trench-perpendicular interseismic velocities decrease slowly and have significant amplitudes (more than a third of the peak value) at the location of the contrast in the reference model (700 km from the trench).

We conclude that a uniform overriding plate cannot simultaneously explain the observed interseismic hurdle and far-field coseismic displacements. A compliance contrast in the overriding plate does explain an interseismic hurdle and far-field coseismic displacements.

2.4.3 Radial Elasticity Variations

Pollitz2011b; Pollitz *et al.* (2011) concluded that radial elasticity layering is needed for fitting both the near- and far-field coseismic static GNSS displacements following the Maule and Tohoku earthquakes. We evaluate to what extent a radial elasticity variation affects the model results. We use elastic moduli varying with depth according to PREM (**Pollitz2011b**; Dziewonski and Anderson, 1981; Pollitz *et al.*, 2011). The modeled interseismic surface velocities differ little from a model with uniform Young's modulus E=100 GPa (Figure 2.29), being less than 5% higher or lower and near-indistinguishable beyond 300 km of distance from the trench. We conclude that the hurdle-type response of interseismic velocities cannot be explained by the radial elasticity layering only. In the context of our numerical models a lateral contrast is thus

needed in the overriding plate to reproduce the hurdle-like observations. In Sections 2.5.2 and 2.5.3 we address the tectonic and rheological viability of a mechanical contrast in overriding plates.

2.4.4 Importance of Near-Trench Elasticity and of Its Contrast With Far-Field Elasticity

The reference model uses a Young's modulus $E = 50$ GPa in the near-trench and $E = 250$ GPa in the far-field of the overriding plate. The latter value is beyond the upper limit of ~ 200 GPa for lithospheric rocks (specifically eclogite; Aoki and Takahashi, 2004; Christensen, 1996). Here we explore the sensitivity of our model results to elastic properties.

We systematically vary the Young's modulus in both the near-trench and the far-field portion of the overriding plate. Figure 2.9a,b shows trench-perpendicular profiles of interseismic velocities through the central asperity for models where the Young's modulus is higher in the far-field than near the trench by a factor of 3 (red) and 5 (purple), with different average values (less continuous line strokes for lower values). We also vary the Young's modulus of the far-field while keeping the near-trench value the same (Figure 2.9c,d), the latter with a value of 50 GPa (purple), 30 GPa (dark red), or 20 GPa (orange) with less continuous line strokes for lower far-field values. In Fig 9e,f we do the opposite, showing the effect of different values of Young's modulus in the near field (less continuous strokes for lower values) while keeping a far-field value of 150 GPa (dark red) or 100 GPa (orange).

Looking at the trench-perpendicular velocities (Figure 2.9a,c,e), the results show that a larger contrast in E result in lower velocity amplitudes trenchward of the contrasts and steeper slopes in velocity, particularly between 200 and 300 km of distance from the trench, and in shallower slopes beyond the contrast (Fig, 9a). Lowering both values of E accordingly, while keeping the amplitude of the contrast unaltered, has a similar effect (Figure 2.9a, different line strokes with the same color). The effect of increasing the far-field value of E while keeping the near-trench value constant (Figure 2.9c) is generally smaller than doing the opposite (Figure 2.9e), but it is still noticeable when the near-trench E is high (Figure 2.9c, purple lines). With lower near-trench E values, increasing the far-field E is hardly noticeable (Figure 2.9c, dark red lines and orange lines). There is no sharp cutoff beyond which hurdle behavior is exhibited, and a break in the slope of the profile is always present at the location of the contrast, if any. We take the trench-perpendicular hurdle to be a good indicator of the location of a compliance contrast in the overriding plate.

The amplitude (i.e., ratio) of the contrast in Young's modulus on trench-parallel velocities (Fig, 9b) is variable. This is because the far-field Young's modulus by itself has very little effect on the profiles of trench-parallel velocities (Figure 2.9d). The near-trench Young's modulus alone controls the decrease in trench-parallel interseismic velocities with distance from the trench, with lower values causing a steeper decrease on the landward side of the peak velocity (Figure 2.9f). We observe however that all curves (including the uniform E model) decrease to low velocities at the contrast, i.e., hurdle behavior of trench-parallel interseismic velocities is not a very strong indicator for a compliance contrast.

Figure 2.10 shows profiles of trench-perpendicular coseismic displacement (corresponding to an earthquake with $M_W = 8.7$) of the same models as in Figure 2.9. The amplitude of the far-field displacement is controlled by the Young's modulus in the near-trench, more compliant portion of the plate, regardless of the contrast with the higher Young's modulus in the less compliant internal portion. Pollitz *et al.* (2011) observed trench-perpendicular coseismic displacements after the $M_W = 8.8$ Maule earthquake up to a few tens of millimeters beyond 700 km from the trench. A near-trench Young's modulus $E \geq 20$ GPa is needed for a coseismic displacement greater than 20 mm 700 km from the trench (where the contrast is located in the reference model), while a modulus of 50 GPa is needed for a displacement of 20 mm 1000 km from the trench. This need for a moderate E in the near-trench region, combined with the need for a sufficient E contrast to reproduce the hurdle behavior in trench-perpendicular interseismic velocities, requires the use of a very high far-field E in the overriding plate of the reference model (Section 2.4.1) to produce realistic behavior both interseismically and coseismically. If the far-field E is only moderately high (~ 100 GPa or less, for instance), the contrast between far-field and relatively near-trench E is probably insufficient to explain hurdle behavior, given that coseismic displacement requires near-trench E to be moderate. In this case, the compliance contrast within the overriding plate, responsible for the hurdle, should be greater than implied by the elastic moduli of the constituent materials alone. In Section 5.3 we discuss the rheological implications of the model sensitivities presented here.

2.4.5 Shear Modulus Contrast in the Overriding Plate

We thus far focused on contrasts in Young's modulus E, which is the resistance to interseismic (elastic) shortening of the overriding plate in response to the head-on component of the convergence velocity. The resistance to (elastic) shear deformation due to the trench-parallel component of the convergence

velocity is better represented by the shear modulus $G = \frac{E}{2(1+\nu)}$.

All presented models used a uniform Poisson's ratio $\nu = 0.25$, meaning that the contrasts in Young's modulus E and shear modulus G are the same. We now test whether varying the contrast in G while keeping the contrast in E constant, affects trench-perpendicular and -parallel velocities. The near-field and far-field values of E are 30 and 150 GPa, respectively, while ν is 0.2. We decrease the near-field G by 14% through a drastic increase (doubling) in Poisson's ratio, to 0.4, which results in a slight change in the trench-parallel velocity, but does not alter the trench-perpendicular velocity (Figure 2.30). Different contrasts in E and G are thus unlikely to affect the apparent hurdle location, particularly as determined in the trench-perpendicular component of velocities, justifying our use of the same contrast in both moduli.

2.4.6 Role of the Location of the Mechanical Contrast

We investigate the sensitivity of the models to the location of the contrast in E by stepwise reducing its distance from the trench to 400 km in 100 km intervals. We do so in a model with a contrast that produces the largest differences in interseismic velocities compared to a uniform E (10 and 100 GPa; Figure 2.9). Bringing the contrast closer to the trench most noticeably affects trench-perpendicular velocity profiles (Figure 2.11a). Increasing the contrast distance produces less uniform decay of such velocities on the trench-ward side of the contrast, as the slope becomes shallower before reaching the contrast. Instead, when the contrast distance is increased, the velocities at the contrast become lower while beyond the contrast, the slopes become flatter. Trench-parallel velocities are much less affected by the location of the contrast (Figure 2.11b), as the near-trench value of E controls the general shape of the decrease. The presence of a single contrast in E can thus produce a varying distance between the apparent location of the hurdle (a sharp transition between a steep decay and near-0 amplitudes) in the two components of horizontal interseismic velocities, depending on the near-trench value of E and its spatial extent. Overall, the two horizontal velocity components not only have different spatial distribution with the same contrast, but also respond differently to variations in distance to the contrast or in the value of E on either side of the contrast. This behavior is compatible with our observations showing that the apparent location of the trench-parallel hurdle relative to the trench-perpendicular one varies along a subduction zone and between subduction zones, rather than coinciding with it or being offset by a constant distance.

Interseismic locking results in steadily increasing shear tractions on asperi-

ties. The slope of the velocity curves in Figure 2.11 represents horizontal strain accumulation rates in the overriding plate. In the region within 200 km from the trench, strain accumulation rates show to be insensitive to the distance of the contrast, and shear tractions on asperities are consequently expected to be insensitive to the width of the zone where strain accumulates. Figure 2.29 shows indeed that the average traction on the middle asperity in the downdip direction increases little with decreasing trench-contrast distance; for instance, the traction becomes only $\sim 3\%$ larger when the distance to the contrast reduces from 700 to 500 km. The temporal rate of change of this traction at the end of the cycle in the late interseismic phase is linear and thus increases by the same, small amount. Overall, the presence and location of the mechanical contrast in the overriding plate has little effect on stressing rates on locked asperities.

2.4.7 Megathrust Locking Pattern Affects the Detectability of Hurdles and Contrasts

To assess the effect of a contrast on interseismic velocities in areas of low interplate locking, such as northern Peru and Ecuador (Herman and Govers, 2020; Nocquet *et al.*, 2017), we run two simulations in which the two intermediate asperities are removed, leaving 3 total asperities (2 lateral asperities centered 200 km from the center of the middle one). We cut a profile halfway between the middle and outer asperities (at y= 100 km) (Figure 2.12). The profile through the former asperity (with 3 remaining asperities in the model) has lower trench-perpendicular velocities than the same profile through the asperity (model with 5 asperities), with a shallower slope of decrease in the near-trench portion of the overriding plate, but still with a clear hurdle in the form of a break in the slope at the location of the contrast in E (Figure 2.12a). Trench-parallel velocities have a similar behavior, except that velocities beyond the contrast are approximately identical.

2.4.8 Lateral Thickness Variation and Sharpness of the Mechanical Contrast

In our models, a contrast in elastic moduli in an overriding plate of uniform thickness is a proxy for a general contrast in the plate's elastic compliance. We test the addition of a step increase in overriding plate thickness, doubling in thickness from 40 km at $x < 700$ km to 80 km at $x \geq 700$ km, to our reference model and to the model with a uniform E of 100 GPa. The trench-perpendicular interseismic velocity decreases $\sim 30\%$ at the contrast

while leaving the peak value unaffected, thus making its decrease with distance from the trench slightly steeper on the oceanward side of the contrast and more gradual on the beyond the contrast (Figure 2.13). Trench-parallel velocities are unaffected by the thickness contrast. Heterogeneity in overriding plate thickness, and particularly a thinner arc region, likely contributes to the observed behavior of interseismic surface velocities, but is not solely responsible for hurdle characteristics.

2.4.9 Effect of the Ratio of the Earthquake Recurrence Interval to the Maxwell Time

The ratio $\frac{T}{\tau}$ of the earthquake recurrence interval T to the characteristic Maxwell relaxation time $\tau = \frac{\eta}{G}$ is an important property of the megathrust system. In fact, it determines to what extent coseismic stresses have relaxed late in the cycle, and thus to what extent late interseismic motion reflects steady-state loading of the plate due to continued convergence and locking (Savage, 1983). Higher $\frac{T}{\tau}$ ratios reduce the slope of trench-perpendicular velocities with distance from the fault trace in a simple 2D dip-slip fault cutting across an elastic lithosphere overlying a Maxwell viscoelastic mantle (Wang *et al.*, 2021). Our models so far use a $\frac{T}{\tau}$ ratio of 37.9, intermediate for the range of possible ratios observed for subduction zones worldwide and representing a case in which the stress changes due to coseismic slip and afterslip have relaxed late in the cycle (Govers *et al.*, 2018).

We now explore the effect of reducing the $\frac{T}{\tau}$ ratio of our model with uniform elastic moduli throughout ($\nu = 0.25$, $E = 100$ GPa in the overriding plate and elsewhere), while keeping the convergence rate and earthquake size constant. Figure 2.14 shows the interseismic velocity profiles for the model with the reference model viscosity of 10^{19} Pa$\cdot$s (black line, same model and curves as in Figures 2.8, 2.9 and 2.13), and for alternative models with higher viscosities (i.e., longer relaxation times and smaller $\frac{T}{\tau}$) of the viscoelastic mantle. The resulting interseismic model velocities decrease more steeply with distance from the trench with decreasing $\frac{T}{\tau}$. The effect is particularly significant for the trench-perpendicular component. When the $\frac{T}{\tau}$ ratio is halved to 18.9, the effect is limited and the trench-perpendicular velocities still decrease shallowly with distance. However, further reducing $\frac{T}{\tau}$ makes the slope at intermediate-field distances even steeper, and particularly $\frac{T}{\tau} < 10$ makes the velocity 700 km away from the trench equal to or lower than 25% of the peak value. This indicates that, for a sufficiently long Maxwell time relative to the earthquake recurrence interval, the hurdle behavior exhibited by observed

trench-perpendicular velocities may be explained without invoking a contrast in the compliance of the overriding plate. We further discuss the viability and implications of such explanation in Section 2.5.2.

2.5 Discussion and Implications

2.5.1 Scope and Limitations of Our Study

We reevaluate published interseismic GNSS velocity observations along three subduction margins: the Peru-Chile Trench (South America), the Sunda Trench (Sumatra, Java), and the Japan Trench (Hokkaido and northern Honshu). In South America, our analysis, not hampered by marine basins, yields the most continuous sampling of the kinematics in the overriding plate. The analysis will need to be extended to other convergent margins before we can conclude that hurdles, breaks in the interseismic velocity gradient, are global features of megathrust margins. Still, with three out of the three margins showing hurdles, we think that we have a basis to hypothesize a more common feature that mechanically separates the deforming margin from a semi-stable overriding plate interior.

Our mechanical models are generic in their geometry, earthquake cycle, and mechanical properties. Further work will be needed to model the specific contribution of regional rheological makeup and active deformation structures to interseismic velocities. It might also be important to include radial elasticity variations and the sphericity of the Earth. Radially-varying elasticity decreases does not affect far-field velocities (**Pollitz2011b**; Pollitz *et al.*, 2011; see also Section 2.4.3). Sphericity was shown to have a negligible effect on modeled coseismic horizontal displacement due to thrust faulting at distances of 0 to 5000 km from the trench (Nostro *et al.*, 1999). Trubienko *et al.* (2013) showed that interseismic displacement, normalized by the coseismic, 700 km from the trench has the same slope towards the end of the cycle, regardless of sphericity, indicating that interseismic velocities at the end of the cycle should also be hardly affected.

2.5.2 Role of the Maxwell Time in Relation to the Earthquake Recurrence Interval

As we show in Section 2.4.9, low values (broadly below 10) of the $\frac{T}{\tau}$ ratio cause the velocities to decrease more steeply with distance from the trench. In that case, coseismic stresses have not fully relaxed before the next earthquake

occurs, and as a result viscoelastic model results become similar to those of fully elastic models. This effect is consistent with the results of the simple 2D models of Wang *et al.* (2021) and of the earthquake cycle models of Li *et al.* (2015) and Trubienko *et al.* (2013). It is also analogous to model results showing that shorter recurrence times lead to greater localization of interseismic deformation around strike-slip faults (Zhu *et al.*, 2020) and, conversely, that recurrence times that are long, compared to relaxation times, lead to substantial deviation between the deformation pattern of viscoelastic and of elastic models (Hetland and Hager, 2005). Trubienko *et al.* (2013) explain the spatial distribution of interseismic velocities in two transects, through central Sumatra and the Malay peninsula and through northern Honshu in Japan, using an earthquake cycle model with a uniform elastic overriding plate. Their model employs a plane-strain approximation, a Burgers viscoelastic rheology for the mantle with a steady-state (Maxwell) viscosity $\eta = 3 \cdot 10^{19}$ Pa·s, asthenospheric elastic parameters from PREM (Dziewonski and Anderson, 1981; giving $G 68$ GPa and $\nu 0.28$ in the asthenosphere), and a return period of 170 years. Their $\frac{T}{\tau}$ is thus ~ 7.2, accounting for the fact that τ is $3\frac{1-\nu}{1+\nu}\frac{\eta}{G}$ higher in the plane strain regime (Melosh and Raefsky, 1983). Li *et al.* (2015) similarly reproduce interseismic velocities in the North Chile portion of the Andean subduction zone using a uniform overriding plate, with a viscosity of $4 \cdot 10^{19}$ Pa · s in the Maxwell viscoelastic mantle wedge and an earthquake cycle duration of 200 years, resulting in a $\frac{T}{\tau}$ of ~ 10.1.

Li *et al.* (2015) and Trubienko *et al.* (2013) do not incorporate finite gradients in slip deficit downdip of the locked interface and instead impose slip deficit to sharply transition from non-zero to zero at the downdip end of the megathrust. A sharp transition in slip deficit is physically unlikely (Herman and Govers, 2020) and precludes the occurrence of the intermediate-depth afterslip (down to at least 80 km depth) that has been inferred from geodetic and seismological observations (Diao *et al.*, 2014; Sun *et al.*, 2014; Yamagiwa *et al.*, 2015; Hu *et al.*, 2016a; Freed *et al.*, 2017). The depth to which slip deficit accumulates is especially important, as Li *et al.* (2015) and Trubienko *et al.* (2013) show that greater locking depths producing larger intermediate- and far-field velocities. These studies rely on shallow locking depths to reproduce interseismic velocities. Furthermore, when inverting observations, Li *et al.* (2015) do not apply a model spin-up, necessary to obtain viscous stresses and strain rates consistent with the long-term repetition of the earthquake cycle. As Li *et al.* (2015) point out, the spin-up would increase horizontal velocities, particularly in the intermediate-field (100–300 km from the trench), decreasing their trench-perpendicular slope. Therefore, the steepness of the decrease in interseismic velocities with distance from the trench is overesti-

mated for a given $\frac{T}{\tau}$ ratio in the models of Li *et al.* (2015) and Trubienko *et al.* (2013). Nevertheless, their results suggest that low $\frac{T}{\tau}$ ratios might explain the apparent hurdle behavior of interseismic velocities in the absence of contrasts in the compliance of the overriding plate.

Models of postseismic relaxation following the 2004 Sumatra-Andaman earthquake, using Burgers rheologies for the asthenospheric mantle, consistently indicate steady-state viscosities of ~ 1019 Pa $\cdot$ s, corresponding to a Maxwell time $\tau of \sim 5$ years (Hu and Wang, 2012; Broerse *et al.*, 2015; Qiu *et al.*, 2018), while the recurrence interval for an earthquake of similar size has been estimated to be between 174 and 600 years (Gahalaut *et al.*, 2008b; Meltzner *et al.*, 2010; Van Veen *et al.*, 2014), yielding $\frac{T}{\tau}$ ratios of 34.8–120. For the Chilean convergent margin, Klein *et al.* (2016) and Li *et al.* (2018a) invert postseismic GNSS observations in the few years (5 and 8, respectively) following the 2010 Maule earthquake, using a Burgers or Maxwell viscoelastic rheology, and consistently find Maxwell viscosities of 5–$6 \cdot 10^{18}$ Pa $\cdot$ s in the continental asthenosphere under the Andes, corresponding to Maxwell times of 2.4–3.0 years. Aron *et al.* (2015) estimate the return period as between 84 and 178 years, which would put $\frac{T}{\tau}$ in the 28.0–74.2 range. In the Japan subduction zone, simultaneous inversions of GNSS time series following the 2011 Tohoku earthquake into afterslip and viscoelastic relaxation parameters, using Burgers or non-linear flow law–based viscoelastic rheologies for the asthenosphere, indicate that the steady-state viscosity of the mantle wedge is in the range of 4–101018 Pa $\cdot$ s (Agata *et al.*, 2019; Muto *et al.*, 2019; Fukuda and Johnson, 2021). This corresponds to Maxwell relaxation times of 2.0–5.0 years and is in agreement with the results of the inversion of gravity data into viscous relaxation parameters only by Cambiotti (2020). The recurrence interval T for events similar to the 2011 Tohoku-oki earthquake is ~ 600 years (Satake, 2015), which puts the $\frac{T}{\tau}$ ratio in the 120–300 range. The ratios (12.1 and 7.2, respectively) used by Trubienko *et al.* (2013) and Li *et al.* (2015) are thus below the low end of the realistic range. Our models reproduce the hurdle-like response for low ratios of $\frac{T}{\tau}$ (Section 2.4.9). Still, higher ratios are more realistic for the active margins that we investigate, and our model results show that hurdle behavior is not reproduced with uniform high $\frac{T}{\tau}$ ratios (mantle viscosities in line with the majority of postseismic studies) combined with uniform elastic compliancy of the overriding plate (Sections 2.4.2 and 2.4.4). This argues for compliancy contrasts in the overriding plate.

2.5.3 Tectonic Significance of a Mechanical Contrast

Klein *et al.* (2016) suggest that stiff cratonic back-arc lithosphere in central Argentina affects horizontal and vertical postseismic surface velocities following the Maule earthquake. Li *et al.* (2018a) invert postseismic displacements, including in the far field, following the Maule earthquake into rheological structures of the upper mantle, finding strong evidence for a stiff (elastic, or viscoelastic with high viscosity) cratonic lithospheric root beneath central Argentina. Seismic data also indicate that the Andean lithosphere has very thick crust and warm lithospheric mantle that contrast with thinner (but still thick) cratonic crust underlain by cold, stiff lithospheric mantle farther to the east, from Venezuela to central Argentina (Chulick *et al.*, 2013). This juxtaposition represents a significant contrast in lithospheric averages of the compliance. The hurdle location that we inferred from the GNSS velocities agrees with the tectonic boundary (Section 2.2.5 and fig. 2.6a). Immediately to the south of the Central Andes, around 30°S, the trench-perpendicular hurdle coincides with different terrane and active tectonic boundaries (Ramos, 1988; Ramos, 1999). In particular, it is located between the eastern front of the active Andean Precordillera fold-and-thrust belt (Baldis *et al.*, 1982; Ortiz and Zambrano, 1981) and the western margin of the Rio de la Plata craton (Álvarez *et al.*, 2012), within a mountain range (the Sierras Pampeanas) characterized by active reverse faults and lateral contrasts in crustal thickness and layering (Perarnau *et al.*, 2012). The eastern edge of the Andes as marked by active faults correlates spatially with the western edge of the distinct, stable, largely cratonic interior of the South America plate. Thus, the general but imperfect coincidence of the hurdle with the active backthrust, where present, is consistent with the hurdle being determined by a contrast in compliance that occurs with different amplitudes and different depth dependences along the orogen.

In Sunda, the overriding plate is a set of Paleozoic-Cenozoic accreted terranes (Hall *et al.*, 2009). We are unaware of independent proof that Sundaland is mechanically stiffer than the Sumatra forearc. However, a significant crustal contrast exists across the Meratus paleosuture in Java (Figure 2.6b; Haberland *et al.*, 2014). Contrasts may also exist across two major structural boundaries. The first of these is peninsular Malaysia's Bentong-Raub suture zone, which separates the Sibumasu terrane to its southwest from the Indochina terrane (Metcalfe, 2000). The second boundary is the Medial Sumatra Tectonic Zone, which separates the Sibumasu terrane to the northeast from the West Sumatra block and the overlying Woyla accretionary complex and volcanic arc (Hutchison, 1994; Hutchison, 2014; Barber, 2000; Barber *et al.*, 2005) and which largely coincides with the strike-slip Sumatran Fault in central and northern

Sumatra. Simons *et al.* (2007) used GNSS data to identify the approximate boundaries of the interseismically nondeforming part of the Sundaland block (Michel *et al.*, 2001); its internal (south and west) boundary aligns roughly with geological suture boundaries. On the other hand, estimates from coherence between gravity and topography show no evidence of a block in the interior of the plate with higher T_e than the forearc region (Audet and Bürgmann, 2011; Shi *et al.*, 2017).

To explain the steep spatial gradient near the trench in horizontal interseismic velocities in Hokkaido, Japan, Itoh *et al.* (2019) and Itoh *et al.* (2021) proposed and modeled the effect of a compliant lithosphere in the volcanic arc and back-arc, in contrast with a less compliant forearc, as evidenced by temperature, heat flux, and seismic wave attenuation (Katsumata *et al.*, 2006; Kita *et al.*, 2014; Liu *et al.*, 2013; Tanaka *et al.*, 2004; Wada and Wang, 2009; Wang and Zhao, 2005). However, in the model of Itoh *et al.* (2019), velocities are restricted by the fixed landward edge of the domain, which localizes shortening and shearing in the compliant material. We propose that velocities are instead restricted by the contrast between the compliant arc and back-arc and the less compliant material farther from the trench, in the Sea of Japan and beyond. The Sea of Japan is a Miocene back-arc basin of the Japan and southern Kurile subduction zones. It is inactive (Karig, 1974), having ceased extending around 14 Mya (Tatsumi *et al.*, 1989), and is likely less compliant than the Japan arc. The Amurian-Okhotsk plate boundary follows the sea's eastern margin (Seno *et al.*, 1996) (Figure 2.6c). The plate boundary mechanically decouples these plates in the long term, but they are coupled during most of the earthquake cycle. The lack of GNSS observations in the Sea of Japan prevents us from determining where exactly the compliance contrast occurs and whether creep along the plate boundary further affects velocities.

2.5.4 Compliance Contrasts in a Rheological and Geodynamic Context

As stated in Section 2.4.4, our model results suggest that interseismic velocities might necessitate a larger contrast in interseismic compliance within the overriding plate than can be provided by realistic elastic parameters. Concretely, the Young's modulus needs to be high enough in the portion of the plate between the trench and the hurdle as to transmit substantial coseismic displacement to the far-field, and low enough in the far-field interior of the plate as to not exceed plausible values. The portion of the plate between the trench and hurdle must thus transition from its greater coseismic compliance, dictated by elastic properties, to lesser compliance in the interseismic period.

This transition might be related to viscous creep of the lower crust and upper mantle (Bürgmann and Dresen, 2008), which reduces flexural rigidity (Ranalli, 1995), and likely also compliance, over time after loading. Low effective elastic thickness is thought to indicate departure from purely elastic rheology, such as due to high temperatures, inherited weak zones, or high horizontal stresses (Burov and Diament, 1995), which are likely to occur in the thermo-mechanically young lithosphere at convergent boundaries. The increased water content at subduction zones also contributes to departure from elasticity by decreasing the viscosity (Kirby, 1983; Chopra and Paterson, 1984; Hirth and Kohlstedt, 1996; Dixon *et al.*, 2004) and lower plastic strength (Blacic and Christie, 1984; Mainprice and Paterson, 1984) of the lower crust and upper mantle. Geodynamical, petrological-thermomechanical numerical modeling of subduction shows that brittle-plastic rheological weakening by both fluids and melts plays an important role in the evolution of the subduction zone and in the development of the volcanic arc and the back-arc region (Gerya and Meilick, 2011). Increased viscosity of the upper mantle under cratons, such as caused by water depletion (Dixon *et al.*, 2004), might also contribute to the effective compliance contrast between the lithosphere-asthenosphere system of the plate interior and that of the near-margin region.

2.5.5 Geodetically Stable Parts of Overriding Plates?

Observations of significant coseismic displacements thousands of km away from the megathrust rupture called into question the concept of an undeforming (rigid) reference plate (Pollitz *et al.*, 2011; Vigny *et al.*, 2005; Wang *et al.*, 2011, see also Section 2.4.1). Our analysis suggests indeed that small but non-zero interseismic velocities and velocity gradients extend beyond the hurdles, and this presents a challenge for defining a reference on a geodetic observation time scale. On time scales spanning the time needed to complete a seismic catalog on the megathrust (tens to thousands of years, e.g., Ward, 1998a; Ward, 1998b, it is possible that the net accumulated strain is zero, i.e., there may exist a fully rigid reference on geological time scales.

2.5.6 Role of Major Faults in the Central Andes

As discussed in Section 2.2.6, previous studies observe and explain the spatial behavior of interseismic velocities, in the context of the Central Andes, as a result of shortening on backthrusts (Norabuena *et al.*, 1998; Bevis *et al.*, 2001; Brooks *et al.*, 2003; Brooks *et al.*, 2011; Kendrick *et al.*, 2006; Weiss *et al.*, 2016; McFarland *et al.*, 2017; Shi *et al.*, 2020). Quantitative models in

these studies use either a uniform elastic half-space, or apply zero-displacement boundary conditions close to the backthrust. Both choices artificially restrict interseismic velocities to the near-trench region, compared to using elastic plates overlying viscoelastic mantle and extending well into the far-field. To explain the observed interseismic surface velocities, most of the studies also need basal thrusts that are more spatially extensive than supported by geological evidence (see Section 2.2.6). However, localized shortening has a more regional role in determining specific trench-perpendicular velocities, particularly in back-arc thrust belts and basal faults and in the interior of active-margin orogens. For instance, when these faults only decouple the shallow lithosphere, they may locally cause discontinuities and increased spatial gradients, without affecting the near-trench portion of the velocity field (Shi *et al.*, 2020). Major, creeping strike-slip faults likely cause large local gradients in trench-parallel velocities, and can localize trench-parallel velocities in a way not necessarily related to the presence of a contrast. Nevertheless, contrasts in lithologies and plate thickness, responsible for hurdles, might also result from continued motion along strike-slip faults. In turn, the presence of such contrasts might localize lateral motion into narrow fault zones.

2.6 Conclusions

Interseismic GNSS velocities from the three studied subduction zones show a broadly linear decrease of the trench-perpendicular velocity with distance from the trench up to what we define as the hurdle, located at variable distances less than 1000 km. Beyond the hurdle, trench-perpendicular velocities are near-zero (less than ~ 5 mm $\cdot$ yr^{-1}) extending over thousands of kilometers away from the trench. Trench-parallel velocities are in some cases affected by presence of strike-slip faults (Sumatra), or are insignificant because of head-on convergence (Japan, Java). In South America, however, they generally also decrease steeply with distance, up to a hurdle. The hurdle roughly coincides with the trench-perpendicular hurdle or is located up to several tens of km closer to the trench. This interseismic deformation restricted to the near-trench region contrasts with significant coseismic displacements that were recorded beyond these hurdles during the large 2004 Sumatra, 2010 Maule and 2011 Tohoku earthquakes.

The location of the hurdle in observed trench-perpendicular velocities often coincides with major tectonic or geological boundaries separating a plate margin region from a distinct, and likely more rigid, plate interior. In South America the trench-perpendicular hurdle generally follows the eastern edge

of the orogen, coinciding with the western margin of the cratonic lithosphere and the eastern margin of the accreted, deformed terranes at the active plate margin. In Sumatra, the hurdle follows the Medial Sumatra Tectonic Zone. Off the shore of northern Honshu and Hokkaido in Japan, the hurdle probably coincides with the boundary between the back-arc region of the islands, to the east, and the inactive back-arc basin and Amur plate interior to the west.

Our numerical modeling results show that a contrast in overriding plate compliance can reproduce the steep, largely linear near-trench decrease in trench-perpendicular velocities with distance. In our models, this decrease ends abruptly at the location of the contrast, i.e., at the hurdle. The value of elastic moduli on either side of the contrast determines the contrast amplitude and thus affects the intensity of the hurdle behavior: a weaker contrast steepens the near-trench slope and/or makes the far-field slope more shallow. Strengthening the contrast by decreasing the near-trench elastic moduli has a greater effect on trench-perpendicular velocities than increasing the far-field moduli, but higher far-field moduli are still important in introducing and defining the hurdle behavior. In contrast, trench-parallel velocities are controlled only by the near-trench elastic moduli and decrease more gradually. The steep decrease in the first couple of hundred km from the trench defines an apparent hurdle that, for the values tested in our models, is closer to the trench than the location of the contrast. The distance between the two depends on the specific elastic moduli and the location of their contrast.

The presence and location of compliance contrasts does not significantly affect the rate at which shear traction increases on the asperities in our models. The width of the zone where interseismic strain primarily accumulates, roughly between the coastline and the hurdle, likely does not generate significant variations in megathrust earthquake magnitude or recurrence interval. Velocities in portions of the subduction zone with little slip deficit, i.e., little apparent interplate coupling on the megathrust, have lower near-trench trench-perpendicular gradients but otherwise similar behavior, particularly in the trench-perpendicular components. Their near-trench trench-parallel components exhibit more complex gradients depending on location with respect to the fully coupled asperities and the direction of trench-parallel, far-field interplate motion.

2.7   Acknowledgments

tion for the velocity data sets that we have used in this study: Laura Sánchez, Jean-Mathieu Nocquet, Corné Kreemer and Achraf Koulali. Insightful reviews by Kelin Wang, Emilie Klein, Rocco Malservisi and two anonymous reviewers contributed significantly to the improvement of earlier versions of the manuscript. We thank editor Kosuke Heki for his constructive evaluation and support.

2.8 Data Availability

The model output files that we used for the figures of this study are digitally stored in the Yoda repository of Utrecht University and are freely available under the CC-BY license at https://doi.org/10.24416/UU01-6SC8XG.

2.9 Supporting Information

2.9.1 Introduction

This supplementary material includes additional information on the processing steps used to process the published horizontal velocities from GNSS sites into interpolated fields of trench-perpendicular and trench-parallel velocities (Section 2.9.2, cf. Section 2.2). We include an accompanying table of data sources for South America (Table S1) and Southeast Asia (Table S2). The figures are related to both the interpolation as well as the numerical modeling portion of the paper, and the latter show model results briefly discussed in Section 2.4. All modeling results, as described in Section 2.3, have been produced using the

GTECTON finite element software package version Parallel 2021.0.0 (Govers and Wortel, 1993; Govers and Wortel, 2005; Govers *et al.*, 2018).

2.9.2 Estimating a Backstop Location from Interseismic Velocities

Collection of Interseismic Velocities

We collect estimates from horizontal velocities from published literature, for the South American margin, the Sunda margin and for (northern) Japan. The velocities are based on repeated GNSS campaign measurements or continuous GNSS observations, where the oldest measurements go back to the early 1990s, and the continuous observations are more recent.

We use velocities expressed in a global reference frame. A number of older studies expressed velocities for South America in a non-explicit stable South America reference frames, that likely differ between studies. Therefore, we use the tables from Kreemer *et al.* (2014), where a translation rate and rotation rate has been estimated for each published set of velocities, using overlapping sites from the various studies, to express velocities in the IGS08 reference frame (the IGS realization of ITRF2008, as defined by Rebischung *et al.*, 2012). For these velocities, and those already expressed with respect to an ITRF (ITRF2005, ITRF2008, or ITRF2014) we apply the South America Euler pole of Kreemer *et al.* (2014). The differences between subsequent ITRF releases are well below the $1 \text{ mm} \cdot \text{yr}^{-1}$ level (Métivier *et al.*, 2020). We also include velocities from Weiss *et al.* (2016), which are only provided in a self-determined, non-explicit South America reference frame; in that case, we show that the residuals between station velocities in that reference frame and velocities at the same stations from other studies (published in an ITRF and rotated into a South America frame) are extremely small (below $0.2 \text{ mm} \cdot \text{yr}^{-1}$).

Table S1 provides an overview of all data sources that we use for South America, including data periods and information on the reference system in which the velocities have been provided by different studies. Table S2 contains the overview for Southeast Asia, where again we have made use of the data selection from Kreemer *et al.* (2014) that is expressed in a consistent reference frame. We add the GPS velocities for Java from Koulali *et al.* (2017) and apply their Euler pole to express the velocities in ITRF. Afterwards we apply the same Sunda Euler pole from Simons *et al.* (2007) to express velocities with respect to the overriding plate. As velocity estimates based on older campaign GNSS observations have higher uncertainties, the velocity field has a heterogeneous noise level. For Japan the velocities have also been taken from

the collection of Kreemer *et al.* (2014), see table S3 for the original sources. We express the velocities for Japan in the Okhotsk frame from (Kreemer *et al.*, 2014).

As multiple earthquakes with magnitudes $M_W > 7.5$ have occurred along the South American, Sunda and Japan margins during the period of collecting GNSS data, coseismic offsets and postseismic transients potentially affect the velocity estimates. For this reason, we often have to resort to older studies that collected pre-earthquake data. We discard velocities from the database that have been derived from observations that may be affected by large earthquakes. As these earthquakes are thrust events, and thrusting leads mostly to coseismic and postseismic displacements towards the rupture, we assume that the affected areas are the areas located in the hinterland of the rupture. Generally, we exclude all velocities postdating major earthquakes up to a 1000 km trench-perpendicular distance of a ruptured area (for an overview of considered $M_W > 7.5$ earthquakes, and the along-strike distance of the affected areas, see Figure 2.2 in the main text). We make exceptions in case studies corrected for postseismic transients in the GNSS timeseries, using either best-fit models or postseismic parameterization of time series, see tables S1 to S3. For the largest earthquakes, the 2004 Sumatra-Andaman, the 2010 Maule and 1960 Valdivia earthquakes, we exclude data within 1500 km from the trench. This implies that we do not consider data from sites in the vicinity of the 1960 Valdivia rupture, as postseismic relaxation due to the 1960 event has been ongoing (Wang *et al.*, 2007). Similarly, for Japan we only use data preceding the 2011 Tohoku earthquake. From the resulting dataset of inter-seismic velocities, we keep the velocity that has been estimated using the longest pre-earthquake time span of observations, as many sites have been revisited at later times.

Once we have obtained the two components of horizontal motion for each observation (Section 2.2), we interpolate each component separately. First, we turn observations at locations less than 1 km apart into single data points by computing the weighted average of the geographical coordinates and the velocity components. In the averaging, we use as weights the inverse of the observation variances, i.e., the squares of the observation uncertainties. We rotate each individual horizontal velocity and associated uncertainty to its local trench-perpendicular and trench-parallel direction (Figures 2.15 to 2.17), as described in Section 2.2.2. We perform the following interpolation procedure twice, separately, on trench-parallel and trench-perpendicular velocities.

Interpolation: Local Ordinary Kriging

We define a structured interpolation grid, with a spacing of 0.25 degrees (South America) or 0.1 degrees (Sunda and Japan) in longitude and latitude, respectively. We use all n velocities and their reported uncertainties at each interpolation grid point using ordinary kriging (Wackernagel, 2003). Kriging is a weighted average method that uses statistical information of the observations (velocities in our case) z_i to determine weights w_i and related interpolation uncertainties and thus compute the interpolated quantity $\widehat{z_0}$ at interpolation point 0:

$$\widehat{z_0} = \sum_{i=1}^{n} w_i z\left(x_i\right) \qquad \text{with} \quad \sum_{i=1}^{n} w_i = 1 \tag{2.1}$$

We compute the weights using covariance functions for velocities at all observation points C_{ij}, the covariance functions C_{i0} for observation points and the interpolation point, and the reported velocity uncertainties σ_i. We assume that the covariance function between sites i and j, $C_{ij} = C(h_{ij})$, depends only on the respective distance h_{ij} (computed over a spherical Earth), and the same holds for the covariance between an observation point i and interpolation point 0. The Lagrange parameter μ is included to ensure that the weights sum up to 1, and the weights can be obtained by solving the ordinary kriging system (e.g., Lindenbergh et $al.$, 2008):

$$w = \begin{bmatrix} w_1 \\ \vdots \\ w_n \\ \mu \end{bmatrix} = \begin{bmatrix} C_{11} + \sigma_1^2 & \dots & C_{1n} & 1 \\ \vdots & \ddots & \vdots & 1 \\ C_{n1} & \dots & C_{nn} + \sigma_n^2 & 1 \\ 1 & \dots & 1 & 0 \end{bmatrix}^{-1} \cdot \begin{bmatrix} C_{10} \\ \vdots \\ C_{n0} \\ 1 \end{bmatrix}. \tag{2.2}$$

We compute every covariance term C_{ij} as a function $C(h)$ of the distance h. Before we can do so, we first compute the empirical covariance $\hat{C}(h)$. This requires the covariance between each pair of observed velocities:

$$\hat{C}_{ij} = (z_i - \hat{\mu})(z_j - \hat{\mu}) \tag{2.3}$$

with mean $\hat{\mu}$. Subsequently we bin the covariances in distance intervals, following the binning procedure used by Machuca-Mory and Deutsch (2013). We finally fit an exponential decay function $\rho(h)$ to the empirical covariance $\hat{C}(h)$ that defines a parameterized covariance function of the form:

$$C(h) = C(0)\,\rho(h) = C(0)\exp\left(-\frac{h}{r}\right), \tag{2.4}$$

with variance $C(0)$. From the exponential correlation function, we construct covariance matrices that are mathematically valid over a sphere (Huang *et al.*, 2011). The range parameter r determines how fast the correlation decreases when observations are farther apart.

The mean, variance and correlation of the velocity components are strongly varying throughout the domain. Computing a single covariance function $C(h)$ for the entire velocity field would thus yield inaccurate results. Therefore, we compute $C(h)$ locally (and we define what "local" means later on), at every third point of the interpolation grid in either direction (which we call an anchor point), in a similar manner as Fouedjio and Séguret (2016) and Machuca-Mory and Deutsch (2013).

To make the local covariance function reflect only the velocities in its vicinity, at each anchor point we use a Gaussian kernel to apply a weight to the observed velocities when binning the empirical covariance as a function of distance to the anchor point. For the definition of locally weighted empirical covariance, we refer to Machuca-Mory and Deutsch (2013). Moreover, we multiply the Gaussian kernel weight with the inverse of the observation variances.

The Gaussian kernel requires a width, which determines the sensitivity of local covariance to velocities at a given distance. We define the width depending on the radius of the natural neighborhood of each anchor point. To determine natural neighbors at each anchor point, we consider the anchor point and all observation points and we construct Voronoi cells, i.e., regions of space nearer to a single point than to other points. We determine the natural neighbors as the observation points whose Voronoi cells border the Voronoi cell of the anchor point (Sibson, 1981). We define the natural neighborhood radius as the mean distance of the natural neighbors to the anchor. We set the Gaussian kernel width such that the kernel has a value of 0.5 at the natural neighborhood radius. To prevent that the locally weighted observation variance is larger than the covariance function variance $C(0)$ (which leads to a discontinuous interpolated field), we require that the local variance is at least 4 times larger than the weighted average of the local observation variance. This we obtain by iteratively increasing the natural neighborhood radius until the requirement is met.

We fit the exponential covariance function to the local experimental covariance using a Trust Region algorithm (Conn et al., 2000), where we apply the same Gaussian kernel to obtain fitting weights for each distance bin in the exponential covariance The range parameter r determines the correlation length in the exponential correlation function $\rho(h)$, and we require the range to be at least 0.5 times the natural neighborhood radius. A smaller range may

lead to absence of correlation between neighboring observations and leads to discontinuities in the interpolated field.

We use natural neighbor interpolation (Sibson, 1981) to interpolate the covariance functions from the anchor points to all the other points on the interpolation grid. Next, we apply ordinary kriging with the interpolated local covariance functions at each grid point to obtain an interpolated velocity and associated uncertainty. Figures 2.3 to 2.5 show the resulting interpolated velocity fields. The kernel widths and covariance function parameters used in the kriging are shown in Figures 2.18 to 2.23.Figures 2.24 to 2.26 depict the estimated uncertainties associated with the interpolated velocity fields. We follow Lindenbergh *et al.* (2008) to estimate interpolation uncertainties.

Hurdle Estimation

We estimate hurdle distances along trench-perpendicular profiles, using the trench-perpendicular and trench-parallel velocity field and associated uncertainties. To do so, we resample the velocity fields and uncertainties using bilinear interpolation. We show a selection of these cross-sections in Figures 2.3 to 2.5. We express the velocities and uncertainties as function of distance along a profile. To estimate a hurdle location, we fit a function f consisting of two linear segments to the velocity y_i, where the breakpoint α between the two lines describes the hurdle distance:

$$y_i = f\left(x_i, \theta, \alpha\right) + \epsilon_i, \tag{2.5}$$

with the continuous two segment function f as a function of distance x_i and bias and slope parameters θ:

$$f\left(x_i, \theta,\ \alpha\right) = \begin{cases} \theta_1 + \theta_2 x_i, & x_i \leq \alpha \\ \theta_3 \left(x_i - \alpha\right) + \theta_1 + \theta_2 x_i, & x_i > \ \alpha \end{cases} \tag{2.6}$$

Using weighted non-linear least squares we minimize the following, using a Trust Region algorithm, applying the standard deviations σ_i estimated in the local kriging as weights.

$$\min\left(\Sigma_{i=1}^n \left(\frac{f\left(x_i, \theta, \alpha\right) - y_i}{\sigma_i}\right)^2\right). \tag{2.7}$$

To estimate uncertainties of the parameters (including the hurdle distance), we linearize at the parameter estimates $\hat{\theta}$, $\hat{\alpha}$ such that we can propagate the

velocity uncertainties to obtain the variances of the estimated parameters:

$$C_{\hat{\theta},\hat{\alpha}} = \left(J^T C_y^{-1} J \right)^{-1}.$$ (2.8)

Here the inverse covariance matrix C_y^{-1} of the velocity fields is a diagonal matrix:

$$C_y^{-1} = diag \left(\frac{1}{\sigma^2} \right)$$ (2.9)

And J is the Jacobian matrix, describing the dependence of the function f to variation in the estimated parameters:
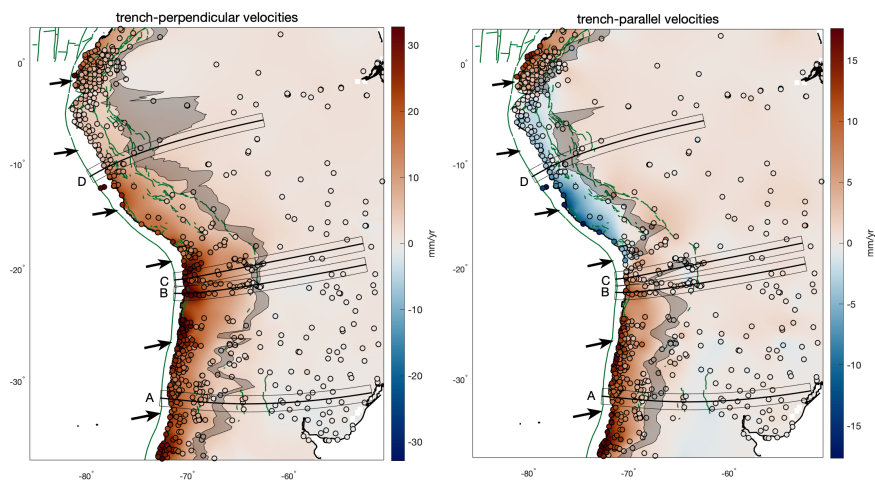
$$J = \frac{\partial f \left(x, \hat{\theta}, \hat{\alpha} \right)}{\partial \theta, \alpha},$$ (2.10)

mumerically evaluated at the estimate for θ and α. We compute the 95% confidence bounds of the hurdle distance by

$$\hat{\alpha} \pm t \left(0.025, n - p \right) \sigma_{\hat{\alpha}},$$ (2.11)

using Student's t-distribution, using n observations and p estimated parameters.
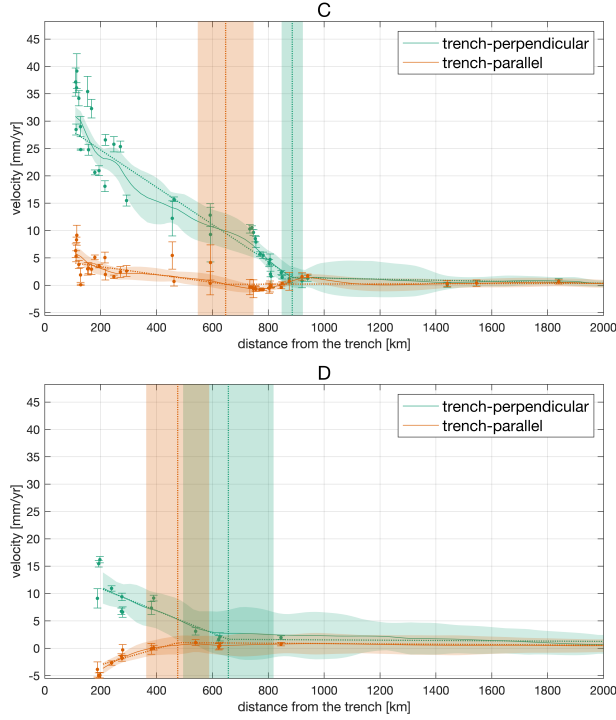
2.9.3   Supplementary Figures and Tables
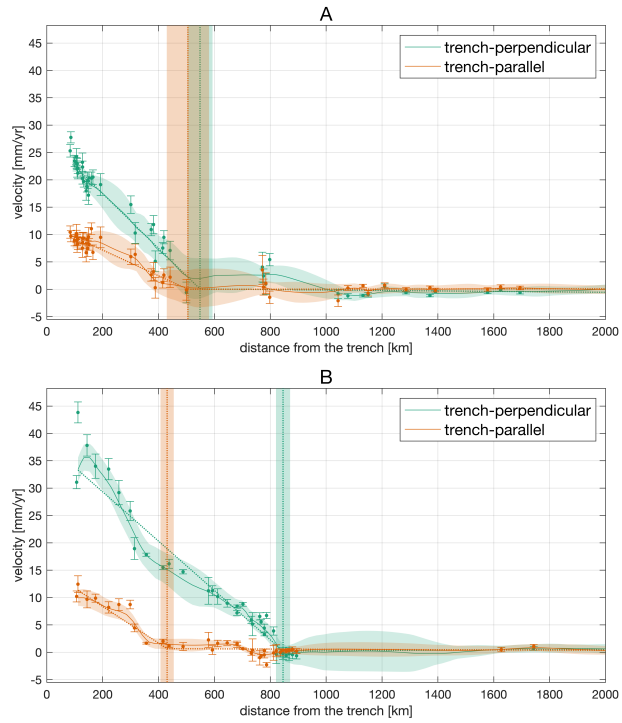
Figure 2.3 Estimated hurdle locations in South America. The maps show interpolated interseismic velocity components (colors, mm · yr^{-1}) and the 95% confidence interval of the location of the hurdle in gray. Active faults (Styron and Pagani, 2020) are shown in green; on the left, we show trench-perpendicular velocities (positive landward), and on the right trench-parallel velocities (positive left-lateral). In both map panels, circles represent GNSS station locations, and their fill color is the observed interseismic velocity component. Arrows show the convergence direction along the Peru-Chile Trench (Kreemer *et al.*, 2014). Coastlines are black. Locations of trench-perpendicular swath profile lines A, B and C are shown on the maps by the thick line surrounded by the thinner lines showing the swath width. The panels below show the velocity profiles along A, B and C, including both interpolated velocity components (continuous lines) with 1–standard deviation uncertainty (transparent bands), and the velocity components at GNSS stations within the swath (dots) with 1–standard deviation error bars. Note that the interpolated velocities are based on all GNSS velocity estimates, and not only those shown in the swath for reference. Dotted green and orange lines depict the piece-wise linear fit. Vertical dotted lines and colored bands outline estimated hurdle distances with 95% confidence intervals.
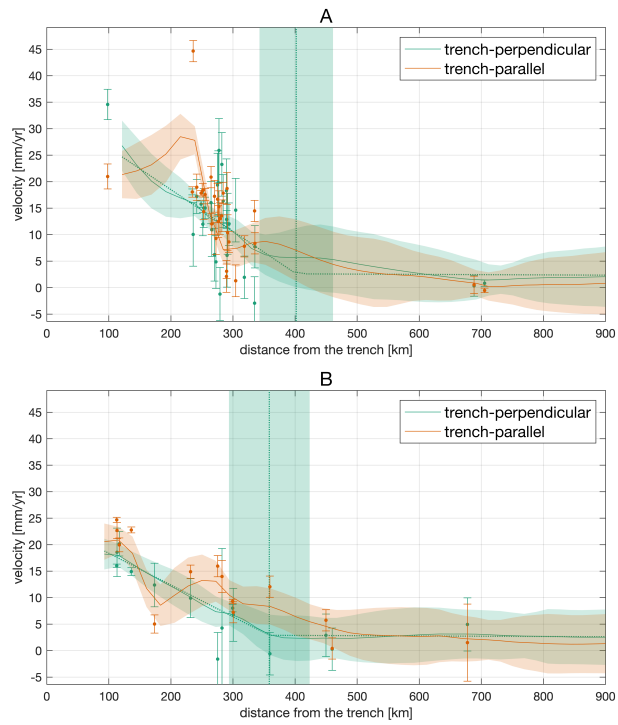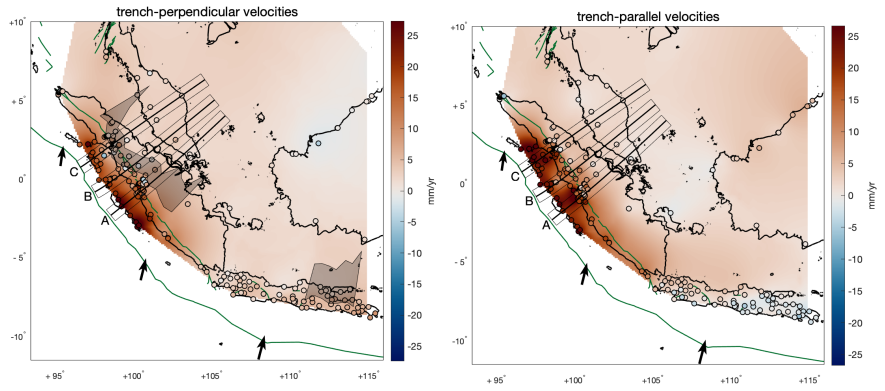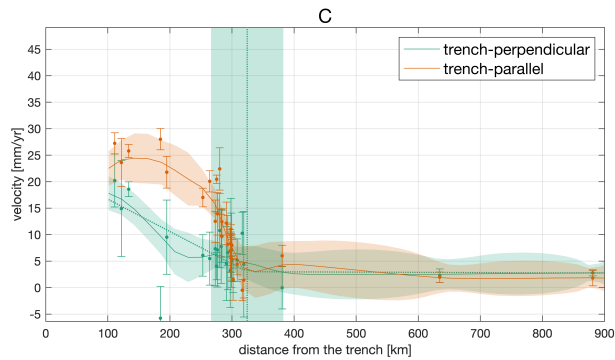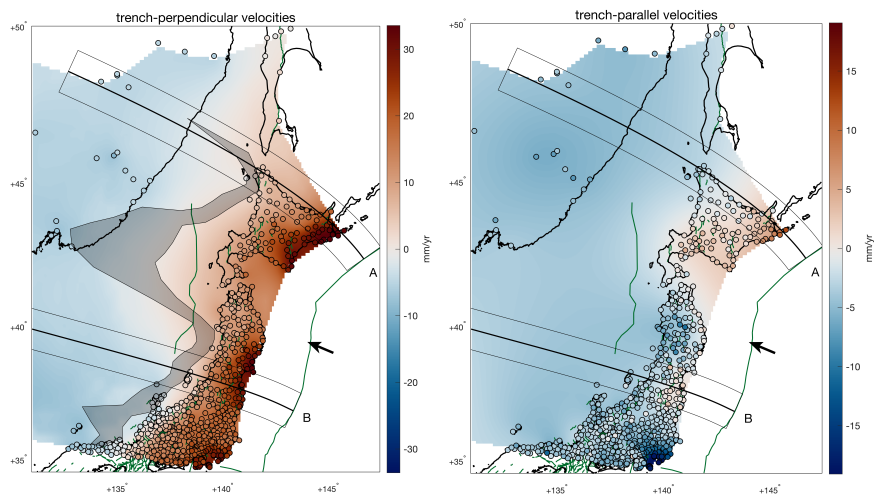
Figure 2.4 Estimated hurdle locations in southeast Asia. Please refer to caption of Figure 2.3. Thick black arrows in the maps show interplate convergence between Sunda and Australian plates (Simons *et al.*, 2007). The panels below the maps show trench-perpendicular and -parallel velocities, and hurdle locations along profiles (A–C) in Indonesia and Malaysia.
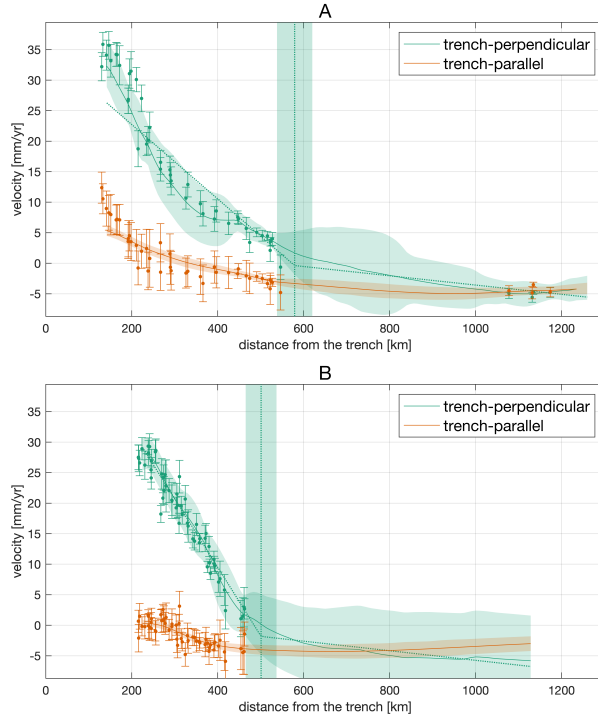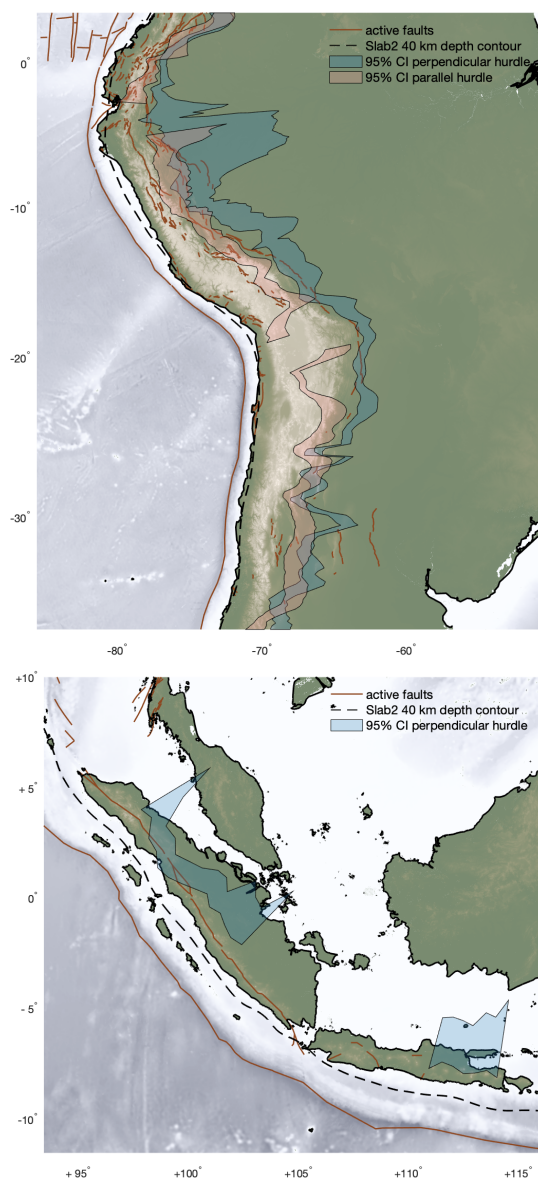
Figure 2.5 Estimated hurdle locations in Honshu and Hokkaido. Please refer to the caption of Figure 2.3. Thick black arrows in the maps show interplate convergence between the Pacific plate and Okhotsk (Kreemer *et al.*, 2014). The panels below the maps show trench-perpendicular and -parallel velocities, and hurdle locations along profiles A (Hokkaido) and B (Honshu).
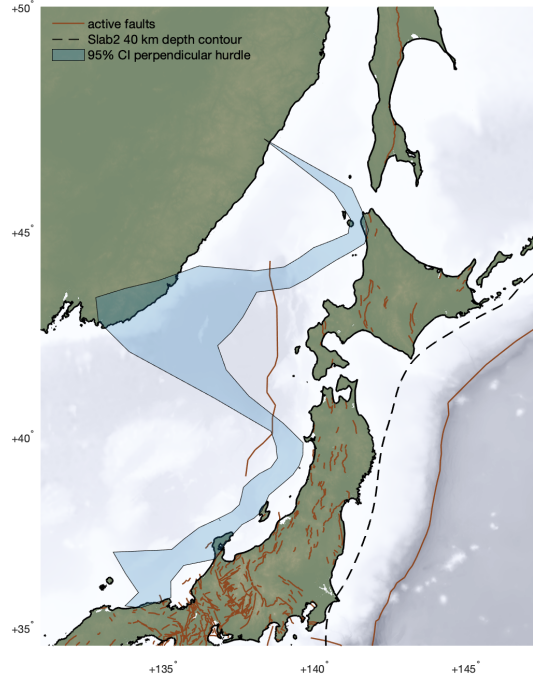
Figure 2.6 Comparison of hurdle locations with main geological features for our study regions. The panels show 1-sigma regions of hurdles for trench-perpendicular velocities in transparent blue regions, and for trench-parallel velocities in pink (c.f. Figures 2.3 to 2.5). Active faults are shown red. The black dashed line shows the 40-km depth contour of the top of the slab (Hayes *et al.*, 2018). The panels show major tectonic and geological features that are discussed in the text, where dashed lines indicate inferred or disputed locations. (a) For South America, the eastern front of the Precordillera, the broad location of the Sierras Pampeanas, and the western edge of the Río de la Plata Craton are taken from Álvarez *et al.* (2012), while the orange line marks the approximate extent of the Proterozoic and older crustal domains (Chulick *et al.*, 2013). (b) For Sunda, the location of the Meratus suture and Southwest Borneo crustal block is taken from (Haberland *et al.*, 2014; Metcalfe, 2011), while the Medial Sumatra Tectonic Zone and the crustal domains in Sumatra and the Malay peninsula are taken from Hutchison (2014) and Metcalfe (2011). (c) For Japan, plate boundaries are from Bird (2003).
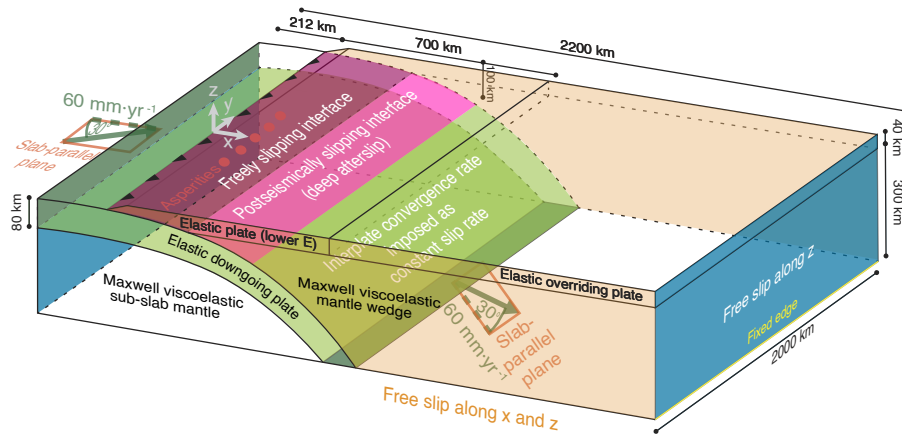
Figure 2.7 Schematic representation of the finite element model domain with its geometry, spatial extent, coordinate system, main mechanical properties, and the applied boundary conditions.
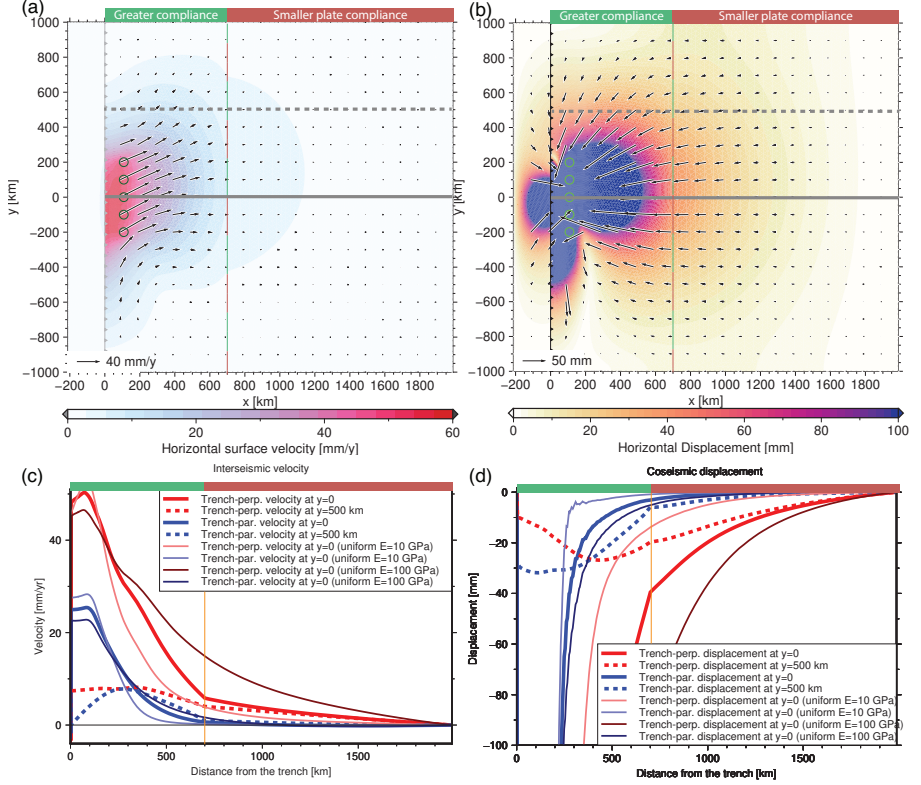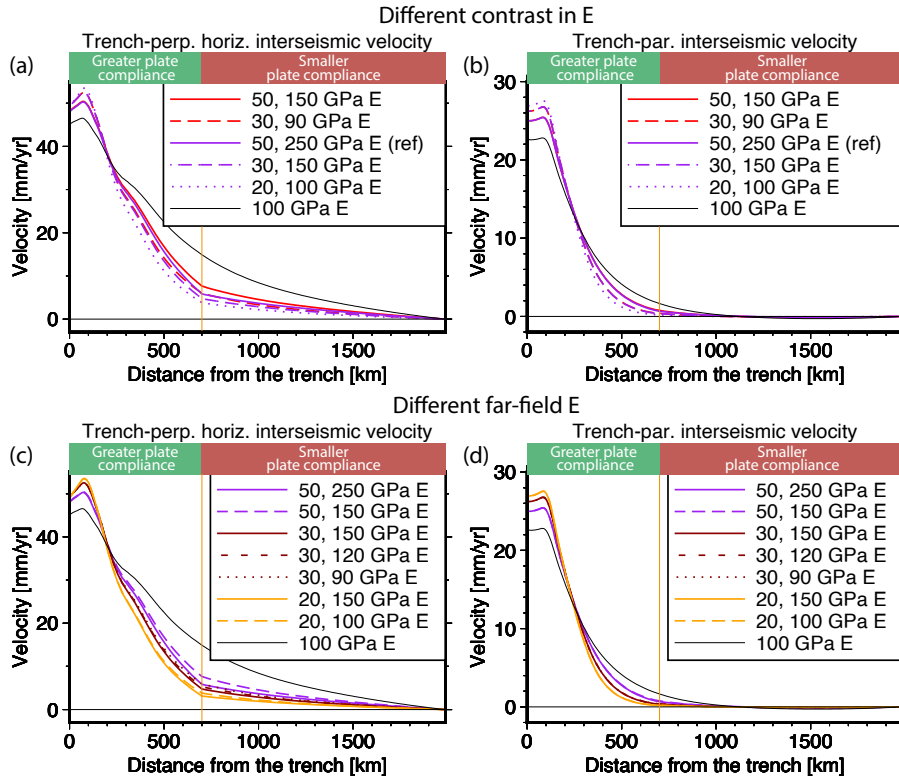
Figure 2.8 Reference model surface deformation and profiles. The extent of the forearc and backarc region with low Young's modulus E, and of the far-field region with high Young's modulus is shown above the panels. (a) Interseismic horizontal velocities at the end of the earthquake supercycle, immediately before the next unlocking of the central asperity. Colors show magnitudes, and vectors show directions and magnitudes. The black barbed line indicates the model trench that separates the subducting plate (left) from the overriding plate (right). Black circles are surface projections of locked asperities. Solid and dashed thick gray lines correspond with transect locations in panels (c) and (d). (b) Coseismic horizontal displacements due to unlocking of the central asperity. Colors show magnitudes, and vectors show directions and magnitudes of horizontal surface displacements. (c) Interseismic surface velocity components along transects on the overriding plate shown in (a) with the same line stroke (continuous or dashed). Positive velocities are landward, to the right. (d) Coseismic displacement components along a trench-perpendicular transects show in (b). Seaward displacement is negative, to the left.

72

Different contrast in E

(a) Trench-perp. horiz. interseismic velocity

Greater plate compliance	Smaller plate compliance

- 50, 150 GPa E
- 30, 90 GPa E
- 50, 250 GPa E (ref)
- 30, 150 GPa E
- 20, 100 GPa E
- 100 GPa E

(b) Trench-par. interseismic velocity

Greater plate compliance	Smaller plate compliance

- 50, 150 GPa E
- 30, 90 GPa E
- 50, 250 GPa E (ref)
- 30, 150 GPa E
- 20, 100 GPa E
- 100 GPa E

Different far-field E

(c) Trench-perp. horiz. interseismic velocity

Greater plate compliance	Smaller plate compliance

- 50, 250 GPa E
- 50, 150 GPa E
- 30, 150 GPa E
- 30, 120 GPa E
- 30, 90 GPa E
- 20, 150 GPa E
- 20, 100 GPa E
- 100 GPa E

(d) Trench-par. interseismic velocity

Greater plate compliance	Smaller plate compliance

- 50, 250 GPa E
- 50, 150 GPa E
- 30, 150 GPa E
- 30, 120 GPa E
- 30, 90 GPa E
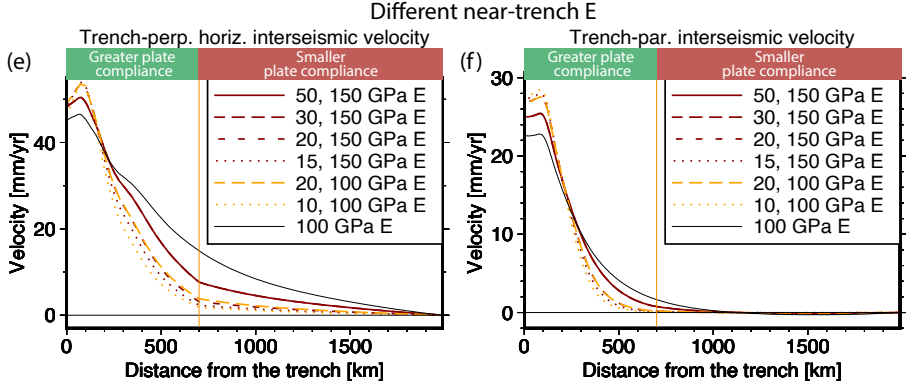- 20, 150 GPa E
- 20, 100 GPa E
- 100 GPa E

Figure 2.9 Sensitivity of interseismic velocities to a compliancy contrast within the overriding plate. Panels show trench-perpendicular and -parallel components of interseismic velocities as function of distance from the trench along a transect through the central asperity (solid grey line in Figure 2.8a). The extent of the forearc and backarc region with low Young's modulus E, and of the far-field region with higher Young's modulus is shown above the panels. The location of the contrast in E, if any, is also marked by the dark orange vertical line. (a,c,d) Trench-perpendicular velocity, and (b,e,f) and trench-parallel velocity. (a,b) Different average E values (different line strokes, less continuous for lower values) with the same contrast (ratio) between near-trench E and far-field E (same color). (c,d) Different far-field E values (different line strokes, less continuous for lower values) with the same near-trench E values (same color). (e,f) Different near-trench E values (different line strokes, less continuous for lower values) with the same far-field E values (same color). The model with a uniform of E of 100 GPa is always shown in black.
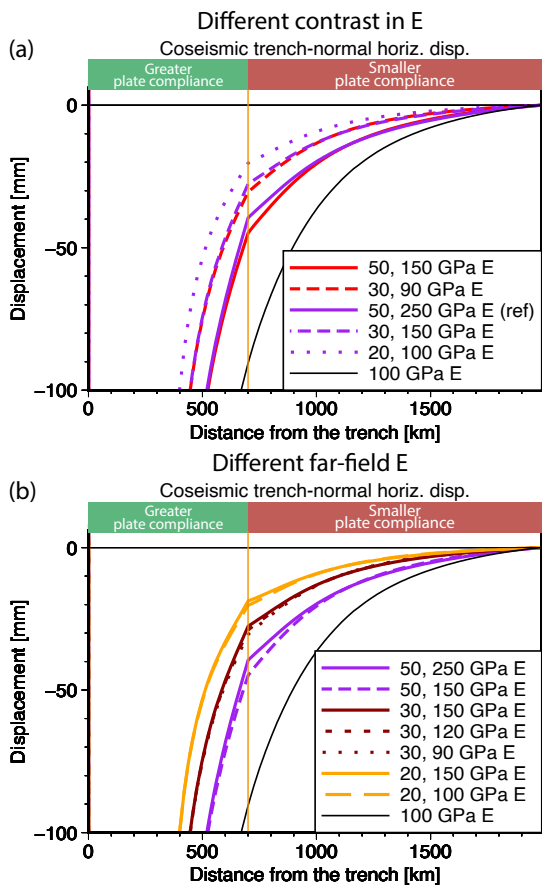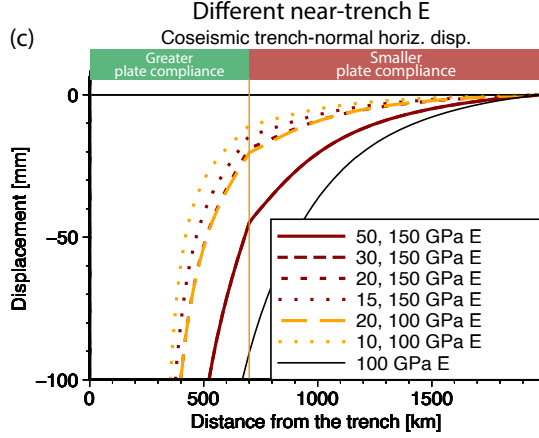
Figure 2.10 Sensitivity of coseismic displacements to a compliancy contrast within the overriding plate. Trench-perpendicular profiles of intermediate- and far-field trench-perpendicular coseismic displacement at $y = 0$, for models with different contrasts in E and for a uniform model as comparison. (a,b) Different average E values (different line strokes, less continuous for lower values) with the same contrast (ratio) between near-trench E and far-field E (same color). (c,d) Different far-field E values (different line strokes, less continuous for lower values) with the same near-trench E values (same color). (e,f) Different near-trench E values (different line strokes, less continuous for lower values) with the same far-field E values (same color). The model with a uniform E of 100 GPa is always shown in black.
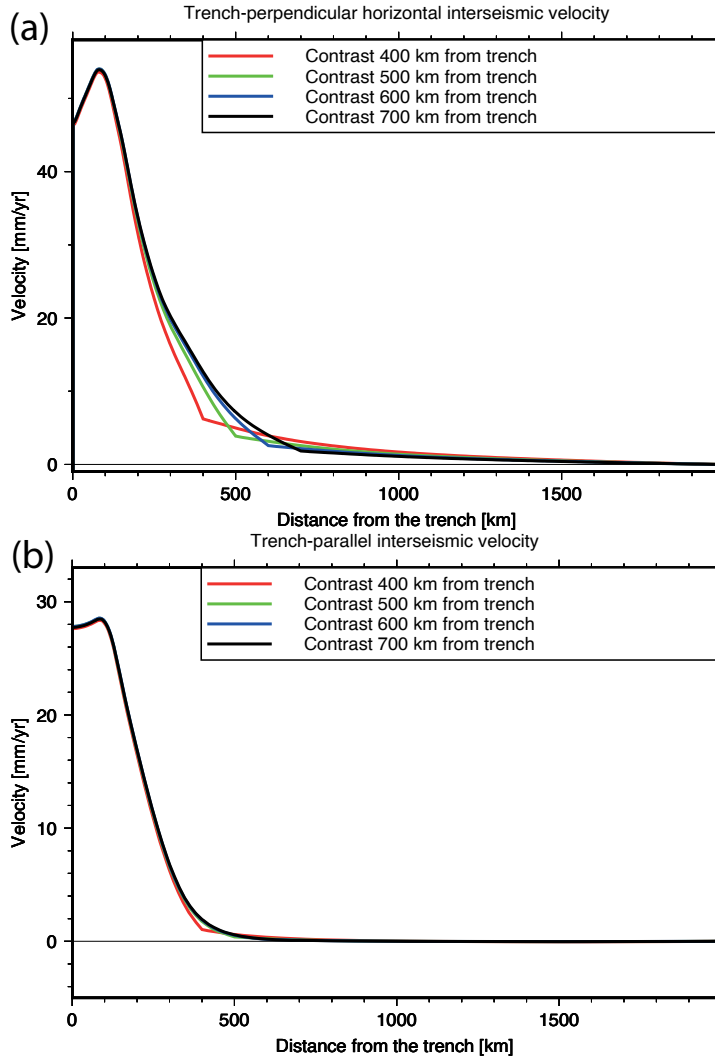
76

Figure 2.11 Sensitivity of interseismic velocities to the location of a compliancy contrast within the overriding plate. Trench-perpendicular profiles are taken through the middle of the model, at $y = 0$, of the interseismic horizontal surface velocity components, trench-perpendicular (a) and trench-parallel (b), respectively, for models with a contrast in the E value of the overriding plate (10 GPa near-trench, 100 GPa in the far-field) for different trench-contrast distances.
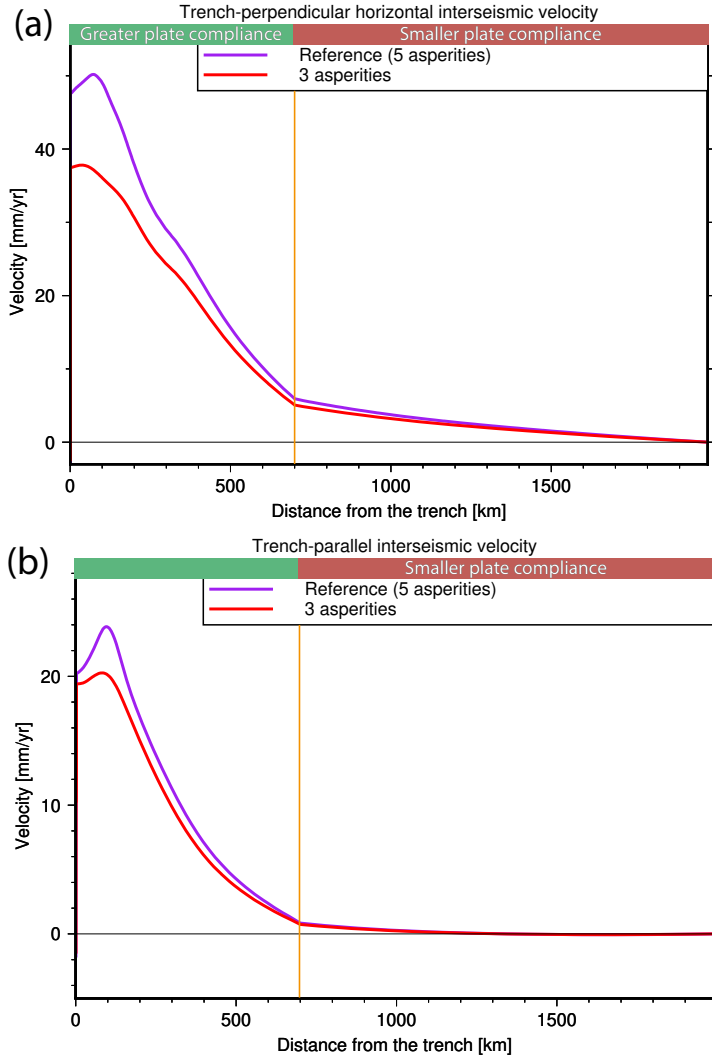
Figure 2.12 Sensitivity of interseismic velocities to the megathrust locking distribution. Trench-perpendicular profiles at $y = 100$ km (through the middle of one of the intermediate asperities, if present) of the two horizontal velocity components, trench-perpendicular (a) and trench-parallel (b), of interseismic velocities in a model with or without an intermediate asperity centered at $y = \pm100$ km, halfway between the middle one (at y=0) and each of the outer ones (at $y = \pm200$ km).
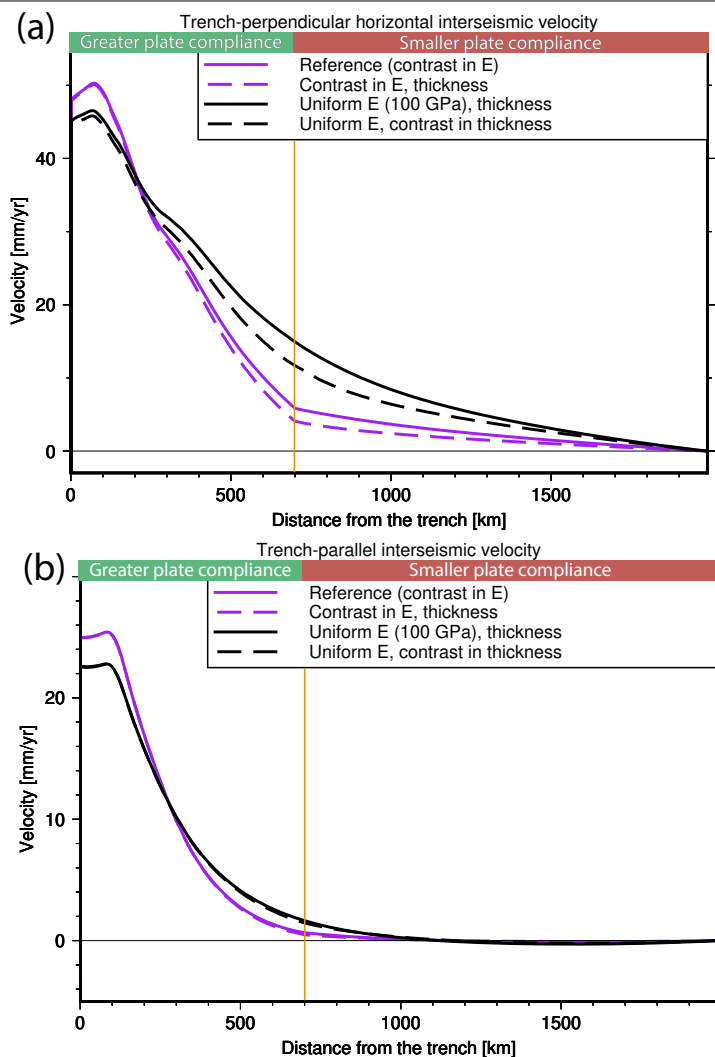
Figure 2.13 Sensitivity of interseismic velocities to the sharpness of the contrast within the overriding plate, and to thickness variations within the overriding plate. Trench-perpendicular profiles at $y = 0$ km of the two horizontal components, trench-perpendicular (a) and trench-parallel (b), of interseismic velocities in a model with or without a contrast in overriding plate thickness (40 km at $x < 700$ km, 80 km at $x > 700$ km) and elastic moduli. In both models with a contrast in overriding plate elastic moduli, the near-trench portion of the plate has $E = 50$ GPa and the plate interior has $E = 250$ GPa.
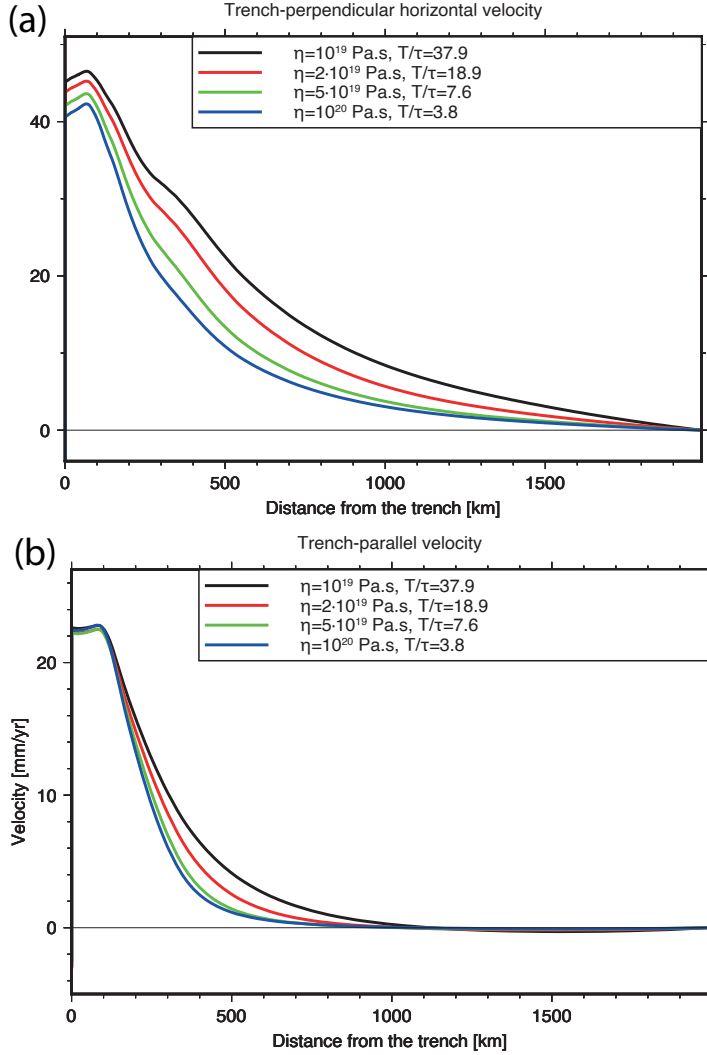
Figure 2.14 Sensitivity of interseismic velocities to the earthquake recurrence time T relative to the characteristic stress relaxation time ("Maxwell time") τ of the viscoelastic asthenosphere. Trench-perpendicular profiles at $y = 0$ km of the two horizontal components, trench-perpendicular (a) and trench-parallel (b), of interseismic velocities in models with an overriding plate without a contrast (uniform E of 100 GPa) and different values of $\frac{T}{\tau}$.

SouthAmerica trench-perpendicular relative velocities
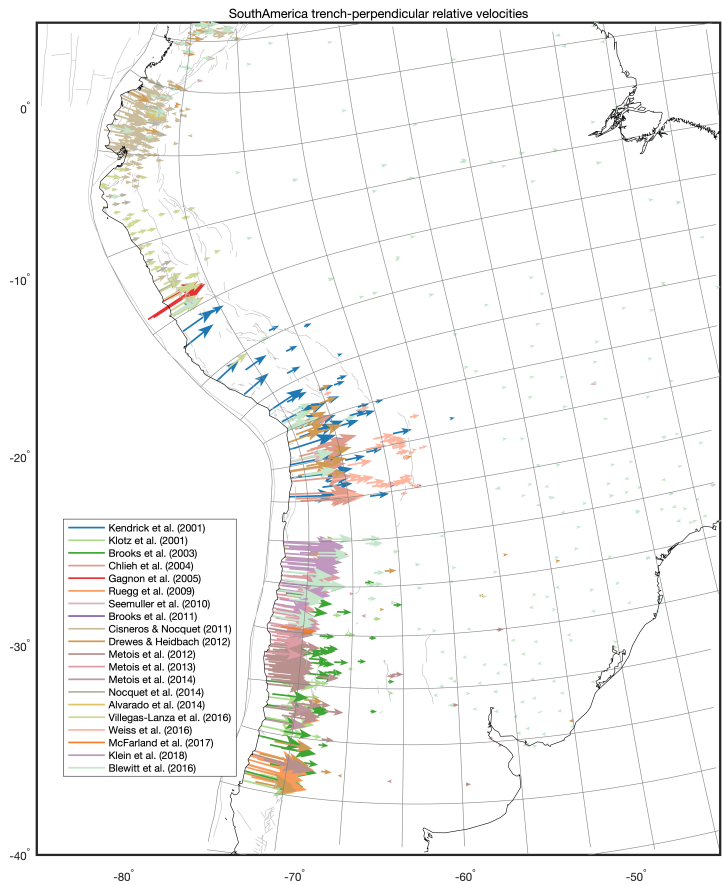
Figure 2.15 Decomposition of interseismic velocities in the South America plate reference into trench-perpendicular and trench-parallel velocities.

Sumatra trench-perpendicular relative velocities
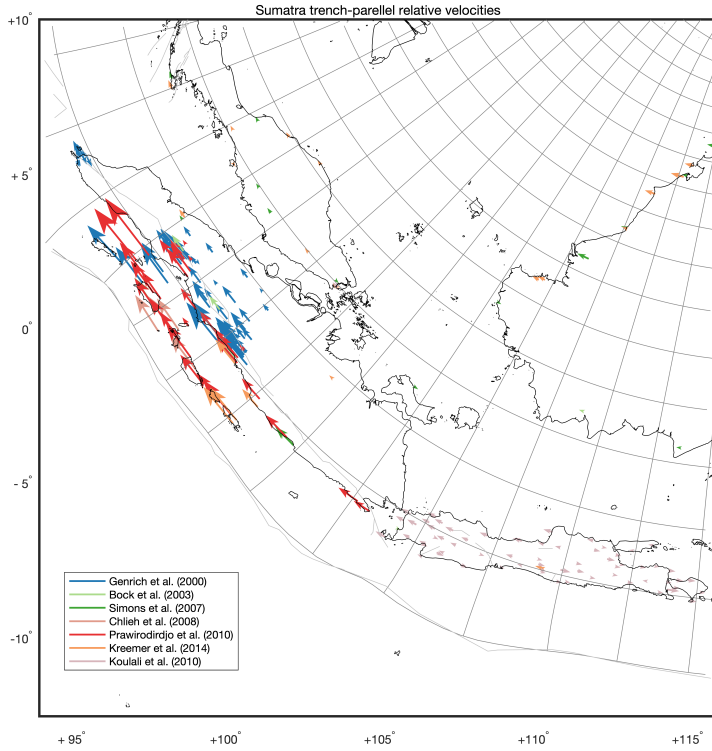
Figure 2.16 Decomposition of interseismic velocities in the Sunda plate reference into trench-perpendicular and trench-parallel velocities.

NorthernJapan trench-perpendicular relative velocities

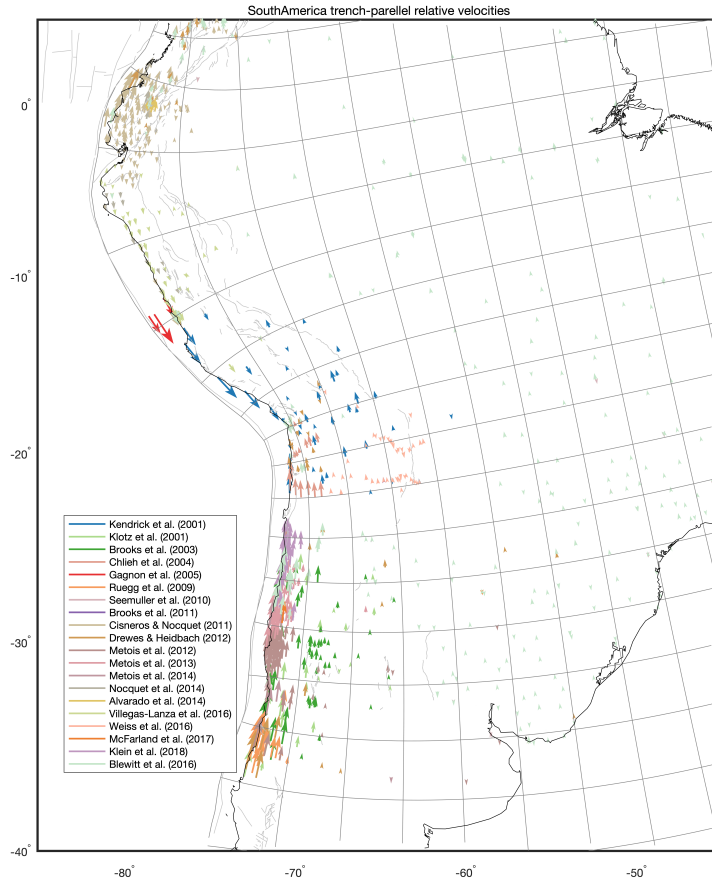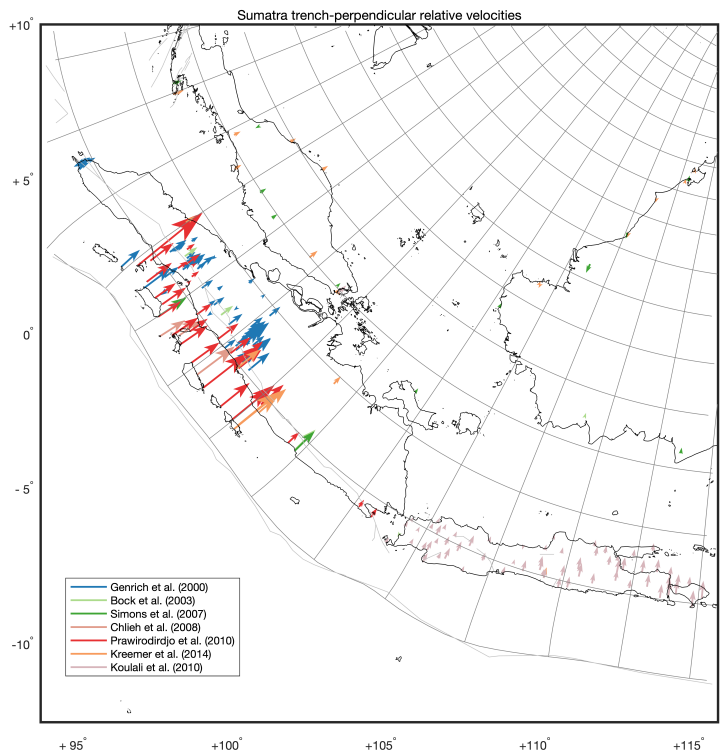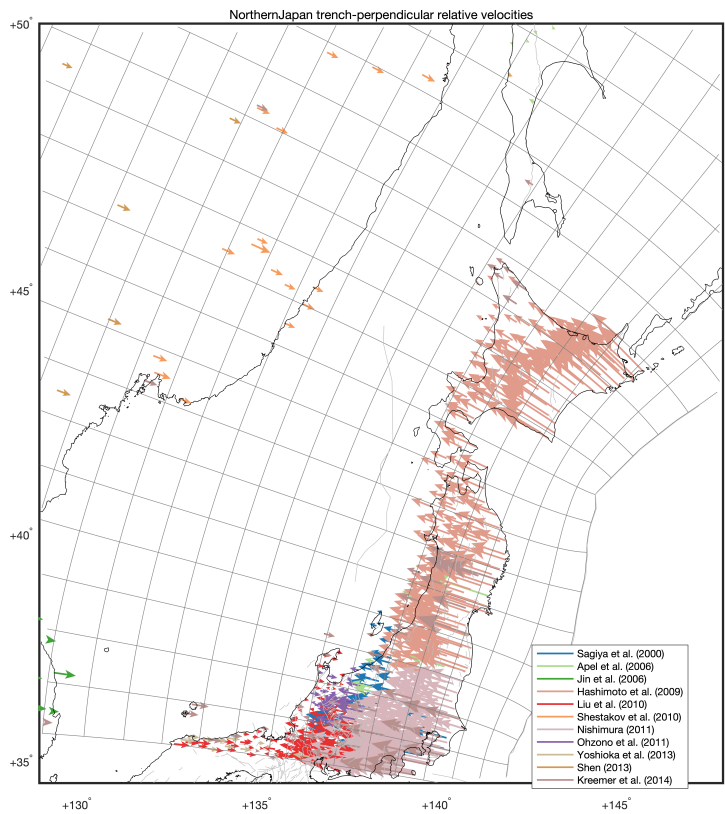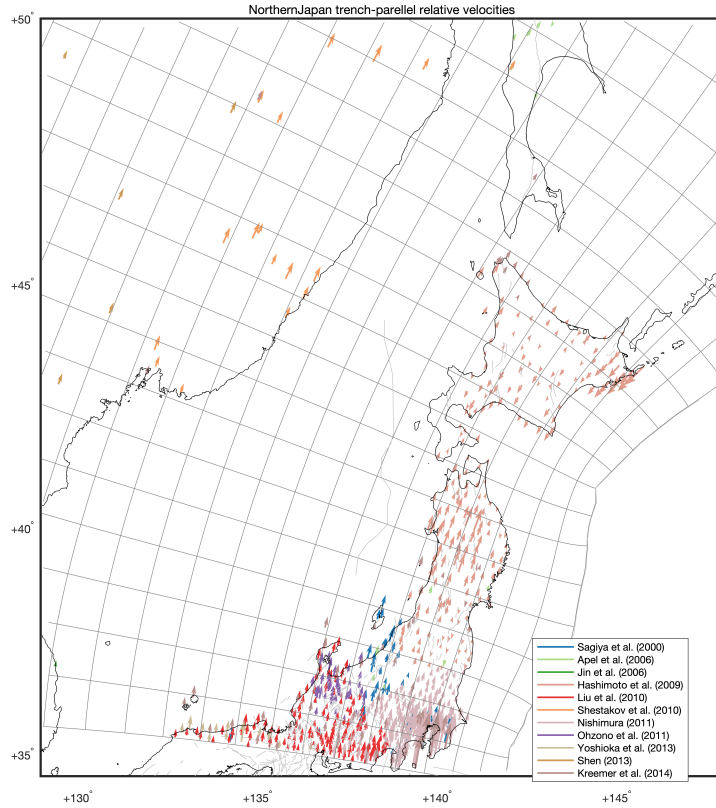**Figure 2.17** Decomposition of Honshu and Hokkaido interseismic velocities in the Okhotsk plate reference into trench-perpendicular and trench-parallel velocities.
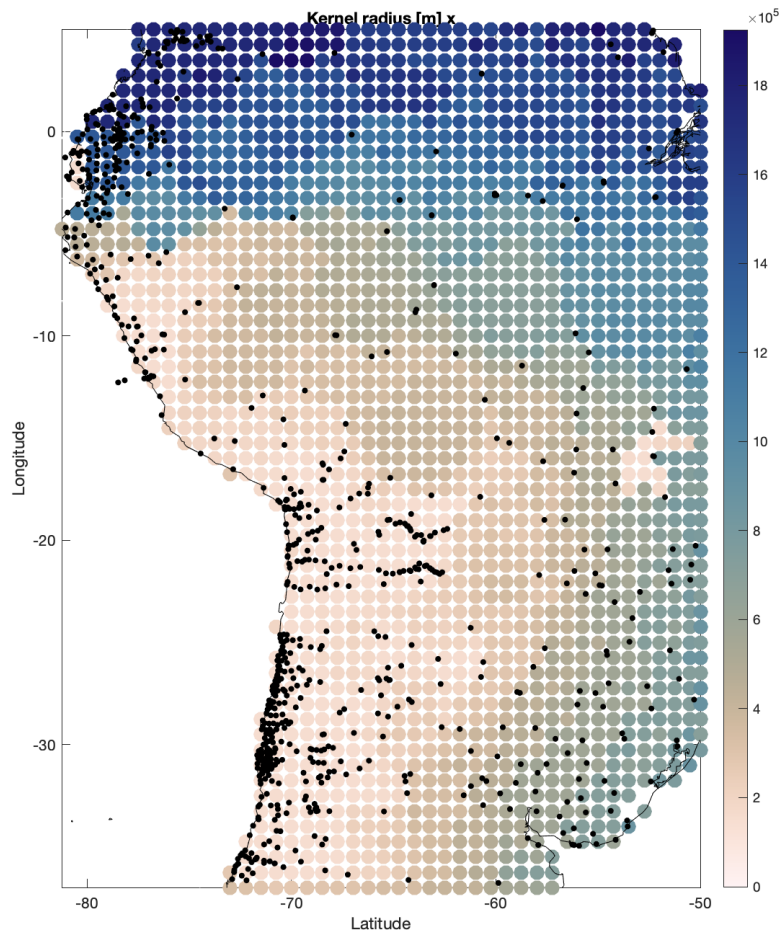
Figure 2.18 Gaussian kernel radius for the weighting of trench-perpendicular (x) and trench-parallel (y) velocities in constructing the local covariance functions at each anchor point in South America. Black dots denote GNSS observation points. As the kernel is defined based on the distance to natural neighbors of the anchor point, densely sampled areas (often near-trench) have a narrow weighting kernel, while sparsely sampled areas have a wide weighting kernel. In some areas a low signal-to-noise may lead to a kernel radius that is larger than the natural neighborhood, to prevent relatively large nugget values, compared to the covariance function variance.

local variance y

Figure 2.19 Estimated local covariance (exponential) parameters: range and variance, for trench-perpendicular (x) and trench-parallel (y) velocities in South America. Range (in meters) describes the decay of the correlation with distance, variance denotes the local observation variance (in $mm^2 \cdot yr^{-2}$). The variance is generally larger if the observation changes much within a natural neighborhood (roughly in between observation points) or in some cases, when the kernel radius is large because of a low signal-to-noise.
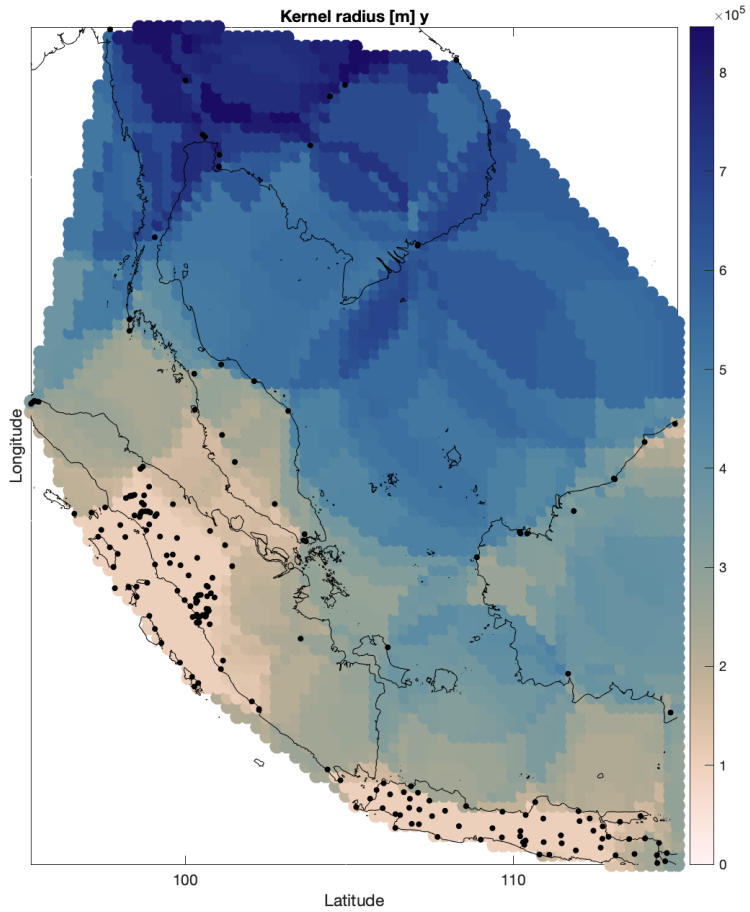
Figure 2.20 Gaussian kernel radius for the weighting of trench-perpendicular (x) and trench-parallel (y) velocities in constructing the local covariance functions at each anchor point in Southeast Asia. Black dots denote GNSS observation points. As the kernel is defined based on the distance to natural n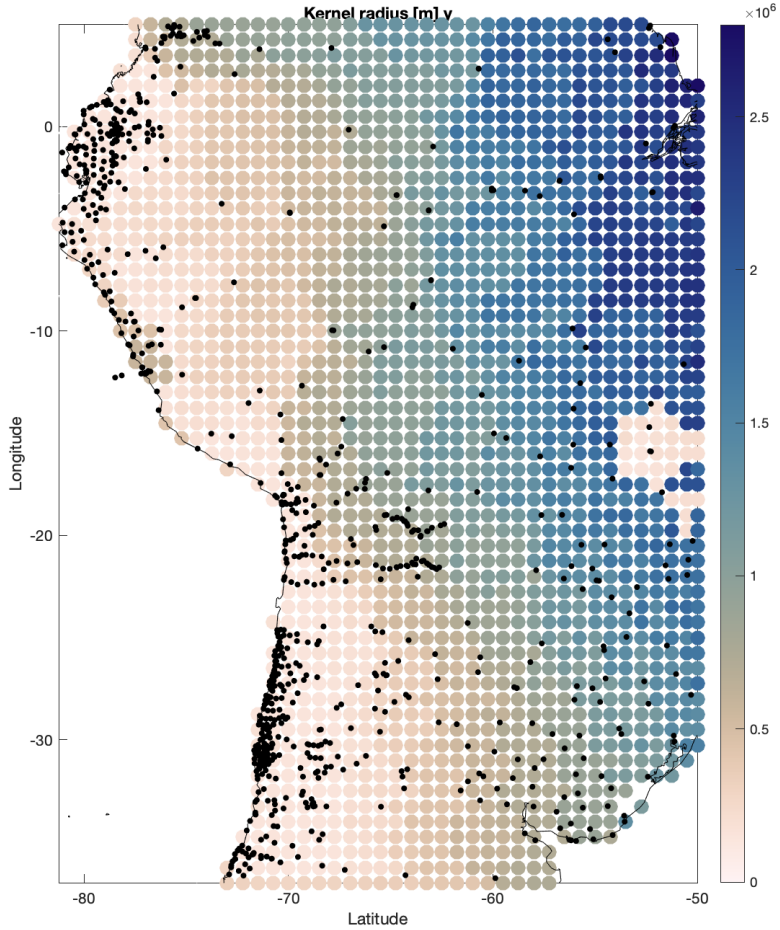eighbors of the anchor point, densely sampled areas (often near-trench) have a narrow weighting kernel, while sparsely sampled areas have a wide weighting kernel. In some areas a low signal-to-noise may lead to a kernel radius that is larger than the natural neighborhood, to prevent relatively large nugget values, compared to the covariance function variance.

local variance x
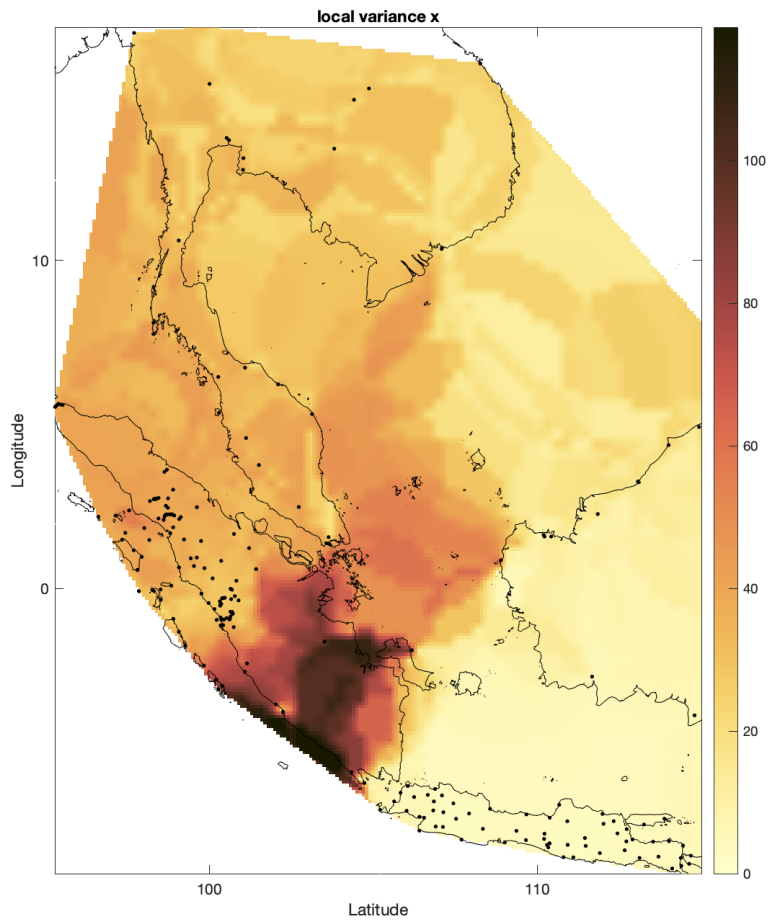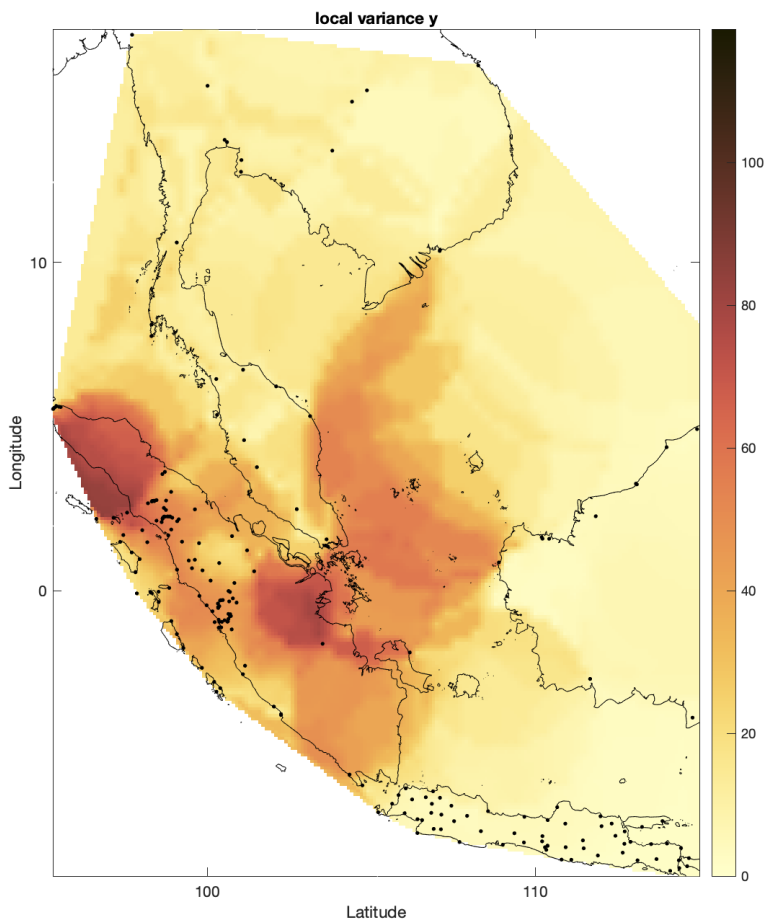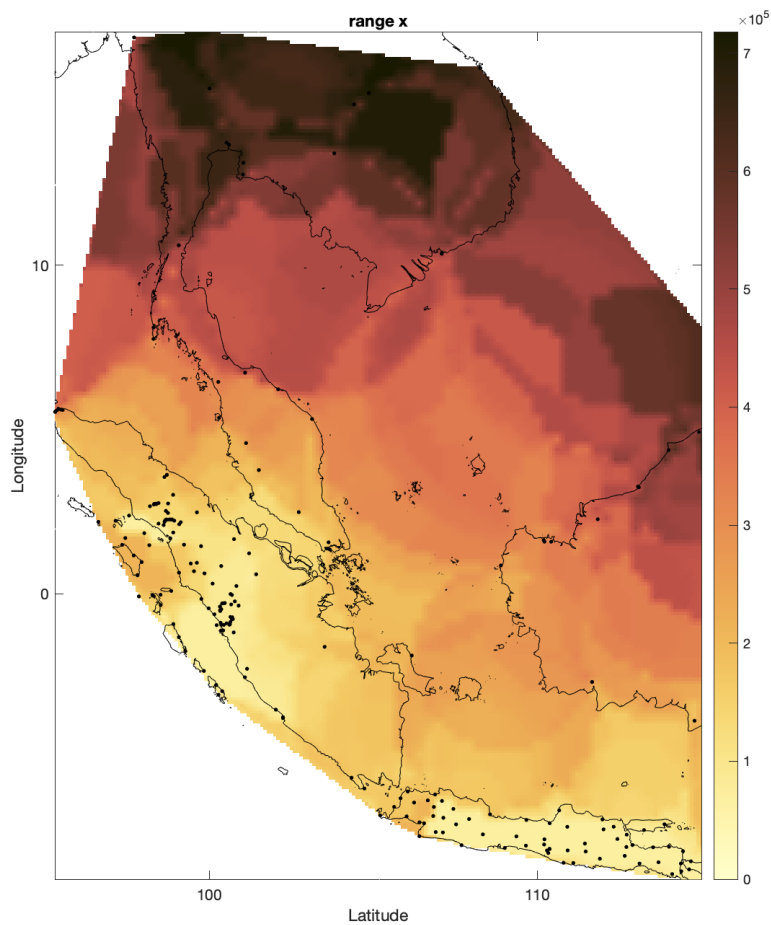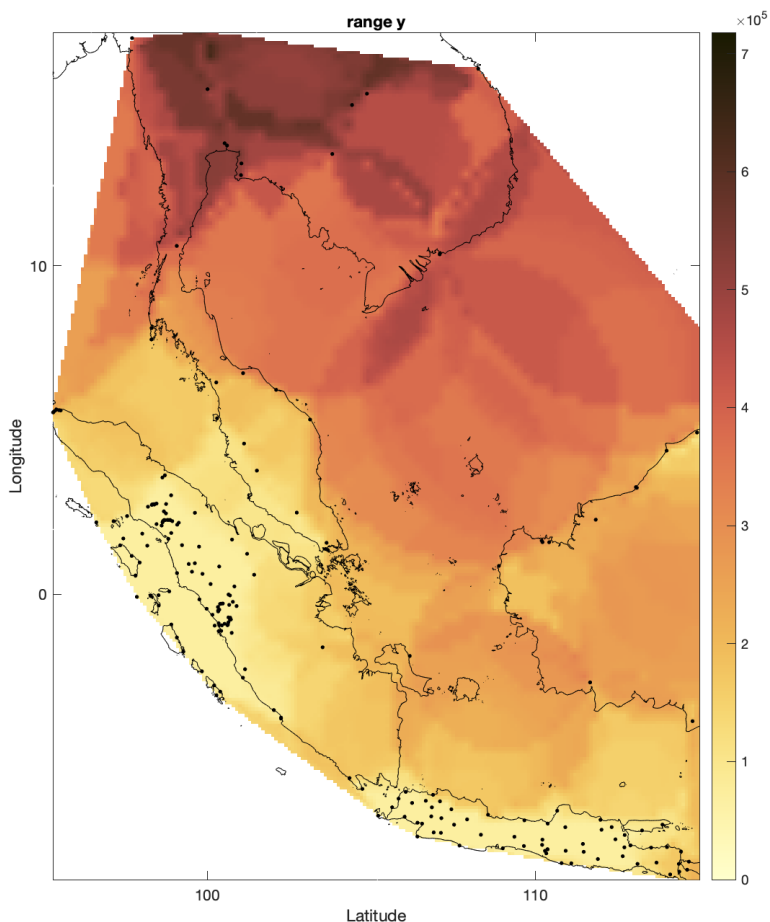
local variance y

Figure 2.21 Estimated local covariance function (exponential) parameters: range and variance, for trench-perpendicular (x) and trench-parallel (y) velocities in Southeast Asia. Range (in meters) describes the decay of the correlation with distance, variance denotes the local observation variance (in $mm^2 \cdot yr^{-2}$). The variance is generally larger if the observation changes much within a natural neighborhood (roughly in between observation points) or in some cases, when the kernel radius is large because of a low signal-to-noise.
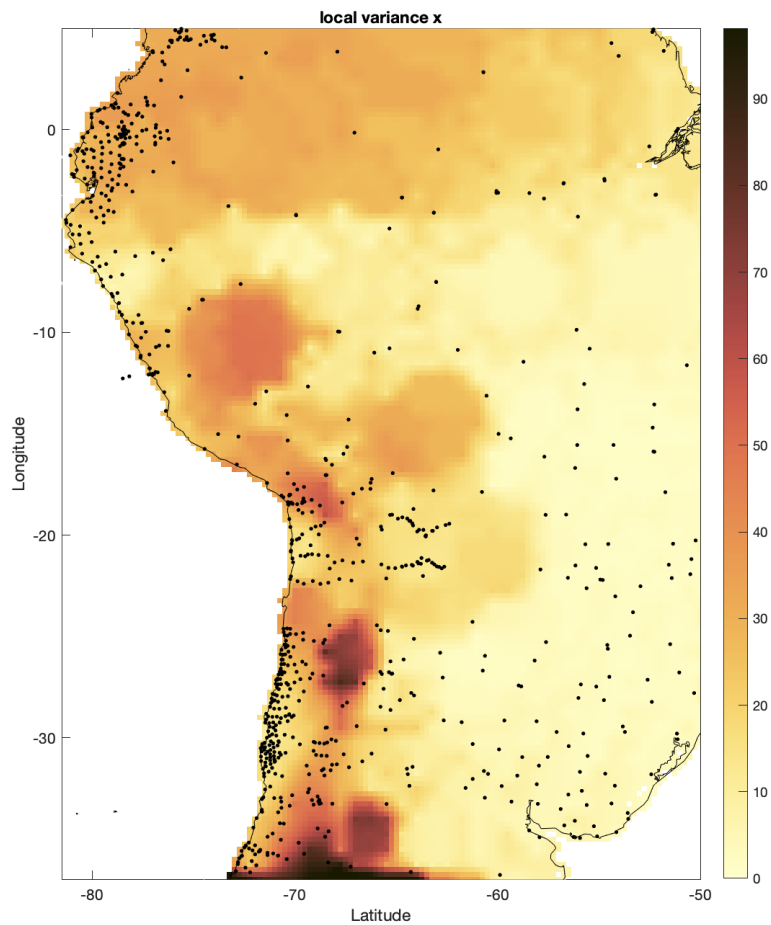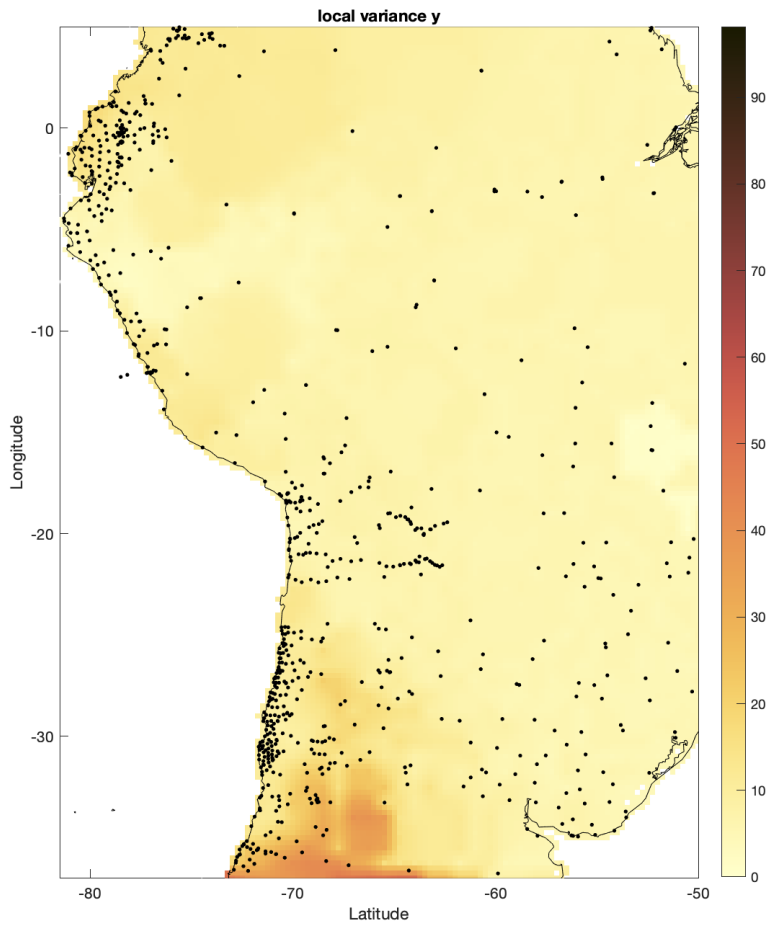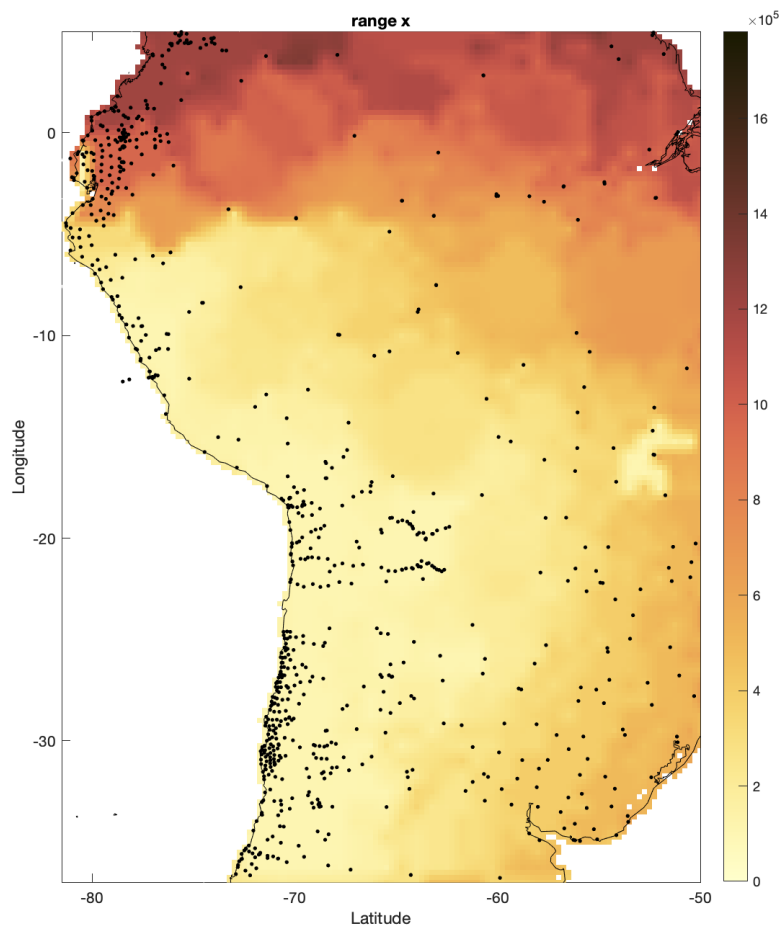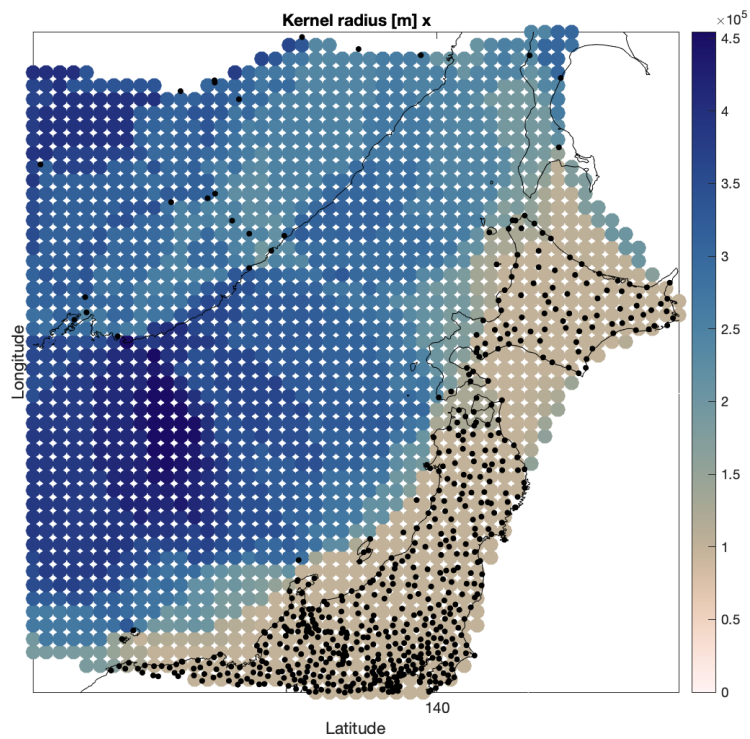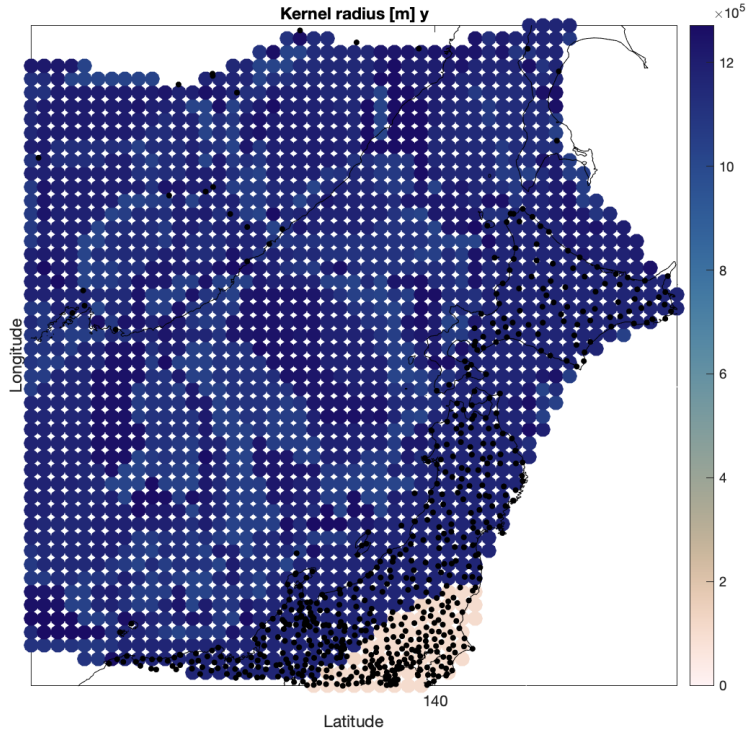
Figure 2.22 Gaussian kernel radius for the weighing of trench-perpendicular (x) and trench-parallel (y) velocities in constructing the local covariance functions at each anchor point in Japan. Black dots denote GNSS observation points. As the kernel is defined based on the distance to natural neighbors of the anchor point, densely sampled areas (often near-trench) have a narrow weighting kernel, while sparsely sampled areas have a wide weighting kernel.
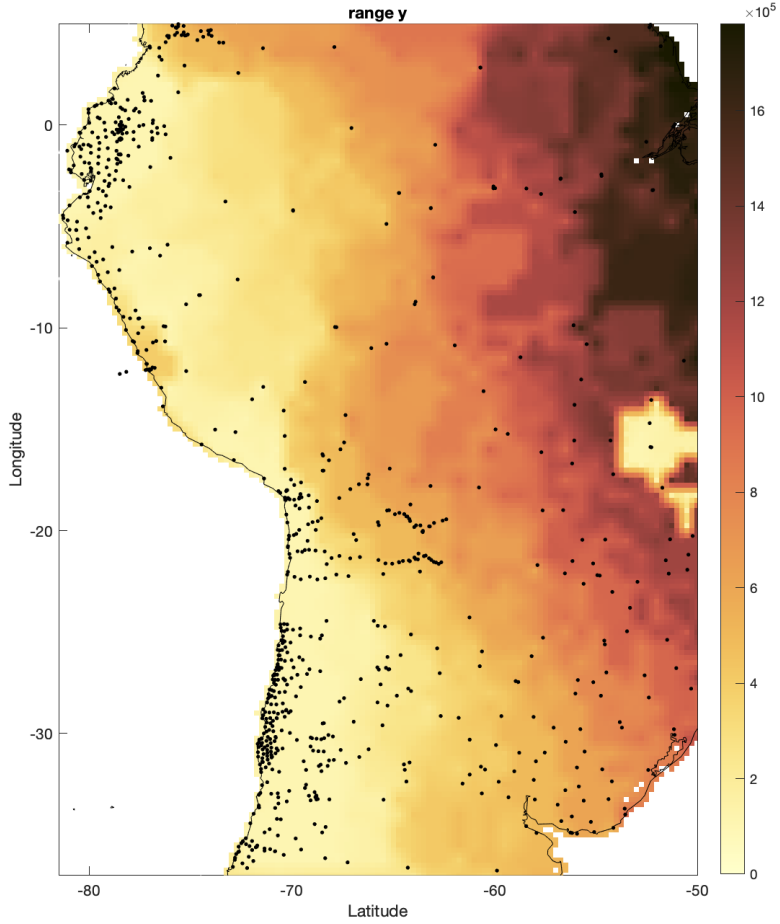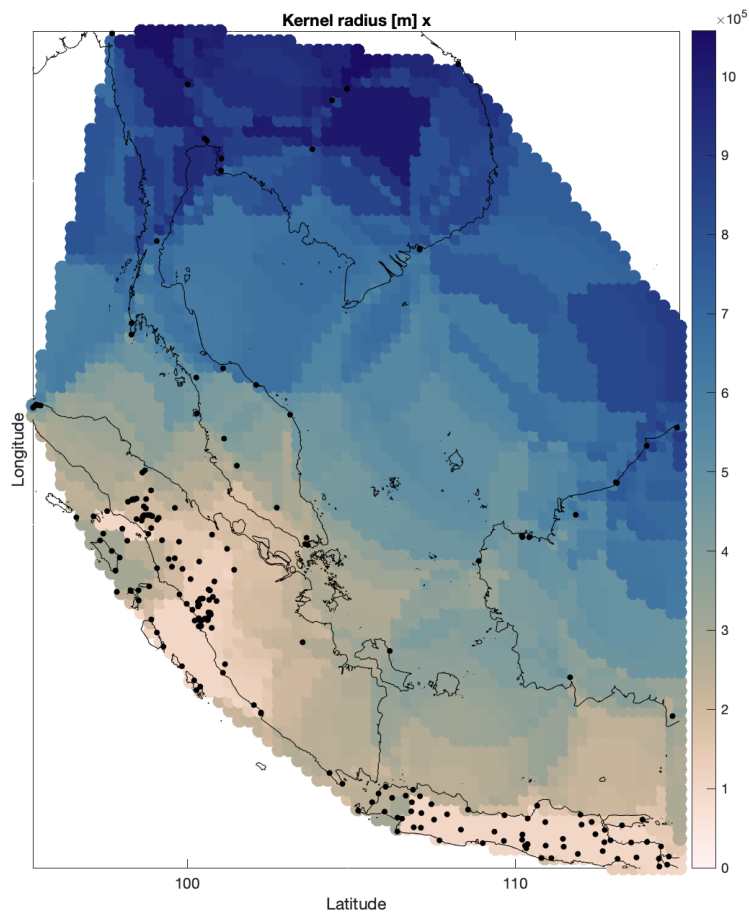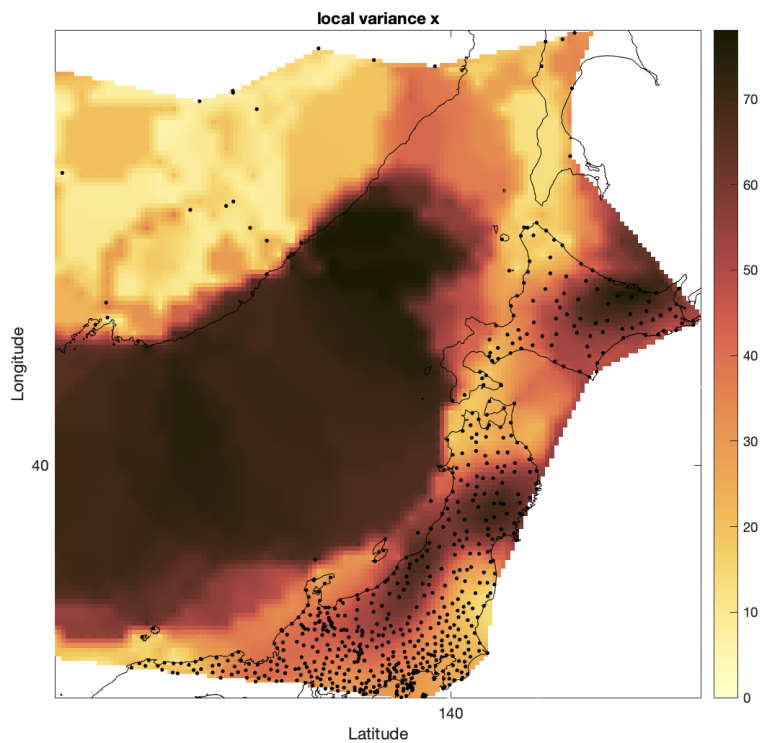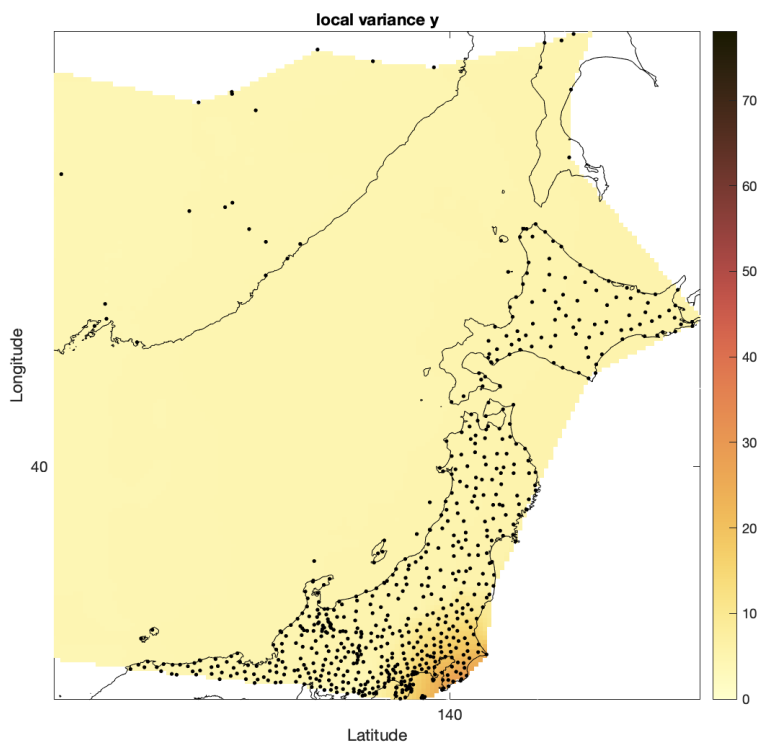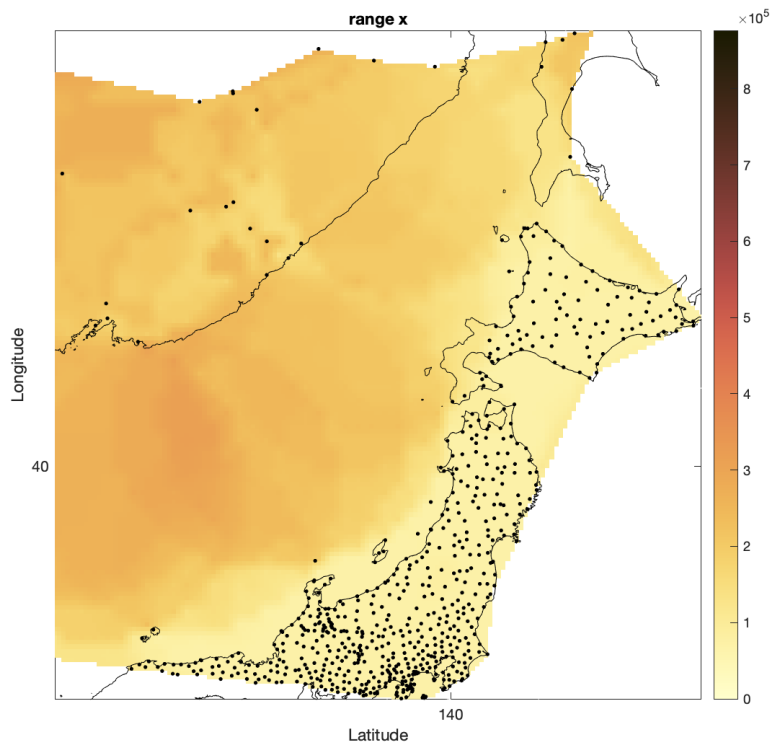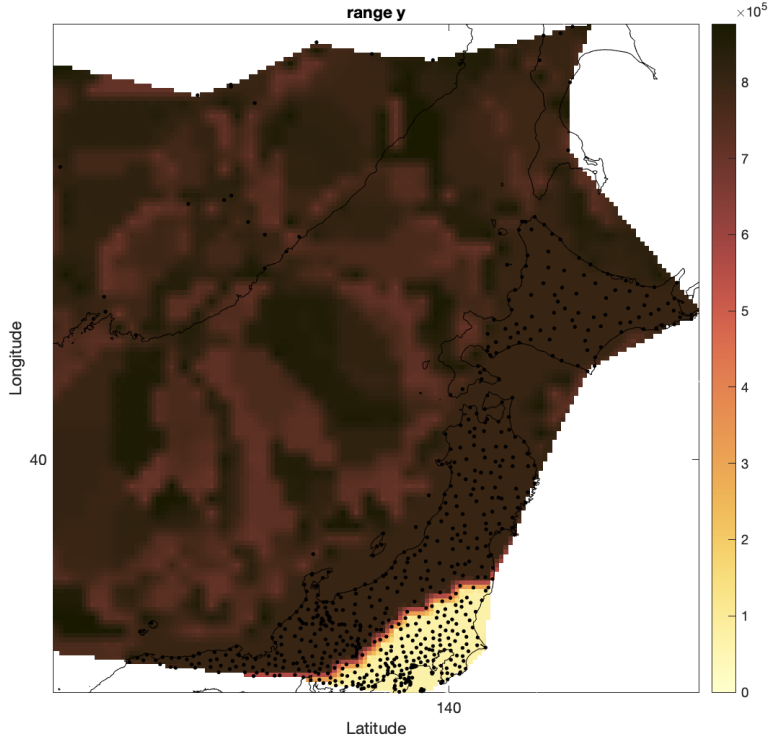
local variance y

Figure 2.23 Estimated local covariance function (exponential) parameters: range and variance, for trench-perpendicular (x) and trench-parallel (y) velocities in Japan. Range (in meters) describes the decay of the correlation with distance, variance denotes the local observation variance (in $mm^2 \cdot yr^{-2}$). The variance is generally larger if the observation changes much within a natural neighborhood (roughly in between observation points) or in some cases, when the kernel radius is large because of a low signal-to-noise. The latter is the case for the trench-parallel variances, as the reported uncertainties are larger than the parallel signal. Still, we find a consistent parallel signal in most of the domain, which suggests that the error is overestimated.

104

uncertainty trench-perpendicular velocities
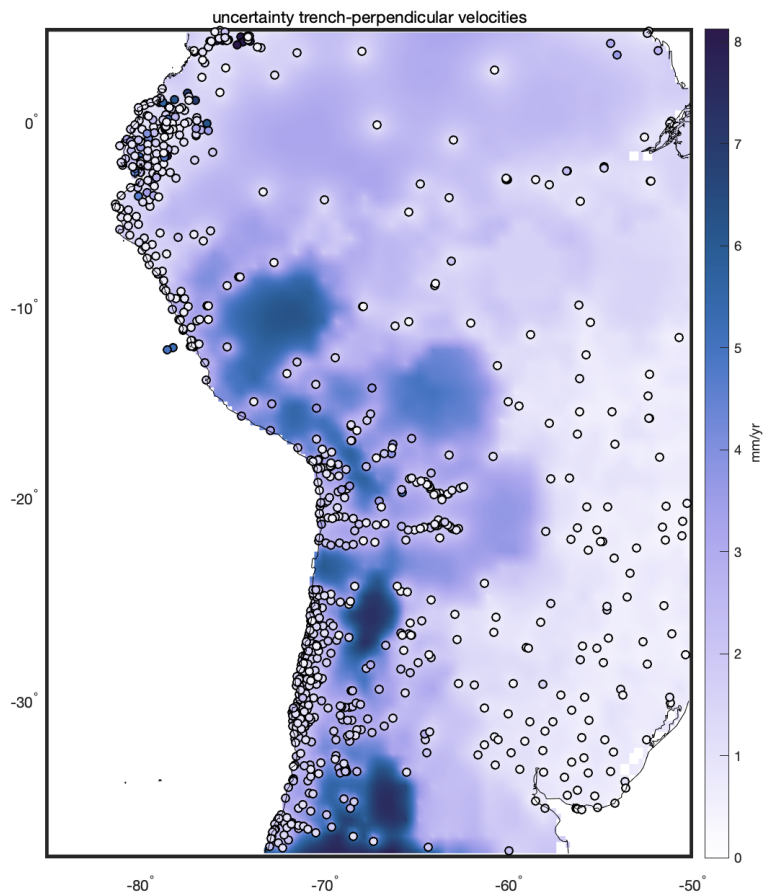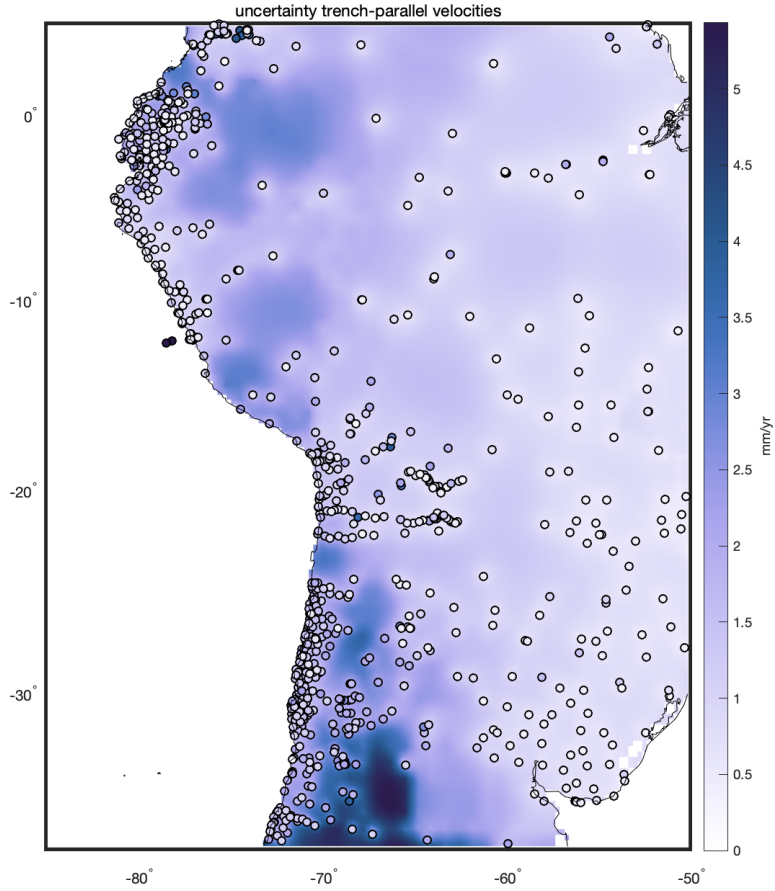
Figure 2.24 Uncertainty estimates (1 standard deviation) from the local ordinary kriging, trench-perpendicular and trench-parallel directions, for interseismic velocities in South America. In kriging uncertainties depend on both (local) variance, as well as on observation variance. In our implementation of local ordinary kriging uncertainties are large in areas with large gradients (especially when natural neighbors are relatively far apart), and small in areas with small gradients, see Figure 2.3 for the interpolated field. Circles denote the GNSS velocity uncertainties.

uncertainty trench-perpendicular velocities
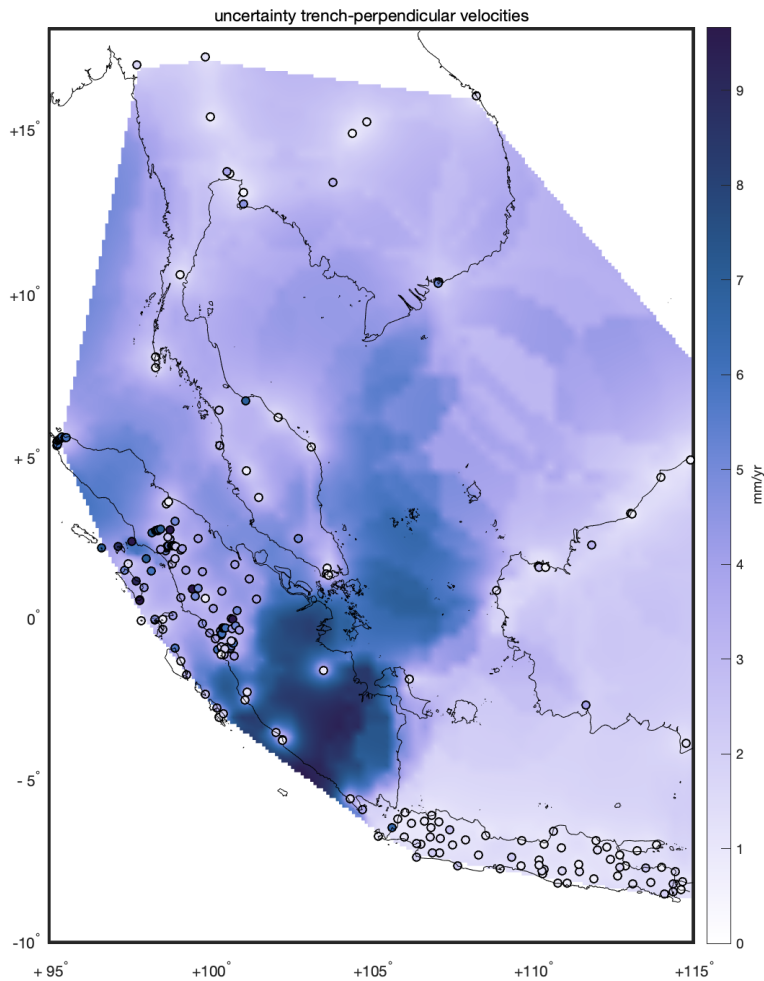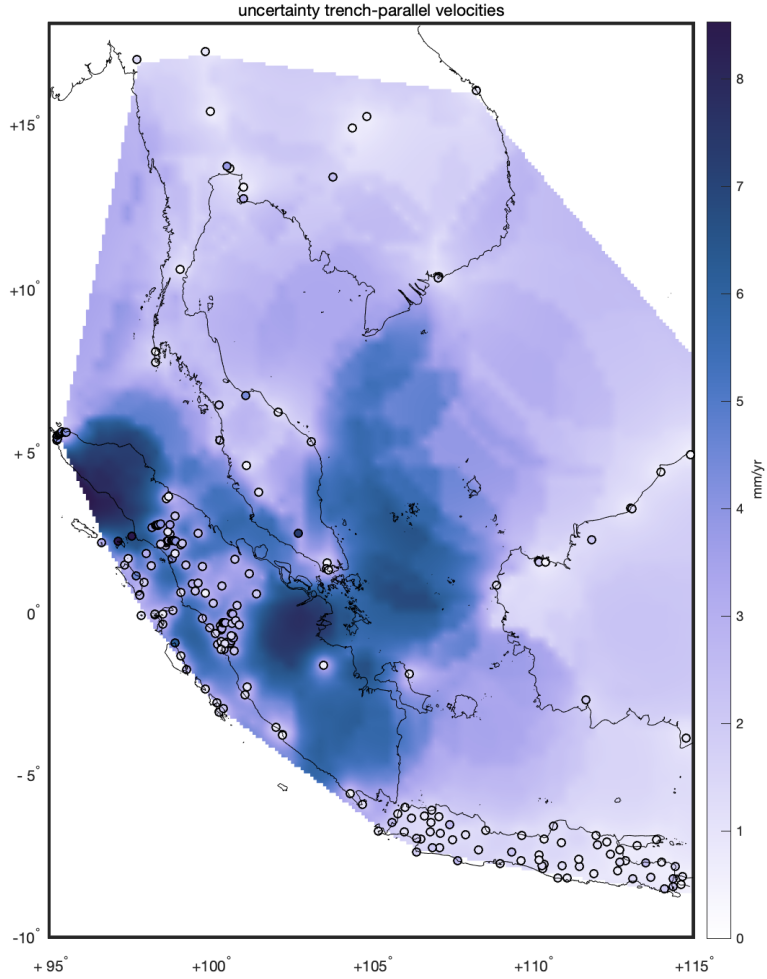
Figure 2.25 Uncertainty estimates (1 standard deviation) from the local ordinary kriging, trench-perpendicular and trench-parallel directions, for interseismic velocities in Southeast Asia. In kriging uncertainties depend on both (local) variance, as well as on observation variance. In our implementation of local ordinary kriging uncertainties are large in areas with large gradients (especially when natural neighbors are relatively far apart), and small in areas with small gradients, see Figure 2.4 in the main text for the interpolated field. Circles denote the GNSS velocity uncertainties.

uncertainty trench-perpendicular velocities
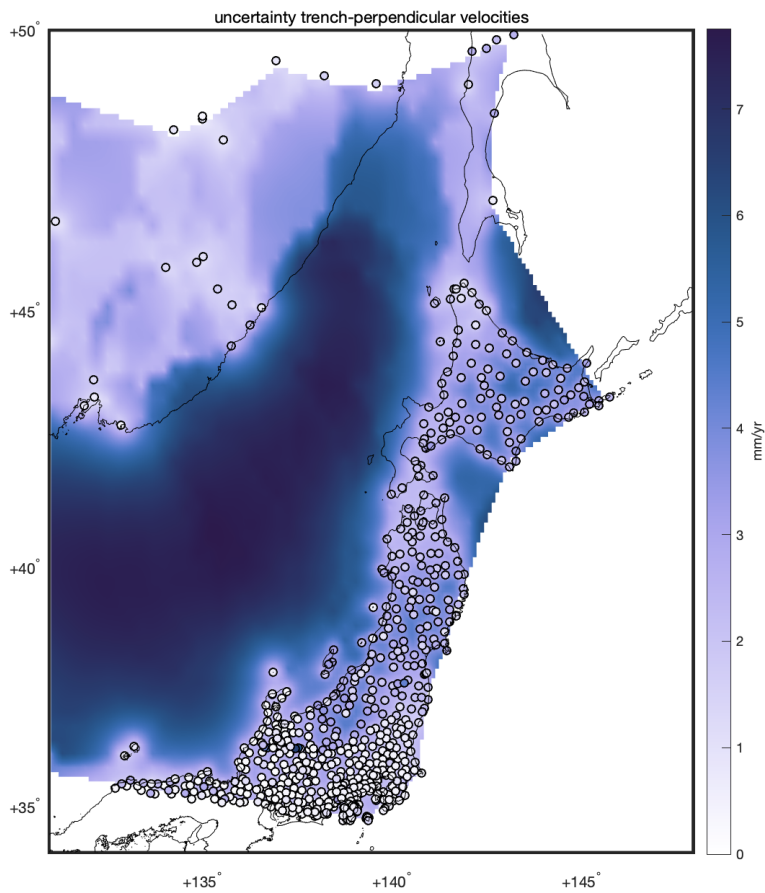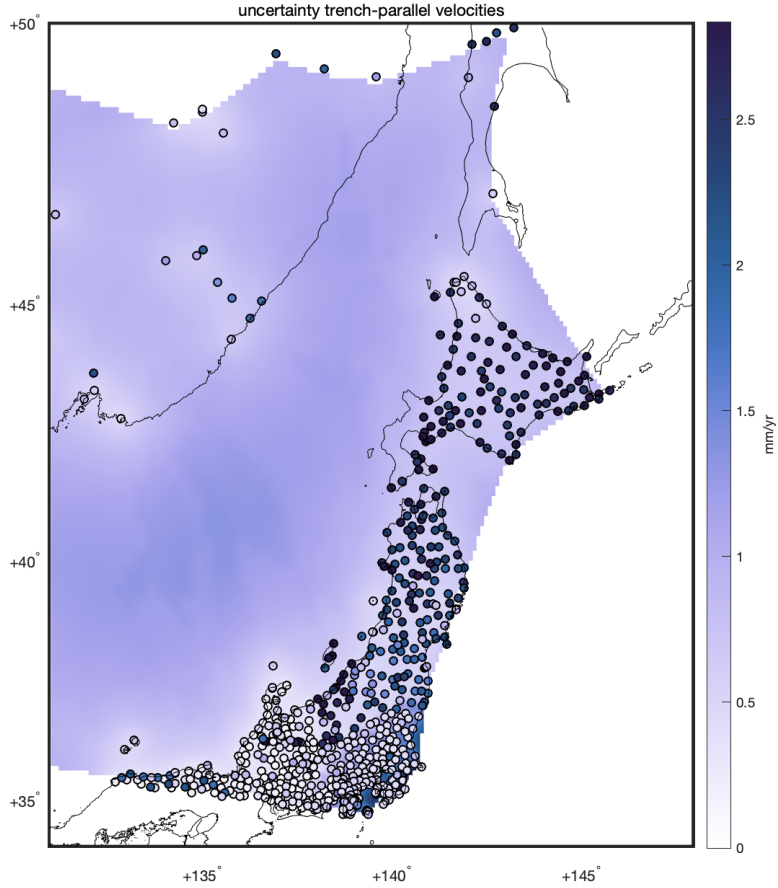
Figure 2.26 Uncertainty estimates (1 standard deviation) from the local ordinary kriging, trench-perpendicular and trench-parallel directions, for interseismic velocities in Japan. In kriging uncertainties depend on both (local) variance, as well as on observation variance. In our implementation of local ordinary kriging uncertainties are large in areas with large variability in observed velocities and large distances between observations, and small in areas with dense data coverage and small variability in observed velocities. See Figure 2.5 in the main text for the interpolated field. Circles denote the GNSS velocity uncertainties.

trench-perpendicular velocities

trench-parallel velocities
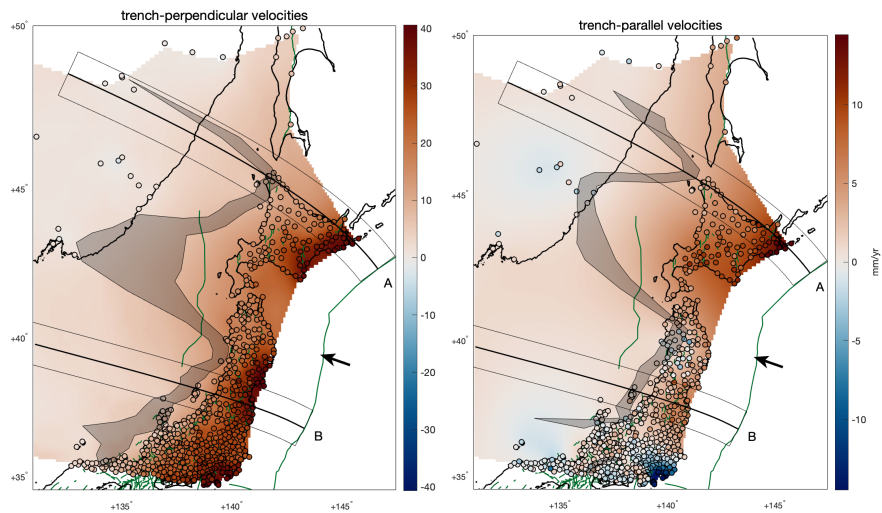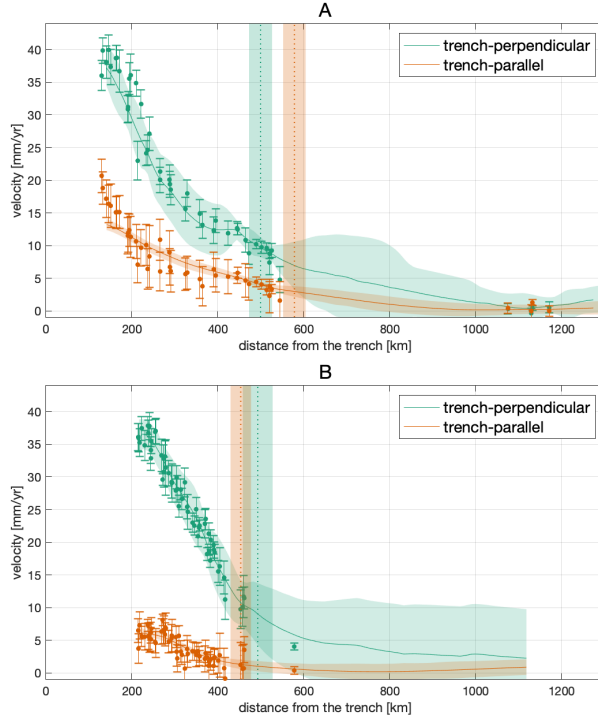
Figure 2.27 Results of the analysis of velocities in Japan, expressed in an Amur plate reference frame, rather than an Okhotsk plate reference frame as in Figure 2.5 in the main text. The maps show interpolated trench-perpendicular (positive landward) and trench-parallel (positive left-lateral) velocity fields with 95% confidence-interval location of the hurdle, together with active faults in green from GEM (Styron and Pagani, 2020). Coastlines are in black and arrows show the interplate convergence direction between the Pacific plate and the Amur plate (Kreemer *et al.*, 2014). Below, we show selected trench-perpendicular profiles, in Honshu and Hokkaido, on the landward side of the Japan Trench, along the profile lines traced in the maps. The velocity profiles show both interpolated velocity components with 1 standard deviation uncertainty (transparent bands), and the velocity components at GNSS stations within the swath with 1 standard deviation error bars. Note that the interpolated velocities are based on all GNSS velocity estimates, and not only those shown in the swath for reference. Vertical green and orange lines and bands outline estimated hurdle distances with 95% confidence intervals.
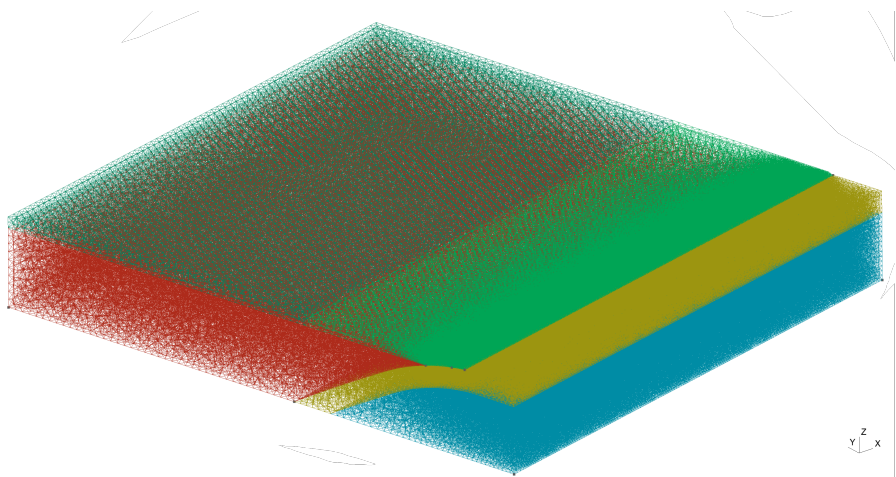
Figure 2.28 Isometric projection of the finite element mesh used in our numerical models.
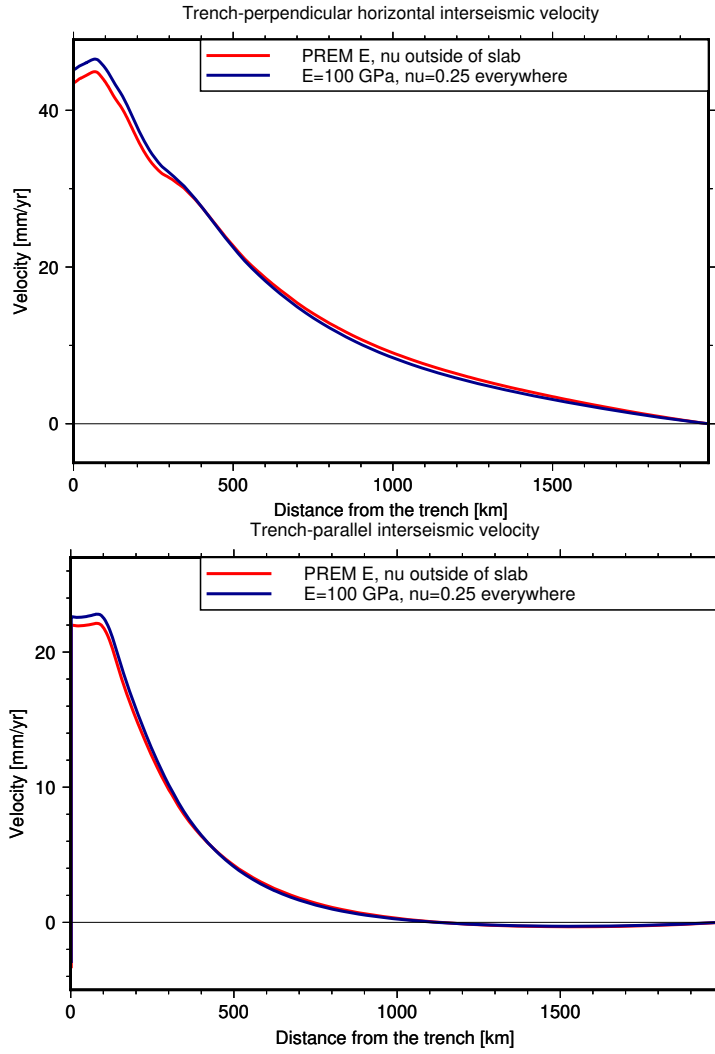
Figure 2.29 Trench-perpendicular profiles at $y = 0$ through the interseismic horizontal surface velocity components, trench-perpendicular (top) and trench-parallel (bottom), respectively, for a model with elastic moduli according to the vertical profile of PREM (Dziewonski and Anderson, 1981) or constant, uniform values. In the slab, E is 100 GPa and ν is 0.25 in both models.
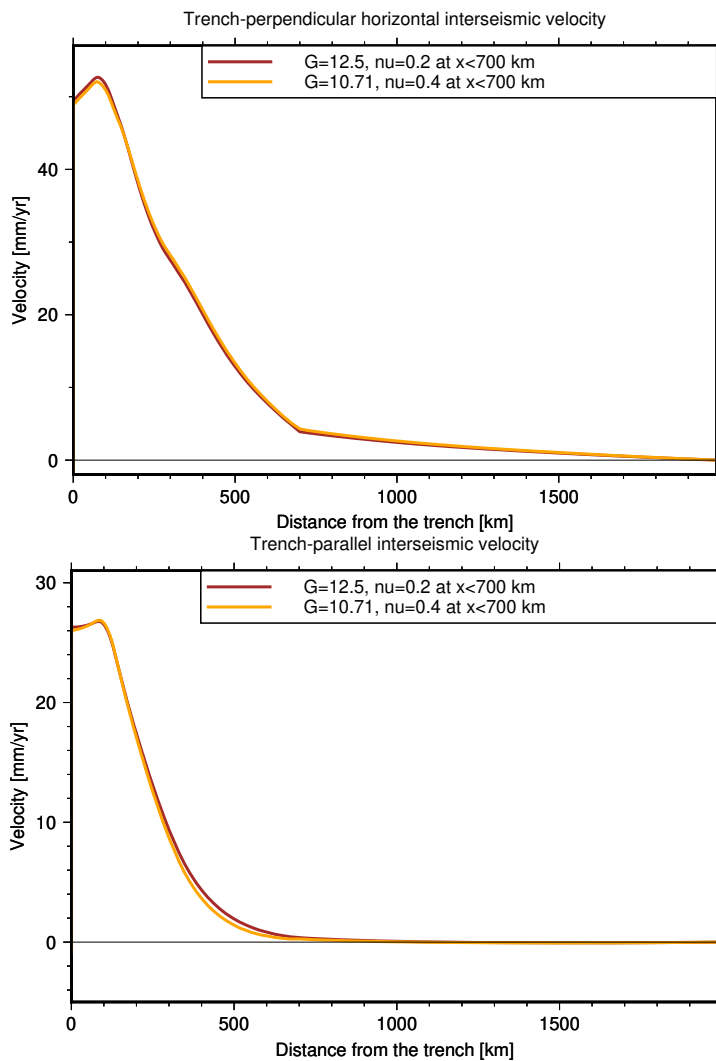
Figure 2.30 Trench-perpendicular profiles at $y = 0$ through the interseismic horizontal surface velocity components, trench-perpendicular (a) and trench-parallel (b), respectively, for models with the same contrast in overriding plate E (30 GPa at x<700 km, 150 GPa at $x > 700$ km), the same overriding plate G (87.5 GPa) and ν (0.2) at $x > 700$ km, and an overriding plate G at $x < 700$ km of either 12.5 GPa (same $\nu = 0.2$ as at $x > 700$ km, same 1:7 ratio to far-field G as between near-field and far-field E) or 10.71 GPa ($\nu = 0.4$, 1:8.17 ratio to far-field G).
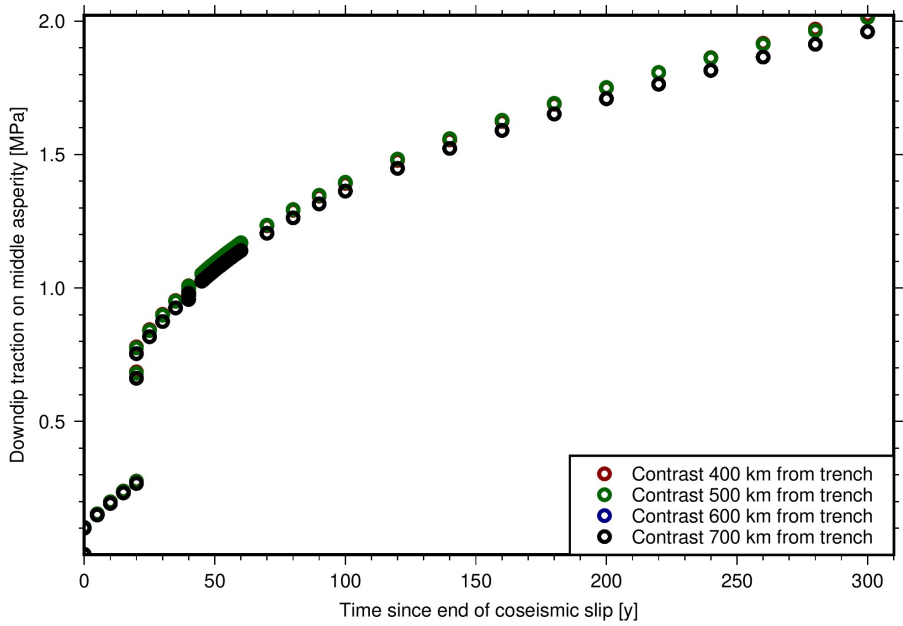
Figure 2.31 Plot of average traction in the downdip direction (interface-parallel, along parallel lines on the interface intersecting the trench at right angles) on the central asperity on the megathrust interface, through time over an earthquake cycle, in models with different horizontal distance between the trench and the contrast in E (10 GPa near-trench, 100 GPa elsewhere). The earthquake on the middle asperity happens at time 0, while the earthquakes on the intermediate and external asperities happen at time 20 and 40 years, respectively.

Study	Obs. Period	Ref. frame	Region
Kendrick *et al.* (2001)	1993–2001	IGS08[a]	23°S–10°S
Klotz *et al.* (2001)	1994–1996	IGS08[a]	22°S–42°S
Brooks *et al.* (2003)	1993–2001	IGS08[a]	26°S–36°S
Chlieh *et al.* (2004)	1996–2000	IGS08[a]	23°S–18°S
Gagnon *et al.* (2005)	2001–2004	IGS08[a]	14°S–11°S
Ruegg *et al.* (2009)	1996–2002	IGS08[a]	37°S–35°S
Seemüller *et al.* (2010)	2000–2010	ITRF2008	South America
Brooks *et al.* (2011)	2000–2003	IGS08[a]	22°S–19°S
Cisneros and Nocquet (2011)	1995–2012	IGS08[a]	5°S–2°N
Drewes and Heidbach (2012)	1995–2009	IGS08[a]	South America
Métois *et al.* (2012)	1993–2009	ITRF2005[b]	38°S–24°S
Métois *et al.* (2013)	2000–2012	IGS08[a]	24°S–18°S
Métois *et al.* (2014)	2004–2012	ITRF2008	30°S–24°S
Nocquet *et al.* (2014)	1994–2012	ITRF2008[c]	12°S–2°N
Alvarado *et al.* (2014)	1996–2012	IGS08[a]	1°S–1°N
Villegas-Lanza *et al.* (2016)	2007–2013	ITRF2008[d]	18°S–2°S
Weiss *et al.* (2016)	2000–2007	Stable plate[e,f]	24°S–16°S
McFarland *et al.* (2017)	2010–2014	ITRF2008[g]	29°S–21°S
Klein *et al.* (2018a)	2010–2015	ITRF2008	30°S–22°S
Blewitt *et al.* (2016)	1996–2021	IGS14[h]	Global

Table 2.1 Overview of the collection of horizontal velocities for the South American margin, including the source, the observational period, the reference frame in which the velocities are reported. [a] We make use of the velocities expressed by Kreemer *et al.* (2014) where all previously published velocities have been transformed to IGS08 in a global inversion to estimate rotation and translation rates based on common sites. [b] We apply the rotation pole 25.4°S, 124.6°W, 0.11° · Myr^{-1} as provided in Métois *et al.* (2012) to transform back to ITRF2005. [c] We apply the rotation pole 18.83°S, 132.21°W, 0.121° · Myr^{-1} as provided by the authors to transform the published plate referenced velocities back to ITRF2008. [d] We apply the rotation pole 18.66°S, 132.72°W, 0.118° · Myr^{-1} as provided in the supplementary information of Villegas-Lanza *et al.* (2016) to transform back to ITRF2008. [e] Weiss et al. (2016) use a South America plate reference, constructed with 44 cGPS sites, mostly located in Brazil, without a prior global solution. [f] Weiss *et al.* (2016) apply a postseismic correction of the 2007 Tocapilla M_w 7.7 earthquake to the velocity estimates, by removing an empirically estimated coseismic step and postseismic decay function. [g] McFarland *et al.* (2017) used the ITRF2008 South American plate motion model (Altamimi *et al.*, 2012), which we subsequently use to transform back to ITRF2008. [h] We exclude sites SURY, RAS, PRMA, LSJ1, SPBP, NXRA, LDO, LPLN, for which observed velocities are anomalously high in comparison to neighboring sites.

Study	Obs. Period	Ref. frame	Region
Genrich *et al.* (2000)	1989–1996	IGS08[a]	Sumatra Fault
Bock *et al.* (2003)	1991–2001	IGS08[a]	Sunda plate
Simons *et al.* (2007)	1994–2004	IGS08[a]	Sunda plate
Chlieh *et al.* (2008)	2002–2004	IGS08[a]	Sumatra trench
Prawirodirdjo *et al.* (2010)	1991–2001[b]	IGS08[a]	Sumatra trench
Prawirodirdjo *et al.* (2010)	2001–2007[c]	IGS08[a]	Sumatra trench
Prawirodirdjo *et al.* (2010)	2002–2006[d]	IGS08[a]	Sumatra trench
Kreemer *et al.* (2014)	1990–2014[e]	IGS08	Global
Koulali *et al.* (2017)	2002–2014[f]	ITRF2008[g]	Java

Table 2.2 Overview of the collection of horizontal velocities for the Sunda margin, including the source, the observational period, the reference frame in which the velocities are reported. [a] We make use of the velocities expressed by Kreemer *et al.* (2014), where all previously published velocities have been transformed to IGS08 in a global inversion to estimate rotation and translation rates based on common sites. [b] Sites from the 1991-2001 have not been affected by major earthquakes. [c,d] We do not use the data from the 2001-2007 and 2002-2006 tables in areas affected by the 2004 Sumatra-Andaman earthquake and the 2005 Nias earthquakes. [e] We use the table with exclusion periods for individual sites to be able to filter sites that are potentially affected by postseismic transients. [f] Velocities obtained from data after the 2006 M_w 7.7 earthquake in west Java has been corrected for coseismic offsets and postseismic transients using a best-fit viscoelastic model. g Published velocities in Koulali *et al.* (2017) are expressed in a Sunda plate reference, we use the Euler pole that we received from the authors to express velocities in ITRF2008. Euler pole parameters: longitude 81.07°W, latitude 32.66°N, angular velocity $0.435924° \cdot \mathrm{Myr}^{-1}$.

Study	Obs. Period	Ref. frame	Region
Sagiya *et al.* (2000)	1995–2000	IGS08[a]	Japan
Apel *et al.* (2006)	1995–2006	IGS08[a]	Northeast Asia
Jin and Park (2006)	2000–2003	IGS08[a]	South Korea
Hashimoto *et al.* (2009)	1996–2000	IGS08[a,b]	Japan
Liu *et al.* (2010)	1996–2005	IGS08[a]	Southwest Japan
Shestakov *et al.* (2011)	1997–2009	IGS08$_a$	Northeast Asia
Nishimura (2011)	2007–2009	IGS08[a]	Southwest Japan
Ohzono *et al.* (2011)	1998–2006	IGS08[a]	Central Japan
Yoshioka and Matsuoka (2013)	2005–2009	IGS08[a]	Southwest Japan
Kreemer *et al.* (2014)	1990–2013	IGS08[a]	Northeast Asia
Kreemer *et al.* (2014)	1990–2014[c]	IGS08[a]	Global

Table 2.3 Overview of the collection of horizontal velocities for the Japan margin in the pre-2011 Tohoku earthquake period, including the source, the observational period, the reference frame in which the velocities are reported. [a] We make use of the velocities expressed by Kreemer *et al.* (2014), where all previously published velocities have been transformed to IGS08 in a global inversion to estimate rotation and translation rates based on common sites. [b] Hashimoto et al., (2009) have corrected for transients of the 1994 Sanriku earthquake. [c] We exclude sites that have velocity estimates based partly on post-2011 Tohoku data.

3

Can Plate Bending Explain the Observed Faster Landward Motion of Lateral Regions of the Subduction Zone After Major Megathrust Earthquakes?

3.1 Introduction and Background

The classical view of the earthquake cycle at subduction zones is that slip deficit is gradually accumulated during the interseismic time period due to locking of the plate interface ("megathrust") and is suddenly released in major earthquakes when the megathrust unlocks (e.g., Plafker, 1972; Shimazaki and Nakata, 1980). Geodetic observations of displacement at the surface of the overriding plate, such as those made at global navigation satellite system (GNSS) stations, generally show landward motion during the interseismic stage. They also show trenchward motion, during the coseismic rupture, that is consistent with the slip deficit accumulated interseismically. The trenchward motion of the overriding plate also continues during the postseismic period, as coseismic stress changes relax (e.g., Azúa *et al.*, 2002; Moreno *et al.*, 2011; Loveless and Meade, 2011; Protti *et al.*, 2014). However, recent analyses of

geodetic observations indicate that not all locations of the overriding plate move trenchward postseismically (Loveless, 2017).

In fact, onshore GNSS stations hundreds of kilometers away from the rupture along the subduction margin move landward faster than before the earthquake. This postseismic enhanced landward motion (ELM) at large along-trench distances from a major megathrust earthquake (we will refer to this region as "far-field") has now been been documented following 6 megathrust events: the 2003 M_W 8.3 Tokachi-oki, 2007 M_W 8.4 Bengkulu, 2010 M_W 8.8 Maule, 2011 M_W 9.1 Tohoku-oki, 2012 M_W 7.4 Oaxaca, and 2014 M_W 8.2 Iquique earthquakes (Heki and Mitsui, 2013; Mavrommatis *et al.*, 2014; Loveless and Meade, 2016; Melnick *et al.*, 2017; Yuzariyadi and Heki, 2021). The observed far-field postseismic ELM has the following general characteristics: (i) maximum trench-perpendicular landward amplitudes between 4 and 22 mm $\cdot$ yr^{-1}, (ii) at minimum along-trench distances from the middle of the rupture 150 and 500 km, (iii) following earthquakes of M_W between 7.1 and 9.1.

More specifically, the velocities in the period between 4.8 and 6.3 years after the Tokachi-oki earthquake were more landward than before by as much as $\sim$ 6 mm $\cdot$ yr^{-1} and at distances of $\sim$ 200–350 km along-trench to the south of the earthquake centroid and $\sim$ 150 km to the northeast (Yuzariyadi and Heki, 2021). Landward velocity increases associated with the Bengkulu earthquake were observed at only one station, located $\sim$ 150 km along-trench from the middle of the rupture. No other GNSS observations were available in its surroundings. The increase was of 5.1 mm $\cdot$ yr^{-1} when computing postseismic velocities in the 2.3 years following the earthquake (Yuzariyadi and Heki, 2021). In the 5.5 years after the 2010 Maule earthquake, landward velocities were greater than preseismic values by as much as $\sim$ 9 mm $\cdot$ yr^{-1}. The increases occurred as close as $\sim$ 500 km along-trench from the middle of the rupture zone (Melnick *et al.*, 2017). Between 0.8 and 3.8 years after the the Tohoku-oki event, the landward velocity increases with respect to preseismic values were as large as $\sim$ 22 mm $\cdot$ yr^{-1} and as close as $\sim$ 400 km along-trench from the mainshock centroid (fig. 3.1) (Yuzariyadi and Heki, 2021). A landward velocity increase of 4.1 mm $\cdot$ yr^{-1} was observed between velocities in the 5 years after the Oaxaca earthquake and preseismic velocities (Yuzariyadi and Heki, 2021). This change is observed at a station $\sim$ 150 km along-trench from the middle of the rupture, with no other nearby stations. Landward velocities up to $\sim$ 4 mm $\cdot$ yr^{-1} greater than before the event were observed in the 5 years after the Iquique earthquake, at stations $\sim$ 300–400 km along-trench on either side of the rupture centroid (Hoffmann *et al.*, 2018; Yuzariyadi and Heki, 2021). Hoffmann *et al.* (2018) found landward increases, with respect to
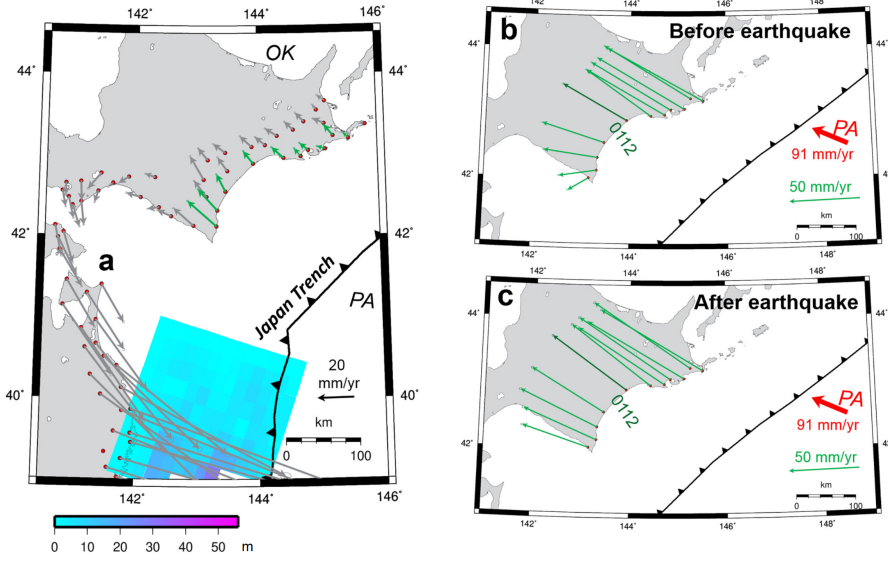
Figure 3.1 (a) Horizontal velocity changes and selected (b) preseismic and (c) post-seismic velocities (from the beginning of 2012 to the end of 2014) used to compute them, associated with the 2011 Tohoku earthquake. The green arrows in (a) represent velocity changes at stations whose velocities are selected to be shown in (b) and (c). The distribution of coseismic slip in the rupture area of the earthquake, as computed by the USGS, is shown in color in (a). Cropped from Figure 6 of Yuzariyadi and Heki (2021), used under CC BY (https://creativecommons.org/licenses/by/4. 0/)

preseismic values, as high as 10 mm $\cdot$ yr^{-1} in the second year after the event.

The magnitudes of landward velocity changes after all six earthquakes initially vary over time in the period shortly after the earthquake (Yuzariyadi and Heki, 2021). This transient period largely coincides with the previously inferred duration of substantial postseismic transients (particularly afterslip) and lasts $\sim$ 5 years after the Tohoku earthquake and $\sim$ 2 years after the other, smaller events. The transient behavior of the trench-perpendicular velocity changes is not consistent across all observations. It includes increases, decreases, and even transitions from trenchward to landward changes within the first 2 years after the Oaxaca (Yuzariyadi and Heki, 2021) and Iquique (Hoffmann *et al.*, 2018) earthquakes. However, in all cases, after this transient period, velocity changes stabilize and remain constant, except for a moderate increase in the following 3 years after the Iquique earthquake (Yuzariyadi and

Heki, 2021).

An increase of the landward velocity can signify changes in the magnitude or timing of the next earthquake in the area, for instance indicating an increase in slip deficit accumulation and seismic hazard. Ascertaining the mechanism responsible for the landward velocity changes can thus clarify what changes to seismic hazard should be expected where the changes are observed. One interpretation of the observed increase in landward velocities is that it results from an increase in frictional interplate coupling on the megathrust in the vicinity of these observations (Loveless and Meade, 2016). The hypothesis stems from the kinematic inversion of observed velocities from different time spans into interplate coupling. This interpretation implies that the frictionally coupled area on the interface would increase due to a megathrust event hundreds of km away.

Another explanation for the increased landward velocities is that the subducting slab accelerates over a wide portion of the margin as a result of the megathrust unlocking in the rupture zone (Heki and Mitsui, 2013). The hypothesis is consistent with marine GPS-acoustic (GPS-A) observations showing increased Pacific plate velocities close to the rupture zone following the 2011 Tohoku-oki earthquake (Tomita *et al.*, 2015). However, slab acceleration due to an altered force balance resulting from the coseismic unlocking of asperities can only occur until the ruptured asperities are relocked. Relocking is sometimes inferred to have occurred within a few months to a year after the 2010 Maule, 2011 Tohoku, and other large megathrust earthquakes (Sato *et al.*, 2011a; Bedford *et al.*, 2016; Remy *et al.*, 2016; Govers *et al.*, 2018). In that case, transient slab acceleration cannot explain postseismic ELM observed over several years. Nevertheless, no consensus exists on whether relocking is universally rapid, or even whether rapid relocking is needed to explain observations after the Tohoku earthquake (Watanabe *et al.*, 2014; Peña *et al.*, 2019). Both increased coupling and slab acceleration require additional postseismic changes to the subduction system other than well-established postseismic processes (e.g., asperity relocking, visco-elastic relaxation, afterslip, poroelastic rebound).

Melnick *et al.* (2017) proposed another mechanism that would be intrinsic to deformation after large megathrust events. In their mechanical models of combined coseismic and postseismic deformation, over a 100-year timestep, resulting from a drop in megathrust friction, they saw a pattern of velocity changes in the far-field similar to what was observed at GNSS stations following the Maule earthquake. Melnick *et al.* (2017) and Loveless (2017) proposed that the elastic bending of the plates, in response to postseismic relaxation, explains the far-field landward increases in landward velocities associated with

the Maule earthquake. They also argued that the bending producing the velocity changes could cause temporal clustering of megathrust earthquakes by triggering ruptures of asperities. The 2015 Illapel, and 2016 Chiloé earthquakes, which followed the 2010 Maule earthquake in Chile, were interpreted as an example of such clustering (Melnick *et al.*, 2017; Loveless, 2017). This interpretation implies that landward velocity changes may also be responsible for increased shortening rates between clustered historical megathrust earthquakes (Melnick *et al.*, 2017), evidenced for instance by increased subsidence rates recorded by Sumatran microatolls (Meltzner *et al.*, 2015; Philibosian *et al.*, 2014). However, Melnick *et al.* (2017) and Loveless (2017) compared the effect of the simulated bending with observations only qualitatively, without analyzing the amplitude or temporal evolution of the velocity changes resulting from relaxation with the observed ones. Furthermore, their investigation of the parameter sensitivities and driving mechanisms of the process is incomplete in that it does not include, for instance, bulk rheological parameters, model domain extent, and preseismic interplate locking pattern.

In this paper, we investigate how far-field enhanced landward motion (ELM) may be produced as part of the megathrust earthquake cycle, assuming no variations in the interplate locking pattern or slab acceleration. More specifically, we study whether the expected acceleration produced by plate bending falls within the observed range and under what conditions this bending driven by postseismic relaxation may occur. As part of this goal, we aim to establish the sensitivity of this bending mechanism to key aspects of the megathrust earthquake cycle, such as the earthquake magnitude, the downdip extent of afterslip, and the rheology and extent of the plates and mantle.

We use numerical models of the earthquake cycle, with physically consistent stresses, strains and megathrust slip, to quantitatively simulate the postseismic deformation field. As ELM is observed at several subduction margins, we build generic seismic cycle models, not tailored towards any specific geographical region or megathrust earthquake. We conclude that in-plane bending of the plate probably does produce some ELM, but by itself cannot explain the global observations of ELM.

3.2 Numerical Model

3.2.1 Concept

We develop three-dimensional mechanical models of the full earthquake cycle. The model geometry involves a realistic slab profile and is uniform in the

trench-parallel direction (fig. 3.2). Deformation is driven by velocities imposed at the ends of the plates and by the locked portions of the megathrust (asperities), which we define and which accumulate slip deficit during the interseismic period.

It is customary to model the earthquake cycle using the backslip approach, in which the downgoing plate (slab) is assumed to deform only according to the imposed distribution of interseismic slip accumulation and coseismic slip, which must be determined independently of the model. Additionally, afterslip is either also imposed arbitrarily or assumed to be driven by coseismic stress changes and arbitrary background stresses only. In contrast, in our methodology the imposed plate velocity and the mechanical continuity of the two plates determine the pattern of interseismic slip deficit accumulation beyond the asperities, on the rest of the megathrust and on the shear zone downdip of it. The plate velocity, asperities, and plate continuity also determine the shortening of the slab updip of the asperity and its downdip lengthening. Deformation in the model during the coseismic and postseismic phases, after the asperity is ruptured, thus reflects the recovery of elastic deformation of the slab, including faster downdip motion of its middle portion as it catches up with the top and bottom. It also includes coseismic and postseismic slip that is fully physically consistent with, and determined by, the background stresses as well coseismic and postseismic stress changes.

As the far-field overriding plate is fixed horizontally, all displacements and velocities, both imposed as boundary conditions and resulting from the models, are expressed with respect to the overriding plate. The megathrust is represented by a discrete fault. We consider the two principal mechanisms of postseismic relaxation, afterslip and viscous relaxation (Ozawa *et al.*, 2004; Ozawa *et al.*, 2011; Bürgmann and Dresen, 2008; Diao *et al.*, 2014). We focus on the postseismic period of repeating earthquake cycles.

3.2.2   Numerical Method

We use a finite element method (FEM) to solve the mechanical equilibrium equations. The massively parallel software package GTECTON (version 2021.0; Govers and Wortel, 1993; Govers and Wortel, 2005; Govers *et al.*, 2018) uses the Portable, Extensible, Toolkit for Scientific Computation (PETSc version 3.10.4; Balay *et al.*, 2021a; Balay *et al.*, 2021b; Balay *et al.*, 1997) and Open-MPI (version 3.0.0 Gabriel *et al.*, 2004). GTECTON provides highly accurate solutions to elastic and visco-elastic problems with arbitrary geometries, a true free surface, and discrete/sharp fault interfaces.

The models have a tetrahedral finite element mesh with a variable resolu-

Figure 3.2 Model setup geometry, subdomains, boundary conditions and dimensions. The colors on the external surfaces indicate the displacement boundary conditions (BCs): light orange—free slip along x and y at the lateral sides; cyan—velocity BCs at the top and bottom of the downgoing plate; dark blue—free slip along z at the landward end). The colors on the top and bottom of the slab distinguish the asperity (red), rest of the brittle megathrust (dark fuchsia), shear zone (bright fuchsia), and interfaces where we impose relative motion at the interplate convergence rate (90 mm · yr^{-1}). Model boundaries without colors have no displacement BCs, and therefore use zero-traction BCs.

tion, with nodes as little as 4 km apart in high-strain areas close to the edges of the megathrust and asperities. The reference model includes 533,755 nodes and 3,114,252 elements and contains 6000 time steps with a size (Δt) of 1 year, corresponding to 20 earthquake cycles. A visualization of the mesh is shown in Fig. S1. Posterior estimates of the model error (Verfürth, 1994) show that the selected mesh is dense enough to support our conclusion that our results are accurate within a few %.

Following each coseismic phase and each afterslip phase, the system is mechanically re-balanced via multiple model iterations. After model spin-up, earthquake cycles are near-identical. There is a difference in surface displacement of less than a few mm between equivalent stages of one cycle and the preceding or following one, while 27 m of interplate convergence occurs over a cycle. We show results from the 19th to 20th cycle.

The models are run in parallel on 10 AMD EPYC 7451 24-core processors with Infiniband, using a Broyden–Fletcher–Goldfarb–Shannon solver (Fletcher, 1988).

3.2.3   Model Domain and Geometry

The model geometry extends for 2000 km along-trench (in the y direction) and 2200 km in the trench-perpendicular horizontal (x) direction (fig. 3.2). The lateral extent of the model domain is chosen so that regions where ELM is expected are not affected by the model edges. We verified that extending the domain further along-trench changes surface motion only minorly and close to the lateral edges. The trench is located at $x = 0$ and the oceanward model boundary at $x = 212$ km. The positive x direction thus points oceanward. The domain has a vertical extent of 338 km, with z positive upward and $z = 0$ at the top of the overriding plate. The distance between the trench and the landward edge of the model is 1988 km. We used pilot models to verify that enlarging the domain in the along-trench or landward directions does not alter the surface deformation of the overriding plate. We deal with enlargement in the other directions in section 3.3.2.

The downgoing plate has a thickness of 80 km, consistent with the seismologically detected depth of the lithosphere–asthenosphere boundary of oceanic plates (e.g., Kawakatsu *et al.*, 2009; Kumar and Kawakatsu, 2011), especially for older lithosphere such as on the margins of the Pacific plate (Liu *et al.*, 2017). The top of the downgoing plate follows a trench-perpendicular cross-section through the Slab2 (Hayes *et al.*, 2018) model geometry for the Japan subduction zone, taken to be representative of a typical subduction zone. The overriding plate is 40 km thick with a flat top surface, except for a taper to

the trench (at $z = -8$ km) over a horizontal distance (along x) of 18 km.

3.2.4 Rheology

The model consists of two elastic plates and two asthenospheric domains with isotropic viscoelastic rheological properties (fig. 3.2). The constitutive equations (Govers and Wortel, 2005) are based on compressible elastic deformation and incompressible viscous deformation. Here we use a linear viscosity so that the viscoelastic properties follow a Maxwell model with a characteristic stress relaxation time τ ("Maxwell time"; Appendix A1 in Govers *et al.* (2018)). Most models have a Young's modulus $E = 100$ GPa and a shear modulus $G = 40$ GPa (corresponding with bulk modulus $K = 66.7$ GPa, compressibility $\beta = 1.5 \cdot 10^{-2}$ GPa^{-1}, and Poisson's ratio $\nu = 0.25$). These elastic parameters are chosen to be consistent with seismological observations (Dziewonski, 1984) as well as spatially uniform, for the sake of simplicity in studying model sensitivity to their value. Below we discuss how a PREM elasticity profile (Dziewonski and Anderson, 1981) affects the results.

The mantle wedge and sub-slab asthenosphere in most of our models have a viscosity $\eta = 10^{19}$ Pa·s. This value is roughly consistent with viscosities determined from observations of postseismic deformation after the 2011 Tohoku-oki (Hu *et al.*, 2016a) and 2010 Maule (Klein *et al.*, 2016) earthquakes. These viscosity and shear modulus values correspond to a Maxwell time $\tau = \eta/G$ of 7.92 yr (e.g., Spence and Turcotte, 1979; Melosh and Raefsky, 1983). In section 3.3.2 we investigate the sensitivity of the results to material properties.

3.2.5 Boundary Conditions

We impose horizontal and trench perpendicular velocity boundary conditions on the oceanic side of the subducting plate (fig. 3.2). The rest of the vertical oceanic side, bounding the sub-slab asthenosphere, is allowed to move only in the vertical direction, because we do not model long-term convective motions. For the same reason, we allow only vertical motion along the vertical continental backside of the model. Slab parallel velocity boundary conditions are imposed where the slab passes through the model bottom boundary. No displacement boundary conditions are applied along the rest of the basal model boundary, corresponding to a zero-traction boundary condition. We apply free-slip boundary conditions at the lateral sides of the model, i.e., we allow no displacement perpendicular to these boundaries. We investigate the effect of altering the boundary condition and of moving the vertical location of this boundary in section 3.3.2.

Isostatic restoring pressures counteract vertical motions of the free surface of both plates (Govers and Wortel, 1993; Wu, 2004). These pressures have a magnitude proportional to vertical displacement. The constant of proportionality is the gravitational acceleration ($9.8 \text{ m} \cdot \text{s}^{-2}$) times the density contrast ($3250 \text{ kg} \cdot \text{m}^{-3}$ at the top of the overriding plate, $2200 \text{ kg} \cdot \text{m}^{-3}$ at the top of the oceanic plate).

3.2.6 The Megathrust

We use the slippery node technique (Melosh and Williams, 1989) to model slip along the megathrust in response to shear tractions that develop in the rest of model. The megathrust is infinitely thin in this formulation, and we impose resistive shear tractions to lock parts of the interface during periods between earthquakes. Herman and Govers (2020) demonstrated that interseismic GPS velocities along the South America subduction margin can be well reproduced using a physical model of fully locked asperities with dimensions of ~ 50 km on a megathrust that can slip freely otherwise. Low shear tractions up- and downdip of seismogenic asperities is consistent with stable sliding at low friction (Hardebeck, 2015; Ikari *et al.*, 2011; Scholz, 1998; Lindsey *et al.*, 2021). Between earthquakes we therefore consider portions of the megathrust as either locked (asperities) or unlocked.

The megathrust outside the asperities is continuously unlocked and can thus slip freely between earthquakes. However, the mechanical continuity of the plates adjacent to the fault results in accumulation of slip deficit within a distance of ~ 50 km from the asperity (Herman *et al.*, 2018). To discourage slip on the uppermost portion of the megathrust (Kanamori, 1972; Moore and Saffer, 2001; Fujiwara *et al.*, 2011; Sladen and Trevisan, 2018), we apply small shear tractions at depths shallower than 15 km. Their direction is opposite to coseismic slip and their amplitude is directly proportional to it, with a spring constant of $200 \text{ Pa} \cdot \text{m}^{-1}$.

We use asperities that are circular in map view and that have a diameter of 50 km. In all models, the center of one asperity is located 120 km landward from the trench ($x = -120$ km) in the middle of the model (y=0). Some models have additional asperities where landward velocity accelerations may be expected (section 3.3.2). A model "earthquake" occurs by slip on the megathrust when the central asperity is unlocked, which is imposed to happen every 300 years. Unlocking relaxes all shear tractions on the asperity, and the numerical model finds a solution to the new force balance and stresses using ten iterations. We assume that nothing resists slip deficit release on the megathrust, thus maximizing earthquake magnitude for a given asperity and

interplate convergence rate, consistently with the free slip allowed interseismically on the non-locked megathrust. The moment magnitude of the model earthquake is determined by the total accumulated slip deficit on the megathrust. The asperity relocks immediately at the end of the coseismic phase.

3.2.7 Shear Zone Downdip of the Megathrust

The contact between the mantle wedge and the slab, downdip of the brittle megathrust that releases slip deficit coseismically, hosts slow slip, tremors and low-frequency earthquakes (Behr and Bürgmann, 2021; Lay *et al.*, 2012; Tichelaar and Ruff, 1993). Geodynamic models show that a viscoelastic shear zone develops on geological time scales that facilitates differential motion between the slab and the mantle wedge (van Keken *et al.*, 2002). The maximum depth extent of rapid postseismic relative motion (afterslip) on the slab-wedge interface is incompletely constrained but is commonly taken to extend to $\sim$ 80–100 km (Diao *et al.*, 2014; Freed *et al.*, 2017; Hu *et al.*, 2016b; Sun *et al.*, 2014; Yamagiwa *et al.*, 2015; Klein *et al.*, 2016) based on postseismic relaxation observations. We simplify the rheological complexity of the contact zone (Perfettini and Avouac, 2004) by representing it by a thin viscoelastic shear zone with a very low viscosity and with the same elastic properties as the surrounding rocks (Govers *et al.*, 2018; Muto *et al.*, 2019). During the (instantaneous) coseismic motion on the megathrust, there is no differential motion (slip) on the shear zone. Immediately after the coseismic phase,the asperity relocks and very rapid viscous shear stress relaxation occurs in the shear zone. We refer to such rapid postseismic shearing as afterslip. Afterslip is effectively instantaneous in our models. We compute it by rebalancing forces and stresses, using ten iterations, immediately following the coseismic phase, during which no differential motion is allowed on the shear zone downdip of the megathrust. Model afterslip is consequently complete before the onset of bulk viscous relaxation in the wedge and sub-slab asthenosphere (Govers *et al.*, 2018; Muto *et al.*, 2019). The shear zone is represented in the numerical model by an infinitesimally thin interface using slippery nodes (Govers *et al.*, 2018). Additional relative motion occurs on the shear zone during postseismic and interseismic periods as a result of viscous relaxation and continued convergence.

At depth, beyond the downdip end of the shear zone, the wedge and slab are modeled as fully viscously coupled, in agreement with the classical geodynamic view of the subduction system (e.g., van Keken *et al.*, 2002; Conder, 2005; Kneller *et al.*, 2005; Long, 2013; Leng and Mao, 2015). In the context of our earthquake cycle models we are not interested in the steady-state convective flow ("corner flow") in the wedge that is driven by slab motion. We therefore

use a similar approach to Savage (1983) along the deeper slab-wedge interface, as follows. The total flow field is the response to both steady subduction and perturbations due to the earthquake cycle. By imposing a steady differential slip rate on the part of the interface where the slab and wedge are fully coupled, we isolate the viscoelastic response to the earthquake cycle only. Using the split node technique (Melosh and Raefsky, 1981), we impose a differential slip equal to the imposed subduction rate.

3.2.8 Slab-Asthenosphere Boundary

We are also uninterested in modeling the steady, long-term, Couette convective flow due to the fact that the slab and underlying asthenosphere are viscously coupled. We thus isolate the response of the sub-slab asthenosphere to the earthquake cycle. Faulted nodes impose the long term subduction velocity as a relative displacement rate along the base of the downgoing plate.

3.2.9 Surface Motion Due to Postseismic Relaxation

Postseismic relaxation in our models involves bulk viscous relaxation and afterslip. Since afterslip is effectively instantaneous in our models, only bulk viscous relaxation produces changes in surface velocities. We compute these velocity changes as $\Delta \vec{v}_{t-\text{pre}} = \vec{v}_t - \vec{v}_{\text{pre}}$, the difference between postseismic velocities $\vec{v}_t$ at time t after the earthquake and the velocities $\vec{v}_{\text{pre}}$ at the last timestep before the earthquake. The latter velocities are taken to represent the near–steady-state contribution of continued convergence with stable coupling at the asperity. When considering cumulative displacement due to both relaxation mechanisms up to a certain time t after the earthquake (section 3.3.1), we remove the contribution of continued convergence by subtracting $t \cdot \vec{v}_{\text{pre}}$.

Before computing the velocity changes and displacement due to postseismic relaxation, we correct the velocities and displacement for the small effect of deformation due to long-term slab bending and unbending under the applied boundary conditions. The correction is computed by subtracting velocities from an identical model without earthquakes and asperities. Changes in velocities and displacements of the overriding plate thus represent the deformation associated with the earthquake cycle only.

Since the model geometry has reflection symmetry about a trench-perpendicular plane through the middle of the model ($y = 0$), we only plot half of the model ($y \geq 0$) when showing surface velocity or displacements.

3.3 Results and Analysis

3.3.1 Reference Model

Model Characteristics

We first present a "reference model", so called as its parameters and features will be the reference point for the sensitivity study of section 3.3.2. The reference model (Ref) has uniform elastic moduli with realistic yet generic values, not aimed at approximating any specific locality: Young's modulus $E = 100$ GPa and shear modulus $G = 40$ GPa. We use a single, central asperity. This way, we prevent additional asperities and their interseismic, coseismic and postseismic signals from interfering with the postseismic relaxation that we study. In later models (section 3.3.2) we discuss the effect of additional coupling in the form of other asperities, placed laterally along-trench. The asperity is located on the megathrust between the depths of 19.5 and 30.2 km from the surface (11.5 and 22.2 km from the trench). Its unlocking causes coseismic slip corresponding to a moment magnitude M_W of 8.9. Afterslip occurs between 40 km (the lower limit of the megathrust interface) and 100 km depth along the slab-wedge interface.

Surface Motion Due to Each Postseismic Relaxation Process

Figure 3.3(a) shows the cumulative surface displacement due to afterslip on the shear zone separating the slab from the asthenospheric wedge. The trench-perpendicular component of surface displacement of the overriding plate is entirely trenchward (positive). Its amplitude is highest (~ 9 m) between the asperity and the trench and decreases with distance, in both the trench-perpendicular and the trench-parallel directions.

Figure 3.3(b) shows horizontal velocity changes at time $t = 1$ yr after the earthquake $\left(\Delta\vec{v}_{1\,\mathrm{yr-pre}}\right)$. These velocity changes are landward as close as 700 km along-trench from the middle of the asperity. The maximum amplitude of the landward velocity change occurs around 110 km from the trench and 1054 km from the middle of the asperity (table 3.2). The trench-perpendicular gradient in landward velocity changes is small in the offshore, near-trench region (Fig. S2). The velocity changes are highest immediately after the earthquake and decay with time. For instance, the maximum landward velocity change $\left(-\Delta v_{xt\mathrm{-pre}}\right)$ is 0.67 mm $\cdot$ yr^{-1} at $t = 1$ yr, 0.62 mm $\cdot$ yr^{-1} at $t = 2$ yr, and 0.58 mm $\cdot$ yr^{-1} at $t = 3$ yr.

Cumulative Motion Due to Postseismic Relaxation

Figure 3.3(c) shows the temporal evolution of trench-perpendicular displacement of one point on the surface of the overriding plate. This point ($x = -170$ km, $y = 1060$ km) is located at the lowest (most landward) $\Delta v_{x\,1\,\mathrm{yr-pre}}$ at the coastline, taken to have the same horizontal location as the downdip end of the megathrust. Displacement is measured as 0 at the end of coseismic slip. Afterslip, instantaneous in the model, produces the trenchward (i.e., positive) displacement at time 0. Landward (i.e., negative) displacement then occurs due to viscous relaxation. At this location, the trenchward displacement due to afterslip is greater than the cumulative ELM due to viscous relaxation at any time. In the 5 years after the earthquakes, the cumulative landward displacement due to viscous relaxation is everywhere smaller than the trenchward displacement due to afterslip. We expect the viscosity of the asthenosphere to control the rate at which viscous relaxation occurs and thus the temporal evolution of the resulting landward displacement. We later explore the effect of different viscosities (section 3.3.2).

Figure 3.3 *(facing page)* Horizontal surface motion due to postseismic relaxation in the reference model. (a) Displacement due to afterslip. The color field shows the amplitude of trench-perpendicular displacement (positive landward), while the vectors show the direction and magnitude of horizontal displacement, including the trench-parallel component. In the cutout, the color scale is clipped at 50 mm to show the displacement in the far-field along-trench region. The cyan contour marks 0 trench-perpendicular displacement, separating landward from oceanward motion. The black barbed line shows the location of the trench. The outline of the asperity is shown in red. The dashed orange lines are 2.5 m contours of slip on the shear zone and megathrust due to afterslip. The approximate location of the coastline, taken to be directly above the downdip limit of the locked asperity, is shown in green. The blue dot marks the point at which displacement is plotted in (c). Only half the model is shown because of symmetry about the middle ($y = 0$). (b) Velocity changes (postseismic minus pre-seismic), 1 year after the earthquake, due to viscous relaxation. The color field shows the amplitude of trench-perpendicular velocity, while the vectors show the direction and magnitude of horizontal velocity. The color scale is clipped at ± 5 mm $\cdot$ yr^{-1} to show landward velocity changes. The cyan contour marks 0 trench-perpendicular velocity. The black barbed line shows the location of the trench. The outline of the asperity is shown in green. The dashed orange lines are 2.5 m contours of coseismic slip on the megathrust. The approximate location of the coastline is shown in green. The purple dot marks the point at which displacement is plotted in (c). Only half the model is shown. (c) Temporal evolution of total trench-perpendicular surface displacement (dots) at one point in the model ($x = -170$ km, $y = 1060$ km), minus the contribution of the velocity at the end of the interseismic stage, beginning immediately after the coseismic stage.

(a) Due to primary afterslip

(b) 1 year after the earthquake

(c)

135
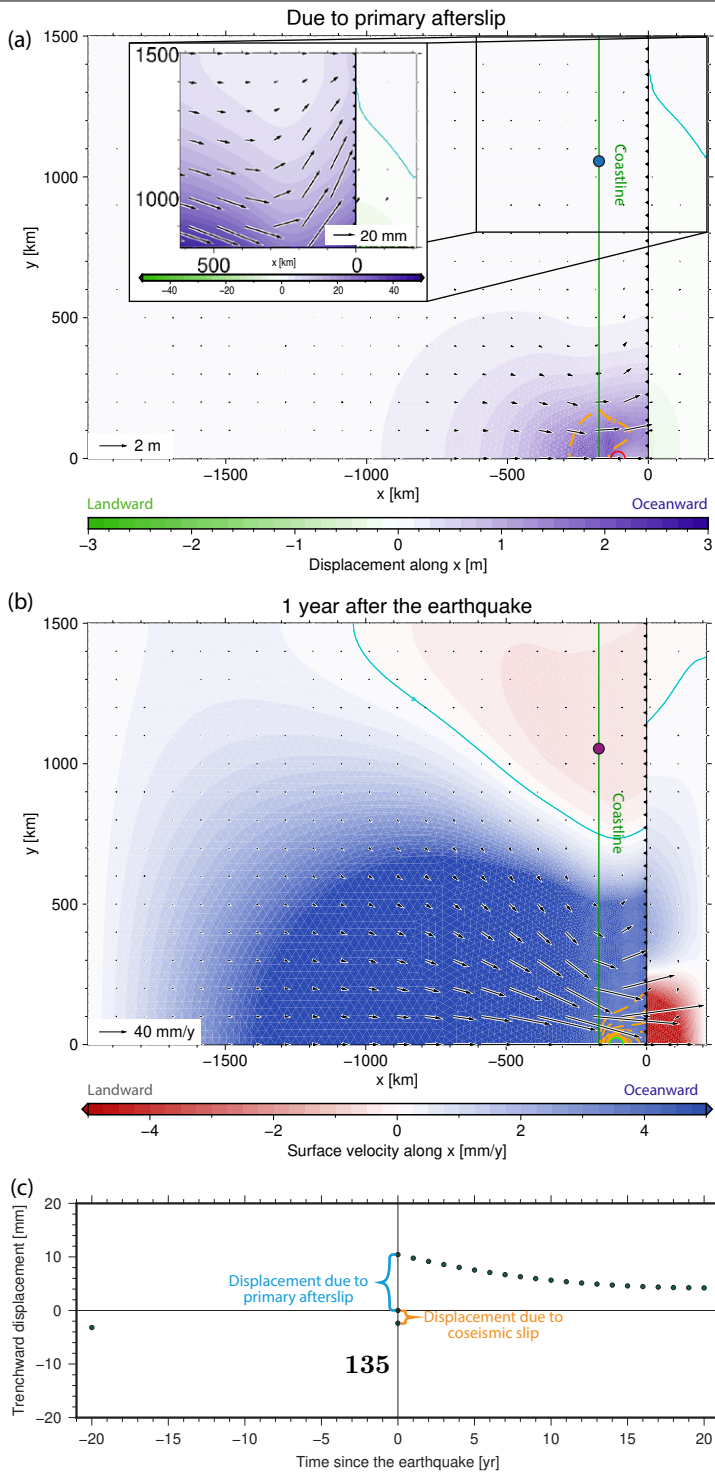
3.3.2   Sensitivity Testing

Maximum Depth Extent of Afterslip

We evaluate the sensitivity of our model results by varying the maximum depth at which the relative motion between the slab and mantle wedge can deviate from the interplate convergence rate. This restricts afterslip and associated slip deficit accumulation on the deep shear zone. This parameter is the major mechanical constraint on material deformation, for a given rheological structure and megathrust locking pattern.

First, we restrict afterslip to moderate depths, shallower than 75 km (model Aft75). The maximum landward velocity change 1 year after the earthquake is slightly lower than that produced in the reference model with a maximum afterslip depth of 100 km (table 3.2). Landward velocity changes also occur ∼ 50 km along-trench closer to the middle of the asperity. We then restrict afterslip on the shear zone (downdip of the megathrust and thus deeper than 40 km) to very shallow depths, less than 45 km (model Aft45). The landward displacement due to afterslip is greatly reduced, but so is the maximum landward velocity change due to viscous relaxation (table 3.2 and Figs. 3.4 and Fig. S3). Next, we allow afterslip to occur at greater depths, as much as 150 km (model Aft150). Compared to the reference model, the landward velocity changes at time $t = 1$ y after the earthquake have a near-identical maximum amplitude, occurring next to the trench and at a greater along-trench distance from the middle of the asperity (table 3.2). Lastly, we completely remove any restriction on afterslip, allowing the relative velocity of the mantle wedge and slab to vary at any depth in response to postseismic deformation (model AllAft). Removing the restriction on afterslip completely eliminates any landward velocity changes due to viscous relaxation.In our models, not allowing time-variable slip rates in the deep shear zone is necessary for enhanced landward velocities to result from postseismic viscous relaxation. The spatial extent of this restriction determines the specific pattern of velocity changes produced.

To better understand the mechanism responsible for ELM generation in our models, we further investigate the relationship between the restriction of motion and the production of ELM by viscous relaxation. We take the model with no limits on afterslip (AllAft) and we introduce a backstop in the overriding plate. We do this by imposing no trench-perpendicular displacement, at all depths within the plate, at a horizontal distance of 400 km from the trench. This model (AllAftB1) produces landward surface velocity changes due to postseismic viscous relaxation (table 3.2). The far-field portion of the
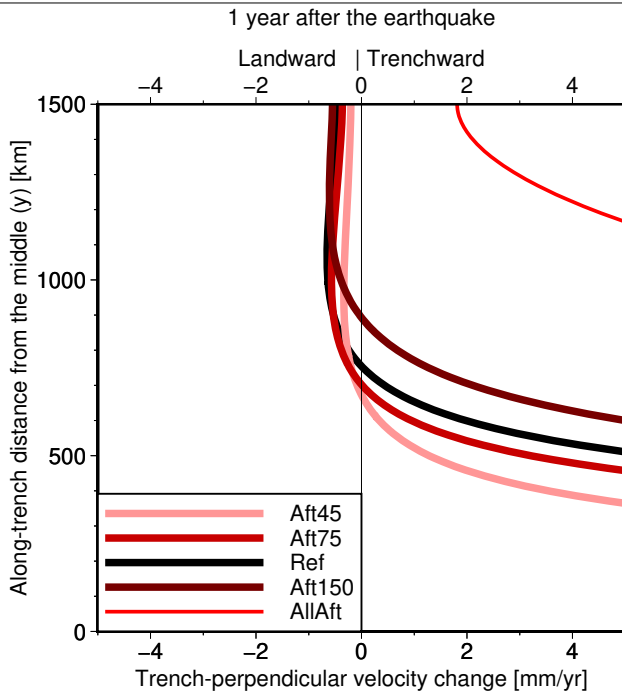
Figure 3.4 Sensitivity to different limits to afterslip on the shear zone downdip of the megathrust of trench-perpendicular surface velocity changes 1 year after the earthquake along trench-parallel profiles 170 km from the trench.

plate has an opposite pattern of trench-perpendicular motion, with landward velocity changes in the central part of the model and lower trenchward velocities farther along-trench. Increasing the horizontal distance from the trench to the free-slip boundary to 700 km (model AllAftB2) decreases the maximum landward velocity change 1 year after the earthquake and increases the minimum along-trench distance from the middle to landward velocity changes at that time.

Earthquake Magnitude

We examine the robustness of our results when the size of the earthquake changes. To this end, we reduce the interplate convergence rate, uniformly lowering the slip deficit accumulated and released over an earthquake cycle without varying its spatial pattern. Halving the convergence rate, and thus

Model name	Model description	Maximum landward $\Delta v_{x\,1\mathrm{yr-pre}}$ $(\mathrm{mm} \cdot \mathrm{yr}^{-1})$	Location (x, y) of maximum landward $\Delta v_{x\,1\mathrm{yr-pre}}$ (km)	Minimum y of landward $\Delta v_{x\,1\,\mathrm{yr-pre}}$ (km) at $x = -170$ km
Ref	Reference model	0.7	$(-110, 1054)$	736
Aft45	Afterslip above 45 km depth	0.3	$(-230, 975)$	975
Aft75	Afterslip above 75 km depth	0.6	$(-138, 995)$	681
Aft150	Afterslip above 150 km depth	0.7	$(-6, 1241)$	879
AllAft	No lower limit to afterslip	0	N/A	N/A
LoEta1	$\eta = 2 \cdot 10^{18}$ Pa·s (both mantles)	2.4	$(-171, 1121)$	806
LoEta2	$\eta = 2 \cdot 10^{18}$ Pa·s (wedge only)	3.6	$(-118, -880)$	897
HiEta1	$\eta = 5 \cdot 10^{19}$ Pa·s (both mantles)	0.1	$(-105, 1051)$	729
HiEta2	$\eta = 5 \cdot 10^{19}$ Pa·s (wedge only)	0.1	$(-430, 1500)$	1125
LoErefK	$E = 20$ GPa, Ref K (ov. plate)	5.6	$(-82, 409)$	295
RefEloK	$K = 33.3$ GPa, Ref E (ov. plate)	0.7	$(-58, 1149)$	834
E30-150	$E = 30$ GPa $(x < 700$ km), 150 GPa $(x > 700$ km) (ov. plate)	2.2	$(-74, 514)$	397
LatAsp	Lateral asperities present	0.6	$(-61, 1500)$	646
AllAftB1	AllAft with no x-displacement in overriding plate at $x = 400$ km	10.5	$(-106, 460)$	300
AllAftB2	AllAft with no x-displacement in overriding plate at $x = 700$ km	5.8	$(-85, 870)$	570
FixBot	Fixed base of mantle	1.5	$(-103, 659)$	515
FBThick	Base of mantle at 660 km depth, fixed	1.1	$(-97, 740)$	571
LongOcean	Oceanic domain extending for 988 km along x	1.3	$(-99, 756)$	572

Table 3.2 Main features of landward velocity changes due to viscous relaxation 1 year after the earthquake in different models

the seismic moment M_0, reduces the moment magnitude M_W from 8.92 to 8.71 and halves the displacement due to afterslip and the velocity changes due to viscous relaxation at any time. Similarly, reducing M_0 by an order of magnitude (and M_W from 8.92 to 8.25) also reduces the velocity changes and displacement to a tenth. Therefore, with a given interplate locking pattern, ELM produced by postseismic relaxation scales linearly with seismic moment M_0. This is unsurprising, given the linear nature of the rheologies used in the model. Given the amplitude of the ELM in the reference model, even an earthquake larger than any ever recorded would produce smaller landward velocity changes than the largest values observed at GNSS stations.

Mantle Viscosity

Mantle viscosity controls the rate of viscous relaxation, which produces enhanced landward velocity changes in our reference model. We alter the viscosity η, and thus the Maxwell relaxation time τ, to investigate its effect on our findings. First, in model LoEta1 we decrease η and τ in both the asthenospheric wedge and sub-slab asthenosphere by a factor of 5 compared to reference values, to $2 \cdot 10^{18}$ Pa·s and ~ 1.59 years, respectively. We decrease the timestep size by the same factor of 5 to accurately resolve the displacement. The earthquake size ($M_W = 8.91$) and recurrence interval ($T = 300$ years) are unaltered. The resulting landward velocity changes are dramatically higher than in the model with reference rheology and earthquake size and a single asperity (table 3.2 and fig. 3.5, Fig. S4a). However, the maximum amplitudes of the landward velocity changes are still smaller than observed (section 3.1 Yuzariyadi and Heki, 2021). The velocity changes decay faster than with the reference viscosity, with the peak amplitude going from 2.5 mm·yr^{-1} at $t = 1$ year to 1.6 mm·yr^{-1} at $t = 2$ years. In a related experiment (LoEta2), we decrease the viscosity compared to the reference model to $2 \cdot 10^{18}$ Pa·s in the mantle wedge only, keeping it at 10^{19} Pa·s in the sub-slab mantle. The maximum landward velocity change after 1 year is more than 50% higher than in LoEta1 (table 3.2 and fig. 3.5, Fig. S4b). However, these velocity changes are still lower than observed after the Tohoku-oki, Tokachi-oki and Maule earthquakes (Yuzariyadi and Heki, 2021). Also, the model velocities decay rapidly, having a maximum amplitude of 3.8 mm·yr^{-1} at $t = 1$ year and 2.0 mm·yr^{-1} at $t = 2$ years. The greater landward velocity changes due to viscous relaxation when the viscosity is lower in the mantle wedge only indicate that they are driven by viscous flow in the wedge itself, while flow in the sub-slab mantle opposes them.

Since the earthquake size and elastic properties have not changed, afterslip

and the surface motion it causes, via elastic deformation, are the same as in the reference model. The displacement due to the instantaneous afterslip in the model is entirely trenchward. In reality, afterslip has a finite, relatively short duration (a few years following the Tohoku earthquake, for instance, per Muto *et al.*, 2019; Yamagiwa *et al.*, 2015). We compare the cumulative surface displacement due to bulk viscous relaxation in the 2 years after the earthquake (and thus after the instantaneous afterslip) with that due to the afterslip. The landward motion due to viscous relaxation does exceed the trenchward motion due to afterslip, in the along-trench far-field portions of the overriding plate, but by a very limited amount, only as high as ~ 1.0 mm.

Increasing the viscosity of both asthenospheric domains by a factor of 5 to $5 \cdot 10^{19}$ Pa $\cdot$ s (model HiEta1), decreases the maximum landward amplitude of velocity changes 1 year after the earthquake (table 3.2 and fig. 3.5, Fig. S5a). It also decreases the rate of decay with time of the velocity changes. For instance, the maximum landward amplitude after 10 years (0.12 mm $\cdot$ yr^{-1}) is only 11.5% lower than after 1 year. Increasing the viscosity only in the mantle wedge has a small effect on the maximum landward velocity change at any time (table 3.2 and fig. 3.5, Fig. S5b). However, it varies the spatial pattern of the velocity changes significantly, pushing the peak landward value far from the trench and at the lateral edge of the model ($y = 1500$ km). This occurs because the relatively small contribution of sub-slab viscous relaxation to surface velocities on the overriding plate is increased.

We have shown how the viscosity of the mantle wedge controls the amplitude and temporal decay of the landward velocity changes. A low viscosity produces large velocity changes, which can even compensate for the trenchward motion due to afterslip and produce net ELM. However, the velocity changes decay rapidly with time as viscous relaxation proceeds and are much smaller already a few years after the earthquake. Higher viscosities produce long-lasting velocity changes due to viscous relaxation, but their amplitudes are very small. Furthermore, the occurrence of afterslip should lead to consistently landward average velocity changes in the months and years after the earthquake during which deep afterslip is occurring. In contrast, velocity changes have been observed to transition from trenchward to landward only after two earthquakes (Iquique and Oaxaca) and within the first year after the event (Yuzariyadi and Heki, 2021; Hoffmann *et al.*, 2018).

Elastic Moduli and Compliance Contrast

We test the sensitivity of our reference model results to changing the elastic parameters of the overriding plate, where the enhanced landward velocities are
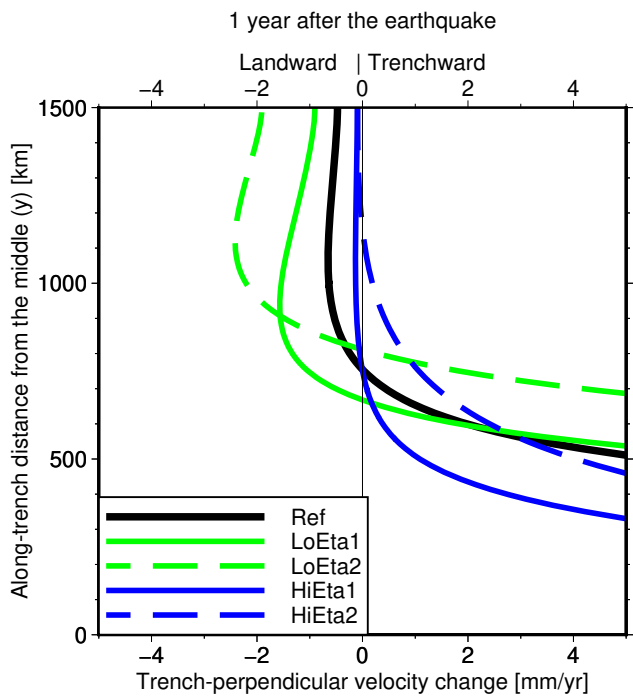
Figure 3.5 Sensitivity to different mantle viscosities of trench-perpendicular surface velocity changes 1 year after the earthquake along trench-parallel profiles 170 km from the trench.

observed. The effect on modeled ELM of varying the parameters within the realistic range for Earth materials is limited. Furthermore, tailoring the values and spatial distribution of model parameters realistically for specific settings and scenarios is outside the scope of this study. We thus vary the parameters uniformly, choosing extreme values to highlight their effect on ELM and help us investigate the mechanism that produces it. In model LoErefK, we reduce Young's modulus E by a factor of 5, from 100 to 20 GPa, and the shear modulus G from 40 to 6.9 GPa, without changing the bulk modulus K (66.7 GPa) and thus the compressibility $\beta = \frac{1}{K}$ ($1.5 \cdot 10^{-11}$ Pa^{-1}). This increases Poisson's ratio from 0.25 to 0.45, close to its uppermost possible value of 0.5. The resulting landward velocity changes are considerably greater and closer to the asperity than in the reference model (table 3.2, Fig. S6a).

In a related but different experiment (RefEloK), we keep the reference E, bring ν to 0 (as low as possible while not negative) and halve K from 66.7 to 33.3 GPa. β is then twice as large ($3.0 \cdot 10^{-11}$ Pa^{-1} instead of $1.5 \cdot 10^{-11}$) and G is 50 GPa. The resulting velocity changes 1 year after the earthquake have a very similar maximum amplitude as the reference model, although with a different pattern (table 3.2, Fig. S6b). In particular, the maximum landward velocity change is closer to the trench but farther from the asperity. The minimum along-trench distance from the middle to the landward velocity changes is greater than in the reference model. The ELM produced by viscous relaxation, when trench-perpendicular displacement is restricted at a certain distance from the trench, is primarily due to the elastic stiffness G of the overriding plate.

We then introduce a contrast in elastic stiffness between the overriding plate within a few hundred km of the trench and the plate farther inland. This represents the contrast between the hot, intensely deformed, tectonically young arc and backarc region, trenchward of the contrast, and the more stable interior of the overriding plate, landward of the contrast. This contrast produces a steep decrease in trench-perpendicular interseismic velocities with distance from the trench in the first few hundred km adjacent to the coast, at the location of the locked asperity, compatibly with observations (e.g., Chlieh *et al.*, 2008; Ruegg *et al.*, 2009; Loveless and Meade, 2010; Métois *et al.*, 2012; Weiss *et al.*, 2016). We use values of Young's modulus E (150 GPa) and shear modulus G (60 GPa) five times greater at horizontal distances from the trench beyond 700 km than closer to the trench (where they are 30 and 12 GPa, respectively). This is roughly the minimum ratio of the contrast that produces a noticeable break in the trench-perpendicular gradient of interseismic velocities and allows for the use of elastic moduli near the bottom and top of the range of realistic values for consolidated rock materials. The surface velocity changes

Figure 3.6 Sensitivity to different overriding plate elastic moduli of trench-perpendicular surface velocity changes 1 year after the earthquake along trench-parallel profiles 170 km from the trench ($x = -170$ km).

1 year after the earthquake, have a maximum amplitude of ~ 2.2 mm $\cdot$ yr^{-1} (table 3.2 and fig. 3.6, Fig. S7). This is considerably more than in the reference model, but still less than the observed landward velocity changes (Yuzariyadi and Heki, 2021, see section 3.1), despite the model earthquake having a greater magnitude than all observed events but Tohoku-oki. The peak landward velocity change at that time is located ~ 520 km along-trench from the middle of the asperity, while the shortest distance from the middle to landward velocity changes then is ~ 400 km. Afterslip still produces substantial displacement there (several tens of mm), causing the average cumulative velocity changes from both afterslip and viscous relaxation to be entirely landward over any length of time after the earthquake.

143

Our previously presented models have a single locked asperity on the megathrust. The observed lateral velocity changes, however, occur in areas with non-zero preseismic landward velocities and thus inferred interplate locking (Yuzariyadi and Heki, 2021; Loveless and Meade, 2016). Therefore, in the LatAsp model we test the effect of locking the megathrust along most of its along-trench extent. Starting with the reference model, we add two intermediate lateral asperities extending from 150 to 650 km along-trench from the middle and two external lateral asperities extending from 800 to 1300 km along-trench. All lateral asperities are identical to each other and ellipsoidal in map view. Their trench-perpendicular horizontal width (50 km) and distance from the trench (centered 120 km away) are the same as for the central asperity. All asperities are locked interseismically and need to periodically undergo coseismic phases for the model to have multiple earthquake cycle and thus develop background stresses. We use the same recurrence interval of 300 years for each asperity, and thus for the resulting earthquake supercycle. The first set of additional asperities has a coseismic phase 20 years after the central asperity and the second set after 20 more years. During each coseismic phase, the relevant asperities are unlocked (locking tractions are removed) and slip by as much as needed to release all the slip deficit they accumulated interseismically. At the end of each instantaneous coseismic phase, the relevant asperities are immediately relocked and undergo an instantaneous afterslip phase, during which the deep shear zone slips in response to coseismic clip on the megathrust. Afterwards, convergence resumes and postseismic viscous relaxation occurs in the region affected by coseismic stress changes, while the other asperities continue their interseismic period. We look at the landward velocity changes due to viscous relaxation 1 year after the earthquake on the central asperity. The amplitude of velocity changes directly above the most external asperities and trenchward of them is decreased, compared to the reference model, to less than $0.5 \text{ mm} \cdot \text{yr}^{-1}$ (Fig. S8). The maximum landward amplitude is decreased and shifted farther from the middle (table 3.2 and fig. 3.7). The overall area occupied by landward velocity changes is very similar, although it locally stretches closer to the middle of the central asperity. Overall, adding additional locked asperities on the lateral portions of the megathrust modifies the specifics of the ELM produced by postseismic viscous relaxation, without fundamentally altering it.
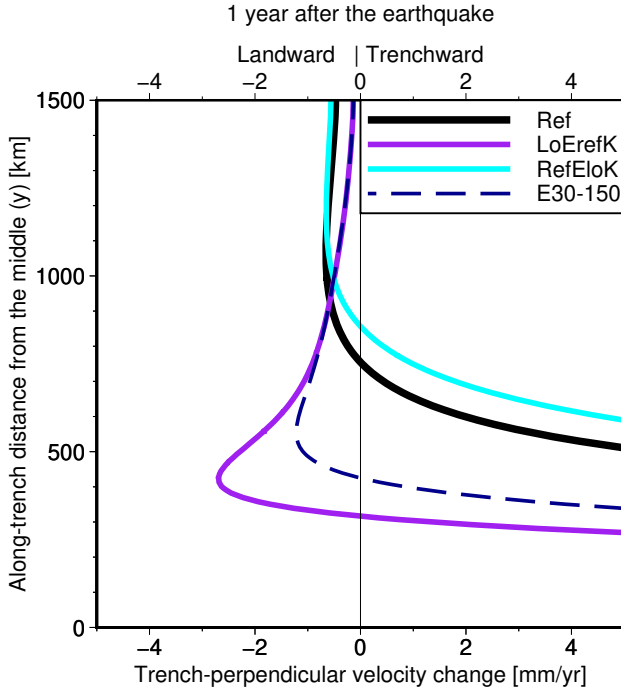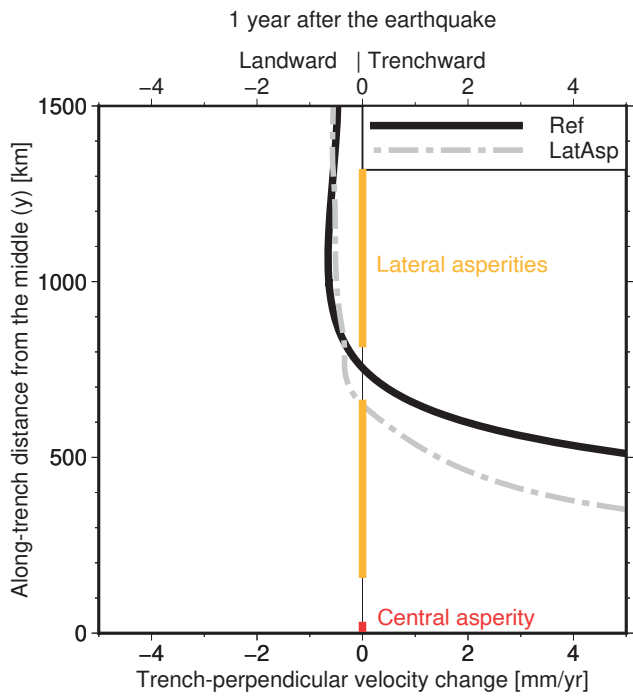
Figure 3.7 Sensitivity to different megathrust locking patterns of trench-perpendicular surface velocity changes 1 year after the earthquake along trench-parallel profiles 170 km from the trench. The colored lines on the vertical axis mark the along-trench spatial extent of the asperities.

Boundary Conditions and Location of Boundaries

In our reference model (Ref), we imposed zero tractions on the bottom of the mantle, leaving it free to move. We now test the opposite end-member boundary condition (BC): a fixed (no displacement) BC at the base of the mantle (FixBot), which restricts motion more than is realistic. The resulting landward velocity changes 1 year after the earthquake ($\Delta v_{x\,1\,\mathrm{yr-pre}}$) are up to 2.5 times larger than in Ref and ~ 400 km along-trench closer to the asperity (table 3.2 and fig. 3.8). However, the peak amplitude ($1.5 \; \mathrm{mm} \cdot \mathrm{yr}^{-1}$) is still far smaller (by up to two orders of magnitude) than observed (section 3.1; Yuzariyadi and Heki, 2021) and decays with time similarly to model Ref. In a separate test (FBThick), we expand the model domain to a depth of 660 km, covering the whole vertical extent of the upper mantle, while keeping the fixed BC at the base of the mantle. This makes the landward velocity changes $\Delta v_{x\,1\,\mathrm{yr-pre}}$ once again smaller (with a maximum value of $1.1 \; \mathrm{mm} \cdot \mathrm{yr}^{-1}$) and farther along-trench from the middle of the asperity, although less so than in Ref (table 3.2 and fig. 3.8).

We also test the effect of extending the horizontal, trench-perpendicular extent of the oceanic plate and sub-slab mantle. Extending it by 800 km, to a distance of 1012 km from the trench (model LongOcean), results in landward velocity changes that are closer along-trench to the asperity and larger in amplitude than in the reference model (table 3.2 and fig. 3.8). However, again, the peak amplitude ($1.3 \; \mathrm{mm} \cdot \mathrm{yr}^{-1}$) is still far smaller (by up to two order of magnitude) than observed (section 3.1 Yuzariyadi and Heki, 2021). The cumulative moment release by coseismic slip and by afterslip before viscous relaxation are both larger than in the reference model, by 0.8% and 4.8 %, respectively.

3.4   Discussion

3.4.1   The Mechanism Producing ELM in Our Models

Our model results show that restricting the maximum depth of afterslip, by applying full viscous coupling between the slab and wedge farther downdip, is needed for ELM to be produced during viscous relaxation. Changing this depth affects the resulting ELM pattern, as does introducing a trench-parallel contrast in overriding plate compliance. These sensitivites suggest that the mechanism producing the ELM relies on restricting trench-perpendicular motion.

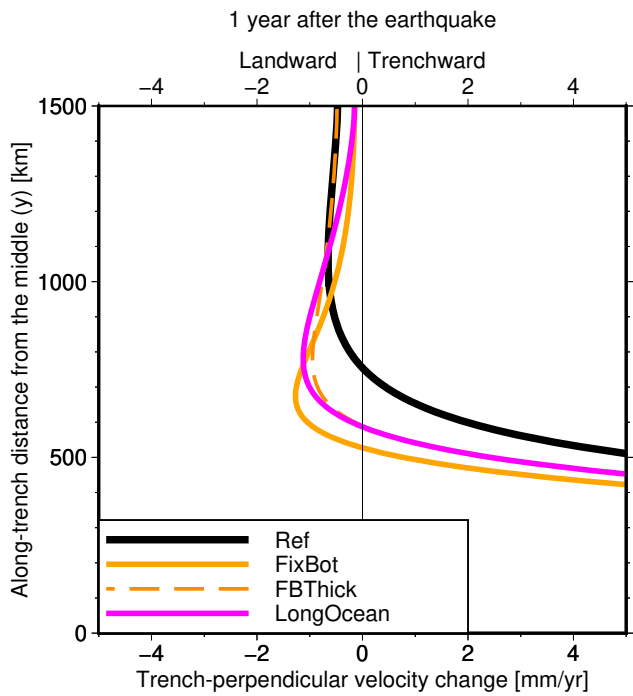**Figure 3.8** Sensitivity to different locations of model boundaries and boundary conditions imposed on them of trench-perpendicular surface velocity changes 1 year after the earthquake along trench-parallel profiles 170 km from the trench ($x = -170$ km)

To better understand why ELM results from viscous relaxation when afterslip is restricted, we simulate the mechanical response of an elastic plate to trenchward tractions, such as those that occur at the base of the overriding plate as the mantle wedge relaxes viscously. Analytical models show that in-plane bending occurs in a semi-infinite elastic plate in response to an outward horizontal force on the free side of the plate (Landau *et al.*, 1986, chapter 13). In the context of the overriding plate in a subduction zone, the free side would correspond to the trench and the force would result from a traction applied at its base. An important result of this conceptually simple analytical solution is that it produces landward displacement of the trench further in the far-field, but only if displacements are imposed to be zero at some distance from the rupture. Although this result is very interesting, it is of limited direct use to ELM because of simplifications in the model setup. Therefore, to identify the nature of the tractions that drive ELM, we explore a two-dimensional (2D) numerical model with a distributions of tractions and boundary conditions closer to the overriding plate in our 3D seismic cycle models.

The 2D model includes only a plate with a uniform thickness of 40 km and the same rheological parameters as in our reference earthquake cycle model. We ignore vertical motion and variation of horizontal motion with depth by using a plane-stress approximation (Govers and Meijer, 2001). We apply a free-slip boundary condition to the lateral and landward edges, while the trenchward edge is left free. A trenchward traction applied on a square patch at the bottom of the plate represents the trenchward tractions due to viscous relaxation in the mantle wedge in the vicinity of the rupture. In response to the traction and boundary conditions, the plate moves trenchward in the middle, but landward laterally. The trench-perpendicular width of the plate determines the location of the trenchward displacement. This conceptually simple model suggests that the ELM produced by viscous relaxation in the 3D earthquake cycle models is due to the fundamental in-plane elastic response to the trenchward viscous flow that occurs in the mantle wedge below.

Figure 3.9 summarizes our understanding of the deformation mechanism that results in ELM due to postseismic relaxation. Viscous relaxation in the mantle wedge produces trenchward motion and applies a trenchward traction to the base of the overriding plate in the vicinity of the asperity, which is absent farther along trench. The viscous coupling of the slab and mantle wedge resists trench-perpendicular motion at a given distance from the trench (~ 335 km) in the wedge and in the overlying overriding plate mechanically attached to it. The combination of trenchward forcing in the middle (along-trench) of the plate and of resistance to trenchward and landward motion all along the trench causes the elastic response of the plate to its in-plane (horizontal) forcings to

consist of bending, that is, to include lateral motion in the opposite (landward) direction to the trenchward tractions it is subject to.

The location of the viscous coupling between slab and mantle wedge, and thus of the downdip limit of afterslip, determines the resulting pattern of motion, given a certain rheology, asperity size, slip deficit, and boundary conditions. The stress changes associated with coseismic slip and afterslip, and thus the force balance during viscous relaxation, are affected by applying different boundary conditions at the base of the mantle, representing the opposite end-member rheology of the deeper asthenosphere, and by extending the model domain in the depth or oceanward directions. However, the response of the plate to viscous relaxation is still of in-plane bending and produces fundamentally similar motion, albeit with different amplitudes and wavelengths. However, we find that, without any viscous coupling at depth, that is, without any downdip limit to afterslip, nothing prevents the entire overriding plate from moving trenchward, and no bending nor ELM occurs.

Our sensitivity study shows that the landward velocity changes depend much less on its compressibility (while the shear modulus is kept constant) than on the elastic stiffness of the plate (when the compressibility is kept constant). This suggests that bending of the plate is not controlled by the finite compressibility. In other words, the enhanced landward motion on either side of the rupture area is not a consequence of a tendency to conserve volume in response to the trenchward displacement of the plate. Rather, the landward motion is part of the elastic in-plane bending of the overriding plate.

3.4.2 Consistency With Previous Research

Plate Bending Due to Postseismic Relaxation

Our model results indicate that viscous relaxation following a megathrust earthquake can, by itself, produce ELM as part of a rotational pattern of velocity changes. This is generally consistent with the model results and interpretations of Melnick *et al.* (2017). In fact, they obtain a pattern of opposing rotation about a vertical axis, including landward motion in the lateral portions of the subduction zone, during the combined coseismic and postseismic deformation caused by a drop in megathrust friction. They propose elastic bending of both plates as the responsible mechanism. Corbi *et al.* (2022) also obtain a similar pattern of opposing rotation about a vertical axes in an analog model with an elastic wedge and a frictional megathrust separating it from a rigid subducting plate with a constant velocity. In their model, the rotational deformation includes landward motion above one asperity that oc-
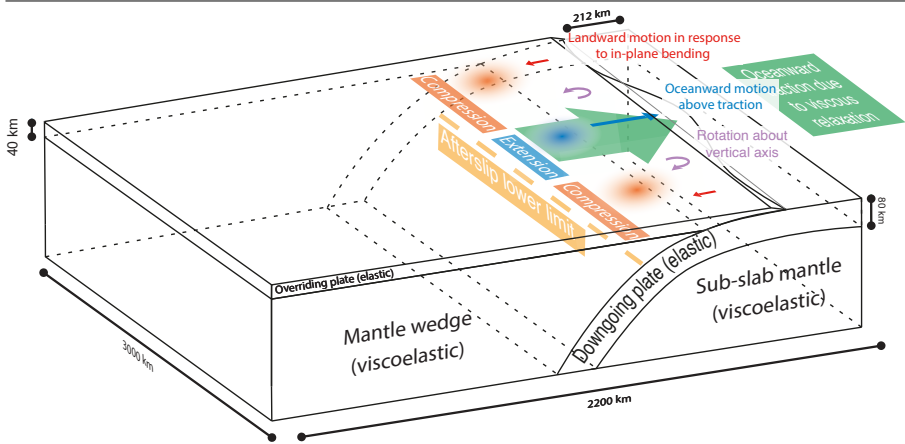
Figure 3.9 Mechanism responsible for ELM during viscous postseismic relaxation: trenchward traction rates on the base of the overriding plate, resulting from postseismic visco-elastic mantle flow, cause elastic in-plane bending of the overriding plate, with rotation about a vertical axis. When there is a downdip limit to afterslip, the bending produces enhanced landward displacement to the sides of the ruptured asperity.

curs as a result of frictional failure, specifically the "slip" phase of stick-slip behavior, which is analog of the combined coseismic and postseismic phase of the Earth's megathrust systems. We focus on postseismic relaxation with the same megathrust locking pattern as preseismically. We do not use variable friction that determines megathrust tractions, but use shear tractions large enough to completely lock the asperities, except during the coseismic phase, when they are completely unlocked. We find that lateral ELM is produced by viscous relaxation because the trenchward flow in the mantle wedge due to the latter generates an elastic response in the overriding plate that produces the former. We characterize this elastic response as consisting primarily of in-plane bending, in agreement with the inferences of Melnick *et al.* (2017) and Loveless (2017).

The ELM in our models relies on the motion of the overriding plate being restricted at a certain distance from the trench. The distance between the trench and this restriction determines the spatial pattern and amplitude of landward velocity changes in response to a given earthquake. Melnick *et al.* (2017) and Corbi *et al.* (2022) applied this restriction in their models in the form of a backstop: they allowed no trench-perpendicular horizontal motion on a vertical model boundary parallel to the trench and located close to it on the

landward side (700 km from the trench in the model of Menlick et al.; roughly 3 asperity lengths in the analog scale model of Corbi et al.). In contrast, our models extend for nearly 2000 km landward of the trench and instead rely on the conditions imposed on the slab-wedge interface to restrict the motion of the overriding plate. Specifically, the restriction is defined by the depth at which the shear zone that hosts afterslip ends and full viscous coupling begins (100 km in the reference model). There is no direct evidence of the depth at which this transition occurs, or even if there is such a depth. Afterslip has been inferred to occur deeper than 40 km, but there is no evidence of it taking place beyond 100 km depth at most (Diao *et al.*, 2014; Freed *et al.*, 2017; Hu *et al.*, 2016b; Sun *et al.*, 2014; Yamagiwa *et al.*, 2015; Klein *et al.*, 2016). It is plausible, although not certain, that substantially deeper afterslip is not only undetectable at the surface, but truly absent because of viscous coupling between the mantle wedge and slab, in the absence of a localized shear zone. In this case, postseismic viscous relaxation is expected to produce no ELM.

Incompatibility With Observations

The rate of ELM, in our models that produce it, is much smaller than in observations. The observed ELM generally increases with the magnitude of the associated earthquake, as does the ELM in our model. However, the largest observed landward velocity change, following the Tohoku earthquake (M_W 9.1), is more than an order of magnitude greater than in our reference model. This is the case even accounting for the smaller magnitude of the model earthquake (M_W 8.9) and for the linear scaling of modeled ELM with seismic moment M_0. For the Maule earthquake, smaller in magnitude ($M_W \sim 8.8$) than our reference model ($M_W \sim 8.9$), the maximum observed landward velocity change ($\sim 9 \text{ mm} \cdot \text{yr}^{-1}$) is an order of magnitude greater than in our reference model ($\sim 0.7 \text{ mm} \cdot \text{yr}^{-1}$). For the smaller earthquakes, the scaling indicates that ELM should be as much as two orders of magnitude smaller (for the Oaxaca earthquake, M_W 7.4). Instead, the observed ELM following those earthquakes is only an order of magnitude smaller than the maximum observed value for the much larger Tohoku-oki event (Yuzariyadi and Heki, 2021). Furthermore, the observed along-trench location of the ELM is also closer to the middle of the rupture than in the reference model, especially after the Iquique, Bengkulu and Oaxaca earthquakes. Although we can modify the boundary conditions and location of model boundaries to increase the amplitude of landward velocity changes and decrease its along-trench distance from the ruptured asperity, these changes are far from bridging the gap with observed amplitudes.

Our sensitivity tests indicate that overriding plate rheology and restrictions on afterslip affect the amplitudes and spatial pattern of the ELM occurring during viscous relaxation. In particular, introducing a lateral contrast between a more compliant overriding plate lithosphere (in the arc and backarc) and a less compliant plate interior increases the landward velocity changes. Such a contrast has also been inferred to determine the localization of high gradients in horizontal interseismic velocities in the arc and backarc, observed in multiple subduction zones. It is thus likely that the same compliance contrast responsible for the distribution of interseismic velocities amplifies the ELM produced by viscous relaxation, making it at least partly responsible for the fluctuations in the landward velocity changes observed in the early postseismic transient period.

Decreasing the viscosity in the mantle wedge can also produce large landward velocity changes, even exceeding the trenchward motion due to afterslip early after the earthquake. However, if the velocity changes are large shortly after the earthquake, they also decay rapidly with time. Conversely, increasing the viscosity produces a slower rate of decay of the velocity changes, but also lower amplitudes. Either way, the results are not in agreement with the observations, which show consistently long-lasting landward velocity changes, starting right after the earthquake and stabilizing to values of several $mm \cdot yr^{-1}$ after the transient period of a few years, while afterslip occurs (Yuzariyadi and Heki, 2021). Different rheologies not used in our models, such as Burgers viscoelasticity, could modulate the decay of velocity changes in different ways. For instance, large landward amplitudes could be achieved in the short term while exhibiting long-term viscosities compatible with the geodynamics of subduction zones. However, such rheologies cannot provide both large amplitudes and slow decay to the velocity changes due to relaxation of the same stress changes. Furthermore, the along-trench vicinity to the rupture of the landward velocity changes observed after the Bengkulu, Tokachi-oki and Oaxaca earthquakes cannot be reproduced by any of the models in our sensitivity testing.

We find that afterslip produces entirely trenchward motion of the overriding plate in all our models. This is in contrast with the hypothesis that the bending producing landward velocity changes is driven by afterslip, proposed by Loveless (2017). In our models, afterslip is modeled as instantaneous and viscous relaxation happens after it has finished. Our implementation of the two postseismic relaxation processes in our models captures the main features of interseismic and coseismic behavior and allows to easily distinguish the contribution of afterslip and viscous relaxation. At the same time, it avoids the computational demands and expanded parameter space caused by simulating

viscous flow in a narrow channel. However, in reality, afterslip has a finite duration and interacts with bulk viscous flow (Masuti *et al.*, 2016; Muto *et al.*, 2019; Agata *et al.*, 2019; Yamagiwa *et al.*, 2015). The degree to which afterslip affects the observed velocity changes depends on its distribution through time, as well as on the observation period and method of computation of the velocity changes from the displacement time series. The lack of a realistic temporal distribution of afterslip and the resulting surface displacement is a limitation of our implementation and precludes a direct comparison with observed displacement time series. Nevertheless, the entirely trenchward motion due to afterslip implies that the observed trench-perpendicular velocity changes, with amplitudes of several $mm \cdot yr^{-1}$, cannot be explained by afterslip supplementing the motion due to viscous relaxation. This conclusion should not be affected by the lack of two-way feedback between afterslip and viscous relaxation, as the mechanical interaction between the two postseismic relaxation mechanisms has a small effect on the cumulative amplitude of horizontal displacement and on its spatio-temporal evolution, compared to the two processes not interacting (Muto *et al.*, 2019; Agata *et al.*, 2019).

We find that the modeled velocity changes due to viscous relaxation decay with time as the stresses are relaxed (fig. 3.3c). The contribution of afterslip, when distributed in time, produces a trenchward signal in trench-perpendicular velocity changes, regardless of the locking pattern on the megathrust. The resulting total velocity change due to both relaxation mechanisms should exhibit highly transient behavior, becoming more landward with time as afterslip decays. It should only reach small values (less than a $mm \cdot yr^{-1}$ in the reference model) and then decay in time as viscous relaxation continues. A transition from trenchward velocity changes in the first year to landward velocity changes in the second year after the Iquique earthquake is indeed observed by Hoffmann *et al.* (2018). Yuzariyadi and Heki (2021) observe generally less drastic temporal evolution of the velocity changes for all the six earthquakes they consider, including Iquique. However, they only analyze the temporal evolution of velocity changes at one station per earthquake. They do observe a transition from trenchward to landward velocity change in the first and second years, respectively, after the Oaxaca earthquake, at the Puerto Escondido station (OXPE). These transitions likely reflect substantial deep afterslip occurring only shortly after the earthquake, ceasing after about 1 year. Both Hoffmann *et al.* (2018) and Yuzariyadi and Heki (2021) agree that the velocity changes remain landward after afterslip is inferred to have ceased. No decay in the amplitudes of the trench-perpendicular velocity changes is observed by Yuzariyadi and Heki (2021) after the transient period. Amplitudes are constant after 2 years, except for a slight decay up to 5 years after the Tohoku earthquake and

for a moderate increase up to 5 years after the Iquique earthquake. The two longest sets of time series, after the Tohoku and Tokachi earthquakes, show constant velocity changes in the last 4 years. This lack of decay cannot be explained by postseismic relaxation in our models, regardless of the peak amplitudes of velocity changes produced, and constitutes the greatest obstacle in explaining the observed ELM as caused by plate bending in response to postseismic relaxation.

Overall, we find that the elastic response of the plate to viscous relaxation, proposed by Melnick *et al.* (2017) and Loveless (2017), can plausibly occur, although only if full viscous coupling between the slab and mantle wedge is assumed to occur at a certain depth. We confirm that this response consists primarily of in-plane bending caused by the trenchward flow in the mantle wedge during viscous relaxation. However, according to our simulations, it is extremely unlikely that the temporal and spatial pattern of observed landward velocity changes later described by Yuzariyadi and Heki (2021) is primarily produced by bending in response to postseismic relaxation.

3.4.3 Seismic Hazard Implications

If the observed velocity changes are not attributable to bending caused by viscous relaxation, they must be caused by other mechanisms. One explanation is that large megathrust earthquakes result in changes in the interplate coupling on the megathrust, specifically an increase in the area of strong frictional coupling on the megathrust in the region where ELM occurs (Loveless and Meade, 2016). An increased area of coupling is a straightforward possible interpretation for any landward change in velocity at subduction zones. However, no explanation has been proposed for a megathrust earthquake rupture causing friction increases hundreds of km away. Another explanation is that the velocity of the slab transiently increases postseismically due to the altered force balance caused by unlocking the megathrust during the earthquake (Heki and Mitsui, 2013). Yuzariyadi and Heki (2021) test the correlations between the ELM they describe and the earthquake features predicted by the transient slab acceleration hypothesis, and find the evidence inconclusive but compatible with the hypothesis.

Both increased coupling and slab acceleration invoke an increased slip deficit, compared to the far-field, steady-state plate convergence rate, under the lateral far-field areas where the ELM is detected. Therefore, regardless of which of the two explanations is correct, it is likely that the seismic hazard increases at the locations and time at which enhanced landward velocities are observed. Yuzariyadi and Heki (2021) observe that the enhanced landward

velocities correlate with increases in the seismic rate in the relevant lateral portions of the megathrust, which they interpret as evidence of increased stressing rates. The in-plane plate bending in our models occurs regardless of the presence of any coupling on the lateral portions of the megathrust, and thus also when the rest of the megathrust cannot have shear traction changes. The observed increase in seismicity is probably caused by a a the mechanism other than plate bending that is needed to explain the observed landward motion requires. This mechanism is likely related to increased stressing and slip deficit accumulation on the lateral portions of the megathrust.

Further research is needed to investigate frictional behavior of the megathrust interface possibly responsible for increased coupling. Discriminating between the two mechanisms proposed to produce this increased slip deficit accumulation is necessary to distinguish whether the increased hazard consists of a greater likelihood of rupture (implied by greater stressing rate due to slab acceleration) or greater peak slip during the future ruptures (a possible consequence of greater frictional coupling on the megathrust). Future studies should also look for further geodetic evidence of transient slab acceleration, including elsewhere in the megathrust subduction system.

3.5 Conclusions

Postseismic viscous relaxation can indeed produce enhanced landward motion (ELM). The mechanism producing ELM in our models is the elastic, in-plane response of the overriding plate to the trenchward viscous flow due to relaxation in the mantle wedge. This elastic response consists largely of in-plane elastic bending of the plate. This mechanism relies on the restriction of afterslip provided by the viscous mechanical coupling of the mantle wedge and slab beyond the maximum depth of afterslip. Megathrust coupling in the lateral portions of the interface, above which ELM is observed, is not needed nor interferes significantly with the production of ELM in the models by postseismic viscous relaxation.

Enhanced landward velocity changes as part of the modeles plate bending due to viscous relaxation are small compared to observations. They also decay noticeably with time. This behavior is inconsistent with the observations of large ELM (several $mm \cdot yr^{-1}$ to a couple $cm \cdot yr^{-1}$) persisting over multiple years and only exhibiting transient behavior shortly after the earthquake. Furthermore, the geodetically observed ELM also occurs at smaller along-trench distances from the rupture than produced by plate bending in our models. We conclude that the observed ELM requires mechanisms other than postseismic

plate bending. The most plausible explanation is thus that slip deficit accumulates at greater rates at the locations and times at which lateral landward velocity changes are observed, increasing seismic hazard there and then.

3.6 Acknowledgements

3.7 Supporting Information

3.7.1 Introduction

This supporting information includes includes additional details of the model results presented in Section 3.3. In particular, it consists of text and figures that briefly describe the quantitative effect of varying model parameters in both the 2D conceptual and 3D seismic cycle models. It complements Sections
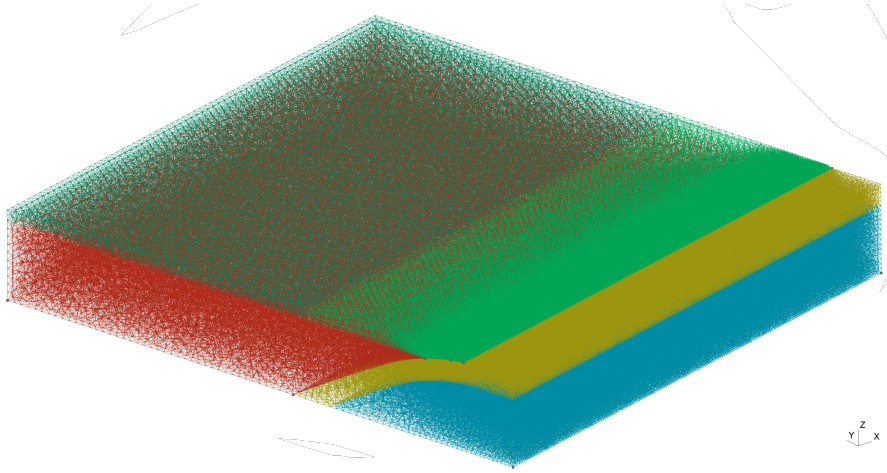
Figure 3.10 Isometric projection of the finite element mesh used in the reference model (Ref).

Sections 3.3.1 and 3.3.2, providing numbers and figures that would otherwise clutter the exposition of the results.

3.7.2   Additional Figures
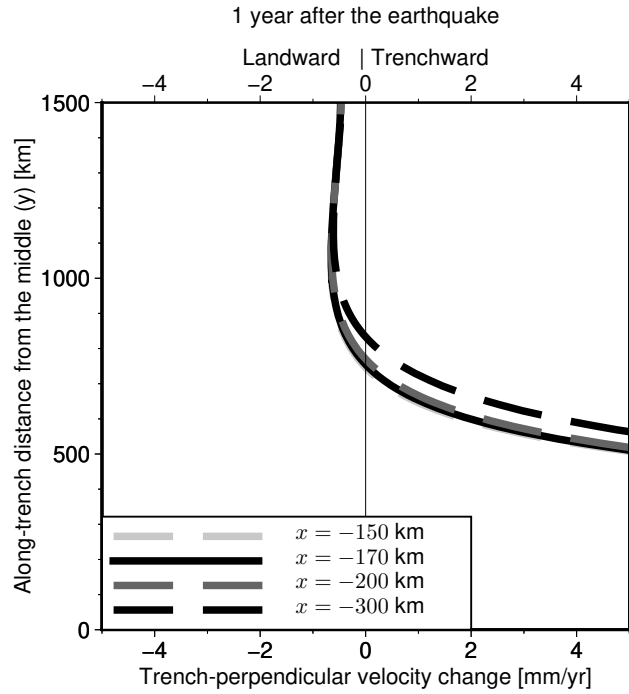
Figure 3.11 Trench-perpendicular surface velocity change 1 year after the earthquake along trench-parallel profiles in the reference model (Ref) at different distances from the trench.
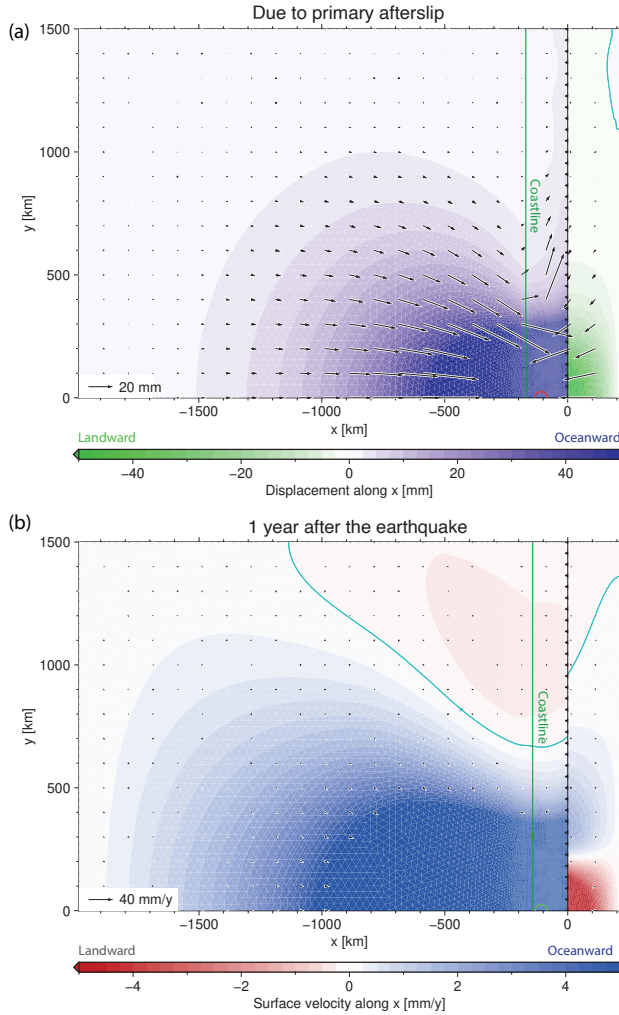
Figure 3.12 Landward motion due to postseismic relaxation in a model with no time-variable relative motion (afterslip or interseismic slip deficit accumulation) between the slab and mantle at depths greater than 45 km. (a) Displacement due to afterslip. (b) Velocity changes, 1 year after the earthquake, due to viscous relaxation.
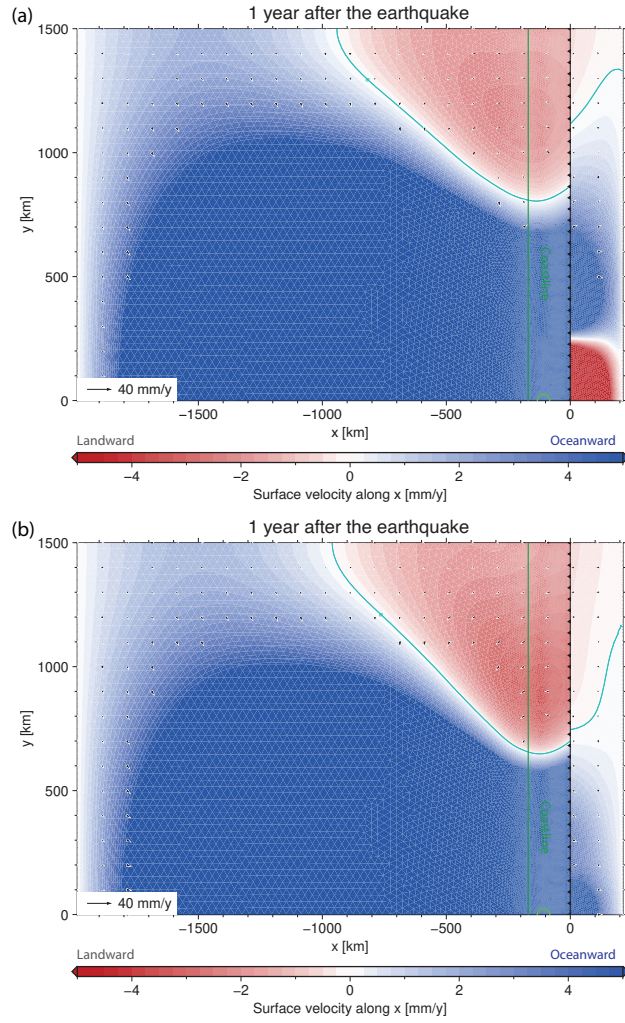
Figure 3.13 Trench-perpendicular velocity changes $\Delta v_{x\,1\,\mathrm{yr-pre}}$, 1 year after the earthquake, due to viscous relaxation, in models with a viscosity of $2 \cdot 10^{18}\ \mathrm{Pa} \cdot \mathrm{s}$ in the visco-elastic mantle in (a) both mantle domains (model LoEta1), or (b) only in the mantle wedge (model LoEta2). In (b), the sub-slab asthenospheric mantle has the same viscosity ($10^{19}\ \mathrm{Pa} \cdot \mathrm{s}$) as both mantle domains in the reference model.
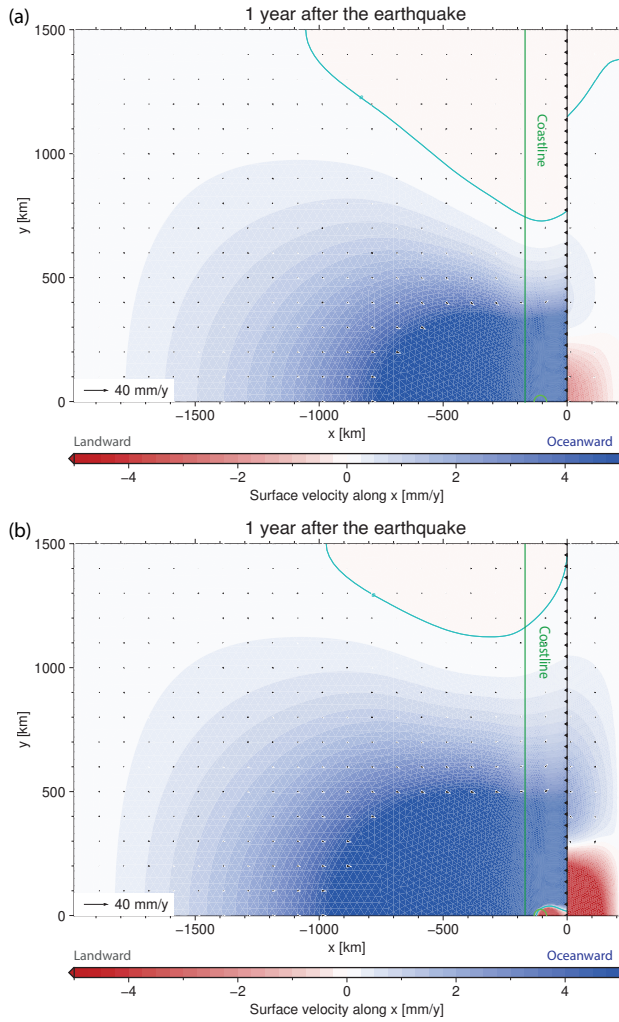
Figure 3.14 Trench-perpendicular velocity changes $\Delta v_{x\,1\,\text{yr}-\text{pre}}$, 1 year after the earthquake, due to viscous relaxation, in models with a viscosity of $5 \cdot 10^{19}$ Pa·s in the visco-elastic mantle in (a) both mantle domains (model LoEta1), or (b) only in the mantle wedge (model LoEta2). In (b), the sub-slab asthenospheric mantle has the same viscosity (10^{19} Pa·s) as both mantle domains in the reference model.
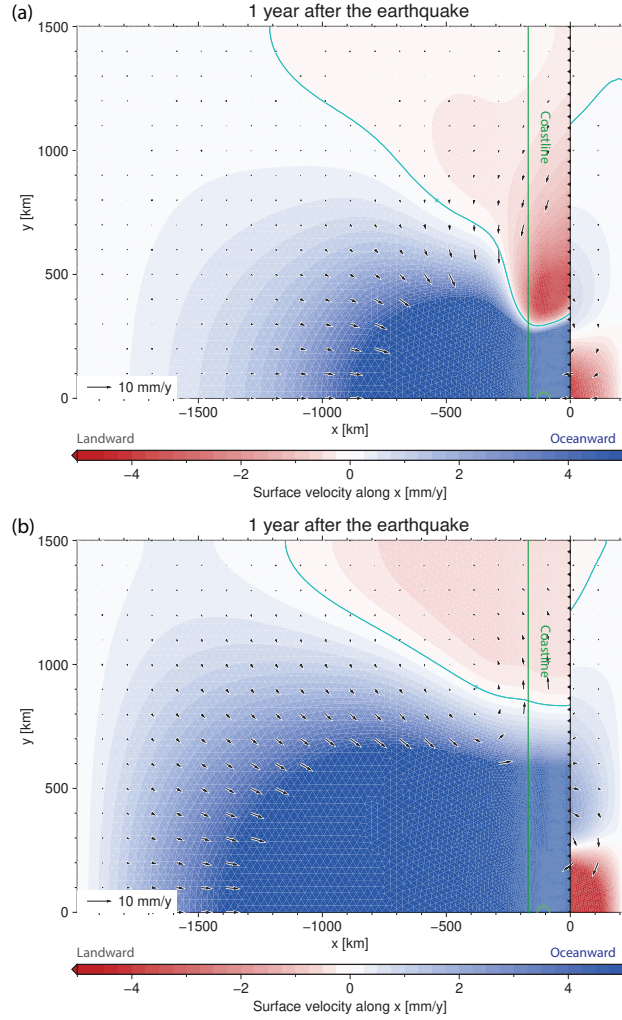
Figure 3.15 Trench-perpendicular velocity changes $\Delta v_{x\,1\,\mathrm{yr-pre}}$, 1 year after the earthquake, due to viscous relaxation, in models with either (a) lower E and G and the same K as in the reference model (LoErefK), or (b) lower K and the same E (RefEloK).
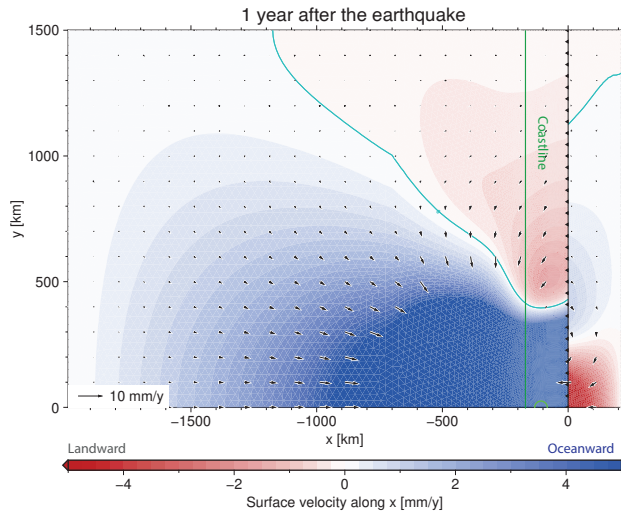
Figure 3.16 Trench-perpendicular velocity changes $\Delta v_{x\,1\,\mathrm{yr-pre}}$, 1 year after the earthquake, due to viscous relaxation, in a model (E30-150) with an overriding plate E of 30 GPa at distances from the trench smaller than 700 km and 150 GPa at greater distances.
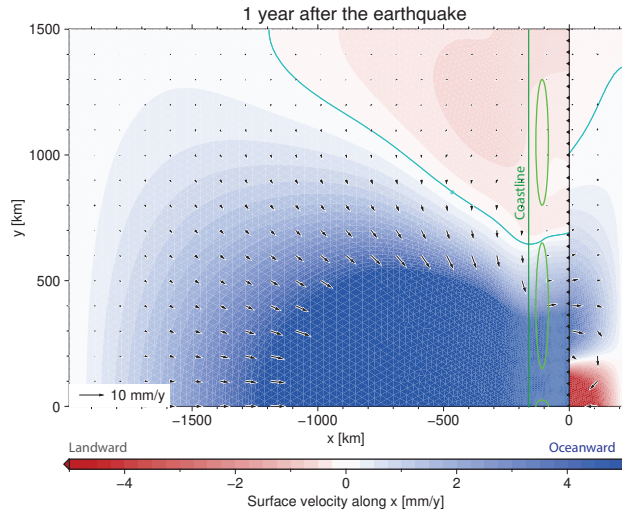
Figure 3.17 Trench-perpendicular velocity changes $\Delta v_{x\,1\,\mathrm{yr-pre}}$, 1 year after the earthquake, due to viscous relaxation, in a model (LatAsp) with lateral asperities in addition to the central one (all outlined in light green), unlocked 20 (intermediate asperities) and 40 years (external asperities) after the central one.

4

Offshore Landward Motion Shortly After a Subduction Earthquake Implies Rapid Relocking of the Shallow Megathrust

4.1 Context, Aims and Approach

The postseismic geodetic signal after a megathrust earthquake consists of several contributions: viscoelastic relaxation in the asthenospheric mantle, postseismic slip (afterslip) on the megathrust and its downdip continuation, poroelastic relaxation, and relocking of the megathrust interface (Bedford *et al.*, 2016; Fialko, 2004; Hoffmann *et al.*, 2018; Hu *et al.*, 2014; Jónsson *et al.*, 2003; Li *et al.*, 2017; Li *et al.*, 2018a; Peltzer *et al.*, 1998; Remy *et al.*, 2016; Wang *et al.*, 2012). Figure 4.1 summarizes the main features of postseismic deformation at subduction zones. Relocking marks the beginning of the accumulation of slip deficit in the new earthquake cycle. It results in shortening of the overriding plate and near-trench landward velocities comparable to, but lower than, the plate convergence rate. As oceanward motion due to viscous relaxation and afterslip wane, the effect of the newly locked megathrust becomes apparent in geodetic displacement time series as landward motion of the surface of the overriding plate. Landward motion progressively reaches

farther from the trench with time (Wang *et al.*, 2012). Detecting the timing of relocking is critical for understanding the mechanical state of the megathrust system and properly assessing the associated seismic hazard.

Evidence suggests that relocking occurs rapidly (within weeks to months) after large megathrust earthquakes (Govers *et al.*, 2018). In particular, rapid relocking has been inferred from the decomposition and inversion of Global Navigation and Satellite Systems (GNSS) displacement time series following the 2010 M_W 8.8 Maule (Chile) and 2007 M_W 8.0 Pisco (Peru) earthquakes (Bedford *et al.*, 2016; Remy *et al.*, 2016). Relocking was also inferred from the occurrence of a normal faulting intraplate earthquake 2 months after the 2006 Kuril Islands (Russia) megathrust rupture, followed 1 year later by a thrust-fault intraplate earthquake (Lay *et al.*, 2009), implying a rapid transition from extension to compression (Govers *et al.*, 2018). Other evidence of the mechanical state of the megathrust may come from offshore observations, via Global Positioning System and acoustic (GPS-A) ranging, of landward horizontal postseismic motion close to the trench. However, these results have been inconclusive.

GPS-A observations at one offshore location above the 2005 M_W 7.2 Miyagi (Japan) megathrust earthquake indicate landward postseismic motion consistent with the signature of locking and interplate convergence starting one year after the event (Sato *et al.*, 2011b). Landward motion was also detected at some offshore GPS-A sites on the overriding plate following the 2011 M_W 9.1 Tohoku (Japan) earthquake (Sun *et al.*, 2014; Tomita *et al.*, 2014; Tomita *et al.*, 2017; Watanabe *et al.*, 2014; Honsho *et al.*, 2019), beginning less than two months after the event (Guard, 2013). In contrast, the postseismic motion observed onshore was consistently oceanward over a period of at least 5 years after the Tohoku earthquake (Wang *et al.*, 2018a). The offshore landward motion following the earthquake amounted to as much as 50 cm in the first year after the event (Sun *et al.*, 2014). This amplitude is significantly more than can be explained merely by relocking and the far-field, steady-state convergence rate (8.3 cm $\cdot$ yr^{-1} locally and as high as 9.1 cm $\cdot$ yr^{-1} elsewhere on the Japan Trench) (Watanabe *et al.*, 2014). Watanabe *et al.* (2014) therefore explicitly concluded that relocking is irrelevant for explaining the observed motion after the Tohoku earthquake. Peña *et al.* (2019) reached the same conclusion for the onshore postseismic displacement field due to the Maule earthquake, whose observed trench-perpendicular components were entirely landward. Explanations have instead focused on postseismic relaxation, particularly viscoelastic relaxation and afterslip, since poroelastic relaxation can only account for relatively small signals (Hu *et al.*, 2004; Peña *et al.*, 2019).

Various studies interpreting the postseismic observations following the To-

hoku earthquake agree that the offshore landward motion is primarily caused by viscous relaxation (Sun *et al.*, 2014; Sun and Wang, 2015; Yamagiwa *et al.*, 2015; Freed *et al.*, 2017; Suito, 2017; Noda *et al.*, 2018; Agata *et al.*, 2019; Muto *et al.*, 2019; Fukuda and Johnson, 2021; Dhar *et al.*, 2022). Specifically, viscous flow in the sub-slab asthenosphere produces landward surface motion, while flow in the asthenospheric wedge produces oceanward motion (Suito, 2017). Noda *et al.* (2018) and Muto *et al.* (2019) also conclude that afterslip contributes to the offshore landward motion on the overriding plate. A consensus is thus forming that the typical evolution of the megathrust system outlined by Wang *et al.* (2012), in which landward motion appears progressively as the effect of locking prevails over diminishing postseismic relaxation, is somewhat complicated by sub-slab postseismic relaxation producing early and strong landward motion of the offshore forearc, regardless of locking. However, there has been no convincing mechanical explanation for why, and under what conditions, the landward motion resulting from viscous relaxation in the sub-slab mantle has a surface expression on the overriding plate.

We suspect that the postseismic observations of rapid landward motion, offshore on the overriding plate, require rapid relocking of the megathrust, as the latter determines the mechanical coupling between the two plates. We use a quasi-dynamic three-dimensional (3D) finite element method (FEM) model with regularly repeating M_W 9.1 earthquakes to investigate this hypothesis (Figure 4.1 and Figure 4.3 in the Supporting Information, Section 4.5). We focus on large megathrust earthquakes that rupture the whole megathrust. We use a uniform slab profile cut perpendicularly across the Japan Trench from the Slab2 model (Hayes *et al.*, 2018), but do not otherwise incorporate the structure nor aim to reproduce the specific observed deformation of the Japan subduction zone. We use uniform elastic plates and linear viscoelastic asthenospheric mantle with a viscosity of 10^{18} Pa$\cdot$s in the postseismic period we study. We impose a constant motion at a rate of 90 mm$\cdot$yr^{-1} at either end of the downgoing plate. Slip deficit accumulates and is released according to megathrust locking and unlocking, similarly to Govers *et al.* (2018). We impose complete locking of portions of the megathrust (asperities) and allow frictionless creep on the rest of the megathrust and on its downdip continuation, consistent with observations Scholz (1998), Ikari *et al.* (2011), and Hardebeck (2015) and inverse model results (Herman and Govers, 2020). We use five asperities, rectangular in plan view, 50 km wide, centered 200 km along-trench from each other. We focus on the earthquake and postseismic deformation following the unlocking of the central asperity. This asperity extends horizontally from a distance of 133 km to 3 km from the trench, reaching very close to it in agreement with the shallow coseismic slip observed during

the Tohoku earthquake (e.g., Meng *et al.*, 2011). The lateral asperities extend horizontally from 83 to 133 km from the trench and serve to provide megathrust coupling elsewhere along the plate margin, as observed along the Japan trench (Yamanaka and Kikuchi, 2004; Hashimoto *et al.*, 2009; Johnson *et al.*, 2016). To complete the supercycle, the two intermediate and two external lateral asperities are unlocked 20 and 40 years after the central asperity, respectively. Every asperity is unlocked every 300 years. When an asperity is unlocked, coseismic slip releases all slip deficit, except for that due to locking of the other asperities. We treat the interface between slab and asthenospheric wedge, downdip of the megathrust, to be a viscoelastic shear zone (Tichelaar and Ruff, 1993; van Keken *et al.*, 2002) with very low viscosity and the same elastic properties as the surrounding material (Govers *et al.*, 2018; Muto *et al.*, 2019). We let the shear zone accommodate relative motion at depths shallower than 80 km, where afterslip is commonly thought to occur (Diao *et al.*, 2014; Sun *et al.*, 2014; Yamagiwa *et al.*, 2015; Hu *et al.*, 2016b; Freed *et al.*, 2017). Afterslip occurs on the shear zone, immediately after the earthquake, relaxing as much as possible the elastic traction changes caused by coseismic deformation. We look at the cumulative horizontal surface motion during the first year after the earthquake, produced by the two major postseismic relaxation processes, afterslip and viscous relaxation, as well as continued plate convergence. The modeling method is described more thoroughly in the Supporting Information (Section 4.5), Section 4.5.2.

4.2   Model Results

In our first model, we immediately relock the entire ruptured asperity, from 3 km of horizontal distance from the trench down to a depth of 30 km and 133 km horizontally from the trench. Figure 4.2 shows that the trench-perpendicular surface displacement in the first year after the earthquake is directed landward next to the trench on the overriding plate, as well as on the oceanic plate. Displacement is trenchward elsewhere on the overriding plate. The amplitude of landward displacement is largest ($\sim$ 30 cm) at the trench and decreases with distance from the trench and, to a lesser extent, with along-trench distance from the central asperity. Landward displacement reaches as far as $\sim$ 45 km horizontally from the trench. Landward motion occurs throughout the oceanic domain, in the slab and sub-slab asthenosphere, and also extends to the mechanically coupled forearc directly above the shallow megathrust, including the solid surface at the tip of the overriding plate (Figure 4.4).
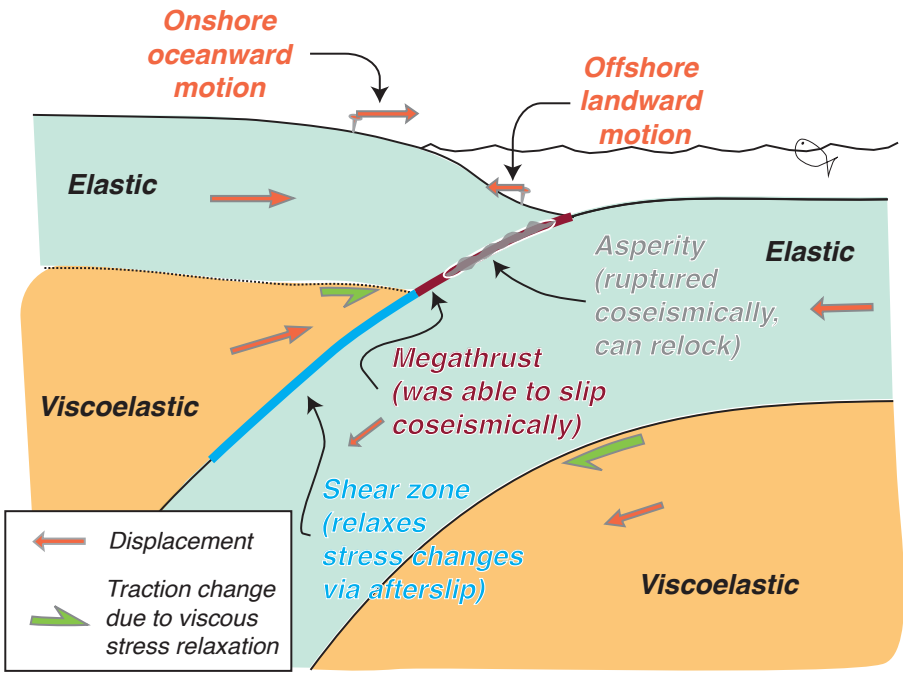
Figure 4.1 Schematic cross-section of deformation during the postseismic stage of the earthquake cycle. The subduction zone consists of two elastic lithospheric plates, separated by the megathrust interface and underlain by viscoelastic asthenospheric mantle. After the asperity ruptured during a megathrust earthquake, causing coseismically slip on the asperity and the rest of the megathrust, coseismic stress changes are relaxed. Postseismic relaxation includes bulk viscous flow in both asthenospheric domains, and rapid deep afterslip on the shear zone downdip of the megathrust. Postseismic relaxation produces additional convergent horizontal motion, with the oceanic domain moving landward and the continental/island arc domain moving landward. Landward surface motion is observed on land on the continental domain. After the 2011 Tohoku earthquake, opposing (landward) motion was observed on the seafloor at the tip of the overriding plate.

169

(a)

Distance from the trench (x) [km]

−1000   0   1000   2000

Distance alogn trench (y) [km]

1000

0

−1000

Coastline

Area shown in (b)

Landward   Oceanward   m

−0.5 −0.4 −0.3 −0.2 −0.1 0.0 0.8 1.6 2.4 3.2 4.0

Trench-perpendicular displacement

170
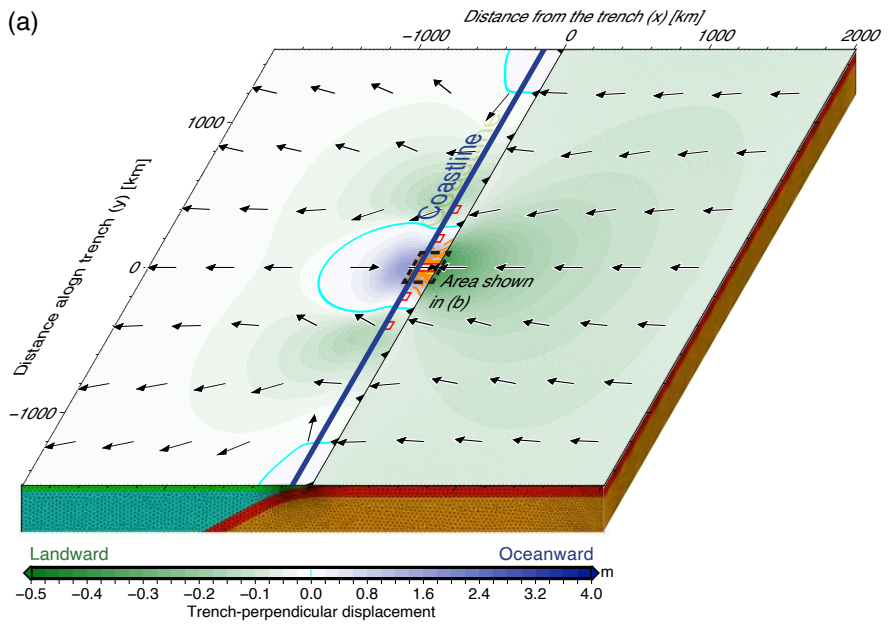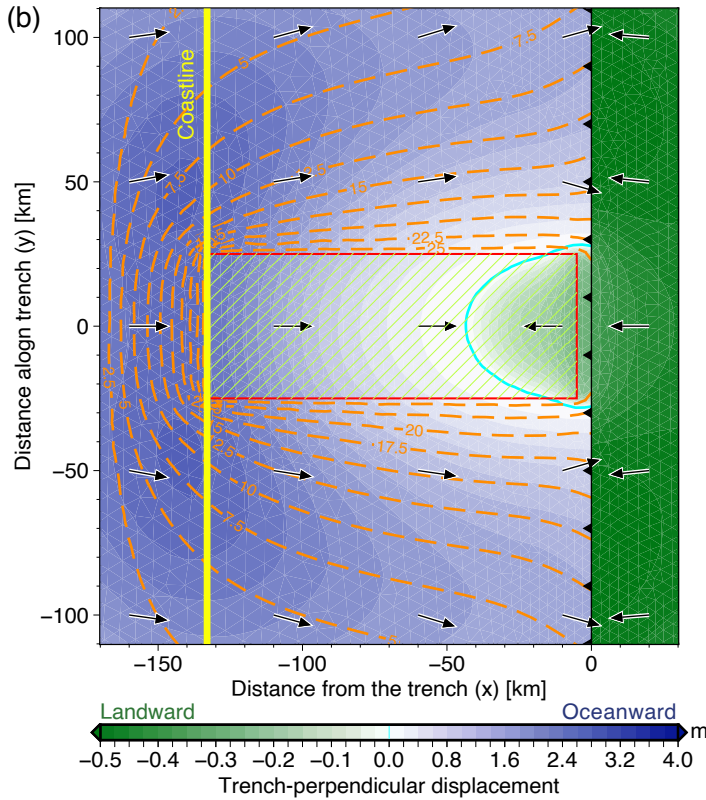
Figure 4.2 The whole asperity relocks instantly after the earthquake. Cumulative horizontal postseismic surface displacement after 1 year, assuming afterslip has ceased by then and including steady-state plate convergence. Colors show the trench-perpendicular displacement. Note that the color scale is asymmetrical, emphasizing the smaller (on the overriding plate) landward motion and de-emphasizing ocean-ward motion. Arrows show the displacement direction. The red rectangles show the surface projection of the outline of the asperities. The approximate location of the coastline, assumed to be directly above the downdip limit of the asperities is shown by the labeled line. The trench is shown as a barbed line. Dashed orange contours show coseismic displacement on the megathrust in 2.5 m increments. (a) Entire model, showing the surface motion and the overriding plate, asthenospheric wedge, subducting oceanic plate, and oceanic asthenosphere. (b) Surface motion in the central part of the model (marked and labeled in (a)). The extent of the relocked portion of the asperity, coinciding here with the whole asperity, is shown by the diagonal light green lines.

In the second experiment, we do not relock any part of the central asperity after the earthquake, letting it slip freely postseismically together with the surrounding subduction interface. Displacement of the overriding plate is trenchward in this case, with no zone of landward motion close to the trench (Figures 4.5 and 4.6).

Does landward motion of the overriding plate require relocking of the entire asperity? Twenty kilometers was sometimes considered the updip limit of the frictionally unstable, potentially seismogenic portion of the megathrust (Byrne *et al.*, 1988; Scholz, 1998). Relocking the deep part of the asperity only, between 20 and 30 km depth, is insufficient to produce landward displacement on the overriding plate during the first year after the earthquake (Figures 4.7 and 4.8). The amplitude of trenchward displacement above the asperity is nevertheless lower (i.e., less oceanward) than with no relocking whatsoever. We note that the shallow unlocked asperity and adjacent portions of the megathrust are not completely free to slip, because the mechanical continuity of both plates limits the slip that can occur in the vicinity of the relocked portion (Herman *et al.*, 2018).

Relocking of only the shallow portion of the central asperity, above 20 km depth, yields landward postseismic surface displacement at the near-trench tip of the overriding plate, at the surface (Figure 4.9) and in the subsurface (Figure 4.10). However, the maximum surface amplitude of landward displacement in the first year (~ 28 cm) and its trench-perpendicular spatial extent (~ 25 km) are both smaller (slightly and substantially, respectively) than with relocking of the whole asperity.

4.3 Discussion and Conclusions

4.3.1 Interpretation, Consistency with Previous Research, and Limitations

In our model results, the oceanic and continental domains generally have convergent, opposing motion, respectively landward and trenchward. Viscous flow and afterslip allow the shallow slab and the overriding plate in the vicinity of the rupture to further extend, continuing to release stresses accumulated during the interseismic period, as they accommodated convergence by shortening. This behavior is consistent with previously published results (Muto *et al.*, 2019; Noda *et al.*, 2018; Suito, 2017; Sun *et al.*, 2014; Yamagiwa *et al.*, 2015, e.g.,) and with the overview of deformation during megathrust earthquake cycles by (Wang *et al.*, 2012). Our results show that landward motion of the

near-trench tip of the overriding plate requires mechanical coupling of the two plates on the megathrust. We interpret the cause of this for this dependency as follows: the near-trench portion of the slab, moving landward because of postseismic viscous relaxation and afterslip, transmits its landward motion to the thin portion of overriding plate directly above it, if and only if the locked megathrust provides mechanical coupling between them. Without any coupling, the megathrust slips freely and accommodates the opposite bulk motion of the two domains.

Our conclusion regarding the link between megathrust relocking and near-trench landward motion seemingly contradicts the studies that explain the postseismic displacement following the Tohoku earthquake with no need for locking (Sun *et al.*, 2014; Sun and Wang, 2015; Yamagiwa *et al.*, 2015; Freed *et al.*, 2017; Suito, 2017; Noda *et al.*, 2018; Agata *et al.*, 2019; Muto *et al.*, 2019; Fukuda and Johnson, 2021; Dhar *et al.*, 2022), as well as the specific claim that relocking is largely irrelevant for explaining the observed offshore landward motion after the Tohoku earthquake (Watanabe *et al.*, 2014). This apparent contradiction is due to those studies considering the effect of relocking to be only the signal due to continued far-field interplate convergence in addition to megathrust locking. This follows from the use of the backslip approach (Matsu'ura and Sato, 1989) in megathrust system models. However, when studying the early postseismic period, we must consider the effect of interplate coupling, if any, interacting with the motion due to postseismic relaxation, not merely with steady-state interplate convergence.

Previous studies generally consider afterslip to consist of all postseismic slip on the interface. This includes slip that releases slip deficit and associated elastic strains that were accumulated interseismically due to megathrust locking and not released coseismically. This afterslip is often assumed to decay in time while spatially stationary (Bedford *et al.*, 2016, e.g.,). However, postseismic slip also occurs passively on unlocked portions of the megathrust as a result of interplate convergence and viscous relaxation. Since a lack of afterslip implies that the interface is locked, i.e., does not slip, we can interpret the results of previous studies in terms of relocking by observing the afterslip distributions they use. Suito (2017) does not include afterslip in his model. Sun *et al.* (2014) impose an afterslip distribution that has near-zero values in the entirety of the rupture zone. Diao *et al.* (2014) and Noda *et al.* (2018) invert exclusively onshore displacement time series into afterslip, with different slab geometries. They find no significant afterslip above a depth of 20 km below solid ground, corresponding to ~ 150 and ~ 90 km of horizontal distance from the trench, respectively, in each geometry. Yamagiwa *et al.* (2015) and Freed *et al.* (2017) invert onshore and offshore geodetic displace-

ment time series into afterslip. They find little afterslip above 25 km depth below sea level, or within ~ 150 km of horizontal distance from the trench, in the region where offshore landward displacements are observed, at any time after the earthquake, although there is some shallow afterslip immediately to the south and, in the results of Freed et al., farther north. Muto *et al.* (2019) and Dhar *et al.* (2022) invert onshore and offshore geodetic observations with stress-driven afterslip. Muto *et al.* (2019) use a two-dimensional (2D) model and find no afterslip within 130 km of horizontal distance from the trench and only very minor afterslip between 130 and 150 km. Dhar *et al.* (2022) use a 3D model and find a lack of afterslip as deep as 40 km below sea level in the central part of the rupture, and generally shallower than 30 km except for shallow afterslip to the south of the coseismic rupture zone and of the observed postseismic landward motion. In all these models, then, the shallow interface is implicitly locked postseismically at the location where landward postseismic displacement is observed geodetically and produced by the models themselves.

The peak amplitude of landward displacement in our fully relocked model results (30 cm) is smaller than that (50 cm) observed in the first year after the Tohoku earthquake and reproduced by previous modeling studies (e.g., Sun *et al.*, 2014). The reason for the smaller amplitude in our results is possibly due to the relatively limited peak amplitude of coseismic slip (27 m). Our choice of a single, uniform Maxwell viscosity also probably plays a role. In fact, previous studies find that explaining observations requires a spatially inhomogeneous, temporally variable effective viscosity, with lower short-term values particularly at the base of the slab (Sun *et al.*, 2014; Freed *et al.*, 2017; Agata *et al.*, 2018; Agata *et al.*, 2019; Muto *et al.*, 2019). However, there is no widespread agreement and best-fitting viscosities vary greatly with modeling methodology (Fukuda and Johnson, 2021). We do not aim to specifically reproduce observations and thus we do not explore different amplitudes and spatio-temporal distributions of viscosity that previous studies consider. Other models study megathrust behavior and include sophisticated methodologies that go beyond continuum mechanics and can provide insight into the specifics of the relocking mechanism. For instance, Caniven *et al.* (2021) use a discrete element method (Cundall and Strack, 1979; Morgan, 2015) that considers elastic particles interacting frictionally and indicates that megathrust relocking is controlled by fault dilatancy and contraction. Our models do not approach the full physical complexity of megathrust and bulk deformation at subduction zones. Rather, they merely establish that relocking, whatever its cause, is needed for the landward motion due to postseismic relaxation to extend from the slab to the top of the overriding plate, consistently with the results of previous modeling studies. Future work that considers additional complexity can investigate

the role of specific relaxation and relocking mechanisms and patterns in explaining specific GNSS observations. Additionally, some interpretations of the likely behavior of the megathrust in vicinity of the Tohoku rupture can be made from the need of relocking to explain the observed presence of landward motion of the offshore portion of the overriding plate.

4.3.2 Spatio-Temporal Features of Relocking and Fault Friction

The necessity of a locked megathrust implies that relocking has already occurred when landward motion is observed there. In the case of the Tohoku earthquake, the earliest, less reliable postseismic GPS-A observations indicate that landward motion was already occurring less than two months after the event (Japan Coast Guard, 2013). This implies that relocking occurred within a few weeks of the Tohoku earthquake. Rapid relocking was previously inferred from the decomposition of geodetic displacement time series after other large megathrust earthquakes, specifically the 2010 M_W 8.8 Maule (Chile) and 2007 M_W 8.0 Pisco (Peru) earthquakes (Bedford et al., 2016; Remy et al., 2016). Malservisi et al. (2015), Dixon et al. (2014) and Voss et al. (2017) invert GNSS time series into afterslip and slow-slip events (SSEs) after the much smaller 2012 M_W 7.6 Nicoya earthquake. They find that afterslip decays with a dominant characteristic timescale of 70 days (Malservisi *et al.*, 2015), after which SSEs only occur later and outside of the coseismic rupture area. Rapid relocking is thus not without support in previous research analyzing geodetic observations.

From the perspective of fault friction theories, rapid relocking of a ruptured fault asperity is compatible with the rate-and-state formulation (Dieterich, 1979; Ruina, 1983). In fact, if the asperity is understood as an unstably sliding, rate-weakening portion of the fault, near-instantaneous relocking is expected, as it immediately follows the end of the unstable sliding episode that constitutes the earthquake. According to the common understanding of rate-and-state fault friction and its role in earthquake cycle behavior, afterslip and stable creep (i.e., a lack of interseismic coupling) occur outside of the velocity-weakening, unstably sliding, seismogenic portion of the fault. This behavior can be seen, for instance, in the synoptic model of Marone (1998), the rupture simulation of Barbot *et al.* (2012) for part of the San Andreas fault, and the sophisticated numerical model of postseismic relaxation after the Tohoku earthquake of Muto *et al.* (2019).

Our model results indicate that near-trench landward postseismic motion of the overriding plate is not produced by relocking the asperity at interme-

diate depths (between 20 and 30 km below sea level), at which the Tohoku earthquake rupture is thought to have nucleated (Chu *et al.*, 2011; Agency, 2012; Freed *et al.*, 2017). Instead, relocking the uppermost portion (above 20 km depth) is necessary and sufficient for producing landward postseismic motion on the overriding plate, although with a smaller amplitude and spatial extent than when the deeper asperity is also relocked. This finding is based on our rather coarse examination, considering cumulatively all postseismic deformation during the first year after the earthquake and only one depth limit between the shallow and deeper megathrust. However, it is consistent with the results of more sophisticated simulations (Sun *et al.*, 2014; Sun and Wang, 2015; Yamagiwa *et al.*, 2015; Freed *et al.*, 2017; Noda *et al.*, 2018; Muto *et al.*, 2019), when interpreting afterslip in terms of locking or lack thereof. Our conclusions indicate that offshore geodetic observations can detect the spatio-temporal evolution of megathrust relocking, which is relevant for seismic hazard assessment and provides insights into the nature of the shallow megathrust. Our work can thus be seen as a pilot study for the SZ4D MegaArray initiative (McGuire *et al.*, 2017).

Our results show a need for rapid relocking of the shallow megathrust to produce landward postseismic motion offshore on the overriding plate. At the same time, the rapidly relocked area of a fault is generally understood to be a frictionally unstable interface. The most straightforward interpretation of these two factors together suggests that the shallow megathrust in the Tohoku region is a true asperity: unstably sliding, slipping coseismically and frictionally locked during the interseismic stage. This is in contrast with the conventional expectation that the shallow megathrust be stably sliding and unlocked interseismically (Tsuru *et al.*, 2000; Loveless and Meade, 2010). This wisdom was partly challenged by observations of unusually large slip hosted by the shallow megathrust during the Tohoku earthquake (Meng *et al.*, 2011). Herman *et al.* (2018) pointed out that slip deficit can accumulate on a low-friction portion of the megathrust passively locked by the mechanical continuity of the plates and the adjacent truly locked asperity, in a process they called pseudo-coupling. Noda and Lapusta (2013) instead proposed a shallow megathrust with frictional properties that allow it to be stably sliding interseismically and still slip substantially coseismically in a dynamic rupture simulation. These proposed mechanisms could reconcile stably sliding interseismic behavior with large coseismic slip. Furthermore, it is unclear whether the behavior of the Tohoku megathrust in the most recent earthquake reflects permanent frictional properties of the megathrust, or whether these properties changed during the last cycle.

In light of our model results, the rapid postseismic landward motion ob-

176

served offshore the Tohoku earthquake suggests that the shallow megathrust there behaved as a true asperity, at least during the last cycle, without requiring the rupture to extend beyond the unstably sliding portion. This would imply that the nature of the shallow megathrust has been misunderstood and in fact resembles that of the deeper megathrust, despite the less consolidated material and different ambient conditions at shallower depths. Alternatively, the shallow megathrust could be stably sliding and have only hosted substantial coseismic slip because of dynamic rupture effects and/or pseudo-coupling. In this case, an explanation must be provided to explain sufficient coupling of the shallow megathrust shortly after the earthquake as to produce postseismic landward motion. In general, future research should use tailored numerical models to test what degree of locking is compatible with the offshore postseismic observations, considering different spatial and temporal distributions of afterslip together with a realistic geometry and rheology.

The conclusion that rapid shallow megathrust relocking is needed to explain the offshore postseismic GPS-A observations following the Tohoku earthquake is in agreement with similar conclusions of rapid relocking drawn from onshore GNSS observations for other earthquakes, such as the 2010 Maule and 2007 Pisco earthquakes (Bedford *et al.*, 2016; Remy *et al.*, 2016). This suggests that rapid relocking is not restricted to a specific event or subduction zone. Near-trench, postseismic geodetic observations should detect evidence of shallow megathrust relocking, if any, following earthquakes producing substantial postseismic relaxation. However, a lack of postseismic landward motion, as for the first year following the 2005 Miyagi earthquake (Sato *et al.*, 2011b), does not necessarily imply a general lack of relocking. In particular, the lack of landward motion might be explained by locking being restricted to greater depths (implying along-trench variations in the frictional character of the shallow megathrust). Alternatively, it might be due to the oceanward signal of deep afterslip overcoming the small landward signal due to interplate convergence in the absence of substantial viscous relaxation, as for the M_W 7.2 Miyagi event. Additionally, the interaction of afterslip distribution with the specific local geometry might determine whether the limit of the landward signature of deep afterslip occurs on the overriding plate, as proposed by Noda *et al.* (2018).

Megathrust relocking, including at shallow depths, is needed to allow postseismic relaxation, which produce landward motion in the slab and sub-slab mantle, to also affect the near-trench tip of the overriding plate. Offshore postseismic observations can differentiate between a locked and unlocked shallow megathrust and provide evidence of very rapid (within two months) shallow relocking after the Tohoku event. Observations suggest that the shallow

177

megathrust above 20 km depth in the Tohoku region behaves as an unstably sliding asperity.

4.4 Acknowledgments and Open Research

The mesh generator program Gmsh (Geuzaine and Remacle, 2009) was used to make the finite element meshes for the numerical models. The Generic Mapping Tools (Wessel *et al.*, 2019) and Adobe Illustrator (Adobe Inc., 2019) were used for visualization.

The model output files that we used for the figures of this paper are digitally stored in the Yoda repository of Utrecht University and are available under the CC-BY license at https://doi.org/10.24416/UU01-SS41UK.

4.5 Supporting Information

4.5.1 Introduction

This supplementary material contains a more detailed description of the numerical modeling methodology used to produce the results shown in Section 4.2 (Section 4.5.2 and fig. 4.3), followed by additional visualizations (cross-sections and map views) of the results of the same models described in Section 4.2.

4.5.2 Numerical modeling method

Geometry and rheology

The model geometry and treatment of boundaries and interfaces is shown in Figure 4.3. The oceanic trench in the model is a straight line, at a depth of 12 km. The model geometry extends for 4,000 km in the trench-perpendicular horizontal (x) direction (2,012 km landward, 1,988 oceanward of it), 3,000 km in the trench-parallel (y) direction, and 338.4 km in the vertical (z) direction. The lateral dimensions were chosen so that boundaries and boundary conditions do not affect the results in our region of interest. The depth extent was chosen so as to include the low-viscosity upper asthenosphere, relaxation within which drives the bulk of postseismic viscous relaxation after the 2011 Tohoku earthquake (Agata *et al.*, 2019; Muto *et al.*, 2019).

178

The model domain includes two elastic plates—the downgoing plate, or slab, and the overriding plate—and two viscoelastic asthenospheric domains—the asthenospheric wedge and oceanic sub-slab asthenosphere. The overriding plate is 40 km thick and horizontal, with its upper surface at elevation 0, except for a linear taper down to the trench in 30 km of horizontal distance. The downgoing plate is 80 km thick, consistent with the seismologically detected depth of the lithosphere-asthenosphere boundary of various oceanic plates (Kawakatsu et al., 2009; Kumar Kawakatsu, 2011). The downgoing plate is flat for 2000 km of trench-perpendicular extent (-2000 km $\leq x \leq$ -12 km), with its upper surface at a depth of 5.7 km, consistent with the bathymetry of the western Pacific (e.g., Group, 2022). Beginning 12 km oceanward of the trench, the top of the slab follows a trench-perpendicular profile through the Slab2 model (Hayes *et al.*, 2018) across the Japan Trench.

For the sake of simplicity and to avoid having rheological complexity complicate the interpretation of results, rheological properties are uniform throughout the model. All material in the model has the same elastic parameters: Young's modulus E is 100 GPa, shear modulus G is 40 GPa, and Poisson's ratio ν is 0.25. The asthenospheric subdomains have a Maxwell viscoelastic rheology with a viscosity η of 10^{18} Pa·s during the last 200 timesteps (20 years) of the model (last postseismic phase) and 10^{19} Pa·s during the previous 3259 timesteps (3259 years). The value of 10^{18} Pa·s is generally consistent with inversion results of postseismic surface displacement following the Tohoku earthquake, although estimates vary substantially (Agata *et al.*, 2019; Muto *et al.*, 2019; Cambiotti, 2020; Fukuda and Johnson, 2021). The higher value of 10^{19} Pa·s allows us to use a timestep size Δt an order of magnitude greater (1 year) during model spin-up, and a smaller one as needed to accurately simulate postseismic relaxation with a lower viscosity. The earthquake recurrence interval for a single asperity is 300 years, while the time elapsed between the last earthquake on any asperity and the next earthquake on the middle asperity is 260 years. Given that the Maxwell relaxation time $\tau = \frac{\eta}{G}$ is 7.9 years for $\eta = 10^{19}$ Pa·s, these time intervals are over 30 times (37.9 and 32.8, respectively) the relaxation time, ensuring the coseismic and postseismic deformation of the earthquake we study (the last one in the model) are not affected by the stress changes due to previous earthquakes (Govers *et al.*, 2018; Zhu *et al.*, 2020; Wang *et al.*, 2021).

Boundaries and interfaces

The megathrust interface between the two plates is included as a discrete interface via the slippery node technique (Melosh and Williams, 1989). Five

asperities on the megathrust are fully coupled (locked) by resisting tractions during all stages of the earthquake cycle, except during the coseismic phase. The rest of the megathrust interface is left free to slip at all times, unrestricted by friction, consistently with observations (Scholz, 1998; Ikari *et al.*, 2011; Hardebeck, 2015), although the mechanical continuity of both plates restricts slip in their vicinity (Almeida *et al.*, 2018; Herman *et al.*, 2018; Herman and Govers, 2020).

Model deformation is ultimately driven by plate motion. Specifically, the overriding plate and mantle wedge are restrained by a vertical free-slip boundary condition applied at their landward, trench-parallel boundaries, while a velocity boundary condition, directed downdip and with a magnitude of 90 mm $\cdot$ yr^{-1}, is applied at the oceanward and bottom end of the slab. Free slip boundary conditions are applied at all other boundaries (in the vertical direction at the oceanward boundary of the sub-slab mantle, in two directions on the others), except for the free surface at the top.

The model asperities are rectangular in plan view, 50 km wide, centered 200 km along-trench from each other. Every asperity has a coseismic phase every 300 years. During the coseismic phase, the asperity is unlocked, removing the resisting tractions that do not allow it to slip, and the megathrust slips as much as needed to again achieve mechanical equilibrium due to the altered force balance. All the slip deficit which is accumulated interseismically due to locking of a single asperity and can be released by slip on the megathrust is thus released during the coseismic phase of that asperity, to the extent that other nearby asperities do not impede it. We focus on the earthquake and postseismic deformation due to the unlocking of the central asperity, extending horizontally from a distance of 3 km from the trench to 145 km from it. The two intermediate and two external lateral asperities have their coseismic phases 20 and 40 years later, respectively, forming a 300-year supercycle. Periodic unlocking allows the model to reach a steady state in which stresses do not vary over a whole supercycle, as the model has spun up and developed background stresses that are physically consistent with deformation. Model spin-up is necessary with a viscoelastic rheology (Hetland and Hager, 2006, e.g.,).

The downdip continuation of the megathrust is the interface between the slab and asthenospheric wedge. It is often viewed as a viscoelastic shear zone (van Keken *et al.*, 2002; Tichelaar and Ruff, 1993). We assume it to be freely creeping interseismically, not slip coseismically, and host deep afterslip, which is all afterslip in our model since slip deficit on the megathrust is released coseismically. We also assume afterslip to occur rapidly, faster than the timescale of bulk viscous relaxation in the asthenosphere. We thus incorporate the shear zone as a discrete interface and model afterslip as the slip on the interface that

relaxes coseismic stress changes as much as possible when the shear zone is allowed to slip, immediately after the coseismic phase, without increasing model time. We allow afterslip at depths shallower than 80 km, consistently with previous results (Diao *et al.*, 2014; Sun *et al.*, 2014; Yamagiwa *et al.*, 2015; Hu *et al.*, 2016b; Freed *et al.*, 2017).

The discrete contact between the slab and asthenospheric wedge beyond 80 km depth, like the discrete contact between the slab and sub-slab asthenosphere at all depths, is imposed to host differential motion at the constant interplate convergence rate ($90 \text{ mm} \cdot \text{yr}^{-1}$), driving the slab without allowing afterslip. We thus exclude from the model the steady-state asthenospheric viscous flow due to drag of the slab on the adjacent asthenosphere.

Finite element method

We use a finite element method (FEM) to solve the mechanical equilibrium equations. The FEM software package GTECTON (version2021.0; Govers *et al.*, 2018; Govers and Wortel, 1993; Govers and Wortel, 2005) uses the Portable, Extensible, Toolkit for Scientific Computation (PETSc,version 3.10.4; Balay *et al.*, 1997; Balay *et al.*, 2021a; Balay *et al.*, 2021b) and OpenMPI (version 3.0.0; Gabriel *et al.*, 2004) to solve the time-dependent problem in a massively parallel fashion. GTECTON provides highly accurate solutions to elastic and visco-elastic problems with arbitrary geometries, a true free surface, and discrete/sharp fault interfaces.

The models have a tetrahedral finite element mesh with a variable resolution, with nodes as little as 4 km apart in high-strain areas (close to the edges of the megathrust and asperities). Each model includes 789,926 nodes arranged in 4,483,391 elements. Posterior estimates of the model error (Verfürth, 1994) show that the selected mesh is dense enough to support our conclusion that our results are accurate within a few %.

Each model includes 3259 time steps with a size (Δt) of 1 year, corresponding to an initial period of 259 years (before the first coseismic phase) and 10 300-years earthquake cycles (minus one year), followed by 200 additional timesteps with a size of 0.1 years. During each coseismic phase and each afterslip phase, 10 consecutive iterations are performed to mechanically re-balance the system. After model spin-up (roughly 7 cycles), earthquake cycles are near-identical. There is a difference in surface displacement of less than a few mm between equivalent stages of one cycle and the preceding or following one, while 27 m of interplate convergence occurs over a cycle. We show results from the last postseismic period, specifically the last afterslip phase and the period with $\Delta t = 0.1$ years and $\eta = 10^{19} \text{ Pa} \cdot \text{s}$.

181

The models are run in parallel on 10 AMD EPYC 7451 24-core processors with Infiniband, using a Broyden–Fletcher–Goldfarb–Shannon solver (Fletcher, 1988).

4.5.3   Additional Figures

Figure 4.3 Schematic representation of the model domain with its geometry, spatial extent, coordinate system, main mechanical properties, and the applied boundary conditions.

Figure 4.4 The whole asperity relocks instantly after the earthquake (same model as in Figure 4.2). Cross-section through the middle of the model and of the central asperity ($y = 0$). Colors show the cumulative trench-perpendicular horizontal post-seismic displacement 1 year after the earthquake, assuming afterslip has ceased by then and including steady-state plate convergence. Arrows show the displacement direction in the plane of the figure (vertical, x–z plane). The orange line shows the along-dip extent of the part of the asperity that relocks, which consists of the whole asperity.

183

Figure 4.5 No part of the asperity relocks after the earthquake. The overall pattern of motion is similar to the fully relocked case (Figure 4.2), but with entirely ocean-ward motion in the tip of the overriding plate and greater landward motion in the immediately underlying portion of the slab (cf. Figures 4.4 and 4.6). Colors show cumulative horizontal postseismic surface displacement during the 1 year after the earthquake, including afterslip and 1 year of viscous relaxation. Graphical choices are the same as in Figure 4.2b.
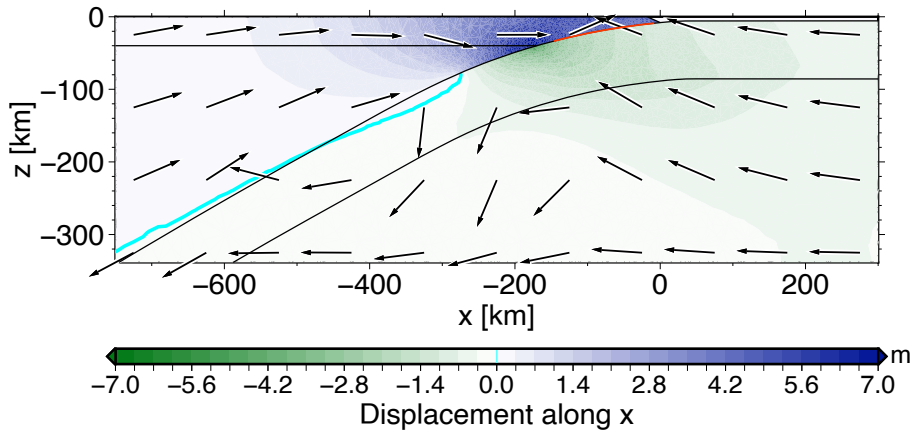
Figure 4.6 No relocking after the earthquake (same model as in Figure 4.5). Cross-section through the middle of the model and of the central asperity ($y = 0$). Colors show the cumulative trench-perpendicular horizontal postseismic displacement 1 year after the earthquake, assuming afterslip has ceased by then and including steady-state plate convergence. Arrows show the displacement direction in the plane of the figure (vertical, x–z plane). The red line shows the along-dip extent of the asperity.
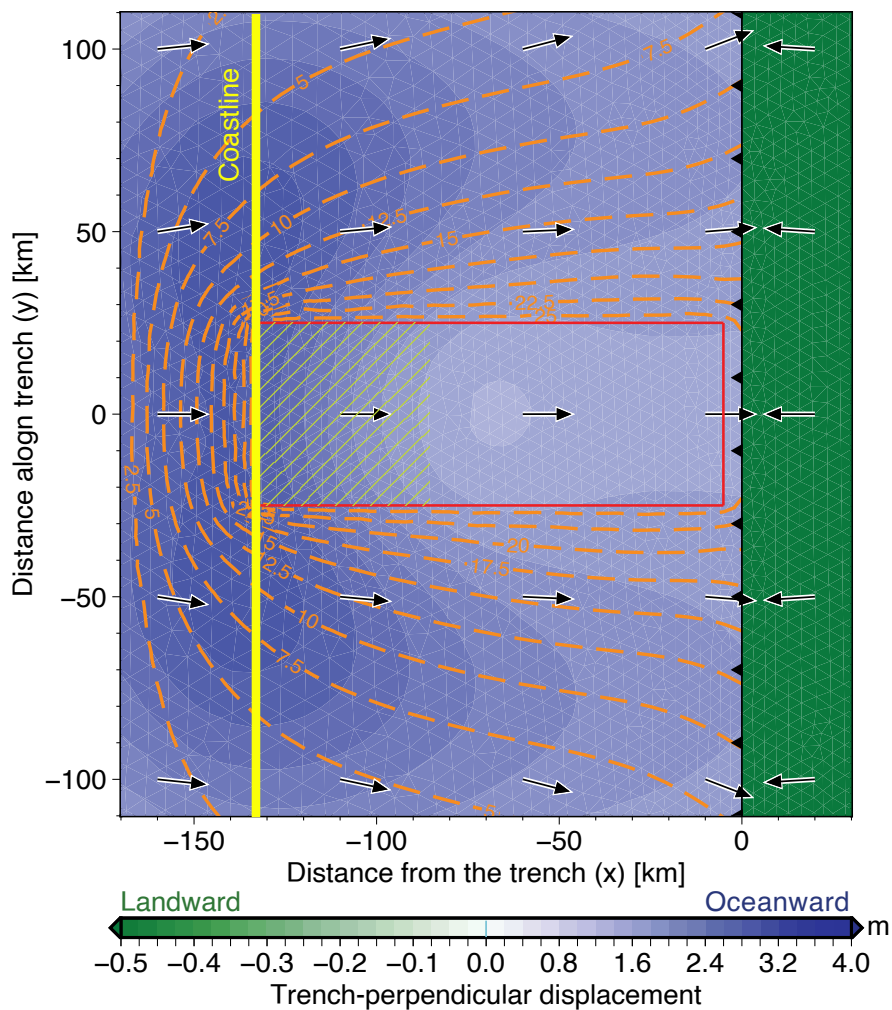
Figure 4.7 Only the deep portion of the asperity (at more than 20 km depth from the surface) relocks after the earthquake. Colors show cumulative horizontal postseismic surface displacement during the 1 year after the earthquake, including afterslip and 1 year of viscous relaxation. Graphical choices are the same as in Figure 4.2b.
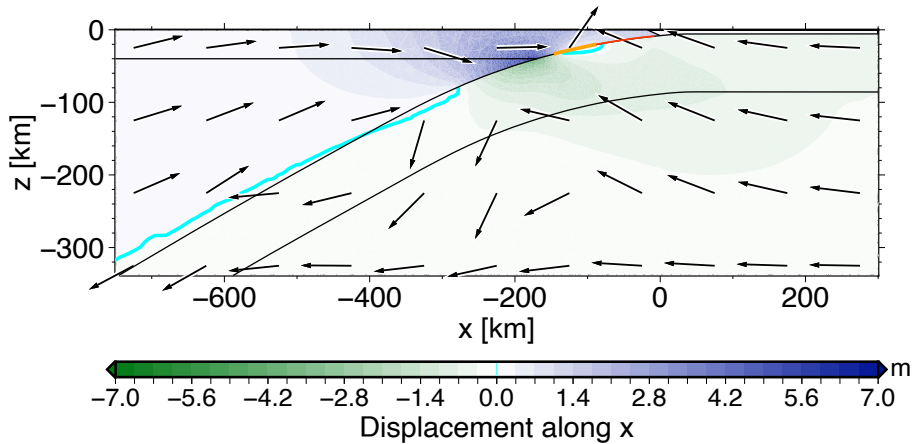
Figure 4.8 Only the deep positions of the asperity (beyond 20 km depth from the surface) relocks after the earthquake (same model as in Figure 4.7). Deep relocking produces a zone of reduced displacement immediately around it, while motion at the surface of the overriding plate is entirely landward. Cross-section through the middle of the model and of the central asperity ($y = 0$). Colors show cumulative trench-perpendicular horizontal postseismic displacement 1 year after the earthquake, assuming afterslip has ceased by then and including steady-state plate convergence. Arrows show the displacement direction in the plane of the figure (vertical, x–z plane). The red line shows the along-dip extent of the part of the asperity that does not relock. The orange line shows the extent of the part of the asperity that relocks.

Figure 4.9 Only the shallow portion of the asperity (at less than 20 km depth from the surface) relocks after the earthquake. Colors show cumulative horizontal postseismic surface displacement during the 1 year after the earthquake, including afterslip and 1 year of viscous relaxation. Graphical choices are the same as in Figure 4.2b.
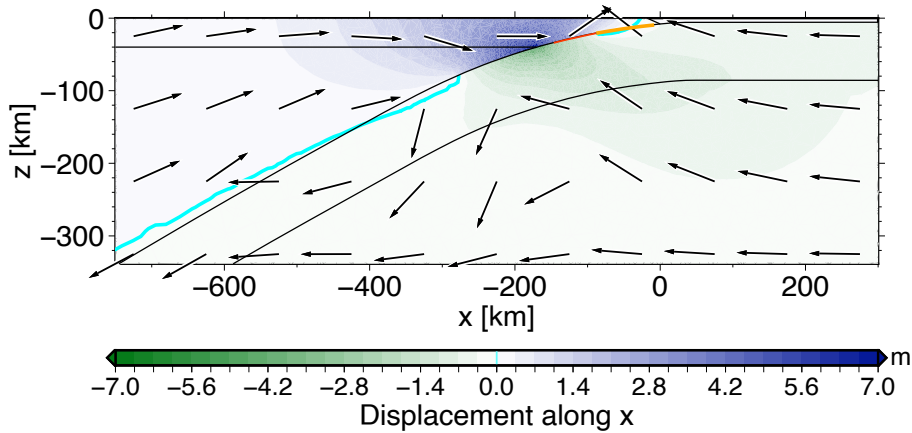
Figure 4.10 Only the shallow positions of the asperity (above 20 km depth from the surface) relocks after the earthquake (same model as in Figure 4.9). Deep relocking produces a zone of reduced displacement immediately around it, while motion at the surface of the overriding plate is entirely landward. Cross-section through the middle of the model and of the central asperity ($y = 0$). Colors show cumulative trench-perpendicular horizontal postseismic displacement 1 year after the earthquake, assuming afterslip has ceased by then and including steady-state plate convergence. Arrows show the displacement direction in the plane of the figure (vertical, x–z plane). The red line shows the along-dip extent of the part of the asperity that does not relock. The orange line shows the extent of the part of the asperity that relocks.

Summary

This thesis focuses on deformation associated with the megathrust earthquake cycle, which produces the largest earthquakes on Earth and is a key component of plate tectonics. Chapter 1 retraces the development of the current understanding of the megathrust earthquake cycle in the scientific literature. This understanding includes two largely elastic plates, one subducting beneath the other, overlying viscoelastic asthenospheric mantle. The plates accumulate strain during the near–steady state interseismic stage of the cycle due to locking of a portion of the megathrust that separates them. This strain is, to a first approximation, entirely released during the earthquake and following rapid postseismic relaxation, consisting mainly, although not solely, of afterslip and viscous flow. This understanding was built through several decades of seismological and, crucially, geodetic observations, together with various interpretations made possible by technical advances in, and clever applications of, physics-based models. Models, in this context, are systems or procedures that link properties and structures to observable quantities, and are crucial to interpreting observed deformation at subduction zones in terms of the processes and materials in the inaccessible subsurface. However, given the complexity of the Earth system, different models can approximate the same observations roughly equally well. Furthermore, more sophisticated models that can better approximate observations do not necessarily reflect better the processes and properties of the subsurface, but, at the same time, simpler models that can explain some observations do not necessarily reflect the key processes occurring throughout the earthquake cycle or over different cycles. This thesis aims to use relatively simple three-dimensional models that still capture the key processes occurring during repeated earthquake cycles, without attempting to reproduce the specific structure or properties of specific subduction zones, to address and examine possible explanations of geodetic observations from global navigation satellite systems (GNSSs) at different stages of the megathrust earthquake cycle.

Chapter 2 focuses on the interseismic, horizontal deformation of the over-

riding plate, which is in apparent contrast with observations of far-reaching coseismic displacement. We estimate the spatial patterns of GNSS velocities in South America, Southeast Asia, and northern Japan and the associated uncertainties. Interseismic velocities with respect to the overriding plate generally decrease with distance from the trench with a steep gradient up to a "hurdle", beyond which the gradient is distinctly lower and velocities are small. The hurdle is located 500–1000 km away from the trench for the trench-perpendicular velocity component, and either at the same distance or closer for the trench-parallel component. We formulate and test the hypothesis that both the interseismic hurdle and the coseismic response result from a mechanical contrast in the overriding plate. Our models show a response similar to the interseismic and coseismic observations for a compliant near-trench overriding plate and an at least 5 times stiffer overriding plate beyond the contrast. The results suggest that hurdles are more prominently expressed in observations near strongly locked megathrusts. Previous studies inferred major tectonic or geological boundaries and seismological contrasts located close to the observed hurdles in the studied overriding plates. The compliance contrast probably results from thermal, compositional and thickness contrasts and might cause the observed focusing of smaller-scale deformation like backthrusting.

Chapters 3 and 4 focus on the horizontal velocities observed after large megathrust earthquakes. Chapter 3 is concerned with the greater landward velocities, compared to before the earthquake, that were recorded onshore after 6 megathrust earthquakes in subduction zone regions adjacent to the ruptured portion. Previous explanations invoked either increased slip deficit accumulation or plate bending during postseismic relaxation, with different implications for seismic hazard. We investigate whether bending can be expected to reproduce this observed enhanced landward motion (ELM). We find that afterslip downdip of the brittle megathrust exclusively produces enhanced trenchward surface motion in the overriding plate. Viscous relaxation produces ELM when a depth limit is imposed on afterslip. This landward motion results primarily from in-plane elastic bending of the overriding plate due to trenchward viscous flow in the mantle wedge near the rupture. Modeled ELM is, however, incompatible with the observations, which are an order of magnitude greater and last longer after the earthquake. This conclusion does not significantly change when varying mantle viscosity, plate elasticity, maximum afterslip depth, earthquake size, megathrust locking outside of the rupture, or nature and location of relevant model boundaries. The observed ELM consequently appears to reflect faster slip deficit accumulation, implying a greater seismic hazard in lateral segments of the subduction zone.

In Chapter 4, we study postseismic landward motion observed, especially

offshore on the overriding plate, the section of the subduction zone that hosted a large megathrust earthquake. Geodetic observations reflect multiple post-seismic processes, including megathrust relocking. The timing of relocking and the observational constraints on it are unclear. Relocking was inferred to explain some observed landward motion that occurs within months. It was also considered unable to explain other, greater landward motion, including that off the coast of Japan beginning weeks after the 2011 Tohoku earthquake, attributed to postseismic relaxation. We argue that relocking, particularly of the shallow interface, is needed for postseismic relaxation to produce landward motion on the tip of the overriding plate. We discuss how that this finding is consistent with previous simulations that implicitly relock the megathrust where afterslip is not included. We conclude that the Tohoku megathrust re-locked within less than two months of the earthquake. This suggests that the shallow megathrust probably behaves as a true, unstably sliding asperity.

Samenvatting

Dit proefschrift gaat over de oorzaken van bodembewegingen die rondom zogenaamde subductiezones worden gemeten. Bij een subductiezone schuift een tektonische plaat onder een andere, en zinkt vervolgens in de diepere visco-elastische mantel. Op het breukvlak tussen de twee platen vinden de allerzwaarste aardbevingen plaats. GNSS-metingen laten zien dat de aardkorst ineens met vele meters kan bewegen tijdens deze aardbevingen ("co-seismisch"), en met millimeters per jaar gedurende de eeuwen tussen opeenvolgende aardbevingen ("inter-seismisch").

Hoofdstuk 1 beschrijft de ontwikkeling van de huidige kennis van de aardbevingscyclus in de wetenschappelijke literatuur. Deze kennis begrip is opgebouwd door tientallen jaren van vooral seismologische, geodetische en geologische waarnemingen in combinatie met natuurkundige modellen. Modellen zijn systemen of procedures die eigenschappen en structuren koppelen aan waarneembare groottheden. In dit proefschrift richten we ons op het omgekeerde, identificatie de processen en materiaaleigenschappen in de ontoegankelijke ondergrond die de observaties veroorzaken. We gebruiken hiervoor driedimensionale modellen waarin alleen de meest relevante processen zijn opgenomen. Regionaal detail in de aardstructuur en gesteente eigenschappen van specifieke subductiezones laten we hierbij achterwege om de oorzaken van wereldwijd waargenomen bodembewegingen te onderzoeken, met nadruk op natuurkundige consistentie in verschillende stadia van de aardbevingscyclus.

In Hoofdstuk 2 onderzoeken we horizontale deformatie van de overrijdende plaat. Het idee van de aardbevingscyclus is dat de netto deformatie na een hele cyclus ongeveer nul is. Geodetische waarnemingen suggereren echter dat de deformatie beperkt is tot ongeveer 700 km van de oceanische trog, terwijl de verplaatsingen na zeer grote aardbevingen duizenden km ver reikten. Eerst kwantificeren we ruimtelijke patronen van inter-seismische GNSS-snelheden in Zuid-Amerika, zuidoost Azië en noord Japan en de bijbehorende onzekerheden. Landwaartse snelheden ten opzichte van de stabiele overrijdende plaat nemen snel af met toenemende afstand vanaf de trog met een steile gradiënt tot

aan een "hindernis". Voorbij deze hindernis zijn de snelheden klein en vrijwel constant. Voor de trog-loodrechte snelheidscomponent bevindt de hindernis zich op 500-1000 km afstand van de trog, en op dezelfde afstand of dichterbij voor de trog-parallelle component. We formuleren en testen de hypothese dat zowel de inter-seismische hindernis als de co-seismische respons het gevolg zijn van een mechanisch contrast in de overheersende plaat. Onze modellen laten een respons zien die vergelijkbaar is met de inter- en coseismische waarnemingen voor een overrijdende plaat met een elasticiteitscontrast van minimaal 5. De resultaten suggereren dat hindernissen prominenter tot uiting komen in GPS waarnemingen in de buurt van sterk vergrendelde subductie contacten. Vergelijking met geologische gegevens suggereert dat mechanische contrasten het gevolg zijn van contrasten in geotherm, samenstelling, en/of plaatdikte.

Hoofdstuk 3 draait om recente publicaties waarin GNSS-metingen werden geïnterpreteerd die werden opgenomen direct na de grootste aardbevingen zoals de Tohoku-oki aardbeving van 2011 in Japan. Doel van het onderzoek was vooral om één van deze interpretaties te toetsen met eindige-elementenmodellen. Deze interpretatie suggereerde dat de metingen veroorzaakt waren door elastisch buigen van de overrijdende plaat. Onze modelresultaten laten inderdaad zien dat deze plaat buigt, maar ruim onvoldoende om de waarnemingen te kunnen verklaren. Met dit resultaat zijn de twee andere hypotheses, versneld zinken van de subducerende plaat of verandering van de wrijving op het plaatcontact, aannemelijker geworden.

In Hoofdstuk 4 bestuderen we postseismische landwaartse bewegingen die zijn waargenomen, met name voor de kust op de overheersende plaat, het deel van de subductiezone waar een grote megathrust-aardbeving plaatsvond. We maakten daarvoor vooral gebruik van heel bijzondere metingen, namelijk die van GNSS-stations op de zeebodem bij Japan. Zo ontdekten we dat de plaatgrensbreuk die losschoot tijdens de aardbeving binnen twee maanden alweer op vast kwam te zitten. Dit was tot nu toe onbekend. Uit onze analyse blijkt dat vooral het meest ondiepe deel van de plaatgrensbreuk weer vastzit - juist het deel dat destijds de enorme tsunami veroorzaakte. De opbouw naar alweer de volgende aardbeving en tsunami is dus vrijwel direct weer begonnen. Nu, in april 2023, is er al genoeg spanning opgebouwd voor een meter breukbeweging, en dat gaat in de nabije toekomst alleen maar meer worden. Dit suggereert dat het ondiepe plaatcontact zich gedraagt als voorspeld voor een frictionele instabiliteit.

Acknowledgements

I would like to thank, first and foremost, my supervisor Rob Govers for his continuous advice, encouragement, availability, insight, willingness to engage in useful discussion, openness to ideas and genuine academic excitement, and contributions as coauthor to all the manuscripts on which I was first author during my PhD. His decades of work on the GTECTON software package also deserves recognition, as it enabled my PhD work on a practical level. I also owe much to Matt Herman, who provided much assistance in getting started, practically, with my numerical models, as well as much insight and constructive criticism of scientific ideas, writing style, graphical choices in figures, planning of publications, and more. He also was an appreciated coauthor on one of my manuscripts. Similarly, I must thank Taco Broerse for his contributions, as coauthor. to one manuscript included in this thesis, and for his great willingness to engage in scientific discussions, from broad ideas to specific implementations. My gratitude also goes to the other coauthors of the manuscripts included in this thesis: Riccardo Riva and Celine Marsman. Their contributions to the manuscripts were very valuable.

Lukas van de Wiel deserves much recognition and gratefulness for his work on maintaining and improving the GTECTON software package and the Eejit scientific computing cluster on which I used it to run my models. I reiterate here my gratitude, expressed in greater details in the Acknowledgements of Chapters 2 to 4, to the journal editors and reviewers who contributed in forging and polishing the manuscripts contained in those chapters. I wish to thank Margot Stoete for designing the cover of this thesis. Moving away from direct assistance in conducting research and writing (and finalizing) manuscripts and this thesis, I wish to thank Marius Wouters—for his company, conversation, and support while we were sharing an office—and all the remaining members of the Tectonophysics research group in the Department of Earth Sciences of Utrecht University for their help and our conversations.

Finally, I must thank my friends in Utrecht and Rome, my former house-

mates Audrey, Adi and Giacomo, my parents Arianna and Leonardo, my sister Chiara, and (last, but definitely not the least) my girlfriend Bea, for being by my side and keeping me sane, especially during the latter half of my PhD, which largely coincided with the COVID-19 pandemic.

References

Abe, D. and S. Yoshioka (2022). "Spatiotemporal Distributions of Interplate Coupling in Tohoku, Northeast Japan, for 14 Years Prior to the 2011 Tohoku-oki Earthquake Inverted from GNSS Data". In: *Tectonophysics* 838, p. 229479. ISSN: 0040-1951. DOI: 10.1016/j.tecto.2022.229479.

Adobe Inc. (2019). *Adobe Illustrator*. Version CC 2019 (23.0.3). URL: https://adobe.com/products/illustrator.

Agata, R., S. D. Barbot, K. Fujita, M. Hyodo, T. Iinuma, R. Nakata, T. Ichimura, and T. Hori (2019). "Rapid Mantle Flow with Power-Law Creep Explains Deformation after the 2011 Tohoku Mega-Quake". In: *Nature Communications* 10.1, pp. 1–11. ISSN: 2041-1723. DOI: 10.1038/s41467-019-08984-7.

Agata, R., T. Ichimura, T. Hori, K. Hirahara, C. Hashimoto, and M. Hori (2018). "An Adjoint-Based Simultaneous Estimation Method of the Asthenosphere's Viscosity and Afterslip Using a Fast and Scalable Finite-Element Adjoint Solver". In: *Geophysical Journal International* 213.1, pp. 461–474. ISSN: 0956-540X. DOI: 10.1093/gji/ggx561.

Agency, J. M. (2012). *Information on the 2011 Great East Japan Earthquake*. URL: https://www.jma.go.jp/jma/en/2011_Earthquake/Information_on_2011_Earthquake.html.

Allen, C. R., P. St. Amand, C. F. Richter, and J. M. Nordquist (1965). "Relationship between Seismicity and Geologic Structure in the Southern California Region". In: *Bulletin of the Seismological Society of America* 55.4, pp. 753–797. ISSN: 0037-1106. DOI: 10.1785/BSSA0550040753.

Allen, C. R., T. Matsuda, and A. Okada (1970). "Relationship between Seismicity and Geologic Structure in Western Japan". In: *Earthquake Notes* 41.4 (4), p. 14. ISSN: 0012-8287. URL: https://resolver.caltech.edu/CaltechAUTHORS:20140922-153115260.

Almeida, R., E. O. Lindsey, K. Bradley, J. Hubbard, R. Mallick, and E. M. Hill (2018). "Can the Updip Limit of Frictional Locking on Megathrusts Be Detected Geodetically? Quantifying the Effect of Stress Shadows on Near-Trench Coupling". In: *Geophysical Research Letters* 45.10, pp. 4754–4763. ISSN: 1944-8007. DOI: 10.1029/2018GL077785.

Altamimi, Z., L. Métivier, and X. Collilieux (2012). "ITRF2008 Plate Motion Model". In: *Journal of Geophysical Research: Solid Earth* 117.B7. ISSN: 2156-2202. DOI: 10.1029/2011JB008930.

Altamimi, Z., X. Collilieux, and L. Métivier (2011). "ITRF2008: An Improved Solution of the International Terrestrial Reference Frame". In: *Journal of Geodesy* 85.8, pp. 457–473. ISSN: 1432-1394. DOI: 10.1007/s00190-011-0444-4.

Alvarado, A., L. Audin, J. M. Nocquet, E. Jaillard, P. Mothes, P. Jarrín, M. Segovia, F. Rolandone, and D. Cisneros (2016). "Partitioning of Oblique Convergence in the Northern Andes Subduction Zone: Migration History and the Present-Day Boundary of the North Andean Sliver in Ecuador". In: *Tectonics* 35.5, pp. 1048–1065. ISSN: 1944-9194. DOI: 10.1002/2016TC004117.

Alvarado, A. *et al.* (2014). "Active Tectonics in Quito, Ecuador, Assessed by Geomorphological Studies, GPS Data, and Crustal Seismicity". In: *Tectonics* 33.2, pp. 67–83. ISSN: 02787407. DOI: 10.1002/2012TC003224.

Alvarado, P. and V. A. Ramos (2011). "Earthquake Deformation in the Northwestern Sierras Pampeanas of Argentina Based on Seismic Waveform Modelling". In: *Journal of Geodynamics* 51.4, pp. 205–218. ISSN: 0264-3707. DOI: 10.1016/j.jog.2010.08.002.

Álvarez, O., M. Gimenez, C. Braitenberg, and A. Folguera (2012). "GOCE Satellite Derived Gravity and Gravity Gradient Corrected for Topographic Effect in the South Central Andes Region". In: *Geophysical Journal International* 190.2, pp. 941–959. ISSN: 0956-540X. DOI: 10.1111/j.1365-246X.2012.05556.x.

Ando, M. (1975). "Source Mechanisms and Tectonic Significance of Historical Earthquakes along the Nankai Trough, Japan". In: *Tectonophysics* 27.2, pp. 119–140. ISSN: 0040-1951. DOI: 10.1016/0040-1951(75)90102-X.

Aoki, I. and E. Takahashi (2004). "Density of MORB Eclogite in the Upper Mantle". In: *Physics of the Earth and Planetary Interiors.* New Developments in High-Pressure Mineral Physics and Applications to the Earth's Interior 143–144, pp. 129–143. ISSN: 0031-9201. DOI: 10.1016/j.pepi.2003.10.007.

Apel, E. V., R. Bürgmann, G. Steblov, N. Vasilenko, R. King, and A. Prytkov (2006). "Independent Active Microplate Tectonics of Northeast Asia from GPS Velocities and Block Modeling". In: *Geophysical Research Letters* 33.11, 2006GL026077. ISSN: 0094-8276, 1944-8007. DOI: 10.1029/2006GL026077.

Aron, F., J. Cembrano, F. Astudillo, R. W. Allmendinger, and G. Arancibia (2015). "Constructing Forearc Architecture over Megathrust Seismic Cycles: Geological Snapshots from the Maule Earthquake Region, Chile". In: *GSA Bulletin* 127.3-4, pp. 464–479. ISSN: 0016-7606. DOI: 10.1130/B31125.1.

Audet, P. and R. Bürgmann (2011). "Dominant Role of Tectonic Inheritance in Supercontinent Cycles". In: *Nature Geoscience* 4.3 (3), pp. 184–187. ISSN: 1752-0908. DOI: 10.1038/ngeo1080.

Azúa, B. M., C. DeMets, and T. Masterlark (2002). "Strong Interseismic Coupling, Fault Afterslip, and Viscoelastic Flow before and after the Oct. 9, 1995 Colima-Jalisco Earthquake: Continuous GPS Measurements from Colima, Mexico". In: *Geophysical Research Letters* 29.8, pp. 122-1-122–4. ISSN: 1944-8007. DOI: 10.1029/2002GL014702.

Balay, S., W. D. Gropp, L. C. McInnes, and B. F. Smith (1997). "Efficient Management of Parallelism in Object Oriented Numerical Software Libraries". In: *Modern Software Tools in Scientific Computing.* Ed. by E. Arge, A. M. Bruaset, and H. P. Langtangen. Birkhäuser Press, pp. 163–202.

Balay, S. *et al.* (2021a). *PETSc Web Page.* URL: https://petsc.org/.

Balay, S. *et al.* (2021b). *PETSc/TAO Users Manual.* ANL-21/39 - Revision 3.16. Argonne National Laboratory.

Baldis, B., M. Beresi, O. Bordonaro, and A. Vaca (1982). "Síntesis evolutiva de la Precordillera Argentina". In: *Actas.* 5 Congreso Latinoamericano

de geología. Vol. 4. Buenos Aires, Argentina: Servicio Geológico Nacional, Subsecretaría de Minería, pp. 399–445.

Banerjee, P., F. Pollitz, and R. Bürgmann (2005). "The Size and Duration of the Sumatra-Andaman Earthquake from Far-Field Static Offsets". In: *Science* 308.5729, pp. 1769–1772. DOI: 10.1126/science.1113746.

Banerjee, P., F. Pollitz, B. Nagarajan, and R. Bürgmann (2007). "Coseismic Slip Distributions of the 26 December 2004 Sumatra–Andaman and 28 March 2005 Nias Earthquakes from Gps Static Offsets". In: *Bulletin of the Seismological Society of America* 97 (1A), S86–S102. ISSN: 0037-1106. DOI: 10.1785/0120050609.

Barber, A. J. (2000). "The Origin of the Woyla Terranes in Sumatra and the Late Mesozoic Evolution of the Sundaland Margin". In: *Journal of Asian Earth Sciences* 18.6, pp. 713–738. ISSN: 1367-9120. DOI: 10.1016/S1367-9120(00)00024-9.

Barber, A. J., M. J. Crow, and J. Milsom (2005). *Sumatra: Geology, Resources and Tectonic Evolution*. Geological Society of London. 308 pp. ISBN: 978-1-86239-180-2. Google Books: NlvUlh1UqwkC.

Barbot, S., N. Lapusta, and J.-P. Avouac (2012). "Under the Hood of the Earthquake Machine: Toward Predictive Modeling of the Seismic Cycle". In: *Science* 336.6082, pp. 707–710. ISSN: 0036-8075, 1095-9203. DOI: 10.1126/science.1218796. pmid: 22582259.

Bathe, K.-J. and E. L. Wilson (1976). *Numerical Methods in Finite Element Analysis*. Prentice-Hall Civil Engineering and Engineering Mechanics Series. Englewood Cliffs, N.J.: Prentice-Hall. xv, 528. ISBN: 978-0-13-627190-1.

Bedford, J., M. Moreno, S. Li, O. Oncken, J. C. Baez, M. Bevis, O. Heidbach, and D. Lange (2016). "Separating Rapid Relocking, Afterslip, and Viscoelastic Relaxation: An Application of the Postseismic Straightening Method to the Maule 2010 cGPS". In: *Journal of Geophysical Research: Solid Earth* 121.10, pp. 7618–7638. ISSN: 2169-9356. DOI: 10.1002/2016JB013093.

Behr, W. M. and R. Bürgmann (2021). "What's down There? The Structures, Materials and Environment of Deep-Seated Slow Slip and Tremor". In: *Philosophical Transactions of the Royal Society A: Mathematical, Physical*

and Engineering Sciences 379.2193, p. 20200218. DOI: 10.1098/rsta.2020.0218.

Benioff, H. (1954). "Orogenesis and Deep Crustal Structure—Additional Evidence from Seismology". In: *Geological Society of America Bulletin* 65.5, p. 385. ISSN: 0016-7606. DOI: 10.1130/0016-7606(1954)65[385:OADCSE]2.0.CO;2.

Bevis, M., E. Kendrick, R. Smalley, B. Brooks, R. Allmendinger, and B. Isacks (2001). "On the Strength of Interplate Coupling and the Rate of Back Arc Convergence in the Central Andes: An Analysis of the Interseismic Velocity Field". In: *Geochemistry, Geophysics, Geosystems* 2.11. ISSN: 1525-2027. DOI: 10.1029/2001GC000198.

Bird, P. (2003). "An Updated Digital Model of Plate Boundaries". In: *Geochemistry, Geophysics, Geosystems* 4.3. ISSN: 1525-2027. DOI: 10.1029/2001GC000252.

Bischke, R. E. (1974). "A Model of Convergent Plate Margins Based on the Recent Tectonics of Shikoku, Japan". In: *Journal of Geophysical Research (1896-1977)* 79.32, pp. 4845–4857. ISSN: 2156-2202. DOI: 10.1029/JB079i032p04845.

Blacic, J. D. and J. M. Christie (1984). "Plasticity and Hydrolytic Weakening of Quartz Single Crystals". In: *Journal of Geophysical Research: Solid Earth* 89.B6, pp. 4223–4239. ISSN: 2156-2202. DOI: 10.1029/JB089iB06p04223.

Blewitt, G., C. Kreemer, W. C. Hammond, and J. Gazeaux (2016). "MIDAS Robust Trend Estimator for Accurate GPS Station Velocities without Step Detection". In: *Journal of Geophysical Research: Solid Earth* 121.3, pp. 2054–2068. ISSN: 2169-9356. DOI: 10.1002/2015JB012552.

Bock, Y., L. Prawirodirdjo, J. F. Genrich, C. W. Stevens, R. McCaffrey, C. Subarya, S. S. O. Puntodewo, and E. Calais (2003). "Crustal Motion in Indonesia from Global Positioning System Measurements". In: *Journal of Geophysical Research: Solid Earth* 108.B8. ISSN: 2156-2202. DOI: 10.1029/2001JB000324.

Bott, M. H. P. and D. S. Dean (1973). "Stress Diffusion from Plate Boundaries". In: *Nature* 243.5406 (5406), pp. 339–341. ISSN: 1476-4687. DOI: 10.1038/243339a0.

Boulze, H., L. Fleitout, E. Klein, and C. Vigny (2022). "Post-Seismic Motion after 3 Chilean Megathrust Earthquakes: A Clue for a Linear Astheno-

spheric Viscosity". In: *Geophysical Journal International*, ggac255. ISSN: 0956-540X. DOI: 10.1093/gji/ggac255.

Broerse, T., R. Riva, W. Simons, R. Govers, and B. Vermeersen (2015). "Post-seismic GRACE and GPS Observations Indicate a Rheology Contrast above and below the Sumatra Slab". In: *Journal of Geophysical Research: Solid Earth* 120.7, pp. 5343–5361. ISSN: 2169-9356. DOI: 10.1002/2015JB011951.

Brooks, B. A., M. Bevis, R. Smalley, E. Kendrick, R. Manceda, E. Lauría, R. Maturana, and M. Araujo (2003). "Crustal Motion in the Southern Andes (26°–36°S): Do the Andes Behave like a Microplate?" In: *Geochemistry, Geophysics, Geosystems* 4.10. ISSN: 1525-2027. DOI: 10.1029/2003GC000505.

Brooks, B. A. *et al.* (2011). "Orogenic-Wedge Deformation and Potential for Great Earthquakes in the Central Andean Backarc". In: *Nature Geoscience* 4.6 (6), pp. 380–383. ISSN: 1752-0908. DOI: 10.1038/ngeo1143.

Brown, L., K. Wang, and T. Sun (2015). "Static Stress Drop in the Mw 9 Tohoku-oki Earthquake: Heterogeneous Distribution and Low Average Value". In: *Geophysical Research Letters* 42.24, pp. 10, 595–10, 600. ISSN: 1944-8007. DOI: 10.1002/2015GL066361.

Bürgmann, R. and G. Dresen (2008). "Rheology of the Lower Crust and Upper Mantle: Evidence from Rock Mechanics, Geodesy, and Field Observations". In: *Annual Review of Earth and Planetary Sciences* 36.1, pp. 531–567. DOI: 10.1146/annurev.earth.36.031207.124326.

Burov, E. B. and M. Diament (1995). "The Effective Elastic Thickness (T e) of Continental Lithosphere: What Does It Really Mean?" In: *Journal of Geophysical Research: Solid Earth* 100.B3, pp. 3905–3927. ISSN: 2156-2202. DOI: 10.1029/94JB02770.

Byrne, D. E., D. M. Davis, and L. R. Sykes (1988). "Loci and Maximum Size of Thrust Earthquakes and the Mechanics of the Shallow Region of Subduction Zones". In: *Tectonics* 7.4, pp. 833–857. ISSN: 1944-9194. DOI: 10.1029/TC007i004p00833.

Cambiotti, G. (2020). "Joint Estimate of the Coseismic 2011 Tohoku Earthquake Fault Slip and Post-Seismic Viscoelastic Relaxation by GRACE Data Inversion". In: *Geophysical Journal International* 220.2, pp. 1012–1022. ISSN: 0956-540X. DOI: 10.1093/gji/ggz485.

Caniven, Y., J. K. Morgan, and D. G. Blank (2021). "The Role of Along-Fault Dilatancy in Fault Slip Behavior". In: *Journal of Geophysical Research: Solid Earth* 126.11, e2021JB022310. ISSN: 2169-9356. DOI: 10.1029/2021JB022310.

Chinnery, M. A. (1961). "The Deformation of the Ground around Surface Faults". In: *Bulletin of the Seismological Society of America* 51.3, pp. 355–372. ISSN: 0037-1106. DOI: 10.1785/BSSA0510030355.

Chlieh, M., J. P. Avouac, K. Sieh, D. H. Natawidjaja, and J. Galetzka (2008). "Heterogeneous Coupling of the Sumatran Megathrust Constrained by Geodetic and Paleogeodetic Measurements". In: *Journal of Geophysical Research: Solid Earth* 113.B5. ISSN: 2156-2202. DOI: 10.1029/2007JB004981.

Chlieh, M., J. B. De Chabalier, J. C. Ruegg, R. Armijo, R. Dmowska, J. Campos, and K. L. Feigl (2004). "Crustal Deformation and Fault Slip during the Seismic Cycle in the North Chile Subduction Zone, from GPS and InSAR Observations". In: *Geophysical Journal International* 158.2, pp. 695–711. ISSN: 0956-540X. DOI: 10.1111/j.1365-246X.2004.02326.x.

Chopra, P. N. and M. S. Paterson (1984). "The Role of Water in the Deformation of Dunite". In: *Journal of Geophysical Research: Solid Earth* 89.B9, pp. 7861–7876. ISSN: 2156-2202. DOI: 10.1029/JB089iB09p07861.

Christensen, N. I. (1996). "Poisson's Ratio and Crustal Seismology". In: *Journal of Geophysical Research: Solid Earth* 101.B2, pp. 3139–3156. ISSN: 2156-2202. DOI: 10.1029/95JB03446.

Chu, R., S. Wei, D. V. Helmberger, Z. Zhan, L. Zhu, and H. Kanamori (2011). "Initiation of the Great Mw 9.0 Tohoku–Oki Earthquake". In: *Earth and Planetary Science Letters* 308.3, pp. 277–283. ISSN: 0012-821X. DOI: 10.1016/j.epsl.2011.06.031.

Chulick, G. S., S. Detweiler, and W. D. Mooney (2013). "Seismic Structure of the Crust and Uppermost Mantle of South America and Surrounding Oceanic Basins". In: *Journal of South American Earth Sciences* 42, pp. 260–276. ISSN: 0895-9811. DOI: 10.1016/j.jsames.2012.06.002.

Cisneros, D. and J. Nocquet (2011). "Campo de velocidades del Ecuador, obtenido a través de mediciones de campañes GPS de los ultimos 15 años y medidas de une red GPS permanente". In: URL: https://www.sirgas.org/fileadmin/docs/Cisneros_2010_Campo_velocidades_Ecuador_web.pdf.

Cohen, S. C. and J. T. Freymueller (1997). "Deformation of the Kenai Peninsula, Alaska". In: *Journal of Geophysical Research: Solid Earth* 102.B9, pp. 20479–20487. ISSN: 2156-2202. DOI: 10.1029/97JB01513.

Conder, J. A. (2005). "A Case for Hot Slab Surface Temperatures in Numerical Viscous Flow Models of Subduction Zones with an Improved Fault Zone Parameterization". In: *Physics of the Earth and Planetary Interiors.* Thermal Structure and Dynamics of Subduction Zones: Insights from Observations and Modeling 149.1, pp. 155–164. ISSN: 0031-9201. DOI: 10.1016/j.pepi.2004.08.018.

Corbi, F., J. Bedford, P. Poli, F. Funiciello, and Z. Deng (2022). "Probing the Seismic Cycle Timing with Coseismic Twisting of Subduction Margins". In: *Nature Communications* 13.1 (1), p. 1911. ISSN: 2041-1723. DOI: 10.1038/s41467-022-29564-2.

Cundall, P. A. and O. D. L. Strack (1979). "A Discrete Numerical Model for Granular Assemblies". In: *Géotechnique* 29.1, pp. 47–65. ISSN: 0016-8505. DOI: 10.1680/geot.1979.29.1.47.

D'Acquisto, M., M. W. Herman, R. E. M. Riva, and R. Govers (2023). "Can Plate Bending Explain the Observed Faster Landward Motion of Lateral Regions of the Subduction Zone After Major Megathrust Earthquakes?" In: *Journal of Geophysical Research: Solid Earth* 128.3. ISSN: 2169-9313, 2169-9356. DOI: 10.1029/2022JB025431.

D'Acquisto, M. and R. Govers (2023). "Offshore Landward Motion Shortly After a Subduction Earthquake Implies Rapid Relocking of the Shallow Megathrust". In: *Geophysical Research Letters* 50.1. ISSN: 0094-8276, 1944-8007. DOI: 10.1029/2022GL101638.

Delouis, B., J.-M. Nocquet, and M. Vallée (2010). "Slip Distribution of the February 27, 2010 Mw = 8.8 Maule Earthquake, Central Chile, from Static and High-Rate GPS, InSAR, and Broadband Teleseismic Data". In: *Geophysical Research Letters* 37.17. ISSN: 1944-8007. DOI: 10.1029/2010GL043899.

Dhar, S., J. Muto, Y. Ito, S. Miura, J. D. P. Moore, Y. Ohta, and T. Iinuma (2022). "Along-Arc Heterogeneous Rheology Inferred from Post-Seismic Deformation of the 2011 Tohoku-oki Earthquake". In: *Geophysical Journal International* 230.1, pp. 202–215. ISSN: 0956-540X. DOI: 10.1093/gji/ggac063.

Diao, F., X. Xiong, R. Wang, Y. Zheng, T. R. Walter, H. Weng, and J. Li (2014). "Overlapping Post-Seismic Deformation Processes: Afterslip and Viscoelastic Relaxation Following the 2011 Mw 9.0 Tohoku (Japan) Earthquake". In: *Geophysical Journal International* 196.1, pp. 218–229. ISSN: 0956-540X. DOI: 10.1093/gji/ggt376.

Dickinson, W. R. (1970). "Global Tectonics". In: *Science*. DOI: 10.1126/science.168.3936.1250.

Dieterich, J. H. (1979). "Modeling of Rock Friction: 1. Experimental Results and Constitutive Equations". In: *Journal of Geophysical Research: Solid Earth* 84.B5, pp. 2161–2168. ISSN: 2156-2202. DOI: 10.1029/JB084iB05p02161.

Dietz, R. S. and J. C. Holden (1970). "Reconstruction of Pangaea: Breakup and Dispersion of Continents, Permian to Present". In: *Journal of Geophysical Research (1896-1977)* 75.26, pp. 4939–4956. ISSN: 2156-2202. DOI: 10.1029/JB075i026p04939.

Dixon, J. E., T. H. Dixon, D. R. Bell, and R. Malservisi (2004). "Lateral Variation in Upper Mantle Viscosity: Role of Water". In: *Earth and Planetary Science Letters* 222.2, pp. 451–467. ISSN: 0012-821X. DOI: 10.1016/j.epsl.2004.03.022.

Dixon, T. H. (1993). "GPS Measurement of Relative Motion of the Cocos and Caribbean Plates and Strain Accumulation across the Middle America Trench". In: *Geophysical Research Letters* 20.20, pp. 2167–2170. ISSN: 1944-8007. DOI: 10.1029/93GL02415.

Dixon, T. H., Y. Jiang, R. Malservisi, R. McCaffrey, N. Voss, M. Protti, and V. Gonzalez (2014). "Earthquake and Tsunami Forecasts: Relation of Slow Slip Events to Subsequent Earthquake Rupture". In: *Proceedings of the National Academy of Sciences* 111.48, pp. 17039–17044. DOI: 10.1073/pnas.1412299111.

Dragert, H. and R. D. Hyndman (1995). "Continuous GPS Monitoring of Elastic Strain in the Northern Cascadia Subduction Zone". In: *Geophysical Research Letters* 22.7, pp. 755–758. ISSN: 1944-8007. DOI: 10.1029/95GL00469.

Dragert, H., R. D. Hyndman, G. C. Rogers, and K. Wang (1994). "Current Deformation and the Width of the Seismogenic Zone of the Northern Cascadia Subduction Thrust". In: *Journal of Geophysical Research: Solid Earth* 99.B1, pp. 653–668. ISSN: 2156-2202. DOI: 10.1029/93JB02516.

Drewes, H. and O. Heidbach (2012). "The 2009 Horizontal Velocity Field for South America and the Caribbean". In: *Geodesy for Planet Earth*. Ed. by S. Kenyon, M. C. Pacino, U. Marti, S. Kenyon, M. C. Pacino, and U. Marti. Vol. 136. Berlin, Heidelberg, pp. 657–664. ISBN: 978-3-642-20337-4. URL: http://link.springer.com/10.1007/978-3-642-20338-1_81.

Driscoll, T. A. (2002). *Schwarz-Christoffel Mapping*. 1st edition. Cambridge ; New York: Cambridge University Press. 150 pp. ISBN: 978-0-521-80726-5.

Dziewonski, A. M. (1984). "Mapping the Lower Mantle: Determination of Lateral Heterogeneity in P Velocity up to Degree and Order 6". In: *Journal of Geophysical Research: Solid Earth* 89.B7, pp. 5929–5952. ISSN: 2156-2202. DOI: 10.1029/JB089iB07p05929.

Dziewonski, A. M. and D. L. Anderson (1981). "Preliminary Reference Earth Model". In: *Physics of the Earth and Planetary Interiors* 25.4, pp. 297–356. ISSN: 0031-9201. DOI: 10.1016/0031-9201(81)90046-7.

(1969). In: *The Application of Modern Physics to the Earth and Planetary Interiors*. Ed. by W. M. Elsasser and S. K. Runcorn. N. A. T. O. Advanced Study Institute. London: Wiley-Interscience, p. 223. ISBN: 978-0-471-74505-1.

Fedotov, S. A. (1965). "Regularities of the Distribution of Strong Earthquakes in Kamchatka, the Kuril Islands, and Northeastern Japan". In: *Transactions () of the Academy of Sciences of the USSR. Earth Sciences Sections* 36, pp. 66–93. URL: https://cir.nii.ac.jp/crid/1574231873833395328.

Fialko, Y. (2004). "Evidence of Fluid-Filled Upper Crust from Observations of Postseismic Deformation Due to the 1992 Mw7.3 Landers Earthquake". In: *Journal of Geophysical Research: Solid Earth* 109.B8. ISSN: 2156-2202. DOI: 10.1029/2004JB002985.

Fitch, T. J. and C. H. Scholz (1971). "Mechanism of Underthrusting in Southwest Japan: A Model of Convergent Plate Interactions". In: *Journal of Geophysical Research (1896-1977)* 76.29, pp. 7260–7292. ISSN: 2156-2202. DOI: 10.1029/JB076i029p07260.

Fletcher, R. (1988). *Practical Methods of Optimization*. Wiley. 450 pp. ISBN: 978-0-471-91547-8. Google Books: gz0BzQEACAAJ.

Flück, P., R. D. Hyndman, and K. Wang (1997). "Three-Dimensional Dislocation Model for Great Earthquakes of the Cascadia Subduction Zone".

In: *Journal of Geophysical Research: Solid Earth* 102.B9, pp. 20539–20550. ISSN: 2156-2202. DOI: 10.1029/97JB01642.

Fouedjio, F. and S. Séguret (2016). "Predictive Geological Mapping Using Closed-Form Non-stationary Covariance Functions with Locally Varying Anisotropy: Case Study at El Teniente Mine (Chile)". In: *Natural Resources Research* 25.4, pp. 431–443. ISSN: 1520-7439, 1573-8981. DOI: 10.1007/s11053-016-9293-4.

Freed, A. M., A. Hashima, T. W. Becker, D. A. Okaya, H. Sato, and Y. Hatanaka (2017). "Resolving Depth-Dependent Subduction Zone Viscosity and Afterslip from Postseismic Displacements Following the 2011 Tohoku-oki, Japan Earthquake". In: *Earth and Planetary Science Letters* 459, pp. 279–290. ISSN: 0012821X. DOI: 10.1016/j.epsl.2016.11.040.

Freymueller, J. T., S. C. Cohen, and H. J. Fletcher (2000). "Spatial Variations in Present-Day Deformation, Kenai Peninsula, Alaska, and Their Implications". In: *Journal of Geophysical Research: Solid Earth* 105.B4, pp. 8079–8101. ISSN: 2156-2202. DOI: 10.1029/1999JB900388.

Freymueller, J. T. and J. N. Kellogg (1993). "Plate Motions and Active Crustal Deformation in the North Andean Region Measured with the Global Positioning System". In: *Recent Geodetic and Gravimetric Research in Latin America*. Ed. by W. Torge, A. G. Fletcher, and J. G. Tanner. International Association of Geodesy Symposia. Berlin, Heidelberg: Springer, pp. 131–145. ISBN: 978-3-642-88055-1. DOI: 10.1007/978-3-642-88055-1_11.

Freymueller, J. T., H. Woodard, S. C. Cohen, R. Cross, J. Elliott, C. F. Larsen, S. Hreinsdóttir, and C. Zweck (2008). "Active Deformation Processes in Alaska, Based on 15 Years of GPS Measurements". In: *Active Tectonics and Seismic Potential of Alaska*. Ed. by J. T. Freymueller, P. J. Haeussler, R. L. Wesson, and G. Ekström. 1st ed. Vol. 179. Geophysical Monograph Ser. Washington, D. C: American Geophysical Union, pp. 1–42. ISBN: 978-0-87590-444-3. DOI: 10.1029/179GM02.

Fujiwara, T., S. Kodaira, T. No, Y. Kaiho, N. Takahashi, and Y. Kaneda (2011). "The 2011 Tohoku-Oki Earthquake: Displacement Reaching the Trench Axis". In: *Science* 334.6060, pp. 1240–1240. DOI: 10.1126/science.1211554.

Fukuda, J. and K. M. Johnson (2021). "Bayesian Inversion for a Stress-Driven Model of Afterslip and Viscoelastic Relaxation: Method and Application

to Postseismic Deformation Following the 2011 MW 9.0 Tohoku-Oki Earthquake". In: *Journal of Geophysical Research: Solid Earth* 126.5, e2020JB021620. ISSN: 2169-9356. DOI: 10.1029/2020JB021620.

Furlong, K. P. and R. Govers (1999). "Ephemeral Crustal Thickening at a Triple Junction:The Mendocino Crustal Conveyor". In: *Geology* 27.2, pp. 127–130. ISSN: 0091-7613. DOI: 10.1130/0091-7613(1999)027<0127:ECTAAT>2.3.CO;2.

Gabriel, E. *et al.* (2004). "Open MPI: Goals, Concept, and Design of a Next Generation MPI Implementation". In: *Recent Advances in Parallel Virtual Machine and Message Passing Interface*. Ed. by D. Kranzlmüller, P. Kacsuk, and J. Dongarra. Red. by D. Hutchison *et al.* Vol. 3241. Lecture Notes in Computer Science. Berlin, Heidelberg: Springer Berlin Heidelberg, pp. 97–104. ISBN: 978-3-540-30218-6. DOI: 10.1007/978-3-540-30218-6_19.

Gagnon, K., C. D. Chadwell, and E. Norabuena (2005). "Measuring the Onset of Locking in the Peru–Chile Trench with GPS and Acoustic Measurements". In: *Nature* 434.7030, pp. 205–208. ISSN: 0028-0836, 1476-4687. DOI: 10.1038/nature03412.

Gahalaut, V. K., J. K. Catherine, S. Jade, R. Gireesh, D. C. Gupta, M. Narsaiah, A. Ambikapathy, A. Bansal, and R. K. Chadha (2008a). "No Evidence of Unusually Large Postseismic Deformation in Andaman Region Immediately after 2004 Sumatra-Andaman Earthquake". In: *Geophysical Research Letters* 35.10. ISSN: 1944-8007. DOI: 10.1029/2008GL033704.

Gahalaut, V. K. *et al.* (2008b). "GPS Measurements of Postseismic Deformation in the Andaman-Nicobar Region Following the Giant 2004 Sumatra-Andaman Earthquake". In: *Journal of Geophysical Research: Solid Earth* 113.B8. ISSN: 2156-2202. DOI: 10.1029/2007JB005511.

Genrich, J. F., Y. Bock, R. McCaffrey, L. Prawirodirdjo, C. W. Stevens, S. S. O. Puntodewo, C. Subarya, and S. Wdowinski (2000). "Distribution of Slip at the Northern Sumatran Fault System". In: *Journal of Geophysical Research: Solid Earth* 105.B12, pp. 28327–28341. ISSN: 01480227. DOI: 10.1029/2000JB900158.

Gerya, T. V. and F. I. Meilick (2011). "Geodynamic Regimes of Subduction under an Active Margin: Effects of Rheological Weakening by Fluids and Melts". In: *Journal of Metamorphic Geology* 29.1, pp. 7–31. ISSN: 1525-1314. DOI: 10.1111/j.1525-1314.2010.00904.x.

Geuzaine, C. and J.-F. Remacle (2009). "Gmsh: A 3-D Finite Element Mesh Generator with Built-in Pre- and Post-Processing Facilities". In: *International Journal for Numerical Methods in Engineering* 79.11, pp. 1309–1331. ISSN: 1097-0207. DOI: 10.1002/nme.2579.

Gombert, B., Z. Duputel, R. Jolivet, M. Simons, J. Jiang, C. Liang, E. J. Fielding, and L. Rivera (2018). "Strain Budget of the Ecuador–Colombia Subduction Zone: A Stochastic View". In: *Earth and Planetary Science Letters* 498, pp. 288–299. ISSN: 0012-821X. DOI: 10.1016/j.epsl.2018.06.046.

Götze, H.-J. and R. Mahatsente (2010). "GOCE Gravity Gradiometry: Examples of Gravity Field Interpretation from the South-Central American Active Continental Margins". In: *Airborne Gravity 2010*. Ed. by R. J. L. Lane. ASEG-PESA, pp. 87–90. ISBN: 978-1-921781-17-9. URL: https://www.researchgate.net/publication/265164440_GOCE_gravity_gradiometry_Examples_of_gravity_field_interpretation_from_the_South-Central_American_active_continental_margins.

Govers, R., K. P. Furlong, L. van de Wiel, M. W. Herman, and T. Broerse (2018). "The Geodetic Signature of the Earthquake Cycle at Subduction Zones: Model Constraints on the Deep Processes". In: *Reviews of Geophysics* 56.1, pp. 6–49. ISSN: 8755-1209. DOI: 10.1002/2017RG000586.

Govers, R. and P. T. Meijer (2001). "On the Dynamics of the Juan de Fuca Plate". In: *Earth and Planetary Science Letters* 189.3, pp. 115–131. ISSN: 0012-821X. DOI: 10.1016/S0012-821X(01)00360-0.

Govers, R. and R. Wortel (1993). "Initiation of Asymmetric Extension in Continental Lithosphere". In: *Tectonophysics* 223.1, pp. 75–96. ISSN: 0040-1951. DOI: 10.1016/0040-1951(93)90159-H.

— (2005). "Lithosphere Tearing at STEP Faults: Response to Edges of Subduction Zones". In: *Earth and Planetary Science Letters* 236.1, pp. 505–523. ISSN: 0012-821X. DOI: 10.1016/j.epsl.2005.03.022.

Group, G. C. (2022). *GEBCO_2022 Grid*. British Oceanographic Data Centre. DOI: 10.5285/e0f0bb80-ab44-2739-e053-6c86abc0289c.

Guard, J. C. (2013). *Seafloor Movements Observed by Seafloor Geodetic Observations after the 2011 off the Pacific Coast of Tohoku Earthquake*. URL: https://cais.gsi.go.jp/YOCHIREN/report/kaihou89/03_04.pdf.

Haberland, C., M. Bohm, and G. Asch (2014). "Accretionary Nature of the Crust of Central and East Java (Indonesia) Revealed by Local Earthquake Travel-Time Tomography". In: *Journal of Asian Earth Sciences* 96, pp. 287–295. ISSN: 1367-9120. DOI: 10.1016/j.jseaes.2014.09.019.

Hackl, M., R. Malservisi, and S. Wdowinski (2009). "Strain Rate Patterns from Dense GPS Networks". In: *Natural Hazards and Earth System Sciences* 9.4, pp. 1177–1187. ISSN: 1561-8633. DOI: 10.5194/nhess-9-1177-2009.

Hall, R. and I. Sevastjanova (2012). "Australian Crust in Indonesia". In: *Australian Journal of Earth Sciences* 59.6, pp. 827–844. ISSN: 0812-0099. DOI: 10.1080/08120099.2012.692335.

Hall, R., B. Clements, and H. R. Smyth (2009). "Sundaland: Basement Character, Structure and Plate Tectonic Development". In: *PROCEEDINGS, INDONESIAN PETROLEUM ASSOCIATION* 33rd Annual Convention, 2009.

Hamilton, W. (1970). "The Uralides and the Motion of the Russian and Siberian Platforms". In: *GSA Bulletin* 81.9, pp. 2553–2576. ISSN: 0016-7606. DOI: 10.1130/0016-7606(1970)81[2553:TUATMO]2.0.CO;2.

Han, S.-C., C. K. Shum, M. Bevis, C. Ji, and C.-Y. Kuo (2006). "Crustal Dilatation Observed by GRACE After the 2004 Sumatra-Andaman Earthquake". In: *Science* 313.5787, pp. 658–662. DOI: 10.1126/science.1128661.

Hanks, T. C. and H. Kanamori (1979). "A Moment Magnitude Scale". In: *Journal of Geophysical Research: Solid Earth* 84.B5, pp. 2348–2350. ISSN: 2156-2202. DOI: 10.1029/JB084iB05p02348.

Hardebeck, J. L. (2015). "Stress Orientations in Subduction Zones and the Strength of Subduction Megathrust Faults". In: *Science* 349.6253, pp. 1213–1216. ISSN: 0036-8075, 1095-9203. DOI: 10.1126/science.aac5625. pmid: 26359399.

Hashimoto, C., A. Noda, T. Sagiya, and M. Matsu'ura (2009). "Interplate Seismogenic Zones along the Kuril–Japan Trench Inferred from GPS Data Inversion". In: *Nature Geoscience* 2.2 (2), pp. 141–144. ISSN: 1752-0908. DOI: 10.1038/ngeo421.

Hashimoto, M., N. Choosakul, M. Hashizume, S. Takemoto, H. Takiguchi, Y. Fukuda, and K. Fujimori (2006). "Crustal Deformations Associated with the Great Sumatra-Andaman Earthquake Deduced from Continuous GPS

Observation". In: *Earth, Planets and Space* 58.2, pp. 127–139. DOI: 10.1186/BF03353369.

Hastie, L. M. and J. C. Savage (1970). "A Dislocation Model for the 1964 Alaska Earthquake". In: *Bulletin of the Seismological Society of America* 60.4, pp. 1389–1392. ISSN: 0037-1106. DOI: 10.1785/BSSA0600041389.

Hayes, G. P., G. L. Moore, D. E. Portner, M. Hearne, H. Flamme, M. Furtney, and G. M. Smoczyk (2018). "Slab2, a Comprehensive Subduction Zone Geometry Model". In: *Science* 362.6410, pp. 58–61. ISSN: 0036-8075, 1095-9203. DOI: 10.1126/science.aat4723. pmid: 30093602.

Heki, K. and Y. Mitsui (2013). "Accelerated Pacific Plate Subduction Following Interplate Thrust Earthquakes at the Japan Trench". In: *Earth and Planetary Science Letters* 363, pp. 44–49. ISSN: 0012-821X. DOI: 10.1016/j.epsl.2012.12.031.

Heki, K., S. Miyazaki, and H. Tsuji (1997). "Silent Fault Slip Following an Interplate Thrust Earthquake at the Japan Trench". In: *Nature* 386.6625 (6625), pp. 595–598. ISSN: 1476-4687. DOI: 10.1038/386595a0.

Herman, M. W., K. P. Furlong, and R. Govers (2018). "The Accumulation of Slip Deficit in Subduction Zones in the Absence of Mechanical Coupling: Implications for the Behavior of Megathrust Earthquakes". In: *Journal of Geophysical Research: Solid Earth* 123.9, pp. 8260–8278. ISSN: 2169-9356. DOI: 10.1029/2018JB016336.

Herman, M. W. and R. Govers (2020). "Locating Fully Locked Asperities Along the South America Subduction Megathrust: A New Physical Interseismic Inversion Approach in a Bayesian Framework". In: *Geochemistry, Geophysics, Geosystems* 21.8. ISSN: 1525-2027. DOI: 10.1029/2020GC009063.

Hetland, E. A. and B. H. Hager (2005). "Postseismic and Interseismic Displacements near a Strike-Slip Fault: A Two-Dimensional Theory for General Linear Viscoelastic Rheologies". In: *Journal of Geophysical Research: Solid Earth* 110.B10. ISSN: 2156-2202. DOI: 10.1029/2005JB003689.

— (2006). "Interseismic Strain Accumulation: Spin-up, Cycle Invariance, and Irregular Rupture Sequences". In: *Geochemistry, Geophysics, Geosystems* 7.5. ISSN: 1525-2027. DOI: 10.1029/2005GC001087.

Hirokichi, H., M. Akira, and E. Kinya (1957). "On the Mechanism of the Earthquakes and the Stresses Producing Them in Japan and Its Vicinity (Second Paper)". In: *Science reports of the Tohoku University*. 8.3, p. 22.

Hirose, H., K. Hirahara, F. Kimata, N. Fujii, and S. Miyazaki (1999). "A Slow Thrust Slip Event Following the Two 1996 Hyuganada Earthquakes beneath the Bungo Channel, Southwest Japan". In: *Geophysical Research Letters* 26.21, pp. 3237–3240. ISSN: 1944-8007. DOI: 10.1029/1999GL010999.

Hirth, G. and D. Kohlstedt (2003). "Rheology of the Upper Mantle and the Mantle Wedge: A View from the Experimentalists". In: *Inside the Subduction Factory*. Geophysical Monograph Series, pp. 83–105. ISSN: 9781118668573. DOI: 10.1029/138GM06.

Hirth, G. and D. L. Kohlstedt (1996). "Water in the Oceanic Upper Mantle: Implications for Rheology, Melt Extraction and the Evolution of the Lithosphere". In: *Earth and Planetary Science Letters* 144.1, pp. 93–108. ISSN: 0012-821X. DOI: 10.1016/0012-821X(96)00154-9.

Hoffmann, F., S. Metzger, M. Moreno, Z. Deng, C. Sippl, F. Ortega-Culaciati, and O. Oncken (2018). "Characterizing Afterslip and Ground Displacement Rate Increase Following the 2014 Iquique-Pisagua Mw 8.1 Earthquake, Northern Chile". In: *Journal of Geophysical Research: Solid Earth* 123.5, pp. 4171–4192. ISSN: 2169-9356. DOI: 10.1002/2017JB014970.

Hofmann, R. B., J. H. Bennett, and D. B. Crice (1968). *Geodimeter Fault Movement Investigations in California*. Bulletin No. 116-6. Sacramento: California Department of Water Resources. viii, 183.

Holmes, A. (1928). "Radioactivity and Continental Drift". In: *Geological Magazine* 65, pp. 236–238.

— (1931). "Radioactivity and Earth Movements". In: *Nature* 128.3227 (3227), pp. 419–419. ISSN: 1476-4687. DOI: 10.1038/128419b0.

Honsho, C., M. Kido, F. Tomita, and N. Uchida (2019). "Offshore Postseismic Deformation of the 2011 Tohoku Earthquake Revisited: Application of an Improved GPS-Acoustic Positioning Method Considering Horizontal Gradient of Sound Speed Structure". In: *Journal of Geophysical Research: Solid Earth* 124.6, pp. 5990–6009. ISSN: 2169-9356. DOI: 10.1029/2018JB017135.

Horai, K.-i. (1982). "A Satellite Altimetric Geoid in the Philippine Sea". In: *Nature* 299.5879 (5879), pp. 117–121. ISSN: 1476-4687. DOI: 10.1038/299117a0.

Hsu, Y.-J., M. Simons, J.-P. Avouac, J. Galetzka, K. Sieh, M. Chlieh, D. Natawidjaja, L. Prawirodirdjo, and Y. Bock (2006). "Frictional Afterslip Following the 2005 Nias-Simeulue Earthquake, Sumatra". In: *Science* 312.5782, pp. 1921–1926. ISSN: 0036-8075, 1095-9203. DOI: 10.1126/science.1126960. pmid: 16809533.

Hu, Y., K. Wang, J. He, J. Klotz, and G. Khazaradze (2004). "Three-Dimensional Viscoelastic Finite Element Model for Postseismic Deformation of the Great 1960 Chile Earthquake". In: *Journal of Geophysical Research: Solid Earth* 109.B12. ISSN: 2156-2202. DOI: 10.1029/2004JB003163.

Hu, Y., R. Bürgmann, P. Banerjee, L. Feng, E. M. Hill, T. Ito, T. Tabei, and K. Wang (2016a). "Asthenosphere Rheology Inferred from Observations of the 2012 Indian Ocean Earthquake". In: *Nature* 538.7625 (7625), pp. 368–372. ISSN: 1476-4687. DOI: 10.1038/nature19787.

Hu, Y., R. Bürgmann, J. T. Freymueller, P. Banerjee, and K. Wang (2014). "Contributions of Poroelastic Rebound and a Weak Volcanic Arc to the Postseismic Deformation of the 2011 Tohoku Earthquake". In: *Earth, Planets and Space* 66.1, p. 106. ISSN: 1880-5981. DOI: 10.1186/1880-5981-66-106.

Hu, Y., R. Bürgmann, N. Uchida, P. Banerjee, and J. T. Freymueller (2016b). "Stress-Driven Relaxation of Heterogeneous Upper Mantle and Time-Dependent Afterslip Following the 2011 Tohoku Earthquake". In: *Journal of Geophysical Research: Solid Earth* 121.1, pp. 385–411. ISSN: 2169-9356. DOI: 10.1002/2015JB012508.

Hu, Y. and K. Wang (2012). "Spherical-Earth Finite Element Model of Short-Term Postseismic Deformation Following the 2004 Sumatra Earthquake". In: *Journal of Geophysical Research: Solid Earth* 117.B5. ISSN: 2156-2202. DOI: 10.1029/2012JB009153.

Huang, C., H. Zhang, and S. M. Robeson (2011). "On the Validity of Commonly Used Covariance and Variogram Functions on the Sphere". In: *Mathematical Geosciences* 43.6, pp. 721–733. ISSN: 1874-8961, 1874-8953. DOI: 10.1007/s11004-011-9344-7.

Hutchison, C. S. (2014). "Tectonic Evolution of Southeast Asia". In: 60, p. 18.

— (1994). "Gondwana and Cathaysian Blocks, Palaeotethys Sutures and Cenozoic Tectonics in South-east Asia". In: *Active Continental Margins — Present*

and Past. Ed. by P. Giese and J. Behrmann. Berlin, Heidelberg: Springer, pp. 388–405. ISBN: 978-3-662-38521-0. DOI: 10.1007/978-3-662-38521-0_14.

Hyndman, R. D. and K. Wang (1993). "Thermal Constraints on the Zone of Major Thrust Earthquake Failure: The Cascadia Subduction Zone". In: *Journal of Geophysical Research: Solid Earth* 98.B2, pp. 2039–2060. ISSN: 2156-2202. DOI: 10.1029/92JB02279.

— (1995). "The Rupture Zone of Cascadia Great Earthquakes from Current Deformation and the Thermal Regime". In: *Journal of Geophysical Research: Solid Earth* 100.B11, pp. 22133–22154. ISSN: 2156-2202. DOI: 10.1029/95JB01970.

Ikari, M. J., C. Marone, and D. M. Saffer (2011). "On the Relation between Fault Strength and Frictional Stability". In: *Geology* 39.1, pp. 83–86. ISSN: 0091-7613. DOI: 10.1130/G31416.1.

Isacks, B., J. Oliver, and L. R. Sykes (1968). "Seismology and the New Global Tectonics". In: *Journal of Geophysical Research (1896-1977)* 73.18, pp. 5855–5899. ISSN: 2156-2202. DOI: 10.1029/JB073i018p05855.

Isacks, B., L. R. Sykes, and J. Oliver (1969). "Focal Mechanisms of Deep and Shallow Earthquakes in the Tonga-Kermadec Region and the Tectonics of Island Arcs". In: *GSA Bulletin* 80.8, pp. 1443–1470. ISSN: 0016-7606. DOI: 10.1130/0016-7606(1969)80[1443:FMODAS]2.0.CO;2.

Itoh, Y., T. Nishimura, K. Wang, and J. He (2021). "New Megathrust Locking Model for the Southern Kurile Subduction Zone Incorporating Viscoelastic Relaxation and Non-Uniform Compliance of Upper Plate". In: *Journal of Geophysical Research: Solid Earth* 126.5, e2020JB019981. ISSN: 2169-9356. DOI: 10.1029/2020JB019981.

Itoh, Y., K. Wang, T. Nishimura, and J. He (2019). "Compliant Volcanic Arc and Backarc Crust in Southern Kurile Suggested by Interseismic Geodetic Deformation". In: *Geophysical Research Letters* 46.21, pp. 11790–11798. ISSN: 0094-8276, 1944-8007. DOI: 10.1029/2019GL084656.

Ivins, E. R. (1996). "Transient Creep of a Composite Lower Crust: 2. A Polymineralic Basis for Rapidly Evolving Postseismic Deformation Modes". In: *Journal of Geophysical Research: Solid Earth* 101.B12, pp. 28005–28028. ISSN: 2156-2202. DOI: 10.1029/96JB02846.

Jaeger, J. C. (C. (1956). *Elasticity, Fracture, and Flow, with Engineering and Geological Applications.* Methuen's Monographs on Physical Subjects. London: Methuen; 152 pp.

Jin, S. and P.-H. Park (2006). "Strain Accumulation in South Korea Inferred from GPS Measurements". In: *Earth, Planets and Space* 58.5, pp. 529–534. ISSN: 1880-5981. DOI: 10.1186/BF03351950.

Johnson, K. M., A. Mavrommatis, and P. Segall (2016). "Small Interseismic Asperities and Widespread Aseismic Creep on the Northern Japan Subduction Interface". In: *Geophysical Research Letters* 43.1, pp. 135–143. ISSN: 1944-8007. DOI: 10.1002/2015GL066707.

Jónsson, S., P. Segall, R. Pedersen, and G. Björnsson (2003). "Post-Earthquake Ground Movements Correlated to Pore-Pressure Transients". In: *Nature* 424.6945 (6945), pp. 179–183. ISSN: 1476-4687. DOI: 10.1038/nature01776.

Jordan, T. E., B. L. Isacks, R. W. Allmendinger, J. A. Brewer, V. A. Ramos, and C. J. Ando (1983). "Andean Tectonics Related to Geometry of Subducted Nazca Plate". In: *GSA Bulletin* 94.3, pp. 341–361. ISSN: 0016-7606. DOI: 10.1130/0016-7606(1983)94<341:ATRTGO>2.0.CO;2.

Kanamori, H. (1972). "Mechanism of Tsunami Earthquakes". In: *Physics of the Earth and Planetary Interiors* 6.5, pp. 346–359. ISSN: 0031-9201. DOI: 10.1016/0031-9201(72)90058-1.

Kanamori, H. and J. J. Cipar (1974). "Focal Process of the Great Chilean Earthquake May 22, 1960". In: *Physics of the Earth and Planetary Interiors* 9.2, pp. 128–136. ISSN: 0031-9201. DOI: 10.1016/0031-9201(74)90029-6.

Karato, S.-I. and H. Jung (2003). "Effects of Pressure on High-Temperature Dislocation Creep in Olivine". In: *Philosophical Magazine* 83.3, pp. 401–414. ISSN: 1478-6435. DOI: 10.1080/0141861021000025829.

Karig, D. E. (1974). "Evolution of Arc Systems in the Western Pacific". In: *Annual Review of Earth and Planetary Sciences* 2.1, pp. 51–75. ISSN: 0084-6597, 1545-4495. DOI: 10.1146/annurev.ea.02.050174.000411.

Katsumata, K., N. Wada, and M. Kasahara (2006). "Three-Dimensional P and S Wave Velocity Structures beneath the Hokkaido Corner, Japan-Kurile Arc-Arc Junction". In: *Earth, Planets and Space* 58.8, e37–e40. ISSN: 1880-5981. DOI: 10.1186/BF03352595.

Kawakatsu, H., P. Kumar, Y. Takei, M. Shinohara, T. Kanazawa, E. Araki, and K. Suyehiro (2009). "Seismic Evidence for Sharp Lithosphere-Asthenosphere Boundaries of Oceanic Plates". In: *Science* 324.5926, pp. 499–502. ISSN: 0036-8075, 1095-9203. DOI: 10.1126/science.1169499. pmid: 19390042.

Kelleher, J., L. Sykes, and J. Oliver (1973). "Possible Criteria for Predicting Earthquake Locations and Their Application to Major Plate Boundaries of the Pacific and the Caribbean". In: *Journal of Geophysical Research (1896-1977)* 78.14, pp. 2547–2585. ISSN: 2156-2202. DOI: 10.1029/JB078i014p02547.

Kellogg, J. N., V. Vega, T. C. Stailings, C. L. V. Aiken, and J. N. Kellogg (1995). "Tectonic Development of Panama, Costa Rica, and the Colombian Andes: Constraints from Global Positioning System Geodetic Studies and Gravity". In: *Geological Society of America Special Paper* 295, pp. 75–90. DOI: 10.1130/SPE295-p75.

Kendrick, E. (1997). "Preliminary Results of the Central Andes GPS Project". In: *Eos Trans. AGU* 78.46.

Kendrick, E., M. Bevis, R. Smalley, and B. Brooks (2001). "An Integrated Crustal Velocity Field for the Central Andes". In: *Geochemistry, Geophysics, Geosystems* 2.11. ISSN: 1525-2027. DOI: 10.1029/2001GC000191.

Kendrick, E., B. A. Brooks, M. Bevis, R. S. Jr, E. Lauria, M. Araujo, and H. Parra (2006). "Active Orogeny of the South-Central Andes Studied with GPS Geodesy". In: *Revista de la Asociación Geológica Argentina* 61.4, pp. 555–566.

Khazaradze, G., K. Wang, J. Klotz, Y. Hu, and J. He (2002). "Prolonged Post-Seismic Deformation of the 1960 Great Chile Earthquake and Implications for Mantle Rheology". In: *Geophysical Research Letters* 29.22, pp. 7-1-7–4. ISSN: 1944-8007. DOI: 10.1029/2002GL015986.

Khazaradze, G. and J. Klotz (2003). "Short- and Long-Term Effects of GPS Measured Crustal Deformation Rates along the South Central Andes". In: *Journal of Geophysical Research: Solid Earth* 108.B6. ISSN: 2156-2202. DOI: 10.1029/2002JB001879.

Kido, M. *et al.* (2017). "Progress in the Project for Development of GPS/Acoustic Technique Over the Last 4 Years". In: *International Symposium on Geodesy for Earthquake and Natural Hazards (GENAH)*. Ed. by

M. Hashimoto. International Association of Geodesy Symposia. Cham: Springer International Publishing, pp. 3–10. ISBN: 978-3-319-39768-9. DOI: 10.1007/1345_2015_127.

Kirby, S. H. (1983). "Rheology of the Lithosphere". In: *Reviews of Geophysics* 21.6, pp. 1458–1487. ISSN: 1944-9208. DOI: 10.1029/RG021i006p01458.

Kita, S., J. Nakajima, A. Hasegawa, T. Okada, K. Katsumata, Y. Asano, and T. Kimura (2014). "Detailed Seismic Attenuation Structure beneath Hokkaido, Northeastern Japan: Arc-arc Collision Process, Arc Magmatism, and Seismotectonics". In: *Journal of Geophysical Research: Solid Earth* 119.8, pp. 6486–6511. ISSN: 2169-9356. DOI: 10.1002/2014JB011099.

Klein, E., M. Métois, G. Meneses, C. Vigny, and A. Delorme (2018a). "Bridging the Gap between North and Central Chile: Insight from New GPS Data on Coupling Complexities and the Andean Sliver Motion". In: *Geophysical Journal International* 213.3, pp. 1924–1933. ISSN: 0956-540X, 1365-246X. DOI: 10.1093/gji/ggy094.

Klein, E., Z. Duputel, D. Zigone, C. Vigny, J.-P. Boy, C. Doubre, and G. Meneses (2018b). "Deep Transient Slow Slip Detected by Survey GPS in the Region of Atacama, Chile". In: *Geophysical Research Letters* 45.22, pp. 12, 263–12, 273. ISSN: 1944-8007. DOI: 10.1029/2018GL080613.

Klein, E., L. Fleitout, C. Vigny, and J. Garaud (2016). "Afterslip and Viscoelastic Relaxation Model Inferred from the Large-Scale Post-Seismic Deformation Following the 2010 Mw 8.8 Maule Earthquake (Chile)". In: *Geophysical Journal International* 205.3, pp. 1455–1472. ISSN: 0956-540X. DOI: 10.1093/gji/ggw086.

Klotz, J., G. Khazaradze, D. Angermann, C. Reigber, R. Perdomo, and O. Cifuentes (2001). "Earthquake Cycle Dominates Contemporary Crustal Deformation in Central and Southern Andes". In: *Earth and Planetary Science Letters* 193.3, pp. 437–446. ISSN: 0012-821X. DOI: 10.1016/S0012-821X(01)00532-5.

Kneller, E. A., P. E. van Keken, S.-i. Karato, and J. Park (2005). "B-Type Olivine Fabric in the Mantle Wedge: Insights from High-Resolution Non-Newtonian Subduction Zone Models". In: *Earth and Planetary Science Letters* 237.3, pp. 781–797. ISSN: 0012-821X. DOI: 10.1016/j.epsl.2005.06.049.

Koulali, A., S. McClusky, S. Susilo, Y. Leonard, P. Cummins, P. Tregoning, I. Meilano, J. Efendi, and A. B. Wijanarto (2017). "The Kinematics of Crustal Deformation in Java from GPS Observations: Implications for Fault Slip Partitioning". In: *Earth and Planetary Science Letters* 458, pp. 69–79. ISSN: 0012-821X. DOI: 10.1016/j.epsl.2016.10.039.

Kreemer, C., G. Blewitt, W. C. Hammond, and H.-P. Plag (2006). "Global Deformation from the Great 2004 Sumatra-Andaman Earthquake Observed by GPS: Implications for Rupture Process and Global Reference Frame". In: *Earth, Planets and Space* 58.2, pp. 141–148. DOI: 10.1186/BF03353370.

Kreemer, C., G. Blewitt, and E. C. Klein (2014). "A Geodetic Plate Motion and Global Strain Rate Model". In: *Geochemistry, Geophysics, Geosystems* 15.10, pp. 3849–3889. ISSN: 1525-2027. DOI: 10.1002/2014GC005407.

Kumar, P. and H. Kawakatsu (2011). "Imaging the Seismic Lithosphere-Asthenosphere Boundary of the Oceanic Plate". In: *Geochemistry, Geophysics, Geosystems* 12.1. ISSN: 1525-2027. DOI: 10.1029/2010GC003358.

Landau, L. D., E. M. Lifshitz, A. M. Kosevich, and L. P. Pitaevskii (1986). *Theory of Elasticity.* 3rd ed. Vol. 7. 10 vols. Course of Theoretical Physics. Elsevier Butterworth Heinemann. 200 pp. ISBN: 978-0-7506-2633-0.

Larson, K. M. and M. Lisowski (1994). "Strain Accumulation in the Shumagin Islands: Results of Initial GPS Measurements". In: *Geophysical Research Letters* 21.6, pp. 489–492. ISSN: 1944-8007. DOI: 10.1029/94GL00417.

Lay, T., H. Kanamori, C. J. Ammon, A. R. Hutko, K. P. Furlong, and L. Rivera (2009). "The 2006–2007 Kuril Islands Great Earthquake Sequence". In: *Journal of Geophysical Research: Solid Earth* 114.B11. ISSN: 2156-2202. DOI: 10.1029/2008JB006280.

Lay, T., H. Kanamori, C. J. Ammon, K. D. Koper, A. R. Hutko, L. Ye, H. Yue, and T. M. Rushing (2012). "Depth-Varying Rupture Properties of Subduction Zone Megathrust Faults". In: *Journal of Geophysical Research: Solid Earth* 117.B4. ISSN: 2156-2202. DOI: 10.1029/2011JB009133.

Leng, W. and W. Mao (2015). "Geodynamic Modeling of Thermal Structure of Subduction Zones". In: *Science China Earth Sciences* 58.7, pp. 1070–1083. ISSN: 1674-7313, 1869-1897. DOI: 10.1007/s11430-015-5107-5.

Li, S., J. Bedford, M. Moreno, W. D. Barnhart, M. Rosenau, and O. Oncken (2018a). "Spatiotemporal Variation of Mantle Viscosity and the Pres-

ence of Cratonic Mantle Inferred From 8 Years of Postseismic Deformation Following the 2010 Maule, Chile, Earthquake". In: *Geochemistry, Geophysics, Geosystems* 19.9, pp. 3272–3285. ISSN: 1525-2027. DOI: 10.1029/2018GC007645.

Li, S., J. Fukuda, and O. Oncken (2020). "Geodetic Evidence of Time-Dependent Viscoelastic Interseismic Deformation Driven by Megathrust Locking in the Southwest Japan Subduction Zone". In: *Geophysical Research Letters* 47.4, e2019GL085551. ISSN: 1944-8007. DOI: 10.1029/2019GL085551.

Li, S., M. Moreno, J. Bedford, M. Rosenau, O. Heidbach, D. Melnick, and O. Oncken (2017). "Postseismic Uplift of the Andes Following the 2010 Maule Earthquake: Implications for Mantle Rheology". In: *Geophysical Research Letters* 44.4, pp. 1768–1776. ISSN: 1944-8007. DOI: 10.1002/2016GL071995.

Li, S., M. Moreno, J. Bedford, M. Rosenau, and O. Oncken (2015). "Revisiting Viscoelastic Effects on Interseismic Deformation and Locking Degree: A Case Study of the Peru-North Chile Subduction Zone". In: *Journal of Geophysical Research: Solid Earth* 120.6, pp. 4522–4538. ISSN: 2169-9356. DOI: 10.1002/2015JB011903.

Li, S., K. Wang, Y. Wang, Y. Jiang, and S. E. Dosso (2018b). "Geodetically Inferred Locking State of the Cascadia Megathrust Based on a Viscoelastic Earth Model". In: *Journal of Geophysical Research: Solid Earth* 123.9, pp. 8056–8072. ISSN: 2169-9356. DOI: 10.1029/2018JB015620.

Lin, Y.-n. N. *et al.* (2013). "Coseismic and Postseismic Slip Associated with the 2010 Maule Earthquake, Chile: Characterizing the Arauco Peninsula Barrier Effect". In: *Journal of Geophysical Research: Solid Earth* 118.6, pp. 3142–3159. ISSN: 2169-9356. DOI: 10.1002/jgrb.50207.

Lindenbergh, R., M. Keshin, H. van der Marel, and R. Hanssen (2008). "High Resolution Spatio-temporal Water Vapour Mapping Using GPS and MERIS Observations". In: *International Journal of Remote Sensing* 29.8, pp. 2393–2409. ISSN: 0143-1161, 1366-5901. DOI: 10.1080/01431160701436825.

Lindsey, E. O., R. Mallick, J. A. Hubbard, K. E. Bradley, R. V. Almeida, J. D. P. Moore, R. Bürgmann, and E. M. Hill (2021). "Slip Rate Deficit and Earthquake Potential on Shallow Megathrusts". In: *Nature Geoscience* 14.5 (5), pp. 321–326. ISSN: 1752-0908. DOI: 10.1038/s41561-021-00736-x.

Liu, X., D. Zhao, and S. Li (2013). "Seismic Heterogeneity and Anisotropy of the Southern Kuril Arc: Insight into Megathrust Earthquakes". In: *Geophysical Journal International* 194.2, pp. 1069–1090. ISSN: 0956-540X. DOI: 10.1093/gji/ggt150.

Liu, X., D. Zhao, S. Li, and W. Wei (2017). "Age of the Subducting Pacific Slab beneath East Asia and Its Geodynamic Implications". In: *Earth and Planetary Science Letters* 464, pp. 166–174. DOI: 10.1016/j.epsl.2017.02.024.

Liu, Z., S. Owen, D. Dong, P. Lundgren, F. Webb, E. Hetland, and M. Simons (2010). "Estimation of Interplate Coupling in the Nankai Trough, Japan Using GPS Data from 1996 to 2006". In: *Geophysical Journal International* 181.3, pp. 1313–1328. ISSN: 0956-540X. DOI: 10.1111/j.1365-246X.2010.04600.x.

Long, M. D. (2013). "Constraints on Subduction Geodynamics from Seismic Anisotropy". In: *Reviews of Geophysics* 51.1, pp. 76–112. ISSN: 1944-9208. DOI: 10.1002/rog.20008.

Loveless, J. P. (2017). "Super-Interseismic Periods: Redefining Earthquake Recurrence: Super-interseismic Periods". In: *Geophysical Research Letters* 44.3, pp. 1329–1332. ISSN: 00948276. DOI: 10.1002/2017GL072525.

Loveless, J. P. and B. J. Meade (2010). "Geodetic Imaging of Plate Motions, Slip Rates, and Partitioning of Deformation in Japan". In: *Journal of Geophysical Research: Solid Earth* 115.B2. ISSN: 2156-2202. DOI: 10.1029/2008JB006248.

— (2011). "Spatial Correlation of Interseismic Coupling and Coseismic Rupture Extent of the 2011 MW = 9.0 Tohoku-oki Earthquake". In: *Geophysical Research Letters* 38.17. ISSN: 1944-8007. DOI: 10.1029/2011GL048561.

— (2016). "Two Decades of Spatiotemporal Variations in Subduction Zone Coupling Offshore Japan". In: *Earth and Planetary Science Letters* 436, pp. 19–30. ISSN: 0012-821X. DOI: 10.1016/j.epsl.2015.12.033.

Machuca-Mory, D. F. and C. V. Deutsch (2013). "Non-Stationary Geostatistical Modeling Based on Distance Weighted Statistics and Distributions". In: *Mathematical Geosciences* 45.1, pp. 31–48. ISSN: 1874-8961, 1874-8953. DOI: 10.1007/s11004-012-9428-z.

Mainprice, D. H. and M. S. Paterson (1984). "Experimental Studies of the Role of Water in the Plasticity of Quartzites". In: *Journal of Geophysical Research: Solid Earth* 89.B6, pp. 4257–4269. ISSN: 2156-2202. DOI: 10.1029/JB089iB06p04257.

Malservisi, R. *et al.* (2015). "Multiscale Postseismic Behavior on a Megathrust: The 2012 Nicoya Earthquake, Costa Rica". In: *Geochemistry Geophysics Geosystems* 16.6, pp. 1848–1864. ISSN: 1525-2027. DOI: 10.1002/2015GC005794.

Marone, C. (1998). "Laboratory-Derived Friction Laws and Their Application to Seismic Faulting". In: *Annual Review of Earth and Planetary Sciences* 26.1, pp. 643–696. ISSN: 0084-6597, 1545-4495. DOI: 10.1146/annurev.earth.26.1.643.

Massonnet, D. and K. L. Feigl (1998). "Radar Interferometry and Its Application to Changes in the Earth's Surface". In: *Reviews of Geophysics* 36.4, pp. 441–500. ISSN: 1944-9208. DOI: 10.1029/97RG03139.

Massonnet, D., M. Rossi, C. Carmona, F. Adragna, G. Peltzer, K. Feigl, and T. Rabaute (1993). "The Displacement Field of the Landers Earthquake Mapped by Radar Interferometry". In: *Nature* 364.6433 (6433), pp. 138–142. ISSN: 1476-4687. DOI: 10.1038/364138a0.

Masterlark, T. (2003). "Finite Element Model Predictions of Static Deformation from Dislocation Sources in a Subduction Zone: Sensitivities to Homogeneous, Isotropic, Poisson-solid, and Half-Space Assumptions". In: *Journal of Geophysical Research: Solid Earth* 108.B11. ISSN: 2156-2202. DOI: 10.1029/2002JB002296.

Masuti, S., S. D. Barbot, S.-i. Karato, L. Feng, and P. Banerjee (2016). "Upper-Mantle Water Stratification Inferred from Observations of the 2012 Indian Ocean Earthquake". In: *Nature* 538.7625 (7625), pp. 373–377. ISSN: 1476-4687. DOI: 10.1038/nature19783.

MATLAB (2018). *R2018b*. Natick, Massachusetts: The MathWorks Inc.

Matsu'ura, M. and T. Sato (1989). "A Dislocation Model for the Earthquake Cycle at Convergent Plate Boundaries". In: *Geophysical Journal International* 96.1, pp. 23–32. ISSN: 0956540X, 1365246X. DOI: 10.1111/j.1365-246X.1989.tb05247.x.

Matuzawa, T. (1964). *Study of Earthquakes*. Tokyo: Shoten.

Mavrommatis, A. P., P. Segall, and K. M. Johnson (2014). "A Decadal-Scale Deformation Transient Prior to the 2011 M_w 9.0 Tohoku-oki Earthquake". In: *Geophysical Research Letters* 41.13, pp. 4486–4494. ISSN: 00948276. DOI: 10.1002/2014GL060139.

— (2017). "A Physical Model for Interseismic Erosion of Locked Fault Asperities". In: *Journal of Geophysical Research: Solid Earth* 122.10, pp. 8326–8346. ISSN: 2169-9356. DOI: 10.1002/2017JB014533.

McAdoo, D. C. (1981). "Geoid Anomalies in the Vicinity of Subduction Zones". In: *Journal of Geophysical Research: Solid Earth* 86.B7, pp. 6073–6090. ISSN: 2156-2202. DOI: 10.1029/JB086iB07p06073.

McCaffrey, R., M. D. Long, C. Goldfinger, P. C. Zwick, J. L. Nabelek, C. K. Johnson, and C. Smith (2000). "Rotation and Plate Locking at the Southern Cascadia Subduction Zone". In: *Geophysical Research Letters* 27.19, pp. 3117–3120. ISSN: 1944-8007. DOI: 10.1029/2000GL011768.

McCaffrey, R., A. I. Qamar, R. W. King, R. Wells, G. Khazaradze, C. A. Williams, C. W. Stevens, J. J. Vollick, and P. C. Zwick (2007). "Fault Locking, Block Rotation and Crustal Deformation in the Pacific Northwest". In: *Geophysical Journal International* 169.3, pp. 1315–1340. ISSN: 1365-246X. DOI: 10.1111/j.1365-246X.2007.03371.x.

McFarland, P. K., R. A. Bennett, P. Alvarado, and P. G. DeCelles (2017). "Rapid Geodetic Shortening Across the Eastern Cordillera of NW Argentina Observed by the Puna-Andes GPS Array". In: *Journal of Geophysical Research*, p. 24. DOI: 10.1002/2017JB014739.

McGuire, J. J. *et al.* (2017). *The SZ4D Initiative: Understanding the Processes That Underlie Subduction Zone Hazards in 4D. Vision Document Submitted to the National Science Foundation.* URL: https://www.sz4d.org/_files/ugd/66466d_c5202b9573e1413eb006995304a4b274.pdf.

McKenzie, K. A. and K. P. Furlong (2021). "Isolating Non-Subduction-Driven Tectonic Processes in Cascadia". In: *Geoscience Letters* 8.1, p. 10. ISSN: 2196-4092. DOI: 10.1186/s40562-021-00181-z.

Meade, B. (1971). "Horizontal Movement along the San Andreas Fault System". In: *Royal Society of New Zealand, Bulletin* 9, pp. 175–179. ISSN: , URL: http://pascal-francis.inist.fr/vibad/index.php?action=getRecordDetail&idt=PASCAL7312016589.

Meade, B. K. (1965). "Horizontal Crustal Movements in the United States". In: *Bulletin Géodésique (1946-1975)* 77.1, pp. 215–236. ISSN: 0007-4632. DOI: 10.1007/BF02525807.

Melnick, D., M. Moreno, J. Quinteros, J. C. Baez, Z. Deng, S. Li, and O. Oncken (2017). "The Super-Interseismic Phase of the Megathrust Earthquake Cycle in Chile: The Super-interseismic Earthquake Cycle". In: *Geophysical Research Letters* 44.2, pp. 784–791. ISSN: 00948276. DOI: 10.1002/2016GL071845.

Melosh, H. J. (1976). "Nonlinear Stress Propagation in the Earth's Upper Mantle". In: *Journal of Geophysical Research (1896-1977)* 81.32, pp. 5621–5632. ISSN: 2156-2202. DOI: 10.1029/JB081i032p05621.

— (1978). "Reply [to "Comment on 'Nonlinear Stress Propagation in the Earth's Upper Mantle' by H. J. Melosh"]". In: *Journal of Geophysical Research: Solid Earth* 83.B10, pp. 5009–5010. ISSN: 2156-2202. DOI: 10.1029/JB083iB10p05009.

Melosh, H. J. and L. Fleitout (1982). "The Earthquake Cycle in Subduction Zones". In: *Geophysical Research Letters* 9.1, pp. 21–24. ISSN: 1944-8007. DOI: 10.1029/GL009i001p00021.

Melosh, H. J. and A. Raefsky (1981). "A Simple and Efficient Method for Introducing Faults into Finite Element Computations". In: *Bulletin of the Seismological Society of America* 71.5, pp. 1391–1400. ISSN: 1943-3573, 0037-1106. DOI: 10.1785/BSSA0710051391.

— (1983). "Anelastic Response of the Earth to a Dip Slip Earthquake". In: *Journal of Geophysical Research: Solid Earth* 88.B1, pp. 515–526. ISSN: 2156-2202. DOI: 10.1029/JB088iB01p00515.

Melosh, H. J. and A. Raefsky (1980). "The Dynamical Origin of Subduction Zone Topography". In: *Geophysical Journal International* 60.3, pp. 333–354. ISSN: 0956-540X. DOI: 10.1111/j.1365-246X.1980.tb04812.x.

Melosh, H. J. and C. A. Williams (1989). "Mechanics of Graben Formation in Crustal Rocks: A Finite Element Analysis". In: *Journal of Geophysical Research: Solid Earth* 94.B10, pp. 13961–13973. ISSN: 2156-2202. DOI: 10.1029/JB094iB10p13961.

Meltzner, A. J., K. Sieh, H.-W. Chiang, C.-C. Shen, B. W. Suwargadi, D. H. Natawidjaja, B. E. Philibosian, R. W. Briggs, and J. Galetzka (2010).

"Coral Evidence for Earthquake Recurrence and an A.D. 1390–1455 Cluster at the South End of the 2004 Aceh–Andaman Rupture". In: *Journal of Geophysical Research: Solid Earth* 115.B10. ISSN: 2156-2202. DOI: 10.1029/2010JB007499.

Meltzner, A. J. *et al.* (2015). "Time-Varying Interseismic Strain Rates and Similar Seismic Ruptures on the Nias–Simeulue Patch of the Sunda Megathrust". In: *Quaternary Science Reviews* 122, pp. 258–281. ISSN: 0277-3791. DOI: 10.1016/j.quascirev.2015.06.003.

Meng, L., A. Inbal, and J.-P. Ampuero (2011). "A Window into the Complexity of the Dynamic Rupture of the 2011 Mw 9 Tohoku-Oki Earthquake". In: *Geophysical Research Letters* 38.7. ISSN: 1944-8007. DOI: 10.1029/2011GL048118.

Mescherikov, J. A. (1968). "Recent Crustal Movements in Seismic Regions: Geodetic and Geomorphic Data". In: *Tectonophysics.* Proceedings of a Symposium Held during the 14th General Assembly of the International Union of Geodesy and Geophysics 6.1, pp. 29–39. ISSN: 0040-1951. DOI: 10.1016/0040-1951(68)90024-3.

Metcalfe, I. (2000). "The Bentong–Raub Suture Zone". In: *Journal of Asian Earth Sciences* 18.6, pp. 691–712. ISSN: 1367-9120. DOI: 10.1016/S1367-9120(00)00043-2.

Metcalfe, I. (2011). "Tectonic Framework and Phanerozoic Evolution of Sundaland". In: *Gondwana Research.* Special Section: The South and East Facades of Sundaland 19.1, pp. 3–21. ISSN: 1342-937X. DOI: 10.1016/j.gr.2010.02.016.

Métivier, L., Z. Altamimi, and H. Rouby (2020). "Past and Present ITRF Solutions from Geophysical Perspectives". In: *Advances in Space Research* 65.12, pp. 2711–2722. ISSN: 02731177. DOI: 10.1016/j.asr.2020.03.031.

Métois, M., A. Socquet, and C. Vigny (2012). "Interseismic Coupling, Segmentation and Mechanical Behavior of the Central Chile Subduction Zone". In: *Journal of Geophysical Research: Solid Earth* 117.B3. ISSN: 2156-2202. DOI: 10.1029/2011JB008736.

Métois, M., A. Socquet, C. Vigny, D. Carrizo, S. Peyrat, A. Delorme, E. Maureira, M.-C. Valderas-Bermejo, and I. Ortega (2013). "Revisiting the North Chile Seismic Gap Segmentation Using GPS-derived Interseismic

Coupling". In: *Geophysical Journal International* 194.3, pp. 1283–1294. ISSN: 0956-540X. DOI: 10.1093/gji/ggt183.

Métois, M., C. Vigny, and A. Socquet (2016). "Interseismic Coupling, Megathrust Earthquakes and Seismic Swarms Along the Chilean Subduction Zone (38°–18°S)". In: *Pure and Applied Geophysics* 173.5, pp. 1431–1449. ISSN: 1420-9136. DOI: 10.1007/s00024-016-1280-5.

Métois, M., C. Vigny, A. Socquet, A. Delorme, S. Morvan, I. Ortega, and C.-M. Valderas-Bermejo (2014). "GPS-derived Interseismic Coupling on the Subduction and Seismic Hazards in the Atacama Region, Chile". In: *Geophysical Journal International* 196.2, pp. 644–655. ISSN: 0956-540X. DOI: 10.1093/gji/ggt418.

Michel, G. W. *et al.* (2001). "Crustal Motion and Block Behaviour in SE-Asia from GPS Measurements". In: *Earth and Planetary Science Letters* 187.3, pp. 239–244. ISSN: 0012-821X. DOI: 10.1016/S0012-821X(01)00298-9.

Miyabe, N. (1955). "Vertical Earth Movement in Nankai District". In: *Bull. Geogr. Surv. Inst.* 4, pp. 1–14. URL: https://cir.nii.ac.jp/crid/1570009751437620992.

Miyabe, N. (1931). "On the Vertical Earth Movement in Kwanto Districts." In: *Bulletin of the Earthquake Research Institute, Tokyo Imperial University* 9, pp. 1–21. URL: http://hdl.handle.net/2261/9977.

Moore, J. C. and D. Saffer (2001). "Updip Limit of the Seismogenic Zone beneath the Accretionary Prism of Southwest Japan: An Effect of Diagenetic to Low-Grade Metamorphic Processes and Increasing Effective Stress". In: *Geology* 29.2, pp. 183–186. ISSN: 0091-7613. DOI: 10.1130/0091-7613(2001)029<0183:ULOTSZ>2.0.CO;2.

Moreno, M. *et al.* (2011). "Heterogeneous Plate Locking in the South–Central Chile Subduction Zone: Building up the next Great Earthquake". In: *Earth and Planetary Science Letters* 305.3, pp. 413–424. ISSN: 0012-821X. DOI: 10.1016/j.epsl.2011.03.025.

Moreno, M. *et al.* (2012). "Toward Understanding Tectonic Control on the Mw 8.8 2010 Maule Chile Earthquake". In: *Earth and Planetary Science Letters* 321–322, pp. 152–165. ISSN: 0012-821X. DOI: 10.1016/j.epsl.2012.01.006.

Moreno, M. S., J. Klotz, D. Melnick, H. Echtler, and K. Bataille (2008). "Active Faulting and Heterogeneous Deformation across a Megathrust Segment Boundary from GPS Data, South Central Chile (36–39°S)". In: *Geo-

chemistry, Geophysics, Geosystems 9.12. ISSN: 1525-2027. DOI: 10.1029/2008GC002198.

Moreno, M., M. Rosenau, and O. Oncken (2010). "2010 Maule Earthquake Slip Correlates with Pre-Seismic Locking of Andean Subduction Zone". In: *Nature* 467.7312, pp. 198–202. ISSN: 1476-4687. DOI: 10.1038/nature09349.

Morgan, J. K. (2015). "Effects of Cohesion on the Structural and Mechanical Evolution of Fold and Thrust Belts and Contractional Wedges: Discrete Element Simulations". In: *Journal of Geophysical Research: Solid Earth* 120.5, pp. 3870–3896. ISSN: 2169-9356. DOI: 10.1002/2014JB011455.

Mouthereau, F., A. B. Watts, and E. Burov (2013). "Structure of Orogenic Belts Controlled by Lithosphere Age". In: *Nature Geoscience* 6.9 (9), pp. 785–789. ISSN: 1752-0908. DOI: 10.1038/ngeo1902.

Muto, J., J. D. P. Moore, S. Barbot, T. Iinuma, Y. Ohta, and H. Iwamori (2019). "Coupled Afterslip and Transient Mantle Flow after the 2011 Tohoku Earthquake". In: *Science Advances* 5.9, eaaw1164. ISSN: 2375-2548. DOI: 10.1126/sciadv.aaw1164.

Muto, K. (1932). "A Study of Displacements of Triangulation Points." In: *Bulletin of the Earthquake Research Institute, Tokyo Imperial University* 10, pp. 384–392. URL: http://hdl.handle.net/2261/10037.

Nishimura, T. (2011). "Back-Arc Spreading of the Northern Izu–Ogasawara (Bonin) Islands Arc Clarified by GPS Data". In: *Tectonophysics* 512.1-4, pp. 60–67. ISSN: 00401951. DOI: 10.1016/j.tecto.2011.09.022.

Nishimura, T., T. Hirasawa, S. Miyazaki, T. Sagiya, T. Tada, S. Miura, and K. Tanaka (2004). "Temporal Change of Interplate Coupling in Northeastern Japan during 1995–2002 Estimated from Continuous GPS Observations". In: *Geophysical Journal International* 157.2, pp. 901–916. ISSN: 0956-540X. DOI: 10.1111/j.1365-246X.2004.02159.x.

Nocquet, J.-M. *et al.* (2014). "Motion of Continental Slivers and Creeping Subduction in the Northern Andes". In: *Nature Geoscience* 7.4 (4), pp. 287–291. ISSN: 1752-0908. DOI: 10.1038/ngeo2099.

Nocquet, J.-M. *et al.* (2017). "Supercycle at the Ecuadorian Subduction Zone Revealed after the 2016 Pedernales Earthquake". In: *Nature Geoscience* 10.2 (2), pp. 145–149. ISSN: 1752-0908. DOI: 10.1038/ngeo2864.

Noda, A., T. Takahama, T. Kawasato, and M. Matsu'ura (2018). "Interpretation of Offshore Crustal Movements Following the 2011 Tohoku-Oki Earthquake by the Combined Effect of Afterslip and Viscoelastic Stress Relaxation". In: *Pure and Applied Geophysics* 175.2, pp. 559–572. ISSN: 1420-9136. DOI: 10.1007/s00024-017-1682-z.

Noda, H. and N. Lapusta (2013). "Stable Creeping Fault Segments Can Become Destructive as a Result of Dynamic Weakening". In: *Nature* 493.7433 (7433), pp. 518–521. ISSN: 1476-4687. DOI: 10.1038/nature11703.

Norabuena, E., L. Leffler-Griffin, A. Mao, T. Dixon, S. Stein, I. S. Sacks, L. Ocola, and M. Ellis (1998). "Space Geodetic Observations of Nazca-South America Convergence Across the Central Andes". In: *Science* 279.5349, pp. 358–362. DOI: 10.1126/science.279.5349.358.

Nostro, C., A. Piersanti, A. Antonioli, and G. Spada (1999). "Spherical versus Flat Models of Coseismic and Postseismic Deformations". In: *Journal of Geophysical Research: Solid Earth* 104.B6, pp. 13115–13134. ISSN: 2156-2202. DOI: 10.1029/1999JB900097.

Nur, A. and G. Mavko (1974). "Postseismic Viscoelastic Rebound". In: *Science* 183.4121, pp. 204–206. ISSN: 0036-8075. JSTOR: 1737368. URL: https://www.jstor.org/stable/1737368.

Ogawa, R. and K. Heki (2007). "Slow Postseismic Recovery of Geoid Depression Formed by the 2004 Sumatra-Andaman Earthquake by Mantle Water Diffusion". In: *Geophysical Research Letters* 34.6. ISSN: 1944-8007. DOI: 10.1029/2007GL029340.

Ohzono, M., T. Sagiya, K. Hirahara, M. Hashimoto, A. Takeuchi, Y. Hoso, Y. Wada, K. Onoue, F. Ohya, and R. Doke (2011). "Strain Accumulation Process around the Atotsugawa Fault System in the Niigata-Kobe Tectonic Zone, Central Japan". In: *Geophysical Journal International* 184.3, pp. 977–990. ISSN: 0956-540X. DOI: 10.1111/j.1365-246X.2010.04876.x.

Okada, A. and T. Nagata (1953). "Land Deformation of the Neighbourhood of Muroto Point after the Nankaido Great Earthquake in 1946". In: *Bull. Earthq. Res. Inst* 31, pp. 169–177.

Okada, Y. (1985). "Surface Deformation Due to Shear and Tensile Faults in a Half-Space". In: *Bulletin of the Seismological Society of America* 75.4, pp. 1135–1154. ISSN: 0037-1106. DOI: 10.1785/BSSA0750041135.

Okuda, T. (1950). "On the Mode of the Vertical Land Deformation Accompanying the Great Nankaido Earthquake 1946". In: *Bull. Geogr. Surv. Inst* 2.1, pp. 37–59.

Ortiz, A. and J. Zambrano (1981). "La Provincia Geológica Precordillera Oriental". In: *Actas.* 8° Congreso Geológico Argentino. Vol. 3. Buenos Aires, Argentina, pp. 59–74.

Ozawa, S., M. Kaidzu, M. Murakami, T. Imakiire, and Y. Hatanaka (2004). "Coseismic and Postseismic Crustal Deformation after the M 8 Tokachi-oki Earthquake in Japan". In: *Earth, Planets and Space* 56.7, pp. 675–680. DOI: 10.1186/BF03352530.

Ozawa, S., T. Nishimura, H. Suito, T. Kobayashi, M. Tobita, and T. Imakiire (2011). "Coseismic and Postseismic Slip of the 2011 Magnitude-9 Tohoku-Oki Earthquake". In: *Nature* 475.7356, pp. 373–376. ISSN: 1476-4687. DOI: 10.1038/nature10227.

Panet, I., V. Mikhailov, M. Diament, F. Pollitz, G. King, O. De Viron, M. Holschneider, R. Biancale, and J.-M. Lemoine (2007). "Coseismic and Post-Seismic Signatures of the Sumatra 2004 December and 2005 March Earthquakes in GRACE Satellite Gravity". In: *Geophysical Journal International* 171.1, pp. 177–190. ISSN: 0956-540X. DOI: 10.1111/j.1365-246X.2007.03525.x.

Paul, J., A. R. Lowry, R. Bilham, S. Sen, and R. Smalley Jr. (2007). "Postseismic Deformation of the Andaman Islands Following the 26 December, 2004 Great Sumatra–Andaman Earthquake". In: *Geophysical Research Letters* 34.19. ISSN: 1944-8007. DOI: 10.1029/2007GL031024.

Pearson, D. M., P. Kapp, P. G. DeCelles, P. W. Reiners, G. E. Gehrels, M. N. Ducea, and A. Pullen (2013). "Influence of Pre-Andean Crustal Structure on Cenozoic Thrust Belt Kinematics and Shortening Magnitude: Northwestern Argentina". In: *Geosphere* 9.6, pp. 1766–1782. ISSN: 1553-040X. DOI: 10.1130/GES00923.1.

Peltzer, G., P. Rosen, F. Rogez, and K. Hudnut (1998). "Poroelastic Rebound along the Landers 1992 Earthquake Surface Rupture". In: *Journal of Geophysical Research: Solid Earth* 103.B12, pp. 30131–30145. ISSN: 2156-2202. DOI: 10.1029/98JB02302.

Peltzer, G., P. Rosen, F. Rogez, and K. Hudnut (1996). "Postseismic Rebound in Fault Step-Overs Caused by Pore Fluid Flow". In: *Science* 273.5279, pp. 1202–1204. DOI: 10.1126/science.273.5279.1202.

Peña, C., O. Heidbach, M. Moreno, J. Bedford, M. Ziegler, A. Tassara, and O. Oncken (2019). "Role of Lower Crust in the Postseismic Deformation of the 2010 Maule Earthquake: Insights from a Model with Power-Law Rheology". In: *Pure and Applied Geophysics* 176.9, pp. 3913–3928. ISSN: 1420-9136. DOI: 10.1007/s00024-018-02090-3.

— (2020). "Impact of Power-Law Rheology on the Viscoelastic Relaxation Pattern and Afterslip Distribution Following the 2010 Mw 8.8 Maule Earthquake". In: *Earth and Planetary Science Letters* 542, p. 116292. ISSN: 0012-821X. DOI: 10.1016/j.epsl.2020.116292.

Peña, C., O. Heidbach, M. Moreno, D. Melnick, and O. Oncken (2021). "Transient Deformation and Stress Patterns Induced by the 2010 Maule Earthquake in the Illapel Segment". In: *Frontiers in Earth Science* 9. ISSN: 2296-6463. URL: https://www.frontiersin.org/articles/10.3389/feart.2021.644834.

Perarnau, M., H. Gilbert, P. Alvarado, R. Martino, and M. Anderson (2012). "Crustal Structure of the Eastern Sierras Pampeanas of Argentina Using High Frequency Local Receiver Functions". In: *TECTONOPHYSICS* 580, pp. 208–217. ISSN: 0040-1951. DOI: 10.1016/j.tecto.2012.09.021.

Pérez-Gussinyé, M., A. R. Lowry, J. P. Morgan, and A. Tassara (2008). "Effective Elastic Thickness Variations along the Andean Margin and Their Relationship to Subduction Geometry". In: *Geochemistry, Geophysics, Geosystems* 9.2. ISSN: 1525-2027. DOI: 10.1029/2007GC001786.

Pérez-Gussinyé, M., A. R. Lowry, and A. B. Watts (2007). "Effective Elastic Thickness of South America and Its Implications for Intracontinental Deformation". In: *Geochemistry, Geophysics, Geosystems* 8.5. ISSN: 1525-2027. DOI: 10.1029/2006GC001511.

Perfettini, H. and J.-P. Avouac (2004). "Stress Transfer and Strain Rate Variations during the Seismic Cycle". In: *Journal of Geophysical Research: Solid Earth* 109.B6. ISSN: 2156-2202. DOI: 10.1029/2003JB002917.

Petit, C. and M. Fournier (2005). "Present-Day Velocity and Stress Fields of the Amurian Plate from Thin-Shell Finite-Element Modelling". In: *Geo-*

physical Journal International 160.1, pp. 357–369. ISSN: 0956-540X. DOI: 10.1111/j.1365-246X.2004.02486.x.

Philibosian, B., K. Sieh, J.-P. Avouac, D. H. Natawidjaja, H.-W. Chiang, C.-C. Wu, H. Perfettini, C.-C. Shen, M. R. Daryono, and B. W. Suwargadi (2014). "Rupture and Variable Coupling Behavior of the Mentawai Segment of the Sunda Megathrust during the Supercycle Culmination of 1797 to 1833". In: *Journal of Geophysical Research: Solid Earth* 119.9, pp. 7258–7287. ISSN: 2169-9356. DOI: 10.1002/2014JB011200.

Philibosian, B. *et al.* (2017). "Earthquake Supercycles on the Mentawai Segment of the Sunda Megathrust in the Seventeenth Century and Earlier". In: *Journal of Geophysical Research: Solid Earth* 122.1, pp. 642–676. ISSN: 2169-9313. DOI: 10.1002/2016JB013560.

Plafker, G. (1965). "Tectonic Deformation Associated with the 1964 Alaska Earthquake". In: *Science* 148.3678, pp. 1675–1687. ISSN: 0036-8075. JSTOR: 1716697. URL: https://www.jstor.org/stable/1716697.

— (1969). "Tectonics of the March 27, 1964 Alaska Earthquake". In: *U.S. Geological Survey Professional Paper* 543.I. URL: https://pubs.usgs.gov/pp/0543i/.

— (1972). "Alaskan Earthquake of 1964 and Chilean Earthquake of 1960: Implications for Arc Tectonics". In: *Journal of Geophysical Research* 77.5, pp. 901–925. ISSN: 2156-2202. DOI: 10.1029/JB077i005p00901.

Plafker, G. and J. C. Savage (1970). "Mechanism of the Chilean Earthquakes of May 21 and 22, 1960". In: *GSA Bulletin* 81.4, pp. 1001–1030. ISSN: 0016-7606. DOI: 10.1130/0016-7606(1970)81[1001:MOTCEO]2.0.CO;2.

Pollitz, F., P. Banerjee, K. Grijalva, B. Nagarajan, and R. Bürgmann (2008). "Effect of 3-D Viscoelastic Structure on Post-Seismic Relaxation from the 2004 M= 9.2 Sumatra Earthquake". In: *Geophysical Journal International* 173.1, pp. 189–204. ISSN: 1365-246X. DOI: 10.1111/j.1365-246X.2007.03666.x.

Pollitz, F., R. Bürgmann, and P. Banerjee (2006). "Post-Seismic Relaxation Following the Great 2004 Sumatra-Andaman Earthquake on a Compressible Self-Gravitating Earth". In: *Geophysical Journal International* 167.1, pp. 397–420. ISSN: 1365-246X. DOI: 10.1111/j.1365-246X.2006.03018.x.

Pollitz, F. and W. Thatcher (2010). "On the Resolution of Shallow Mantle Viscosity Structure Using Postearthquake Relaxation Data: Application to the 1999 Hector Mine, California, Earthquake". In: *Journal of Geophysical Research: Solid Earth* 115.B10. ISSN: 2156-2202. DOI: 10.1029/2010JB007405.

Pollitz, F. F. (2003). "Post-Seismic Relaxation Theory on a Laterally Heterogeneous Viscoelastic Model". In: *Geophysical Journal International* 155.1, pp. 57–78. ISSN: 0956-540X. DOI: 10.1046/j.1365-246X.2003.01980.x.

Pollitz, F. F. *et al.* (2011). "Coseismic Slip Distribution of the February 27, 2010 Mw 8.8 Maule, Chile Earthquake". In: *Geophysical Research Letters* 38.9. ISSN: 1944-8007. DOI: 10.1029/2011GL047065.

Prawirodirdjo, L., R. McCaffrey, C. D. Chadwell, Y. Bock, and C. Subarya (2010). "Geodetic Observations of an Earthquake Cycle at the Sumatra Subduction Zone: Role of Interseismic Strain Segmentation". In: *Journal of Geophysical Research: Solid Earth* 115.B3. ISSN: 2156-2202. DOI: 10.1029/2008JB006139.

Protti, M., V. González, A. V. Newman, T. H. Dixon, S. Y. Schwartz, J. S. Marshall, L. Feng, J. I. Walter, R. Malservisi, and S. E. Owen (2014). "Nicoya Earthquake Rupture Anticipated by Geodetic Measurement of the Locked Plate Interface". In: *Nature Geoscience* 7.2 (2), pp. 117–121. ISSN: 1752-0908. DOI: 10.1038/ngeo2038.

Purcell, G. J., L. Young, F. Spiess, D. Boegeman, R. Lawhead, H. Dragert, M. Schmidt, G. Jewsbury, M. Lisowski, and D. DeMets (1993). "Status of GPS/Acoustic Measurements of Seafloor Strain Accumulation Across the Cascadia Subduction Zone". In: URL: https://trs.jpl.nasa.gov/handle/2014/36043.

Qiu, Q., J. D. P. Moore, S. Barbot, L. Feng, and E. M. Hill (2018). "Transient Rheology of the Sumatran Mantle Wedge Revealed by a Decade of Great Earthquakes". In: *Nature Communications* 9.1 (1), p. 995. ISSN: 2041-1723. DOI: 10.1038/s41467-018-03298-6.

Ramos, V. A. (1988). "Late Proterozoic-Early Paleozoic of South America -a Collisional History". In: *Episodes Journal of International Geoscience* 11.3, pp. 168–174. DOI: 10.18814/epiiugs/1988/v11i3/003.

Ramos, V. A. (1999). "Plate Tectonic Setting of the Andean Cordillera". In: *Episodes Journal of International Geoscience* 22.3, pp. 183–190. DOI: 10.18814/epiiugs/1999/v22i3/005.

Ranalli, G. (1995). *Rheology of the Earth.* London; New York: Chapman & Hall. ISBN: 978-0-412-54670-9.

Rebischung, P., J. Griffiths, J. Ray, R. Schmid, X. Collilieux, and B. Garayt (2012). "IGS08: The IGS Realization of ITRF2008". In: *GPS Solutions* 16.4, pp. 483–494. ISSN: 1521-1886. DOI: 10.1007/s10291-011-0248-2.

Reid, H. F. (1908). "The Mechanics of the Earthquake". In: Lawson, A. C. and H. F. Reid. *The California Earthquake of April 18, 1906: Report of the State Earthquake Investigation Commission...* Vol. II. 87. Washington, D. C.: Carnegie institution of Washington.

Remy, D., H. Perfettini, N. Cotte, J. P. Avouac, M. Chlieh, F. Bondoux, A. Sladen, H. Tavera, and A. Socquet (2016). "Postseismic Relocking of the Subduction Megathrust Following the 2007 Pisco, Peru, Earthquake". In: *Journal of Geophysical Research: Solid Earth* 121.5, pp. 3978–3995. ISSN: 2169-9356. DOI: 10.1002/2015JB012417.

Rivas, C., G. Ortiz, P. Alvarado, M. Podesta, and A. Martin (2019). "Modern Crustal Seismicity in the Northern Andean Precordillera, Argentina". In: *Tectonophysics* 762, pp. 144–158. ISSN: 0040-1951. DOI: 10.1016/j.tecto.2019.04.019.

Ruegg, J. C., A. Rudloff, C. Vigny, R. Madariaga, J. B. de Chabalier, J. Campos, E. Kausel, S. Barrientos, and D. Dimitrov (2009). "Interseismic Strain Accumulation Measured by GPS in the Seismic Gap between Constitución and Concepción in Chile". In: *Physics of the Earth and Planetary Interiors.* Earthquakes in Subduction Zones: A Multidisciplinary Approach 175.1, pp. 78–85. ISSN: 0031-9201. DOI: 10.1016/j.pepi.2008.02.015.

Ruina, A. (1983). "Slip Instability and State Variable Friction Laws". In: *Journal of Geophysical Research: Solid Earth* 88.B12, pp. 10359–10370. ISSN: 2156-2202. DOI: 10.1029/JB088iB12p10359.

Rundle, J. B. (1976). "Anelastic Processes in Strike Slip Faulting: Application to the San Francisco Earthquake of 1906". URL: https://ui.adsabs.harvard.edu/abs/1976PhDT........17R.

Rundle, J. B. and D. D. Jackson (1977). "A Three-Dimensional Viscoelastic Model of a Strike Slip Fault". In: *Geophysical Journal of the Royal Astronomical Society* 49.3, pp. 575–591. ISSN: 0016-8009. DOI: 10.1111/j.1365-246X.1977.tb01305.x.

Rundle, J. B. (1978). "Viscoelastic Crustal Deformation by Finite Quasi-Static Sources". In: *Journal of Geophysical Research: Solid Earth* 83.B12, pp. 5937–5945. ISSN: 2156-2202. DOI: 10.1029/JB083iB12p05937.

— (1980). "Static Elastic-Gravitational Deformation of a Layered Half Space by Point Couple Sources". In: *Journal of Geophysical Research: Solid Earth* 85.B10, pp. 5355–5363. ISSN: 2156-2202. DOI: 10.1029/JB085iB10p05355.

— (1982). "Viscoelastic-Gravitational Deformation by a Rectangular Thrust Fault in a Layered Earth". In: *Journal of Geophysical Research: Solid Earth* 87.B9, pp. 7787–7796. ISSN: 2156-2202. DOI: 10.1029/JB087iB09p07787.

Sagiya, T., S. Miyazaki, and T. Tada (2000). "Continuous GPS Array and Present-day Crustal Deformation of Japan". In: *Pure and Applied Geophysics* 157.11, pp. 2303–2322. DOI: 10.1007/PL00022507.

Saillard, M., L. Audin, B. Rousset, J.-P. Avouac, M. Chlieh, S. R. Hall, L. Husson, and D. L. Farber (2017). "From the Seismic Cycle to Long-Term Deformation: Linking Seismic Coupling and Quaternary Coastal Geomorphology along the Andean Megathrust". In: *Tectonics* 36.2, pp. 241–256. ISSN: 1944-9194. DOI: 10.1002/2016TC004156.

Sales, J. K. (1968). "Regional Tectonic Setting and Mechanics of Origin of the Black Hills Uplift". In: pp. 10–27. URL: http://archives.datapages.com/data/wga/data/069/069001/10_wga0690010.htm.

Sandwell, D. T., J. A. Goff, J. Gevorgian, H. Harper, S.-S. Kim, Y. Yu, B. Tozer, P. Wessel, and W. H. F. Smith (2022). "Improved Bathymetric Prediction Using Geological Information: SYNBATH". In: *Earth and Space Science* 9.2, e2021EA002069. ISSN: 2333-5084. DOI: 10.1029/2021EA002069.

Sato, M., T. Ishikawa, N. Ujihara, S. Yoshida, M. Fujita, M. Mochizuki, and A. Asada (2011a). "Displacement Above the Hypocenter of the 2011 Tohoku-Oki Earthquake". In: *Science* 332.6036, pp. 1395–1395. ISSN: 0036-8075, 1095-9203. DOI: 10.1126/science.1207401. PMID: 21596950.

Sato, M., H. Saito, T. Ishikawa, Y. Matsumoto, M. Fujita, M. Mochizuki, and A. Asada (2011b). "Restoration of Interplate Locking after the 2005 Off-

Miyagi Prefecture Earthquake, Detected by GPS/Acoustic Seafloor Geodetic Observation". In: *Geophysical Research Letters* 38.1. ISSN: 1944-8007. DOI: 10.1029/2010GL045689.

Sauber, J., G. Carver, S. Cohen, and R. King (2006). "Crustal Deformation and the Seismic Cycle across the Kodiak Islands, Alaska". In: *Journal of Geophysical Research: Solid Earth* 111.B2. ISSN: 2156-2202. DOI: 10.1029/2005JB003626.

Savage, J. C. (1983). "A Dislocation Model of Strain Accumulation and Release at a Subduction Zone". In: *Journal of Geophysical Research: Solid Earth* 88.B6, pp. 4984–4996. ISSN: 2156-2202. DOI: 10.1029/JB088iB06p04984.

Savage, J. C. and R. O. Burford (1973). "Geodetic Determination of Relative Plate Motion in Central California". In: *Journal of Geophysical Research (1896-1977)* 78.5, pp. 832–845. ISSN: 2156-2202. DOI: 10.1029/JB078i005p00832.

Savage, J. C. and W. H. Prescott (1978). "Asthenosphere Readjustment and the Earthquake Cycle". In: *Journal of Geophysical Research: Solid Earth* 83.B7, pp. 3369–3376. ISSN: 2156-2202. DOI: 10.1029/JB083iB07p03369.

Savage, J. C., J. L. Svarc, and W. H. Prescott (1999). "Deformation across the Alaska-Aleutian Subduction Zone near Kodiak". In: *Geophysical Research Letters* 26.14, pp. 2117–2120. ISSN: 1944-8007. DOI: 10.1029/1999GL900471.

Savage, J. C., J. L. Svarc, W. H. Prescott, and W. K. Gross (1998). "Deformation across the Rupture Zone of the 1964 Alaska Earthquake, 1993–1997". In: *Journal of Geophysical Research: Solid Earth* 103.B9, pp. 21275–21283. ISSN: 2156-2202. DOI: 10.1029/98JB02048.

Scholz, C. H. and T. J. Fitch (1969). "Strain Accumulation along the San Andreas Fault". In: *Journal of Geophysical Research (1896-1977)* 74.27, pp. 6649–6666. ISSN: 2156-2202. DOI: 10.1029/JB074i027p06649.

Scholz, C. H. (1972). "Crustal Movements in Tectonic Areas". In: *Tectonophysics* 14.3, pp. 201–217. ISSN: 0040-1951. DOI: 10.1016/0040-1951(72)90069-8.

— (1998). "Earthquakes and Friction Laws". In: *Nature* 391.6662 (6662), pp. 37–42. ISSN: 1476-4687. DOI: 10.1038/34097.

Sébrier, M., J. L. Mercier, J. Macharé, D. Bonnot, J. Cabrera, and J. L. Blanc (1988). "The State of Stress in an Overriding Plate Situated above a Flat Slab: The Andes of Central Peru". In: *Tectonics* 7.4, pp. 895–928. ISSN: 02787407. DOI: 10.1029/TC007i004p00895.

Seemüller, W., L. Sánchez, M. Seitz, and H. Drewes (2010). "The Position and Velocity Solution SIR10P01 of the IGS Regional Network Associate Analysis Centre for SIRGAS (IGS RNAAC SIR)". In: URL: http://www.sirgas.org/fileadmin/docs/SIR10P01_DGFI_Report_86.pdf.

Segall, P. and J. L. Davis (1997). "GPS Applications for Geodynamics and Earthquake Studies". In: *Annual Review of Earth and Planetary Sciences* 25.1, pp. 301–336. ISSN: 0084-6597, 1545-4495. DOI: 10.1146/annurev.earth.25.1.301.

Seno, T., T. Sakurai, and S. Stein (1996). "Can the Okhotsk Plate Be Discriminated from the North American Plate?" In: *Journal of Geophysical Research: Solid Earth* 101.B5, pp. 11305–11315. ISSN: 2156-2202. DOI: 10.1029/96JB00532.

Shestakov, N. V. *et al.* (2011). "Present Tectonics of the Southeast of Russia as Seen from GPS Observations: Present Tectonics of the Southeast of Russia". In: *Geophysical Journal International* 184.2, pp. 529–540. ISSN: 0956540X. DOI: 10.1111/j.1365-246X.2010.04871.x.

Shi, F., S. Li, and M. Moreno (2020). "Megathrust Locking and Viscous Mantle Flow Induce Continental Shortening in Central Andes". In: *Pure and Applied Geophysics* 177.6, pp. 2841–2852. ISSN: 1420-9136. DOI: 10.1007/s00024-019-02403-0.

Shi, X., J. Kirby, C. Yu, A. Jiménez-Díaz, and J. Zhao (2017). "Spatial Variations in the Effective Elastic Thickness of the Lithosphere in Southeast Asia". In: *Gondwana Research* 42, pp. 49–62. ISSN: 1342-937X. DOI: 10.1016/j.gr.2016.10.005.

Shimazaki, K. (1972). "Focal Mechanism of a Shock at the Northwestern Boundary of the Pacific Plate: Extensional Feature of the Oceanic Lithosphere and Compressional Feature of the Continental Lithosphere". In: *Physics of the Earth and Planetary Interiors* 6.5, pp. 397–404. ISSN: 0031-9201. DOI: 10.1016/0031-9201(72)90064-7.

Shimazaki, K. and T. Nakata (1980). "Time-Predictable Recurrence Model for Large Earthquakes". In: *Geophysical Research Letters* 7.4, pp. 279–282. ISSN: 1944-8007. DOI: 10.1029/GL007i004p00279.

Sibson, R. (1981). "A Brief Description of Natural Neighbour Interpolation". In: *Interpreting Multivariate Data*. URL: https://ci.nii.ac.jp/naid/10022185042/.

Sieh, K. E. (1981). "A Review of Geological Evidence for Recurrence Times of Large Earthquakes". In: *Earthquake Prediction*. American Geophysical Union (AGU), pp. 181–207. ISBN: 978-1-118-66574-9. DOI: 10.1029/ME004p0181.

Simons, M. *et al.* (2011). "The 2011 Magnitude 9.0 Tohoku-Oki Earthquake: Mosaicking the Megathrust from Seconds to Centuries". In: *Science* 332.6036, pp. 1421–1425. ISSN: 0036-8075, 1095-9203. DOI: 10.1126/science.1206731.

Simons, W. J. F. *et al.* (2007). "A Decade of GPS in Southeast Asia: Resolving Sundaland Motion and Boundaries". In: *Journal of Geophysical Research: Solid Earth* 112.B6. ISSN: 2156-2202. DOI: 10.1029/2005JB003868.

Sladen, A. and J. Trevisan (2018). "Shallow Megathrust Earthquake Ruptures Betrayed by Their Outer-Trench Aftershocks Signature". In: *Earth and Planetary Science Letters* 483, pp. 105–113. ISSN: 0012821X. DOI: 10.1016/j.epsl.2017.12.006.

Smith, A. T. (1975). "Time-Dependent Strain Accumulation and Release at Island Arcs: Implications for the 1946 Nankaido Earthquake". PhD thesis. Massachusetts Institute of Technology.

Snay, R. A. and T. Matsikari (1991). "Horizontal Deformation in the Cascadia Subduction Zone as Derived from Serendipitous Geodetic Data". In: *Tectonophysics* 194.1, pp. 59–67. ISSN: 0040-1951. DOI: 10.1016/0040-1951(91)90272-T.

Spence, D. A. and D. L. Turcotte (1979). "Viscoelastic Relaxation of Cyclic Displacements on the San Andreas Fault". In: *Proceedings of the Royal Society of London. Series A, Mathematical and Physical Sciences* 365.1720, pp. 121–144. ISSN: 0080-4630. JSTOR: 79813. URL: https://www.jstor.org/stable/79813.

Steketee, J. A. (1958). "On Volterra's Dislocations in a Semi-Infinite Elastic Medium". In: *Canadian Journal of Physics* 36.2, pp. 192–205. ISSN: 0008-4204. DOI: 10.1139/p58-024.

Stewart, J. and A. B. Watts (1997). "Gravity Anomalies and Spatial Variations of Flexural Rigidity at Mountain Ranges". In: *Journal of Geophysical Research: Solid Earth* 102.B3, pp. 5327–5352. ISSN: 2156-2202. DOI: 10.1029/96JB03664.

Styron, R. and M. Pagani (2020). "The GEM Global Active Faults Database". In: *Earthquake Spectra* 36 (1_suppl), pp. 160–180. ISSN: 8755-2930. DOI: 10.1177/8755293020944182.

Suito, H. (2017). "Importance of Rheological Heterogeneity for Interpreting Viscoelastic Relaxation Caused by the 2011 Tohoku-Oki Earthquake". In: *Earth, Planets and Space* 69.1, p. 21. ISSN: 1880-5981. DOI: 10.1186/s40623-017-0611-9.

Suito, H. and J. T. Freymueller (2009). "A Viscoelastic and Afterslip Postseismic Deformation Model for the 1964 Alaska Earthquake". In: *Journal of Geophysical Research: Solid Earth* 114.B11. ISSN: 2156-2202. DOI: 10.1029/2008JB005954.

Sun, T. and K. Wang (2015). "Viscoelastic Relaxation Following Subduction Earthquakes and Its Effects on Afterslip Determination". In: *Journal of Geophysical Research: Solid Earth* 120.2, pp. 1329–1344. ISSN: 2169-9356. DOI: 10.1002/2014JB011707.

Sun, T., K. Wang, T. Fujiwara, S. Kodaira, and J. He (2017). "Large Fault Slip Peaking at Trench in the 2011 Tohoku-oki Earthquake". In: *Nature Communications* 8.1 (1), p. 14044. ISSN: 2041-1723. DOI: 10.1038/ncomms14044.

Sun, T. *et al.* (2014). "Prevalence of Viscoelastic Relaxation after the 2011 Tohoku-oki Earthquake". In: *Nature* 514.7520, pp. 84–87. ISSN: 1476-4687. DOI: 10.1038/nature13778.

Suwa, Y., S. Miura, A. Hasegawa, T. Sato, and K. Tachibana (2006). "Interplate Coupling beneath NE Japan Inferred from Three-Dimensional Displacement Field". In: *Journal of Geophysical Research: Solid Earth* 111.B4. ISSN: 2156-2202. DOI: 10.1029/2004JB003203.

Tajima, F., J. Mori, and B. L. N. Kennett (2013). "A Review of the 2011 Tohoku-Oki Earthquake (Mw 9.0): Large-scale Rupture across Heteroge-

neous Plate Coupling". In: *Tectonophysics*. Recent Megathrust Earthquakes and Tsunamis: Observations and Processes 586, pp. 15–34. ISSN: 0040-1951. DOI: 10.1016/j.tecto.2012.09.014.

Tanaka, A., M. Yamano, Y. Yano, and M. Sasada (2004). "Geothermal Gradient and Heat Flow Data in and around Japan (I): Appraisal of Heat Flow from Geothermal Gradient Data". In: *Earth, Planets and Space* 56.12, pp. 1191–1194. ISSN: 1880-5981. DOI: 10.1186/BF03353339.

Tatsumi, Y., Y.-I. Otofuji, T. Matsuda, and S. Nohda (1989). "Opening of the Sea of Japan Back-Arc Basin by Asthenospheric Injection". In: *Tectonophysics* 166.4, pp. 317–329. ISSN: 0040-1951. DOI: 10.1016/0040-1951(89)90283-7.

Thatcher, W. and J. B. Rundle (1979). "A Model for the Earthquake Cycle in Underthrust Zones". In: *Journal of Geophysical Research: Solid Earth* 84.B10, pp. 5540–5556. ISSN: 2156-2202. DOI: 10.1029/JB084iB10p05540.

— (1984). "A Viscoelastic Coupling Model for the Cyclic Deformation Due to Periodically Repeated Earthquakes at Subduction Zones". In: *Journal of Geophysical Research: Solid Earth* 89.B9, pp. 7631–7640. ISSN: 2156-2202. DOI: 10.1029/JB089iB09p07631.

Tichelaar, B. W. and L. J. Ruff (1993). "Depth of Seismic Coupling along Subduction Zones". In: *Journal of Geophysical Research: Solid Earth* 98.B2, pp. 2017–2037. ISSN: 2156-2202. DOI: 10.1029/92JB02045.

Tobin, D. G. and L. R. Sykes (1968). "Seismicity and Tectonics of the Northeast Pacific Ocean". In: *Journal of Geophysical Research (1896-1977)* 73.12, pp. 3821–3845. ISSN: 2156-2202. DOI: 10.1029/JB073i012p03821.

Tomita, F., M. Kido, Y. Ohta, T. Iinuma, and R. Hino (2017). "Along-Trench Variation in Seafloor Displacements after the 2011 Tohoku Earthquake". In: *Science Advances* 3.7, e1700113. ISSN: 2375-2548. DOI: 10.1126/sciadv.1700113.

Tomita, F., M. Kido, Y. Osada, R. Hino, Y. Ohta, and T. Iinuma (2015). "First Measurement of the Displacement Rate of the Pacific Plate near the Japan Trench after the 2011 Tohoku-Oki Earthquake Using GPS/Acoustic Technique". In: *Geophysical Research Letters* 42.20, pp. 8391–8397. ISSN: 1944-8007. DOI: 10.1002/2015GL065746.

Tomita, F., M. Kido, Y. Osada, R. Azuma, R. Hino, H. Fujimoto, T. Iinuma, Y. Ohta, and I. Wada (2014). "Postseismic Seafloor Deformation Associated with the 2011 Tohoku-Oki Earthquake Revealed by Repeated GPS/Acoustic Observations". Oral presentation. International Symposium on Geodesy for Earthquake and Natural Hazards (GENAH) (Matsushima, Japan).

Tong, X. *et al.* (2010). "The 2010 Maule, Chile Earthquake: Downdip Rupture Limit Revealed by Space Geodesy". In: *Geophysical Research Letters* 37.24. ISSN: 1944-8007. DOI: 10.1029/2010GL045805.

Trubienko, O., L. Fleitout, J.-D. Garaud, and C. Vigny (2013). "Interpretation of Interseismic Deformations and the Seismic Cycle Associated with Large Subduction Earthquakes". In: *Tectonophysics* 589, pp. 126–141. ISSN: 0040-1951. DOI: 10.1016/j.tecto.2012.12.027.

Tsuru, T., J.-O. Park, N. Takahashi, S. Kodaira, Y. Kido, Y. Kaneda, and Y. Kono (2000). "Tectonic Features of the Japan Trench Convergent Margin off Sanriku, Northeastern Japan, Revealed by Multichannel Seismic Reflection Data". In: *Journal of Geophysical Research: Solid Earth* 105.B7, pp. 16403–16413. ISSN: 2156-2202. DOI: 10.1029/2000JB900132.

Ueda, H., M. Ohtake, and H. Sato (2003). "Postseismic Crustal Deformation Following the 1993 Hokkaido Nansei-oki Earthquake, Northern Japan: Evidence for a Low-Viscosity Zone in the Uppermost Mantle: POSTSEISMIC CRUSTAL DEFORMATION". In: *Journal of Geophysical Research: Solid Earth* 108.B3. ISSN: 01480227. DOI: 10.1029/2002JB002067.

Van Veen, B. A. D., D. Vatvani, and F. Zijl (2014). "Tsunami Flood Modelling for Aceh & West Sumatra and Its Application for an Early Warning System". In: *Continental Shelf Research*. Numerical Modelling of Tsunamis 79, pp. 46–53. ISSN: 0278-4343. DOI: 10.1016/j.csr.2012.08.020.

Van Keken, P. E., B. Kiefer, and S. M. Peacock (2002). "High-Resolution Models of Subduction Zones: Implications for Mineral Dehydration Reactions and the Transport of Water into the Deep Mantle". In: *Geochemistry, Geophysics, Geosystems* 3.10. ISSN: 1525-2027. DOI: 10.1029/2001GC000256.

Veloza, G., R. Styron, M. Taylor, and A. Mora (2012). "Open-Source Archive of Active Faults for Northwest South America". In: *GSA Today* 22.10, pp. 4–10. ISSN: 10525173. DOI: 10.1130/GSAT-G156A.1.

Vening Meinesz, F. A. (1931). "Une Nouvelle Méthode Pour la Réduction Iso-statique Régionale de L'intensité de la Pesanteur". In: *Bulletin géodésique* 29.1, pp. 33–51. ISSN: 1432-1394. DOI: 10.1007/BF03030038.

Vening Meinesz, F. A. (1932). "The Expeditions, the Computations and the Results". In: *Gravity Expeditions at Sea, 1923-1930*. Vol. 1. Delft: Nether-lands Geodetic Commission. JSTOR: 1785636. URL: https://www.jstor.org/stable/1785636?origin=crossref.

Verdonck, D. (1995). "Three-Dimensional Model of Vertical Deformation at the Southern Cascadia Subduction Zone, Western United States". In: *Geology* 23.3, pp. 261–264. ISSN: 0091-7613. DOI: 10.1130/0091-7613(1995)023<0261:TDMOVD>2.3.CO;2.

Verfürth, R. (1994). "A Posteriori Error Estimation and Adaptive Mesh-Refinement Techniques". In: *Journal of Computational and Applied Mathematics* 50.1, pp. 67–83. ISSN: 0377-0427. DOI: 10.1016/0377-0427(94)90290-9.

Vigny, C. *et al.* (2005). "Insight into the 2004 Sumatra–Andaman Earthquake from GPS Measurements in Southeast Asia". In: *Nature* 436.7048 (7048), pp. 201–206. ISSN: 1476-4687. DOI: 10.1038/nature03937.

Vigny, C. *et al.* (2011). "The 2010 Mw 8.8 Maule Megathrust Earthquake of Central Chile, Monitored by GPS". In: *Science* 332.6036, pp. 1417–1421. ISSN: 0036-8075, 1095-9203. DOI: 10.1126/science.1204132. pmid: 21527673.

Villegas-Lanza, J. C., M. Chlieh, O. Cavalié, H. Tavera, P. Baby, J. Chire-Chira, and J.-M. Nocquet (2016). "Active Tectonics of Peru: Heterogeneous Interseismic Coupling along the Nazca Megathrust, Rigid Motion of the Peruvian Sliver, and Subandean Shortening Accommodation". In: *Journal of Geophysical Research: Solid Earth* 121.10, pp. 7371–7394. ISSN: 2169-9356. DOI: 10.1002/2016JB013080.

Voss, N. K., R. Malservisi, T. H. Dixon, and M. Protti (2017). "Slow Slip Events in the Early Part of the Earthquake Cycle". In: *Journal of Geophysical Research: Solid Earth* 122.8, pp. 6773–6786. ISSN: 2169-9356. DOI: 10.1002/2016JB013741.

Wackernagel, H. (2003). "Ordinary Kriging". In: *Multivariate Geostatistics: An Introduction with Applications*. Ed. by H. Wackernagel. Berlin, Heidelberg: Springer, pp. 79–88. ISBN: 978-3-662-05294-5. DOI: 10.1007/978-3-662-05294-5_11.

Wada, I. and K. Wang (2009). "Common Depth of Slab-Mantle Decoupling: Reconciling Diversity and Uniformity of Subduction Zones". In: *Geochemistry, Geophysics, Geosystems* 10.10. ISSN: 1525-2027. DOI: 10.1029/2009GC002570.

Wadati, K. (1935). "On the Activity of Deep Focus Earthquakes and in the Japan Island and Neighbourhoods". In: *Geophysical Magazine* 8, pp. 305–325. URL: https://cir.nii.ac.jp/crid/1573950399350020224.

Walsh, J. B. (1968). "Mechanics of Strike-Slip Faulting with Friction". In: *Journal of Geophysical Research (1896-1977)* 73.2, pp. 761–776. ISSN: 2156-2202. DOI: 10.1029/JB073i002p00761.

Wang, J., P. Mann, and R. R. Stewart (2018a). "Late Holocene Structural Style and Seismicity of Highly Transpressional Faults in Southern Haiti". In: *Tectonics* 37.10, pp. 3834–3852. ISSN: 1944-9194. DOI: 10.1029/2017TC004920.

Wang, K. (2007). "17. Elastic and Viscoelastic Models of Crustal Deformation in Subduction Earthquake Cycles". In: *The Seismogenic Zone of Subduction Thrust Faults*. Ed. by T. H. Dixon and C. Moore. New York Chichester, West Sussex: Columbia University Press. ISBN: 978-0-231-51201-5. DOI: 10.7312/dixo13866-017.

Wang, K., H. Dragert, and H. J. Melosh (1994). "Finite Element Study of Uplift and Strain across Vancouver Island". In: *Canadian Journal of Earth Sciences* 31.10, pp. 1510–1522. ISSN: 0008-4077. DOI: 10.1139/e94-134.

Wang, K., J. He, H. Dragert, and T. S. James (2001). "Three-Dimensional Viscoelastic Interseismic Deformation Model for the Cascadia Subduction Zone". In: *Earth, Planets and Space* 53.4, pp. 295–306. DOI: 10.1186/BF03352386.

Wang, K., Y. Hu, M. Bevis, E. Kendrick, R. Smalley Jr., R. B. Vargas, and E. Lauría (2007). "Crustal Motion in the Zone of the 1960 Chile Earthquake: Detangling Earthquake-Cycle Deformation and Forearc-Sliver Translation". In: *Geochemistry, Geophysics, Geosystems* 8.10. ISSN: 1525-2027. DOI: 10.1029/2007GC001721.

Wang, K., Y. Hu, and J. He (2012). "Deformation Cycles of Subduction Earthquakes in a Viscoelastic Earth". In: *Nature* 484.7394, pp. 327–332. ISSN: 00280836. DOI: 10.1038/nature11032.

Wang, K., T. Sun, L. Brown, R. Hino, F. Tomita, M. Kido, T. Iinuma, S. Kodaira, and T. Fujiwara (2018b). "Learning from Crustal Deformation

Associated with the M9 2011 Tohoku-oki Earthquake". In: *Geosphere* 14.2, pp. 552–571. ISSN: 1553-040X. DOI: 10.1130/GES01531.1.

Wang, K., R. Wells, S. Mazzotti, R. D. Hyndman, and T. Sagiya (2003). "A Revised Dislocation Model of Interseismic Deformation of the Cascadia Subduction Zone". In: *Journal of Geophysical Research: Solid Earth* 108.B1. ISSN: 2156-2202. DOI: 10.1029/2001JB001227.

Wang, K., Y. Zhu, E. Nissen, and Z.-K. Shen (2021). "On the Relevance of Geodetic Deformation Rates to Earthquake Potential". In: *Geophysical Research Letters* 48.11, e2021GL093231. ISSN: 1944-8007. DOI: 10.1029/2021GL093231.

Wang, M., Q. Li, F. Wang, R. Zhang, Y. Wang, H. Shi, P. Zhang, and Z. Shen (2011). "Far-Field Coseismic Displacements Associated with the 2011 Tohoku-oki Earthquake in Japan Observed by Global Positioning System". In: *Chinese Science Bulletin* 56.23, pp. 2419–2424. ISSN: 1861-9541. DOI: 10.1007/s11434-011-4588-7.

Wang, Z. and D. Zhao (2005). "Seismic Imaging of the Entire Arc of Tohoku and Hokkaido in Japan Using P-wave, S-wave and sP Depth-Phase Data". In: *Physics of the Earth and Planetary Interiors* 152.3, pp. 144–162. ISSN: 0031-9201. DOI: 10.1016/j.pepi.2005.06.010.

Ward, S. N. (1998a). "On the Consistency of Earthquake Moment Rates, Geological Fault Data, and Space Geodetic Strain: The United States". In: *Geophysical Journal International* 134.1, pp. 172–186. ISSN: 1365-246X.

— (1998b). "On the Consistency of Earthquake Moment Release and Space Geodetic Strain Rates: Europe". In: *Geophysical Journal International* 135.3, pp. 1011–1018. ISSN: 1365-246X.

Watanabe, S.-i., M. Sato, M. Fujita, T. Ishikawa, Y. Yokota, N. Ujihara, and A. Asada (2014). "Evidence of Viscoelastic Deformation Following the 2011 Tohoku-Oki Earthquake Revealed from Seafloor Geodetic Observation". In: *Geophysical Research Letters* 41.16, pp. 5789–5796. ISSN: 1944-8007. DOI: 10.1002/2014GL061134.

Watts, A. B. (1981). "The U.S. Atlantic Continental Margin: Subsidence History, Crustal Structure and Thermal Evolution". In: Bally, A. W. *Geology of Passive Continental Margins: History, Structure and Sedimentologic Record (with Special Emphasis on the Atlantic Margin)*. American Associ-

ation of Petroleum Geologists, pp. 1–75. URL: http://archives.datapages.com/data/specpubs/history2/data/a123b/a123/0001/0000/0001.htm.

— (2015). "6.01 - Crustal and Lithosphere Dynamics: An Introduction and Overview". In: *Treatise on Geophysics (Second Edition)*. Ed. by G. Schubert. Oxford: Elsevier, pp. 1–44. ISBN: 978-0-444-53803-1. DOI: 10.1016/B978-0-444-53802-4.00110-X.

Watts, A. B., S. H. Lamb, J. D. Fairhead, and J. F. Dewey (1995). "Lithospheric Flexure and Bending of the Central Andes". In: *Earth and Planetary Science Letters* 134.1, pp. 9–21. ISSN: 0012-821X. DOI: 10.1016/0012-821X(95)00095-T.

Weaver, R., A. P. Roberts, R. Flecker, D. I. M. Macdonald, and L. M. Fot'yanova (2003). "Geodynamic Implications of Paleomagnetic Data from Tertiary Sediments in Sakhalin, Russia (NW Pacific)". In: *Journal of Geophysical Research: Solid Earth* 108.B2. ISSN: 2156-2202. DOI: 10.1029/2001JB001226.

Weertman, J. and J. R. Weertman (1964). *Elementary Dislocation Theory*. Macmillan Series in Materials Science. New York etc.: Macmillan. ix, 213.

Wegener, A. (1912). "Die Entstehung der Kontinente". In: *Geologische Rundschau* 3.4, pp. 276–292. ISSN: 1432-1149. DOI: 10.1007/BF02202896.

Wegener, A. L. (1924). *The Origin of Continents and Oceans*. New York: Dutton. 212 pp.

Weischet, W. and R. V. Huene (1963). "Further Observations of Geologic and Geomorphic Changes Resulting from the Catastrophic Earthquake of May 1960, in Chile". In: *Bulletin of the Seismological Society of America* 53.6, pp. 1237–1257. ISSN: 0037-1106. DOI: 10.1785/BSSA0530061237.

Weiss, J. R. *et al.* (2016). "Isolating Active Orogenic Wedge Deformation in the Southern Subandes of Bolivia". In: *Journal of Geophysical Research: Solid Earth* 121.8, pp. 6192–6218. ISSN: 2169-9356. DOI: 10.1002/2016JB013145.

Wessel, P., J. F. Luis, L. Uieda, R. Scharroo, F. Wobbe, W. H. F. Smith, and D. Tian (2019). "The Generic Mapping Tools Version 6". In: *Geochemistry, Geophysics, Geosystems* 20.11, pp. 5556–5564. ISSN: 1525-2027. DOI: 10.1029/2019GC008515.

White, S. M., R. Trenkamp, and J. N. Kellogg (2003). "Recent Crustal Deformation and the Earthquake Cycle along the Ecuador–Colombia Subduction

Zone". In: *Earth and Planetary Science Letters* 216.3, pp. 231–242. ISSN: 0012-821X. DOI: 10.1016/S0012-821X(03)00535-1.

Williams, T. B., H. M. Kelsey, and J. T. Freymueller (2006). "GPS-derived Strain in Northwestern California: Termination of the San Andreas Fault System and Convergence of the Sierra Nevada–Great Valley Block Contribute to Southern Cascadia Forearc Contraction". In: *Tectonophysics* 413.3, pp. 171–184. ISSN: 0040-1951. DOI: 10.1016/j.tecto.2005.10.047.

Wilson, J. T. (1963). "Continental Drift". In: *Scientific American* 208.4, pp. 86–103. ISSN: 0036-8733. JSTOR: 24936535. URL: https://www.jstor.org/stable/24936535.

— (1965). "A New Class of Faults and Their Bearing on Continental Drift". In: *Nature* 207.4995 (4995), pp. 343–347. ISSN: 1476-4687. DOI: 10.1038/207343a0.

— (1966). "Did the Atlantic Close and Then Re-Open?" In: *Nature* 211.5050 (5050), pp. 676–681. ISSN: 1476-4687. DOI: 10.1038/211676a0.

Wimpenny, S., A. Copley, C. Benavente, and E. Aguirre (2018). "Extension and Dynamics of the Andes Inferred From the 2016 Parina (Huarichancara) Earthquake". In: *Journal of Geophysical Research: Solid Earth* 123.9, pp. 8198–8228. ISSN: 2169-9356. DOI: 10.1029/2018JB015588.

Wu, P. (2004). "Using Commercial Finite Element Packages for the Study of Earth Deformations, Sea Levels and the State of Stress". In: *Geophysical Journal International* 158.2, pp. 401–408. ISSN: 0956-540X. DOI: 10.1111/j.1365-246X.2004.02338.x.

Yamagiwa, S., S. Miyazaki, K. Hirahara, and Y. Fukahata (2015). "Afterslip and Viscoelastic Relaxation Following the 2011 Tohoku-oki Earthquake (M_w 9.0) Inferred from Inland GPS and Seafloor GPS/Acoustic Data". In: *Geophysical Research Letters* 42.1, pp. 66–73. ISSN: 00948276. DOI: 10.1002/2014GL061735.

Yamanaka, Y. and M. Kikuchi (2004). "Asperity Map along the Subduction Zone in Northeastern Japan Inferred from Regional Seismic Data". In: *Journal of Geophysical Research: Solid Earth* 109.B7. ISSN: 2156-2202. DOI: 10.1029/2003JB002683.

Yoshioka, S. and Y. Matsuoka (2013). "Interplate Coupling along the Nankai Trough, Southwest Japan, Inferred from Inversion Analyses of GPS Data:

Effects of Subducting Plate Geometry and Spacing of Hypothetical Ocean-Bottom GPS Stations". In: *Tectonophysics*. Great Earthquakes along Subduction Zones 600, pp. 165–174. ISSN: 0040-951. DOI: 10.1016/j.tecto.2013.01.023.

Yoshioka, S., K. Wang, and S. Mazzotti (2005). "Interseismic Locking of the Plate Interface in the Northern Cascadia Subduction Zone, Inferred from Inversion of GPS Data". In: *Earth and Planetary Science Letters* 231.3, pp. 239–247. ISSN: 0012-821X. DOI: 10.1016/j.epsl.2004.12.018.

Yuzariyadi, M. and K. Heki (2021). "Enhancement of Interplate Coupling in Adjacent Segments after Recent Megathrust Earthquakes". In: *Tectonophysics*, p. 228719. ISSN: 0040-951. DOI: 10.1016/j.tecto.2021.228719.

Zhu, Y., K. Wang, and J. He (2020). "Effects of Earthquake Recurrence on Localization of Interseismic Deformation Around Locked Strike-Slip Faults". In: *Journal of Geophysical Research: Solid Earth* 125.8. ISSN: 2169-9356. DOI: 10.1029/2020JB019817.

Zienkiewicz, O. C. (1971). *The Finite Element Method in Engineering Science*. London: McGraw-Hill. xiv, 521. ISBN: 978-0-07-094138-0.

Zweck, C., J. T. Freymueller, and S. C. Cohen (2002). "Three-Dimensional Elastic Dislocation Modeling of the Postseismic Response to the 1964 Alaska Earthquake". In: *Journal of Geophysical Research: Solid Earth* 107.B4, ECV 1-1-ECV 1–11. ISSN: 2156-2202. DOI: 10.1029/2001JB000409.

Curriculum Vitae

Experience and education

2022–present
Research Scientist
GFZ German Research Centre for Geosciences Potsdam, Germany

2018–2022
PhD Candidate
Utrecht University, the Netherlands

2016–2018
MSc Earth Sciences
ETH Zürich, Switzerland
Thesis: *Modelling tectonics and seismicity due to lower lithosphere delamination-retreat across the northern Apennines thrust belt*

2013–2016
BSc Geophysics with Geology
Durham University, England
Dissertation: *2D resistivity survey across the north margin of the Stainmore Basin*

Publications

D'Acquisto, M., L. Dal Zilio, I. Molinari, E. Kissling, T. Gerya, and Y. van Dinther (2020). "Tectonics and Seismicity in the Northern Apennines Driven by Slab Retreat and Lithospheric Delamination". In: *Tectonophysics* 789, p. 228481. ISSN: 0040-1951. DOI: 10.1016/j.tecto.2020.228481.

D'Acquisto, M., M. W. Herman, R. E. M. Riva, and R. Govers (2023). "Can Plate Bending Explain the Observed Faster Landward Motion of Lateral Regions of the Subduction Zone After Major Megathrust Earthquakes?" In: *Journal of Geophysical Research: Solid Earth* 128.3. ISSN: 2169-9313, 2169-9356. DOI: 10.1029/2022JB025431.

D'Acquisto, M. and R. Govers (2023). "Offshore Landward Motion Shortly After a Subduction Earthquake Implies Rapid Relocking of the Shallow Megathrust". In: *Geophysical Research Letters* 50.1. ISSN: 0094-8276, 1944-8007. DOI: 10.1029/2022GL101638.